

COMPUTATIONAL FLUID DYNAMIC MODELLING OF BAFFLED OPEN VOLUMETRIC RECEIVER OPERATION

Mathew Jo Mathew

Submitted in fulfilment of the academic requirements for the degree of Master of Science in Mechanical Engineering, College of Agriculture, Engineering and Science, University of KwaZulu-Natal

Durban, South Africa

4th December 2020

Supervisor: Dr. Jean-Francois Philippe Pitot de la Beaujardiere

Co-Supervisor: Dr. Michael J. Brooks

COLLEGE OF AGRICULTURE, ENGINEERING AND SCIENCE

DECLARATION 1 - PLAGIARISM

I, Mathew Jo Mathew, declare that

1. The research reported in this thesis, except where otherwise indicated, is my original research.
2. This thesis has not been submitted for any degree or examination at any other university.
3. This thesis does not contain other persons' data, pictures, graphs or other information, unless specifically acknowledged as being sourced from other persons.
4. This thesis does not contain other persons' writing, unless specifically acknowledged as being sourced from other researchers. Where other written sources have been quoted, then:
 - a. Their words have been re-written but the general information attributed to them has been referenced
 - b. Where their exact words have been used, then their writing has been placed in italics and inside quotation marks, and referenced.
5. This thesis does not contain text, graphics or tables copied and pasted from the Internet, unless specifically acknowledged, and the source being detailed in the thesis and in the References sections.

Signed,

DECLARATION – SUPERVISOR

As the candidate's Supervisor I agree to the submission of this thesis.

Supervisor signature:

Date:

ABSTRACT

An Open Volumetric Receiver (OVR) is a type of solar energy receiver that is able to heat atmospheric air volumetrically via a porous absorber exposed to concentrated solar radiation, through which the air flows. OVRs have the potential to attain higher operational efficiency than tubular or cavity type receivers, and they have been extensively investigated for use in concentrating solar power (CSP) plants. In CSP applications, the hot air leaving the OVR is typically passed through a heat recovery steam generator to generate steam for the plant's steam turbine, after which it is returned to the OVR. Here, it is injected back into the atmosphere near the receiver inlet where some of the warm return air is re-entrained along with fresh air entering it. The amount of air that is re-entrained into the OVR is quantified by the air return ratio, and the higher this ratio, the lower the energy lost from the receiver. One of the factors limiting the operational efficiency of OVRs is fairly poor ARR performance, in the region of 50 % for state-of-the-art OVR designs.

This research aims to evaluate the effectiveness of the addition of the vertical air flow baffles in improving the air re-entrained performance of an OVR. The evaluation was carried out numerically using Ansys Fluent Computational Fluid Dynamics (CFD) modelling software. Prior to the core investigation, cold and hot flow validation studies were conducted with respect to a generalized porous absorber and an arrangement of HiTRec-II OVR modules. The corresponding CFD models were successfully validated against experimental data and the methodology used to model the HiTRec-II modules was used to model an arrangement of SolAir OVR modules and modified arrangements incorporating air flow baffles of varying lengths.

OVR air re-entrainment performance was evaluated in terms of the module air outlet temperature. The performance of the SolAir modules was evaluated when exposed to wind at varying magnitude and direction. The results from this study were used as a baseline against which the performance predicted for the SolAir modules modified with baffles (of different lengths) could be compared. A comparison of the results indicates that there is a clear increase in mean module air outlet temperature, when air flow baffles are incorporated with the lowest being 2.5 % and highest being 60.7 % increase in the temperature among the wind conditions and baffle lengths investigated for the study. The increase in the temperature also implies an improvement in air re-entrainment and thus OVR efficiency. The results also suggested the existence of an optimal baffle length for the receiver modules, beyond which the air outlet temperature drops and the OVR efficiency deteriorates.

ACKNOWLEDGMENTS

I would like to acknowledge the constant support and encouragement provided by my supervisor, Dr. Jean-Francois Philippe Pitot de la Beaujardiere and co-supervisor Dr. Michael J. Brooks throughout the course of the Master's degree. Thank you for providing me with valuable advice and insights as well as all of the technical resources I needed to complete my Master's degree. To the Aerospace Research Group (ASReG) and Group for Solar Energy Thermodynamics (GSET) teams at University of KwaZulu-Natal (UKZN) for providing the computational resources, and for the cheerful banter. I would also like to thank National Research Foundation (NRF) for their sponsorship. Last, but surely not least, to my mother for your constant moral support during this long and arduous journey and making delicious meals for those late nights on campus, to my father and Thanghu (my sister) for cheering me on and lifting up my spirits in times of need.

NOMENCLATURE

Roman Symbols

a_{vs}	Specific surface area of a porous absorber	$[m^{-1}]$
A_a	Area of an absorbing surface	$[m^2]$
A_{ch}	Channel area of an extruded absorber	$[m^2]$
A_e	Area of an emitting surface	$[m^2]$
A_s	Area of a flat surface	$[m^2]$
c_p	Specific heat capacity	$[J/kg.K]$
c_μ	Constant (used in turbulence modelling)	
C_2	Inertial resistance	$[m^{-1}]$
d_p	Mean pore diameter of an absorber	$[m]$
D_h	Hydraulic diameter of an absorber pore	$[m]$
e_b	Black body emission flux	
E	Total energy	$[W]$
E_{cv}	Energy contained within control volume	$[W]$
f_μ	Constant (used in turbulence modelling)	
F	External body force	$[N]$
g	Acceleration due to gravity	$[m/s^2]$
G	Diffuse irradiation	$[W/m^2]$
h	Specific enthalpy	$[J/kg]$
h	Convective heat transfer coefficient	$[W/m^2.K]$
\bar{h}	Average convective heat transfer coefficient	$[W/m^2.K]$
h_{tower}	Height of the solar tower	$[m]$
H	Enthalpy	$[J]$

i	Radiation propagation	
I	Incident solar radiation	[W]
I_v	Volumetric heat source	[W/m ³]
k	Thermal conductivity	[W/m.K]
k_1	Viscous resistance coefficient	[m ⁻²]
k_2	Inertial resistance coefficient	[m ⁻¹]
l or L	Length of the absorber	[m]
\dot{m}	Air mass flow rate	[kg/s]
Nu	Nusselt number	
p	Pressure drop	[Pa]
P	Channel perimeter	[m]
P_{stat}	Static pressure	
Pr	Prandtl number	
\dot{q}	Total heat transfer rate	[W]
q_{loss}	Loss of heat	[W]
q_r	Radiative flux	[W/m ²]
q_{vol}	Heat generation per unit volume	[W/m ³]
q_x''	Heat flux	[W/m ²]
\dot{Q}	Rate of heat transfer to air flowing through an absorber	[W]
\dot{Q}_{CV}	Rate of heat transfer into a control volume	[W]
\dot{Q}_{int}	Magnitude of solar irradiation	[W]
\dot{Q}_{solar}	Total heat imparted to the absorber through solar radiation	[W]
Re	Reynolds number	
S_k	User defined source term	
S_w	User defined source term	

S_T	Energy source term used for turbulence modelling	
S_U	Momentum source term	
T	Temperature	[K]
u	Superficial velocity	[m/s]
$u'(t)$	Fluctuating component of flow	[m/s]
U	Mean velocity component	[m/s]
V	Velocity of air	[m/s]
\dot{W}	Work transfer	[W]
\dot{W}_{cv}	Work transferred into or out of a control volume	

Greek Symbols

α	Absorptance coefficient	[m^{-1}]
β	Extinction coefficient	[m^{-1}]
Γ	Diffusion coefficient	[m^2/s]
ε	Dissipation of turbulent kinetic energy	
ϵ	Emissivity	
η	Efficiency	[%]
κ	Absorption coefficient	[m^{-1}]
μ	Dynamic viscosity	[N.s/m ²]
μ_t	Turbulent viscosity	
μ_{eff}	Effective viscosity	[N.s/m ²]
ρ	Density	[kg/m ³]
ϕ	Porosity	
σ	Stefan-Boltzmann constant (5.67×10^{-8})	[W/m ² .K ⁴]
σ_s	Scattering coefficient	[m^{-1}]

τ_{opt}	Optical thickness
$\bar{\tau}$	Stress tensor
Ψ	Empirical coefficient
ω	Rate of dissipation of turbulent kinetic energy
Ω	Scattering albedo

Subscripts and superscripts

<i>amb</i>	Ambient
<i>cv</i>	Control Volume
<i>e</i>	Exit from the control volume
<i>eff</i>	effective
<i>f</i>	fluid
<i>g</i>	ground
<i>i</i>	Inlet to the control volume
<i>l</i>	loss
<i>mix</i>	Air mixing
<i>rad</i>	Radiation
<i>rec, in</i>	Inlet to the absorber module
<i>rec, out</i>	Outlet to the absorber module
<i>s</i>	Solid (porous absorber)
<i>th</i>	thermal
<i>v</i>	Volumetric
<i>x</i>	Direction along the x-axis (horizontal)
<i>y</i>	Direction along the y-axis (vertical)
<i>z</i>	Direction along the z-axis (out of the page)
+	Forward propagation
–	Backward propagation

Abbreviations

ARR	Air Return Ratio
CFD	Computational Fluid Dynamics
CRS	Central Receiver System
CSP	Concentrating Solar Power
HRSG	Heat Recovery Steam Generator
HTF	Heat Transfer Fluid
IRENA	International Renewable Energy Agency
LTE	Local Thermal Equilibrium
LTNE	Local Thermal Non-Equilibrium
STPP	Solar Thermal Power Plant
OVR	Open Volumetric Receiver
TES	Thermal Energy Storage

Table of Contents

DECLARATION 1 - PLAGIARISM	i
DECLARATION – SUPERVISOR.....	ii
ABSTRACT.....	iii
ACKNOWLEDGMENTS	iv
NOMENCLATURE.....	v
LIST OF FIGURES	xiii
LIST OF TABLES	xxi
1. INTRODUCTION.....	1
1.1. Concentrating Solar Power (CSP).....	2
1.2. Central Receiver Systems	2
1.3. Open Volumetric Receivers	3
1.4. Problem Statement	5
1.5. Aims and Objectives	5
1.6. Thesis Outline	6
2. LITERATURE REVIEW.....	7
2.1. Receiver Technology	7
2.2. Volumetric Receivers (OVR).....	8
2.2.1. Open volumetric receiver with metal absorbers.....	9
2.2.2. Pressurized volumetric receivers with metal absorbers	9
2.2.3. Open volumetric receivers with ceramic absorbers	10
2.2.4. Pressurized volumetric receivers with ceramic absorbers.....	16
2.2.5. Challenges associated with OVR technology	18
2.3. Numerical modelling of OVRs	20
2.3.1. Analytical modelling of OVRs	21
2.3.2. Computational modelling of OVRs	22
2.3.3. Alternative OVR designs	29
2.4. Conclusion	33
3. THEORY	34
3.1. Air Return Ratio.....	34
3.2. Heat conduction	35
3.3. Convection.....	36

3.4.	Radiation.....	38
3.4.1.	Radiation attenuation	39
3.4.2.	Optical thickness	40
3.4.3.	Radiation modelling: extruded absorber structures versus open ceramic foam	41
3.5.	Conservation equations of the porous medium	43
3.6.	Pressure drop in the porous absorber	45
3.7.	Computational Fluid Dynamics modelling	46
3.7.1.	Grid generation	48
3.7.2.	Pressure-Velocity coupling scheme	48
3.7.3.	Convection –Diffusion modelling.....	48
3.7.4.	Turbulence modelling and solution controls.....	49
4.	CFD MODELLING OF AN OVR POROUS ABSORBER	54
4.1.	Introduction.....	54
4.2.	Numerical modelling of porous media.....	55
4.3.	Cold flow validation	55
4.4.	Hot flow validation	58
4.4.1.	Experimental set-up	58
4.4.2.	Generation of a baseline model for hot flow validation.....	60
4.4.3.	Cell zones and boundary conditions	72
4.4.4.	Model setup.....	78
4.4.5.	Mesh design	79
4.4.6.	Grid convergence study	79
4.4.7.	Validation study	85
4.5.	Discussion	87
4.6.	Conclusion	90
5.	WIND EFFECTS STUDY ON SOLAIR-200 ABSORBER MODULES	91
5.1.	SolAir material properties.....	92
5.2.	Porous medium characteristics of the SolAir module.....	93
5.3.	Limitations of the Local Thermal Equilibrium (LTE) model	94
5.4.	Operating parameters for wind effects study	96
5.5.	Cell zones and boundary conditions	98
5.6.	Grid convergence study	102
5.7.	Results - Wind effects study on the SolAir receiver	105

5.8.	Discussion	111
5.9.	Conclusion	112
6.	WIND EFFECTS STUDY ON BAFFLED SOLAIR-200 RECEIVER DESIGN	114
6.1.	Simulation methodology of the wind effects study.....	115
6.2.	Results - Wind effects study on the baffled SolAir receiver models	116
6.2.1.	Baffle length: 70 mm	117
6.2.2.	Baffle length: 50 mm	124
6.2.3.	Baffle length: 30 mm	133
6.2.4.	Performance comparison of the baffled SolAir models.....	143
6.3.	Discussion	145
6.4.	Conclusion	146
7.	CONCLUSION	148
	REFERENCES.....	150
	APPENDIX.....	156
a.	Appendix A.....	156
b.	Appendix B	158
c.	Appendix C.....	160

LIST OF FIGURES

Figure 1-1: Working principle of a typical CRS (Ávila-Marín, 2011)	3
Figure 1-2: Array of OVR modules (Agrafiotis et al., 2007).....	3
Figure 1-3: Ideal variation of the air and absorber temperature through the thickness of the absorber (Pitot de la Beaujardiere et al., 2016).....	4
Figure 2-1: Crescent dune solar tower (LHS) and Ivanpah solar tower (RHS) (Dieterich, 2018).....	7
Figure 2-2: Cavity Receiver (Lubkoll et al., 2014).....	8
Figure 2-3: REFOS receiver (Buck et al., 2001).....	10
Figure 2-4: Extruded absorbers (LHS) and Open Ceramic Foam (RHS) (Gomez-Garcia et al., 2016)	11
Figure 2-5: HiTRec principle (Ávila-Marín, 2011)	12
Figure 2-6: HiTRec-I stainless steel construction (LHS) and absorber module, extruded absorber and cup (RHS) (Hoffschmidt, 2001)	12
Figure 2-7: HiTRec-II sketch (Hoffschmidt et al., 2003)	13
Figure 2-8: 200 kW HiTRec-II set-up (Hoffschmidt, 2001).....	14
Figure 2-9: SolAir-200 Setup - Configuration 1 (Agrafiotis et al., 2007)	15
Figure 2-10: SolAir-3000 Receiver (Agrafiotis et al., 2007)	15
Figure 2-11: Solar Tower Julich (Fend, 2010).....	16
Figure 2-12: Central receiver plant featuring OVR in Daegu, South Korea (Lee et al., 2015)	16
Figure 2-13: PLVCR-500 Receiver Scheme (Ávila-Marín, 2011)	17
Figure 2-14: Schematic cross-section of DIAPR (Kribus et al., 2001).....	18
Figure 2-15: Multistage DIAPR consisting of preheaters and secondary concentrators (Ávila-Marín, 2011)	18
Figure 2-16: Mechanism of ARR in OVRs	19
Figure 2-17: Influence of inlet air temperature and air return ratio on the air mixing efficiency (Á. Marcos <i>et al.</i> , 2004).....	20
Figure 2-18: Absorber temperature profiles obtained through different radiation models (Mey et al., 2013)	21
Figure 2-19: Temperature profile of solid and fluid phase in an absorber (Kribus et al., 2014)	22
Figure 2-20: Quadratic pressure drop versus the air temperature for extruded absorbers (Becker et al., 2006)	23
Figure 2-21: Quadratic pressure drop versus temperature for open ceramic foams (Becker et al., 2006)..	23
Figure 2-22: Computational domain for hotspot simulation (Becker et al., 2006)	24

Figure 2-23: Rate of disappearance of hotspot depending on the material property (Becker et al., 2006).	24
Figure 2-24: Solution domain for absorber with constant porosity (Roldán et al., 2014)	25
Figure 2-25: The velocity distribution in the absorber modules (Roldán et al., 2016)	26
Figure 2-26: Predicted temperature distribution for the solid and fluid phase (Wu et al., 2011a).....	27
Figure 2-27: Absorber temperatures at the inlet surface (with frustum left, without frustum right) (Fend et al., 2013)	28
Figure 2-28: CFD model of OVR solar tower in Jülich, with external air return ducts (Stadler et al., 2019)	29
Figure 2-29: Warm air temperature plot (LHS) and return air concentration (RHS) (Stadler et al., 2019)	29
Figure 2-30: Dual receiver concept – top view (LHS), front view (RHS) (Buck et al., 2006a)	30
Figure 2-31: Multi-component geometric model (Buck et al., 2006a)	31
Figure 2-32: HiTRec-II single channel (LHS) and new channel geometry (RHS) (Capuano et al., 2017)	31
Figure 2-33: New absorber design (Capuano et al., 2017)	32
Figure 2-34: Graphs comparing the HiTRec absorber thermal efficiency (LHS) and outlet air temperature (RHS) to those of the new geometry (original numerical and scaled up model) (Capuano et al., 2017) ...	33
Figure 3-1: Multiple reflections inside the channel of the absorber (Elnoumeir et al., 2017)	39
Figure 3-2: Heat transfer mechanism in an OVR.....	44
Figure 3-3: Pressure drop in OCF and extruded absorbers (Fend et al., 2004).....	46
Figure 3-4: Typical point velocity measurement in turbulent flows (Malalasekera and Versteeg, 1995) ..	49
Figure 4-1: Pressure drop in an OCF (Wu et al., 2010)	54
Figure 4-2: Experimental Pressure-Velocity characteristic curve (Wu et al., 2010)	56
Figure 4-3: Cell zones for cold flow validation	57
Figure 4-4: Static pressure contour plot at an inlet velocity of 2 m/s	57
Figure 4-5: Schematic diagram of the test rig (Hoffschmidt et al., 2003)	59
Figure 4-6: Dimensions of the CFD model of the HiTRec-II modules (Roldán et al., 2016)	60
Figure 4-7: Mesh design and boundary conditions of CFD model (Roldán et al., 2016)	61
Figure 4-8: Dimensioning notation for 2D atmospheric domain (Patel et al., 2015).....	62
Figure 4-9: Shape of a HiTRec-II module	62
Figure 4-10: 2-D model of the heat source equation for test 3 (Roldán et al., 2016)	64
Figure 4-11: Pressure contour plot under test 3 conditions.....	66
Figure 4-12: Temperature contour plot under test 3 conditions.....	66
Figure 4-13: Velocity vector plot under test 3 conditions.....	67
Figure 4-14: Pressure Contour plot under test 3 conditions using constant volumetric heat source	68
Figure 4-15: Temperature plot under test 3 conditions using constant volumetric heat source.....	68

Figure 4-16: Velocity vector plot under test 3 conditions using constant volumetric heat source	68
Figure 4-17: Velocity vector in the 3 rd module.....	69
Figure 4-18: HiTRec-II Module (Full assembly) (a)	70
Figure 4-19: HiTRec-II Module (Full assembly) (b)	70
Figure 4-20: Porous Zone	70
Figure 4-21: Hot Air Zone	70
Figure 4-22: Insulation Zone	71
Figure 4-23: Cup Zone.....	71
Figure 4-24: HiTRec-II modules that were modelled for CFD simulations (Roldán et al., 2016)	71
Figure 4-25: 14 HiTRec-II Modules CFD Model.....	72
Figure 4-26: Full computational model used for the validation study	72
Figure 4-27: Cell zones of the computational model.....	75
Figure 4-28: Location of boundary condition (a).....	76
Figure 4-29: Location of boundary condition (b)	76
Figure 4-30: Location of boundary condition (c).....	76
Figure 4-31: Location of boundary condition (d)	76
Figure 4-32: Location of boundary condition (e).....	76
Figure 4-33: Selective Meshing Flowchart.....	79
Figure 4-34: Reference cell size of 6 mm	80
Figure 4-35: Reference cell size of 3 mm	80
Table 4-36: Reference cell size of 1,5 mm	81
Figure 4-37: Graphical representation of the grid convergence study.....	82
Figure 4-38: Graphical representation of the grid convergence study	84
Figure 4-39: Static Temperature Contour Plot (under Test 3 conditions).....	86
Figure 4-40: Magnified image of the temperature contour plot.....	86
Figure 4-41: Velocity Vector Plot (a) (under Test 3 conditions)	87
Figure 4-42: Velocity Vector Plot (b) (under Test 3 conditions).....	87
Figure 5-1: Mechanism of ARR in OVRs	91
Figure 5-2: Basic dimensions of a SolAir module.....	93
Figure 5-3: Energy balance of porous medium.....	94
Figure 5-4: Scatter plot of the SolAir-200 experimental campaign data	97
Figure 5-5: SolAir absorber module	99
Figure 5-6: Porous absorber.....	99
Figure 5-7: Outer Cup.....	99

Figure 5-8: Insulation.....	99
Figure 5-9: Hot Air Zone	99
Figure 5-10: 3 x 6 configuration of SolAir modules.....	100
Figure 5-11: CFD model used for the wind analysis	100
Figure 5-12: Front view of the SolAir model, with boundary conditions.....	101
Figure 5-13: Side view of the SolAir model with boundary conditions	101
Figure 5-14: Centre row of the SolAir model	103
Figure 5-15: General cross-sectional view of an example model mesh.....	103
Figure 5-16: Magnified cross-sectional view of an example absorber module mesh.....	104
Figure 5-17: Graphical illustration of the grid convergence study of the SolAir receiver model.....	105
Figure 5-18: Outlet temperature of the absorber modules for various wind speeds at an incidence angle of 90°	106
Figure 5-19: Outlet temperature of the absorber modules for various wind speeds at an incidence angle of 60°	106
Figure 5-20: Outlet temperature of the absorber modules for various wind speeds at an incidence angle of 30°	107
Figure 5-21: Outlet temperature of the absorber modules for various wind speeds at an incidence angle of 0°	107
Figure 5-22: Outlet air temperature of the SolAir receiver in the wind analysis	108
Figure 5-23: Flow domain temperature contour plot for a wind speed of 15 m/s flowing at an incidence angle of 0°	108
Figure 5-24: Flow domain temperature contour plot for a wind speed of 15 m/s flowing at an incidence angle of 30°	109
Figure 5-25: Flow domain temperature contour plot for a wind speed of 15 m/s flowing at an incidence angle of 60°	109
Figure 5-26: Flow domain temperature contour plot for a wind speed of 15 m/s flowing at an incidence angle of 90°	109
Figure 5-27: Flow domain velocity vector plot for a wind speed of 15 m/s flowing at an angle of 0°	110
Figure 5-28: Flow domain velocity vector plot for a wind speed of 15 m/s flowing at an angle of 30° ..	110
Figure 5-29: Flow domain velocity vector plot for a wind speed of 15 m/s flowing at an angle of 60° ..	110
Figure 5-30: Flow domain velocity vector plot for a wind speed of 15 m/s flowing at an angle of 90° ..	111
Figure 6-1: Potential obstruction of solar radiation caused by baffle	114
Figure 6-2: Baffled SolAir receiver model computational domain	115
Figure 6-3: Baffled SolAir simulation workflow.....	116

Figure 6-4: 3-D model of the baffled SolAir model with baffle length of 70 mm.....	117
Figure 6-5: Cross-sectional view of the meshed model of the SolAir receiver with 70 mm vertical baffles	117
Figure 6-6: Outlet temperature of the absorber modules for wind direction perpendicular to the modules	118
Figure 6-7: Outlet temperature of the absorber modules for wind direction 60° to the modules	118
Figure 6-8: Outlet temperature of the absorber modules for wind direction 30° to the modules	119
Figure 6-9: Outlet temperature of the absorber modules when wind flows parallel to the absorber surface	119
Figure 6-10: Temperature contour plot for wind speed at 15 m/s flowing parallel to the absorber surface, for the 70 mm baffled SolAir model.....	120
Figure 6-11: Velocity vector plot for wind at 15 m/s flowing parallel to absorber surface, for the 70 mm baffled SolAir model.....	120
Figure 6-12: Temperature contour plot for wind speed at 15 m/s incident at angle of 30°, for of the 70 mm baffled SolAir model.....	121
Figure 6-13: Velocity vector plot for 15 m/s incident at an angle of 30°, for the 70 mm baffled SolAir model	121
Figure 6-14: Temperature contour plot for wind speed at 15 m/s incident at angle of 60°, for of the 70 mm baffled SolAir model.....	122
Figure 6-15: Velocity vector plot for 15 m/s incident at an angle of 60°, for the 70 mm baffled SolAir model	122
Figure 6-16: Temperature contour plot for wind speed at 15 m/s incident at angle of 90°, for of the 70 mm baffled SolAir model.....	123
Figure 6-17: Velocity vector plot for 15 m/s incident at an angle of 90°, for the 70 mm baffled SolAir model	123
Figure 6-18: Outlet air temperature of the 70 mm Baffled SolAir receiver as a function of the angle of incidence for wind speeds of 15 m/s and 25 m/s	124
Figure 6-19: 3-D model of the SolAir model with a baffle length of 50 mm	124
Figure 6-20: Meshed model of the SolAir receiver with 50 mm vertical baffles	125
Figure 6-21: Outlet temperature of the absorber modules for wind direction perpendicular to the modules	125
Figure 6-22: Outlet temperature of the absorber modules for wind direction 60° to the modules	126
Figure 6-23: Outlet temperature of the absorber modules for wind direction 30° to the modules	126

Figure 6-24: Outlet temperature of the absorber modules when wind flows parallel to the absorber surface	127
Figure 6-25: Temperature contour plot for wind speed at 15 m/s flowing parallel to the absorber surface, for the 50 mm baffled SolAir model.....	127
Figure 6-26: Velocity vector plot for a wind speed of 15 m/s for wind flowing parallel to the absorber surface, for the 50 mm baffled SolAir model	128
Figure 6-27: Temperature contour plot for wind speed at 15 m/s incident at angle of 30°, for the 50 mm baffled SolAir model.....	128
Figure 6-28: Velocity vector plot for a wind speed of 15 m/s at an angle of 30°, for the first three absorber modules from the left of the 50 mm baffled SolAir model.....	129
Figure 6-29: Velocity vector plot for a wind speed of 15 m/s at an angle of 30°, for the first three absorber modules from the right of the 50 mm baffled SolAir model.....	129
Figure 6-30: Temperature contour plot for wind speed at 15 m/s incident at angle of 60°, of the 50 mm baffled SolAir model.....	130
Figure 6-31: Velocity vector plot for a wind speed of 15 m/s at an angle of 60°, for the first two absorber modules from the left of the 50 mm baffled SolAir model.....	130
Figure 6-32: Velocity vector plot for a wind speed of 15 m/s at an angle of 60°, for the first four absorber modules from the right of the 50 mm baffled SolAir model.....	130
Figure 6-33: Temperature contour plot for wind speed at 15 m/s incident at angle of 90°, for the 50 mm baffled SolAir model.....	131
Figure 6-34: Velocity vector plot for a wind speed of 15 m/s at an angle of 90°, for the 50 mm baffled SolAir model.....	131
Figure 6-35: Velocity vector plot for a wind speed of 15 m/s at an angle of 90°, for the first three absorber modules from the left of the 50 mm baffled SolAir model.....	132
Figure 6-36: Velocity vector plot for a wind speed of 15 m/s at an angle of 90°, for the first three absorber modules from the right of the 50 mm baffled SolAir model.....	132
Figure 6-37: Outlet air temperature of the 50 mm baffled SolAir receiver as a function of the incidence angle for wind speeds of 15 m/s and 25 m/s	133
Figure 6-38: 3-D model of the SolAir model with baffle length of 30 mm.....	133
Figure 6-39: Meshed model of the SolAir receiver with 30 mm vertical baffles	134
Figure 6-40: Outlet temperature of the absorber modules for wind direction perpendicular to the modules	134
Figure 6-41: Outlet temperature of the absorber modules for wind direction 60° to the modules	135
Figure 6-42: Outlet temperature of the absorber modules for wind direction 30° to the modules	135

Figure 6-43: Outlet temperature of the absorber modules when wind flows parallel to the absorber surface	136
Figure 6-44: Temperature contour plot for wind speed at 15 m/s flowing parallel to the absorber surface, for the 30 mm baffled SolAir model.....	136
Figure 6-45: Velocity vector plot for a wind speed of 15 m/s for wind flowing parallel to the absorber surface, for the 30 mm baffled SolAir model	137
Figure 6-46: Temperature contour plot for wind speed at 15 m/s incident at angle of 30°, for the 30 mm baffled SolAir model.....	137
Figure 6-47: Velocity vector plot for a wind speed of 15 m/s at an angle of 30°, for the first three absorber modules from the left of the 30 mm baffled SolAir model.....	138
Figure 6-48: Velocity vector plot for a wind speed of 15 m/s at an angle of 30°, for the first three absorber modules from the right of the 30 mm baffled SolAir model.....	138
Figure 6-49: Temperature contour plot for wind speed at 15 m/s incident at angle of 60°, of the 30 mm baffled SolAir model.....	139
Figure 6-50: Velocity vector plot for a wind speed of 15 m/s at an angle of 60°, for the first three absorber modules from the left of the 30 mm baffled SolAir model.....	139
Figure 6-51: Velocity vector plot for a wind speed of 15 m/s at an angle of 60°, for the first three absorber modules from the right of the 30 mm baffled SolAir model.....	140
Figure 6-52: Temperature contour plot for wind speed at 15 m/s incident at angle of 90°, for the 30 mm baffled SolAir model.....	140
Figure 6-53: Velocity vector plot for a wind speed of 15 m/s at an incident angle of 90°, for the 30 mm baffled SolAir model.....	141
Figure 6-54: Velocity vector plot for a wind speed of 15 m/s at an angle of 90°, for the first two absorber modules from the left of the 30 mm baffled SolAir model.....	141
Figure 6-55: Velocity vector plot for a wind speed of 15 m/s at an angle of 90°, for the first two absorber modules from the right of the 30 mm baffled SolAir model.....	142
Figure 6-56: Outlet air temperature of the 30 mm Baffled SolAir receiver for wind speeds of 15 m/s and 25 m/s.....	142
Figure 6-57: Comparative illustration of the outlet air temperatures for the baffled model at wind speed of 15 m/s	143
Figure 6-58: Comparative illustration of the outlet air temperatures for the baffled model at wind speed of 25 m/s.....	143
Figure 6-59: Increase in the outlet air temperature of the baffled SolAir models at wind speed of 15 m/s	144

Figure 6-60: Increase in the outlet air temperature of the baffled SolAir models at wind speed of 25 m/s
..... 144

LIST OF TABLES

Table 2-1: Thermal efficiencies of the different SolAir-200 receiver configurations (Télléz, 2003).....	15
Table 4-1: Percentage deviation between experimental and numerical pressure drop	57
Table 4-2: Experimental data from SolAir 200 Receiver	59
Table 4-3: Experimental measurement of outlet air temperatures	60
Table 4-4: Heat source equations for the tests	63
Table 4-5: Results from Roldán et al. (2016) used to validate against the experimental data	64
Table 4-6: Solar power incident on each module.....	65
Table 4-7: Verification Results	66
Table 4-8: Air outlet temperature for constant volumetric heat source	67
Table 4-9: The various zones of the CFD model	73
Table 4-10: Material Properties of the Solid Zones	74
Table 4-11: Summarized boundary conditions	78
Table 4-12: Grid Convergence Study	81
Table 4-13: Percentage deviation of temperatures between consecutive meshes	82
Table 4-14: Sensitivity of the air outlet temperatures to spatial discretization schemes	83
Table 4-15: Stage 1 grid convergence study using power law scheme.....	83
Table 4-16: Percentage deviation of temperature between consecutive meshes	84
Table 4-17: Solution Controls.....	85
Table 4-18: Numerical results of temperature values obtained from the validation study	85
Table 4-19: Percentage deviation of the numerical results from the experimental measurement of outlet air temperatures.....	86
Table 5-1: Atmospheric boundary conditions for the SolAir model.....	102
Table 5-2: Fluent settings for the wind effects study of standard SolAir receiver.....	102
Table 5-3: Grid convergence study conducted on the SolAir receiver model	104
Table 5-4: Percentage deviation in the module air outlet temperatures between the consecutive cell sizes	105
Table A-1: SolAir-200 receiver test rig experimental data.....	158
Table A-2: Outlet air temperatures obtained from wind study of standard SolAir model.....	160
Table A-3: Wind study carried out on SolAir model with 70 mm vertical baffle	161
Table A-4: Wind study carried out on SolAir model with 50 mm vertical baffle	161
Table A-5: Wind study carried out on SolAir model with 30 mm vertical baffle	162

1. INTRODUCTION

Accelerated global warming is a reality of the 21st century, with the four warmest years recorded in history being the last four, according to the World Meteorological Organisation (WMO) (WMO, 2019). It is believed that the dramatic rise in greenhouse gases emissions, predominantly carbon dioxide, is responsible for this warming effect. The increase can mainly be associated with human activities such as the burning of fossil fuels (coal, gas and petroleum) for electricity and transportation needs, as well as the energy-intensive steel and cement manufacturing industry.

The consequences of climate change are indicated to include the frequent occurrence of deadly heat waves and bushfires, the rise in the ocean temperatures and acidity levels, leading, for example, to accelerated bleaching of the coral reefs (Moses, 2017), unseasonal rainfall and the increased occurrence of devastating floods and storms.

As per the IRENA report for 2019, 75% of carbon emission can be reduced by exploiting sources of renewable energy to generate power that will electrify the spatial heating needs of civilian homes and apartments using electric heat pumps and transitioning to electric vehicles in the transportation sector (IRENA, 2019). Therefore, a transition to renewable energy technologies would be an effective approach to curbing greenhouse gas emissions and the impact of climate change.

In recent years, the cost of electricity generation from wind (onshore and offshore), solar (Photo-voltaic and concentrating solar power), bioenergy, hydropower and geothermal have fallen within the price range of fossil fuel. It is predicted by IRENA that by the year 2020, the onshore wind and PV generation will compete head-to-head with fossil fuels (IRENA, 2018).

A common drawback of renewable energy technologies, especially solar and wind technology is its reliance on the weather pattern and hence its volatility in power generation. However concentrating solar power (CSP), a sub-category of solar power along with photo-voltaic (PV) technology has a significant advantage of being dispatchable i.e. it can incorporate thermal storage, allowing power generation based on consumer demand during the evening hours when there is less or no solar radiation.

1.1. Concentrating Solar Power (CSP)

In CSP technology, reflective optical surfaces are used to concentrate the energy from the sun onto a receiver carrying a heat transfer fluid (HTF) which is heated by solar radiation and is in turn used to generate steam that powers a steam turbine. CSP technologies are sub-categorized based on the solar radiation focussing techniques viz. line focussing technology which includes parabolic trough and linear fresnel concentrators, and point focusing technology which includes the central receiver system and parabolic dish configurations.

Molten salt thermal storage is typically used in CSP plants. It can double as the heat transfer fluid and storage medium since the thermophysical properties of molten salt is also favourable for storage purposes. It has low vapour pressure, allowing it to be stored at atmospheric pressure, has high density allowing it to retain more energy per volume as compared to oil-based HTFs, high heat transfer coefficient and can be stored at high temperatures of around 556 °C until it is needed for power generation (Al-juboori, 2018).

The incorporation of thermal storage into CSP plants has provided it with a distinct advantage of being dispatchable, over PV and wind technologies which uses the more expensive lithium-ion battery storage. Such an advantage has allowed CSP projects to procure higher tariff rates during hours of high power demand when there is less or no solar radiations. For example, under the renewable energy independent power producer procurement programme (REIPPPP), a competitive single stage bidding process for renewable energy in South Africa, the tariff rates for producing electricity during peak hours between 16h00 and 21h30 is 270 % higher than standard rates for off-peak hours (Relancio et al., 2017). Another advantage of a CSP technology is that it can be integrated to enhance the efficiency of power plants such as the natural gas-fired combined cycle (NGCC) power plant (Price, 2010).

1.2. Central Receiver Systems

The central receiver system (CRS), a sub-category of CSP, consists of a field of heliostats, having tracking in two axes that reflects solar radiation onto a receiver placed at the top of a centrally-located tower. The receiver imparts the heat energy from the incident solar radiation to the HTF, which may comprise air, nitrate salt or steam, for example. In plants featuring Rankine cycle power blocks, the HTF is then passed through a heat exchanger/ steam generator where the water (which is the working fluid) is converted to steam which, in turn, is used to drive a steam turbine. The working principle of a typical central receiver system is illustrated in Fig. 1-1 (Ávila-Marín, 2011).

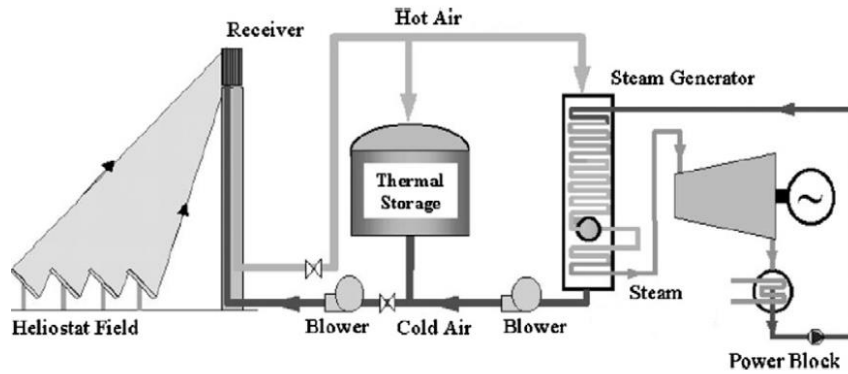


Figure 1-1: Working principle of a typical CRS (Ávila-Marín, 2011)

1.3. Open Volumetric Receivers

The configuration of the receiver in a CRS can affect the thermal efficiency of the plant. The three main categories of receiver configuration include tubular receivers, cavity receivers and open volumetric receivers (OVR). An OVR consists of a vast array of absorber modules stacked next to each other, as in Fig. 1-2 (Agrafiotis et al., 2007). The air at atmospheric pressure is drawn through a porous absorber (embedded into the absorber module) which is heated by the solar radiation, and the heat is transferred to the air by volumetric convection and radiation. The hot air is then transmitted to the power block of the plant where it is used to generate steam in the heat recovery steam generator (HRSG). Packed bed thermal storage is typically used when the HTF is a gas, such as air in OVRs (Anderson et al., 2015).

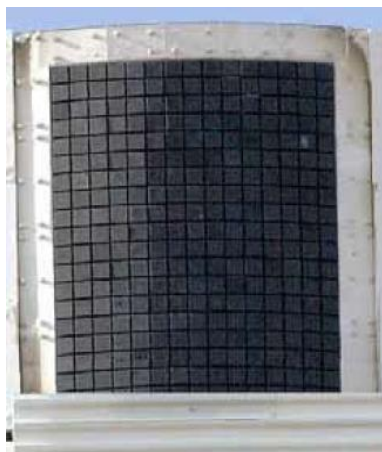


Figure 1-2: Array of OVR modules (Agrafiotis et al., 2007)

The warm air that exits the HRSG is ejected into the atmosphere through the gaps between absorber modules and a portion of this warm air (now mixed with ambient air) is drawn back in through the

absorber modules. The mixing of warm and the ambient air, results in a drop in the overall enthalpy. The ratio of the enthalpy of the warm air (with the lowered enthalpy) that is drawn back into the absorber modules to that of the warm air that leaves the receiver system is known as the air return ratio (ARR). The ARR along with the absorber material as well as its geometrical characteristics play a vital role in the performance of OVRs.

The OVRs have the potential to achieve a higher thermal efficiency than the other configurations of receivers due to the possibility of the volumetric effect, whereby the front irradiated section of the absorber, is at a lower temperature than the air leaving the absorber under ideal conditions (Kribus et al., 2014), as shown in Fig. 1-3 (Pitot de la Beaujardiere et al., 2016).

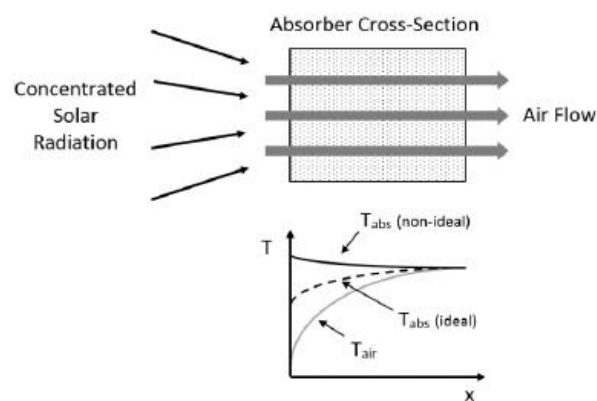


Figure 1-3: Ideal variation of the air and absorber temperature through the thickness of the absorber (Pitot de la Beaujardiere et al., 2016)

The unique benefit of using OVRs is that the effective area of heat transfer is much larger as it occurs through the volume of the absorber, reducing the radiation losses (Hoffschmidt et al., 2003). The other major advantage is the usage of air as the heat transfer fluid as it is readily available, non-toxic and does not require heat tracing. The low heat capacity of air can lead to quicker plant start-up. Air is also chemically stable at high temperatures (Pitot de la Beaujardiere et al., 2016). The first commercial central receiver system that employed the OVR technology is the 1.5 MW_e Solar Power Tower in Jülich, Germany that began operation in 2009 (Hennecke, et al., 2009).

Further details about the evolution of OVR technology, the various configurations as well as prominent studies on OVRs conducted in literature are detailed in the Chapter 2.

1.4. Problem Statement

In spite of the advantageous characteristics of OVRs, the technology suffers from some major drawbacks such as the poor heat transfer characteristics of air, causing the temperature of the porous absorber to rise higher than that of the air, possibility of high radiation losses to the atmosphere from the front surface at very high temperatures of the absorber (van de Merwe, 2016), low ARR which is aggravated under windy conditions (Roldán et al., 2016) and finally, the failure to achieve the volumetric effect in the practice.

The ARR recorded for the state-of-the-art OVR known as the SolAir receiver shown in Fig. 1-2 ranges between 0.35 and 0.45 (Téllez, 2003). Furthermore, very limited research has been conducted in literature to investigate ways to improve ARR in volumetric absorbers. Hence, the research work undertaken aims to fill this gap and address the issue of low ARR by placing thin vertical air flow baffles/plates (straight and contoured) in the gap between the SolAir modules through which the warm air escapes into the atmosphere. This is done in an effort to redirect most of the warm air that leaves the receiver system back into the absorber modules with as little mixing with ambient air as possible to prevent any reduction in enthalpy. A computational model of an array of SolAir modules will be developed, and using computational fluid dynamic (CFD) modelling, the behaviour of the air in the vicinity of and within the absorber modules will be studied. The ultimate aim of the study is to establish whether any improvements in the ARR of the SolAir modules can be achieved.

1.5. Aims and Objectives

The aim of this research is to investigate the sensitivity of the air return ratio (ARR) in an open volumetric receiver such as the SolAir-200 modules to the presence of straight and contoured baffles in between the modules.

The objectives of the study are to:

1. Formulate and validate a CFD modelling methodology that suitably captures the air flow characteristics in the absorber region of an OVR receiver.
2. Develop a representative CFD model of a set of SolAir OVR absorber modules and employ the model to predict the nominal ARR associated with the modules operating under varying conditions.
3. Develop a representative CFD model of the SolAir OVR absorber modules with vertical baffles/plates placed in between the modules and run the simulation under identical operating conditions to that of the standard SolAir model CFD study to determine the ARR.

4. Draw a comparison between the ARR calculated for the SolAir modules with and without the baffles, and determine whether the inclusion of baffles improves the re-entrainment of the warm air.

1.6. Thesis Outline

Chapter 2: This chapter provides a literature review detailing the development of OVR technology. It includes a critical analysis of the associated experimental, analytical and CFD studies.

Chapter 3: This chapter presents the theory relating to the fluid mechanics and heat transfer mechanisms associated with OVR operation, along with the applicable concepts concerning the CFD modelling.

Chapter 4: This chapter details the development of a suitable CFD modelling methodology for capturing the airflow and heat transfer phenomena associated with the operation of an OVR module, based on cold and hot flow condition validation studies.

Chapter 5: This chapter details the CFD modelling on the array of state-of-the-art SolAir OVR modules using the methodology established in Chapter 4 and quantitatively predicts the ARR under various operating conditions.

Chapter 6: This chapter involves a study using a CFD model of the SolAir module array that is modified to accommodate the presence of air flow baffles (straight and contoured) in between the modules. Simulations are carried out to investigate their effect on ARR under the same operating conditions as the nominal model described above.

2. LITERATURE REVIEW

2.1. Receiver Technology

The solar-thermal receiver is an essential component of the central receiver system, and is placed at the top of a tower adjacent to a heliostat field. Three potential receiver types are:

1. External tubular receivers
2. Cavity receivers
3. Volumetric receivers

In an external tubular receiver, the redirected sunlight which is incident on its outer surface heats up metal tubes and this heat is imparted directly to the working fluid (molten salts, water/steam) through conduction. The 110 MW_e Crescent Dunes Solar Energy Facility constructed by Solar Reserve uses a tubular receiver and molten salt as the working fluid and achieves a receiver outlet temperature of 565 °C (Hoffschmidt, 2014). It also has a molten salt thermal energy storage system capable of 10 hours of full load storage.

Tubular receivers can also be implemented using multiple ‘billboard’ receivers which consists of a flat panel of parallel aligned tubes exposed to the heliostat field. Multiple such panels can be joined to form rectangular or cylindrical shapes (Lubkoll et al., 2014) such as the 337 MW Ivanpah Solar Electric Generating System (Dieterich, 2018) which produces steam at 550 °C. Both of the mentioned tubular receivers are shown in Fig. 2-1.



Figure 2-1: Crescent dune solar tower (LHS) and Ivanpah solar tower (RHS) (Dieterich, 2018)

The material properties of the tubular receivers place an upper limit to the solar flux that is allowed to strike them before deformation sets in. Phenomena such as heat loss by natural convection to the surrounding environment due to the high temperature of the receiver tubes and the inhomogeneous heat

heat transfer of thermal energy from the absorber to the air should prevent it from overheating. However, the poor heat transfer characteristics of air could prevent effective heat transfer and cause the absorber temperatures to soar. A high temperature gradient between the absorber and the surrounding ambient environment forms and leads to a high rate of convection and radiation losses from the absorber.

Volumetric receivers can be broadly categorized on the basis of their operating mode (i.e. pressurized volumetric receiver and open volumetric receiver) and the absorber material (metal and ceramic). The development of absorbers in each of these categories is elaborated in the following section.

2.2.1. Open volumetric receiver with metal absorbers

According to the research conducted by Ávila-Marín (2011), the first promising concept of an OVR absorber came about in 1983, made out of thin wire mesh of AISI 310 stainless steel and was referred to as the MK-1 receiver. The concept was tested and produced outlet air at 842 °C at an estimated thermal efficiency ranging from 70 - 90 %. This success led to various other iterations of metal absorbers that were tested in Plataforma Solar de Almeria (PSA) in Spain. These included absorbers made out of coiled knit wires (in the Sulzer 2 receiver), metal foil (in the Catrec 1 receiver), and cup-shaped coil knit wires (in the Phoebus-TSA receiver). A modular metal receiver configuration was experimentally evaluated by the Betchel Corporation, where the absorber was composed of 54 mm deep multi-layered mesh made out of knitted oxidized nichrome resistance wire (Ávila-Marín, 2011). This experiment yielded an average outlet air temperature of 710 °C.

A major drawback of using metallic absorbers is the limitation that is placed upon the average outlet air temperature which is around 700 °C due to the thermal properties of the metal substrate.

2.2.2. Pressurized volumetric receivers with metal absorbers

Pressurized volumetric receivers have been developed for use in a combined cycle power plant configuration where the air entering the gas turbine's combustor is pre-heated using solar radiation to decrease fuel usage and thus greenhouse gas emissions. These receivers are expected to produce outlet air with temperatures ranging from 800 - 1200 °C, and at working pressures of 4 – 30 bar (Poživil et al., 2014).

The Receiver for Solar Fossil Power Plant (REFOS), developed by DLR in 1996 shown in Fig. 2-3 (Buck et al., 2001), had a domed shaped window made out of quartz glass and used a heat resistant wire screen absorber as well as secondary concentrators to increase the concentration ratio and capture area. Other projects which dealt with this type of receiver include the SOLGATE project which commenced in 2001, followed by SOLHYCO, SOLUGAS and SOLTREC; all with the main aim of achieving outlet

air temperatures of above 1000 °C (Río et al., 2015). One of the advantages of this type of volumetric receiver is the attainment of higher temperatures with lower radiation losses. However, the secondary concentrators and quartz window would require periodic maintenance and increases the overall cost of installation (Wang et al., 2014).

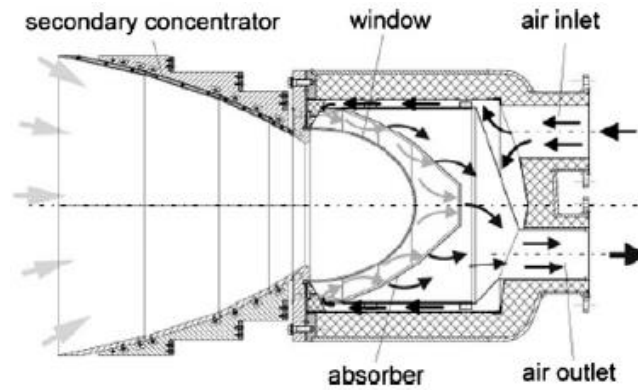


Figure 2-3: REFOS receiver (Buck et al., 2001)

2.2.3. Open volumetric receivers with ceramic absorbers

The limitations placed on air outlet temperature by metal absorbers led to investigations into ceramic materials for OVR absorbers. The primary materials that have been considered are silicon carbide (SiC), silicon infiltrated silicon carbide (SiSiC) and alumina (Al_2O_3). This is mainly due to their high thermal conductivity and low thermal expansion compared to metals, their higher resistance to solar flux and higher thermal gradients, reducing the required receiver aperture and thermal losses.

Two types of ceramics structures have been evaluated for testing; namely, extruded structures consisting of tessellated parallel channels in the flow direction, and Open Ceramic Foam (OCF), which has a porous structure consisting of a large number of randomly packed open cells (Gomez-Garcia et al., 2016). Figure 2-4 depicts the extruded and open ceramic foam absorbers structures commonly used in the OVRs.

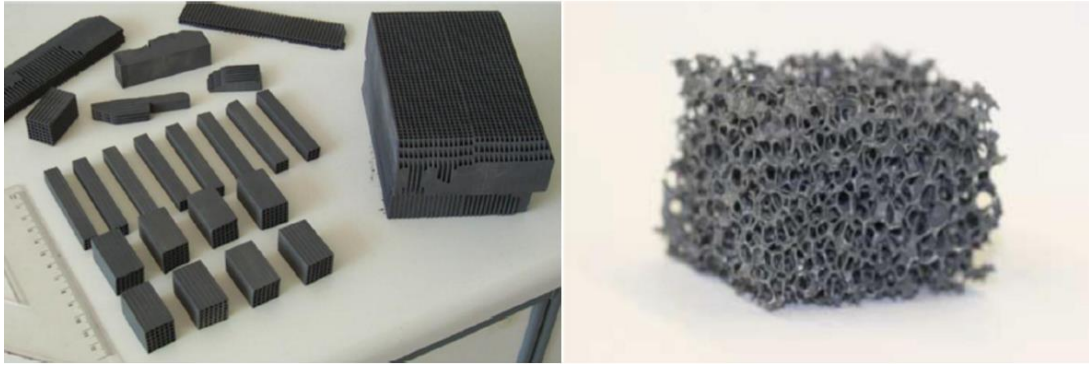


Figure 2-4: Extruded absorbers (LHS) and Open Ceramic Foam (RHS) (Gomez-Garcia et al., 2016)

The development of ceramic foams began in 1987 with the Ceram Tech Receiver that managed to heat air to between 700 - 790 °C at an incident solar flux of 660 kW/m², followed by the Sandia Foam Receiver in 1989 that heated air to 730 °C with a corresponding thermal efficiency of 54 % and Corec Receiver in 1995 that heated air to 880 °C with a corresponding thermal efficiency of 79 % (Hoffschmidt, 2001).

Although the developed ceramic receivers showed better resilience to high solar fluxes than the metallic counterparts, they couldn't easily be scaled up to be used in a central receiver system. Nearly all the ceramic absorbers tested until 1995 showed structural failures, due to the high tensile stresses common in large extruded ceramic structures (Hoffschmidt, 2001).

Inhomogeneous solar irradiation on these ceramic absorber surfaces can also lead to local regions where temperatures become high enough to cause local structural deformation of the ceramic absorbers. Therefore, an approach of splitting the receiver into a collection of modules, consisting of ceramic absorbers, and regulating the air flow through each module with a flow control device was necessary, separating the development of the absorber and the module in which it was housed.

The HiTRec receiver technology was conceived out of such a need to develop a modular design for OVR, which will allow various types of absorbers to be tested on a single receiver system (Hoffschmidt, 2001). The HiTRec-I receiver, shown in Fig. 2-5 (Ávila-Marín, 2011), consisted of modular hexagonal ceramic cups, each holding silicon carbide extruded absorber, with each cups being housed in a stainless steel structure. The space between the absorber modules is used as a channel for the injection of warm air returning to the receiver from the power block back into the absorber modules.

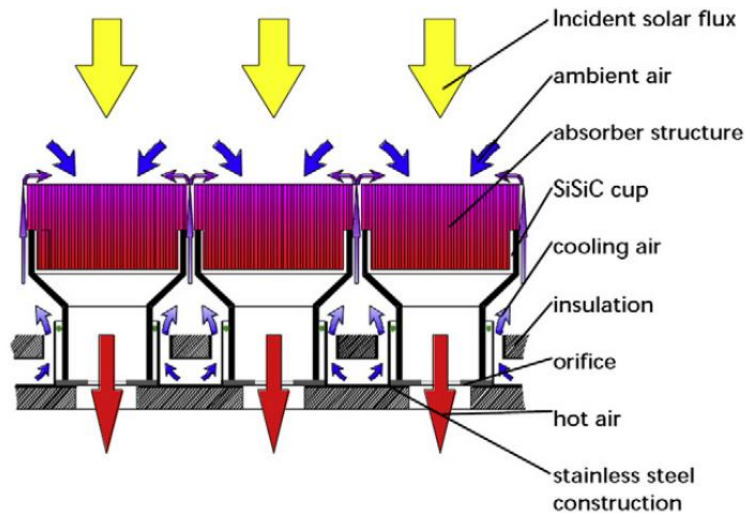


Figure 2-5: HiTRec principle (Ávila-Marín, 2011)

A 200 kW HiTRec-I test rig was assembled at the Sulzer Test Bed set atop the Plataforma Solar de Almeria (PSA) CRS tower to demonstrate the durability of the newly proposed volumetric receiver design, having the potential to yield outlet air temperatures exceeding 1000 °C. The stainless steel construction of the test rig and the individual modules of HiTRec-I is shown in Fig. 2-6 (Hoffschmidt, 2001). A maximum receiver outlet temperature of 980 °C was achieved (the maximum outlet air temperature was limited by the Sulzer Test bed), with a thermal efficiency of 75 – 80 % at 800 °C. A major drawback of this receiver design was that the steel structure behind the absorber modules deformed during the testing process due to uncontrolled mass flow of the return air. Although the deformation did not affect the overall performance, it was not acceptable for larger receivers (Ávila-Marín, 2011).

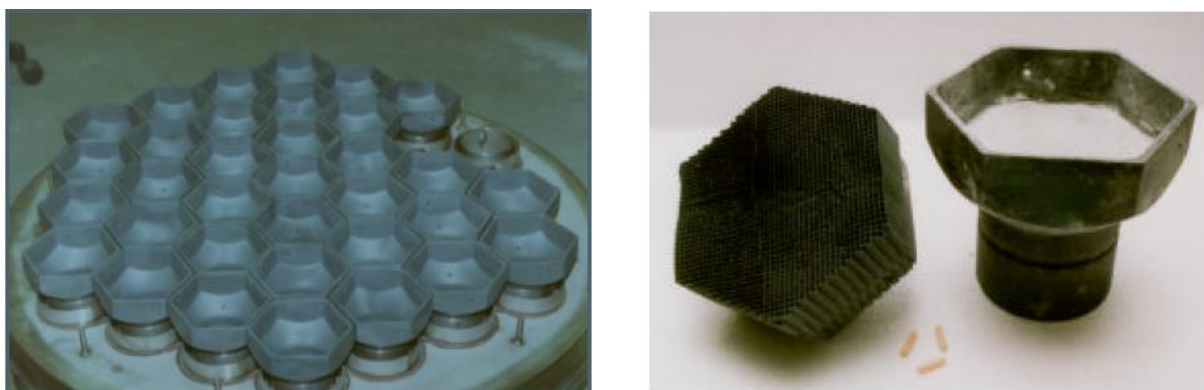


Figure 2-6: HiTRec-I stainless steel construction (LHS) and absorber module, extruded absorber and cup (RHS) (Hoffschmidt, 2001)

To rectify the failures of HiTRec-I, HiTRec-II, shown in Fig. 2-7 (Roldán et al., 2016), was designed with an improved retainer for accurate positioning of the modules and easy module replacement, a simplified absorber shape that was directly extruded into the final extruded structure, and employed a double sheet membrane for the holding structure. The absorber was made out of recrystallized silicon carbide (SiC) and the cups were manufactured from infiltrated siliconized silicon carbide (SiSiC). Solar flux simulations were used to size the orifices at the outlet of the absorber modules, to control the mass flow rate and maintain homogeneous receiver outlet air temperature.

The testing campaign yielded data from over 155 operating hours. The test included warm-up tests, tests to measure the Air Return Ratio and tests to measure steady-state outlet temperatures. The test campaign resulted in an overall receiver efficiency of $(76 \pm 7) \%$ at $700 \text{ }^\circ\text{C}$ and an ARR of 45 %. Due to the formation of excess thermal gradient in one of the ceramic modules, cracks formed in two of the module cups that were placed in the centre of the rig. The HiTRec-II 200 kW receiver, shown in Fig. 2-8 (Hoffschmidt, 2001), reached similar levels of efficiency at moderate air temperatures when compared to HiTRec-I receiver, and the steel structure did not deform. The second iteration of the HiTRec receiver concept therefore seemed promising (Hoffschmidt et al., 2003).

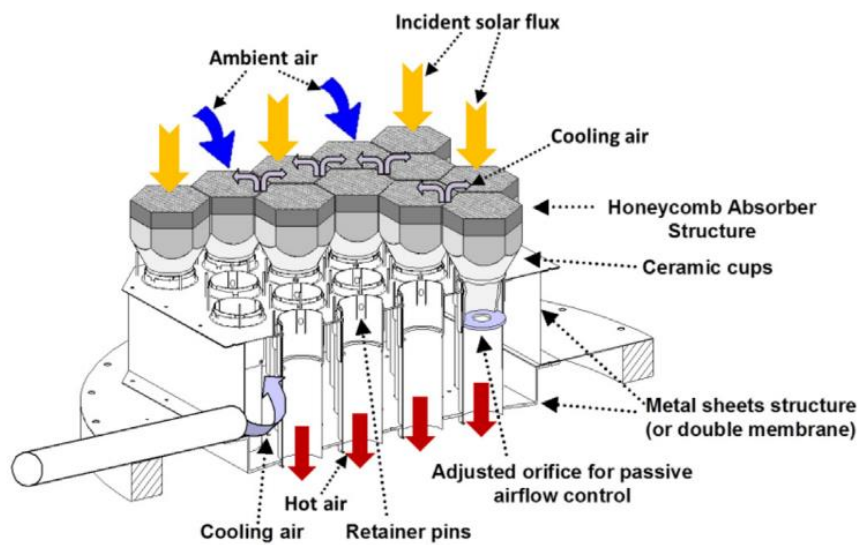


Figure 2-7: HiTRec-II sketch (Hoffschmidt et al., 2003)



Figure 2-8: 200 kW HiTRec-II set-up (Hoffschmidt, 2001)

Further development of the HiTRec receiver technology was carried out to make it suitable for assembly on solar towers through the SOLAIR test campaign. This campaign was carried out in two stages, the first being a 200 kW experimental run known as SolAir-200 followed by a 3 MW experimental run, known as SolAir-3000.

For the SolAir campaign, certain modifications to the overall receiver and absorber design of the HiTRec-II were implemented. The outer shape of the absorber module was changed from hexagonal to square (131 mm in length) for easier assembly of the absorber modules, and a double membrane structure was adopted to hold the absorber module array. The ceramic orifices (for mass flow control) were replaced with a passive control element, to prevent the formation of hotspots, by drawing more cooling air through the absorber where necessary. Attempts to reduce the construction costs were made by replacing the material of the double membrane from Incoloy 800 to stainless steel 1.4858.

The SolAir-200 test campaign consisted of 36 absorber modules stacked in a 6-by-6 configuration, as shown in Fig. 2-9 (Agrafiotis et al., 2007). Tests on three different configurations of the absorber modules were carried out in the 50-day test campaign. Only two of the three configurations achieved mean outlet air temperatures of over 800 °C. Details of the configuration 1 and 2 and the corresponding thermal efficiencies at 700 °C and 800 °C are tabulated in Table 2-1. The third configuration, which consisted of a porous fibre plate placed on the left half part over configuration 2, did not achieve a mean outlet air temperature of 800 °C (Télliez, 2003).

Table 2-1: Thermal efficiencies of the different SolAir-200 receiver configurations (Télez, 2003)

	Set-up	Thermal Efficiency at 700 °C	Thermal Efficiency at 800 °C
Configuration 1	36 recrystallized SiC cups	81 ± 6 %	75 %
Configuration 2	18 recrystallized SiC cups and 18 SiSiC cups	83 ± 6 %	74 %

The SolAir-3000 receiver, depicted in Figure 2-10 (Agrafiotis et al., 2007) , a 3 kW_{th} test rig, consisting of 270 absorber modules, was designed to provide mean outlet air temperatures of 680 – 800 °C. The cups of the absorber modules were made out of SiSiC and the absorbers were made from recrystallized SiC. The test campaign began at the PSA facility in June 2003 and accumulated over 115 operating hours. Nominal outlet air temperatures of 750 °C were achieved at efficiencies of 70 – 75 %.



Figure 2-9: SolAir-200 Setup - Configuration 1 (Agrafiotis et al., 2007)

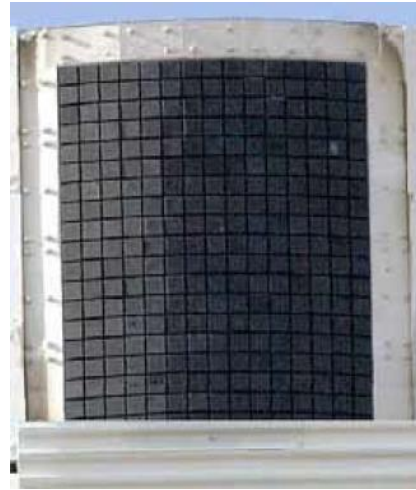


Figure 2-10: SolAir-3000 Receiver (Agrafiotis et al., 2007)

In 2009, a 1.5 MW_e pilot power plant was built in Julich, Germany that used the OVR technology. The Solar Tower Julich consisted of 1080 HiTRec absorber modules used in the SolAir campaign and the heliostat field consisted of 2000 heliostats, making up a total of 20000 m² of mirror area. Figure 2-11 illustrates the facility (Fend, 2010).



Figure 2-11: Solar Tower Julich (Fend, 2010)

The most recent development of a solar tower that uses the open volumetric receiver technology was the development of STPP built in Daegu, South Korea in 2011 with a power rating of 200 kW_e. The tower is 49 meters tall and the concentrator field consisting of around 450 heliostats, and is depicted in Fig. 2-12 (Lee et al., 2015).



Figure 2-12: Central receiver plant featuring OVR in Daegu, South Korea (Lee et al., 2015)

2.2.4. Pressurized volumetric receivers with ceramic absorbers

The first scaled-down model for the demonstration of the pressurized volumetric receiver concept was built by the German Aerospace Centre (DLR) and the Israeli Weizmann Institute of Science (WIS). In 1989, DLR developed a demonstration model called the Pressure Loaded Volumetric Ceramic Receiver (PLVCR-5) with a Si₃N₄ foam absorber, coated in pyromak paint. The PLVCR-5 heated air to 1050 °C at working pressures of 4.2 bar and with a corresponding thermal efficiency of 71 %. Although the

receiver was designed to work at 10 bar, sealing problems in the design prevented it from working at that pressure.

The next version of the receiver, known as the PLVCR-500 receiver, shown in Fig. 2-13 (Ávila-Marín, 2011), which was meant to compensate for the shortcomings of the PLVCR-5, managed to only heat up pressurized air to 960 °C, at 4.15 bar with a corresponding efficiency of 57.3 %. The sub-optimal performance was again attributed to sealing issues in the receiver.

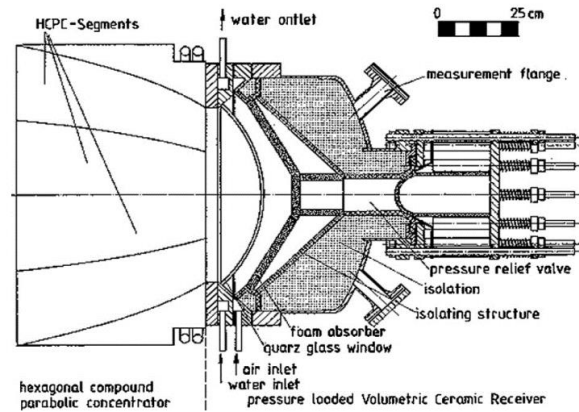


Figure 2-13: PLVCR-500 Receiver Scheme (Ávila-Marín, 2011)

WIS developed the Directly Irradiated Annular Pressurized Receiver (DIAPR) in 1992 shown in Fig. 2-14 (Kribus et al., 2001) which consisted of a porcupine volumetric absorber made out of Pythagoras alumina-silica tubes, a frustum-like high-pressure window made out of fused-silica as well as secondary concentrators. The DIAPR receiver showed robustness at high pressures of up to 30 bar after 250 hours of testing, generating air at 1200 °C at a working pressure of 17-20 bar with working efficiencies of up to 70 – 80 %. The fused-silica window did not show any significant damage due to local hot spot formations, as in the case of PLVCR-500, due to settling of contaminants like dirt and ceramic insulation on its surface (Kribus et al., 2001).

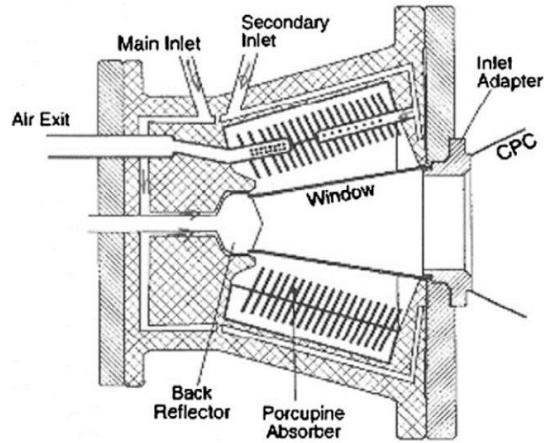


Figure 2-14: Schematic cross-section of DIAPR (Kribus et al., 2001)

A multistage DIAPR model, shown in Fig. 2-15 (Ávila-Marín, 2011) consisting of preheaters and respective secondary concentrators around the centre was designed by WIS. The preheaters acted as cavity receivers with Inconel 600 tubes, to heat the air from ambient temperatures and to convey it to the porcupine absorber via a pipe. This design achieved a maximum outlet temperature of 1000 °C at working pressures of 16 -19 bar.

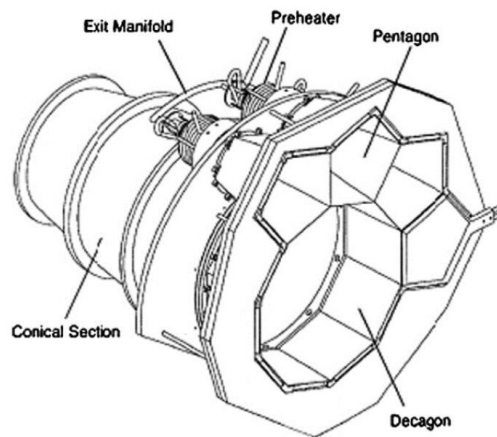


Figure 2-15: Multistage DIAPR consisting of preheaters and secondary concentrators (Ávila-Marín, 2011)

2.2.5. Challenges associated with OVR technology

In general, thermal efficiency of open volumetric receivers is mediocre; mainly due to low return air re-entrainment and radiation losses that occur at the front surface of the porous absorber. The ARR can be defined as the proportion of the warm return airflow emitted into the open atmosphere (through the

gaps between the modules) that is re-entrained back into the absorber modules. The main objective is to utilize the waste heat in the range of 150 °C from the exhaust stream coming from the Heat Transfer Fluid (HTF) circuit.

Factors which affect the ARR in an OVR include the effects of the receiver perimeter geometry, the lateral wind conditions and the air injection angle. The basic ARR mechanism of a modular OVR such as the SolAir receiver is illustrated in Fig. 2-16.

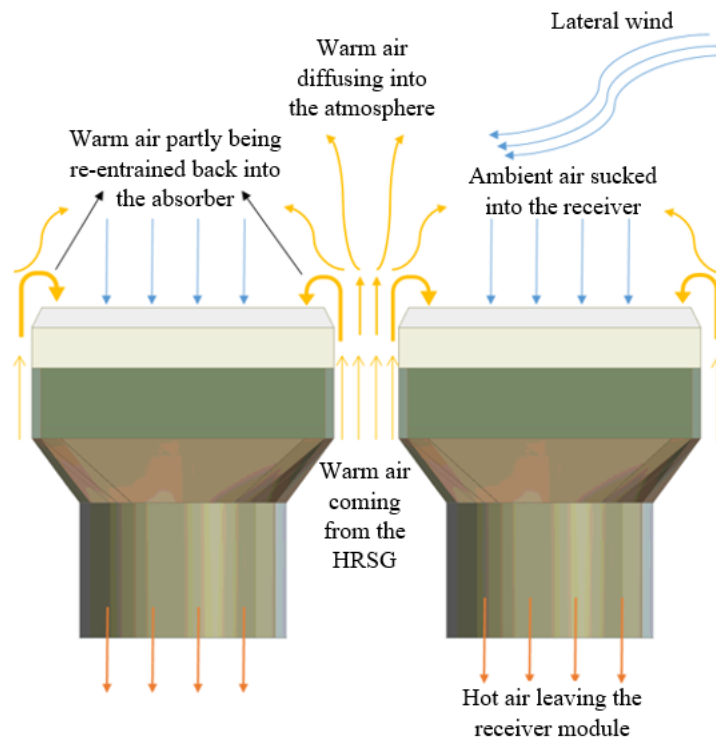


Figure 2-16: Mechanism of ARR in OVRs

Thermal losses occur when the warm air returning from the HTF circuit is only partially re-entrained by the receiver. The warm air therefore mixes with the ambient air leading to a degradation in the thermal energy of the air re-entering the receiver (Á. Marcos *et al.*, 2004). The mixing efficiency can be defined by equation (2.1).

$$\eta_{mix} = \frac{H_{Rec.out} - H_{Rec.in}}{H_{Rec.out} - H_{mix}} \quad (2.1)$$

Here, $H_{Rec.out}$ is the enthalpy of the air at the outlet of the absorber, $H_{Rec.in}$ is the enthalpy of the air at the inlet of the absorber, and H_{mix} is the air mixing enthalpy. Details regarding the calculation of the

H_{mix} is provided in Marcos et al. (2004). The general relationship between the air mixing efficiency and the air return ratio for different inlet air temperatures is given in Fig. 2-17.

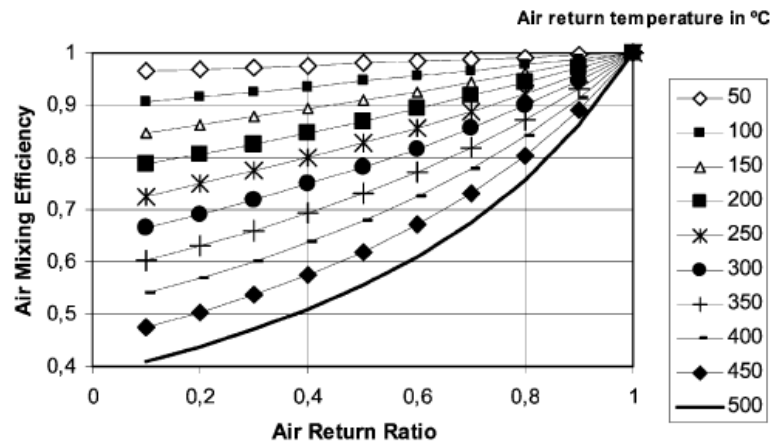


Figure 2-17: Influence of inlet air temperature and air return ratio on the air mixing efficiency (Á. Marcos *et al.*, 2004)

The graph indicates that at higher inlet air temperatures at the absorber, a high air mixing efficiency requires a high ARR. Therefore, a significant improvement in ARR will yield a significant improvement in the competitiveness of an OVR CSP plant.

Receiver airflow instabilities can also occur in OVR porous absorber structures due to uneven temperature distribution in the absorber caused by the non-homogeneous distribution of solar radiation incident on the receiver surface. The uneven flux distribution causes some regions of the absorber to be at a higher temperature than the others. Since the viscosity of the air increases with temperature, this phenomenon causes the air to be drawn in the cooler region than the warmer regions and reduces the heat carried away by the air from the hotter regions of the porous absorber (Bai, 2010). Local overheating can exacerbate thermo-mechanical stresses leading to structural failure, or can result in melting (Gomez-Garcia et al., 2016).

2.3. Numerical modelling of OVRs

Experimental evaluation of OVR performance is an expensive, time-consuming, and an inflexible procedure, which has motivated researchers to evaluate them computationally using CFD and FEA software. One and two-dimensional analytical models of the porous absorber have also been developed by Mey et al. (2013), Kribus et al. (2013) and Kribus et al. (2014) to study the impact of absorber cell

size, porosity, thermal conductivity, and incident solar radiation. on the temperature profiles of the air and solid material. The following subsections summarize the significant findings of researches related to thermal and radiation modelling of OVRs – both analytically and computationally.

2.3.1. Analytical modelling of OVRs

The effect of absorber properties such as porosity and pore size, optical properties such as reflectance and emittance and thermal properties such as thermal conductivity and convective heat transfer coefficient on the efficiency of an OVR were studied by Kribus et al. (2013). A one-dimensional analytical model was developed where separate energy equations were defined for the porous absorber and the air flowing through it; that is, the absorber was modelled under local thermal non-equilibrium (LTNE) conditions. The temperature profiles of the solid (absorber) and the fluid (air) were generated for varying parameters of porosity, pore size and absorber thermal conductivity. The study revealed that parameters such as high porosity and smaller pore size are favourable as they can improve the thermal efficiency, and that choosing a material with lower thermal conductivity can significantly reduce the emission losses.

Mey et al. (2013) researched the accuracy of three radiation modelling approaches in volumetric absorbers, viz. the two-flux approximation, the P1 method and the Rosseland conductivity method, by comparing the final temperature profiles of the air and the porous absorber to that obtained through the much accurate Monte-Carlo Ray Tracing (MCRT) method. The results showed that the solid temperature profile obtained through the two-flux method fared the best as compared to the other radiation models. The absorber (solid) temperature profile obtained using the mentioned radiation models is compared to the one obtained using the MCRT method as shown in Fig. 2-18 (Mey et al., 2013).

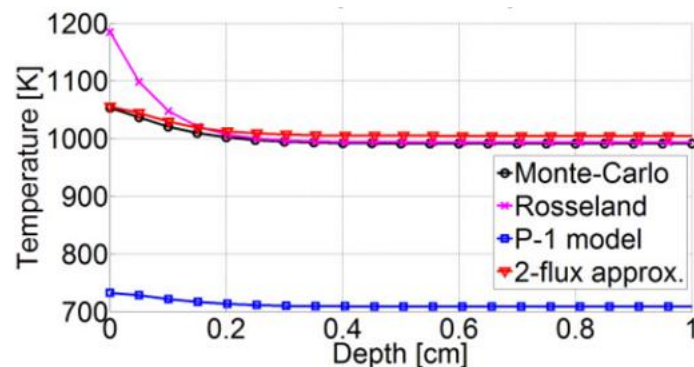


Figure 2-18: Absorber temperature profiles obtained through different radiation models (Mey et al., 2013)

Kribus et al. (2014) carried out a similar analytical study where temperature profiles of the solid phase obtained through the two-flux approximation, the P1 method and the Discrete Ordinate Method (DOM) radiation models were compared to Monte Carlo (MC) ray-tracing results, with the Discrete Ordinate method faring the best. The research also went on to suggest that a high convective heat transfer coefficient and a lower thermal conductivity, beyond the capability of ceramic foams, will achieve higher thermal efficiency in volumetric absorbers. A comparison between the air and absorber temperature profiles obtained using DOM and MC ray-tracing method is illustrated in Fig. 2-19 (Kribus et al., 2014).

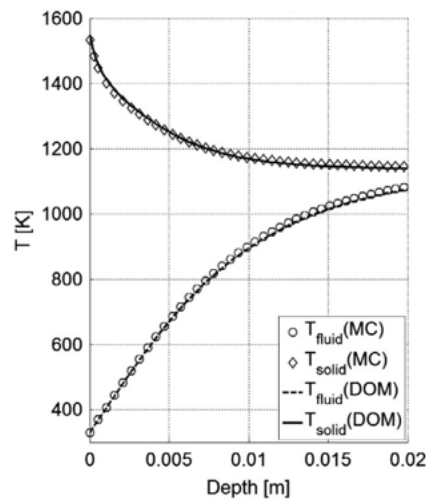


Figure 2-19: Temperature profile of solid and fluid phase in an absorber (Kribus et al., 2014)

Historically, the absorbers used in volumetric receivers were mostly limited to commercially available porous structures, limiting any control over the choice of the material properties. A common suggestion among the mentioned analytical studies is that the optimization of geometrical characteristics such as porosity and pore size, promote radiation penetration into the absorber. Such an optimization process will also establish a large thermal gradient across the absorber, improving its thermal efficiency. Hence, further R&D must be carried out in the field of new fabrication methods, such as additive manufacturing, which allows a certain level over control of critical properties of the absorber.

2.3.2. Computational modelling of OVRs

Becker et al. (2006) studied the possibility of unstable flow in ceramic foam absorbers under the influence of different values of solar flux using theoretical analysis as well as numerical modelling in Ansys Fluent. The structure of a porous absorber determines the nature of the pressure drop across it, which can be predicted using the Darcy-Forchheimer equation given by equation (2.2).

$$\frac{\Delta p}{l} = \frac{\mu}{k_1}(u) + \frac{\rho}{k_2}(u^2) \quad (2.2)$$

Here, Δp is the pressure drop across the absorber, l is the absorber thickness, μ is the dynamic viscosity of the air, ρ is the air density, k_2 is the inertial coefficient, k_1 is the viscous coefficient and u is the superficial air velocity. For an extruded porous absorber, it was theoretically determined that the pressure drop takes a linear form ($k_2 = \infty$) and there is a risk of air flow instability due to the possibility of multiple temperature values at constant pressure and solar irradiance, as shown in Fig. 2-20 (Becker et al., 2006). However, for an OCF porous absorber, the pressure drop is quadratic in nature (low inertial coefficient) and there is less risk of flow instability, as illustrated in Fig. 2-21 (Becker et al., 2006).

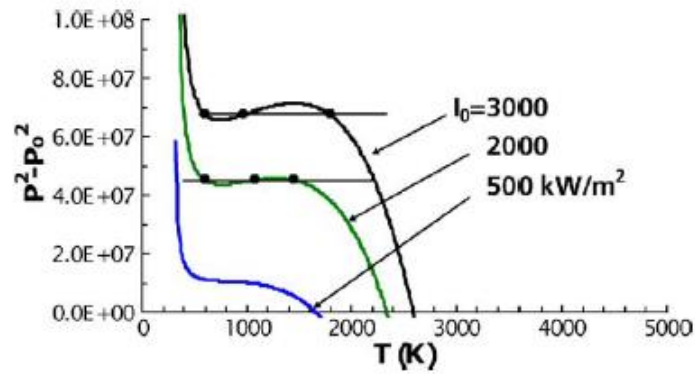


Figure 2-20: Quadratic pressure drop versus the air temperature for extruded absorbers (Becker et al., 2006)

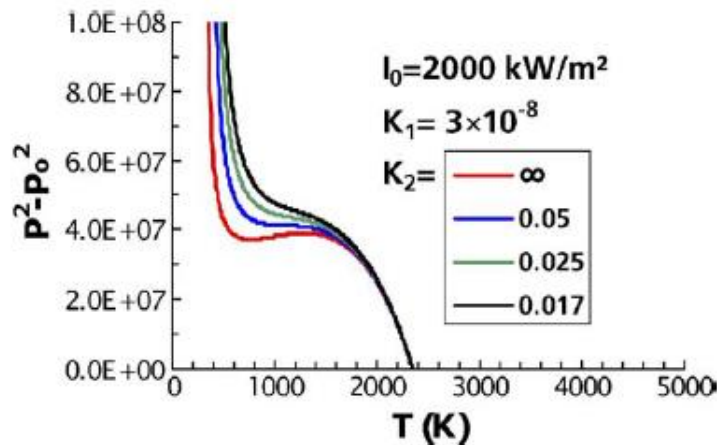


Figure 2-21: Quadratic pressure drop versus temperature for open ceramic foams (Becker et al., 2006)

The formation and the disappearance of hotspots in porous absorbers investigated through local thermal non-equilibrium (LTNE) CFD simulations consisted of three blocks representing the boundary

conditions to the inlet flow into the absorber (blue block), the porous medium (green block) and the outflow of hot air (red block) as shown in Fig. 2-22 (Becker et al., 2006). In transient simulations, a region of high radiation flux density was applied to the model to create the hotspot. Thereafter, heating was interrupted and the rate at which the hotspot reduced in size and intensity was studied (Fig. 2-23) for variations in the absorber's effective heat conductivity and inertial co-efficient. The numerical and the theoretical results indicate that a higher thermal conductivity and quadratic pressure drop and low inertial co-efficient will reduce the risk of instability, and thus the formation of hotspots within the absorber.

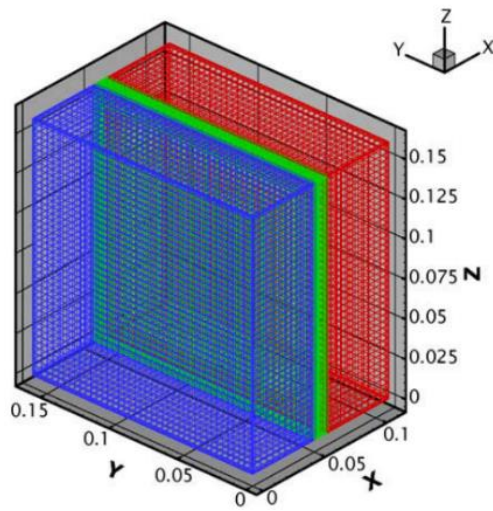


Figure 2-22: Computational domain for hotspot simulation (Becker et al., 2006)

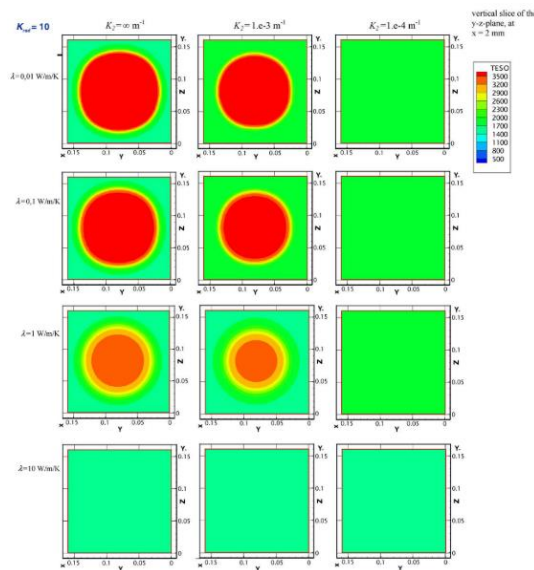


Figure 2-23: Rate of disappearance of hotspot depending on the material property (Becker et al., 2006)

The effect of constant and varying porosity in the radial and axial directions on the outlet air temperature and velocity field was investigated in Roldán et al. (2014) using the CFD code Ansys Fluent. The study was carried out on an axisymmetric half-model of a solar receiver that employed a user-defined function to model a volumetric heat source in the absorber region. The turbulence model chosen for the analysis was the RNG $k - \varepsilon$ turbulence model. Figure 2-24 represents one of the computational domains used in the study.

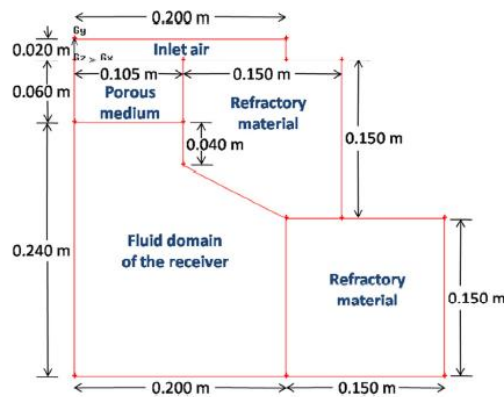


Figure 2-24: Solution domain for absorber with constant porosity (Roldán et al., 2014)

The thermal efficiency of the receiver was calculated for each of the configurations and in the constant porosity case, the highest porosity was found to have achieved the highest thermal efficiency, reinforcing the findings of Kribus et al. (2013). From the simulation results, it was inferred that a decreasing porosity with depth and in the radial direction yielded higher outlet air temperatures.

Another detailed CFD analysis was carried out on four HiTRec-II absorber modules by Roldán et al. (2016). The simulations employed a Local Thermal Equilibrium (LTE) condition and were carried out in Ansys Fluent. The set-up of the model was similar to that of the axisymmetric solar receiver model set-up in Roldán et al. (2014).

The CFD model was validated against experimental data obtained from the 200 kW HiTRec-II tests. The study mainly dealt with the effect of wind on receiver performance, and thermal efficiencies were evaluated for variations in wind speed, wind incidence angles, return air velocity and return air temperature. The study concluded that the HiTRec modules generated highest air outlet temperatures at lower angles of wind incidence (highest incidence angle being perpendicular to the modules). As far as the warm air from the HTF loop is concerned, higher temperatures and lower ejection velocity was favourable for higher outlet temperatures. The effect of wind was found to be detrimental to the thermal efficiency in all instances, increasing in severity with magnitude and incidence angle. Figure 2-25 illustrates the velocity distribution in the absorber modules that was obtained when the effects of wind

were being simulated (Roldán et al., 2016). Palero et al. (2008) highlighted another side-effect of direct wind interaction with the absorber modules, which is the non-uniform temperature distribution across the absorber, possibly leading to the deterioration of its structural integrity.

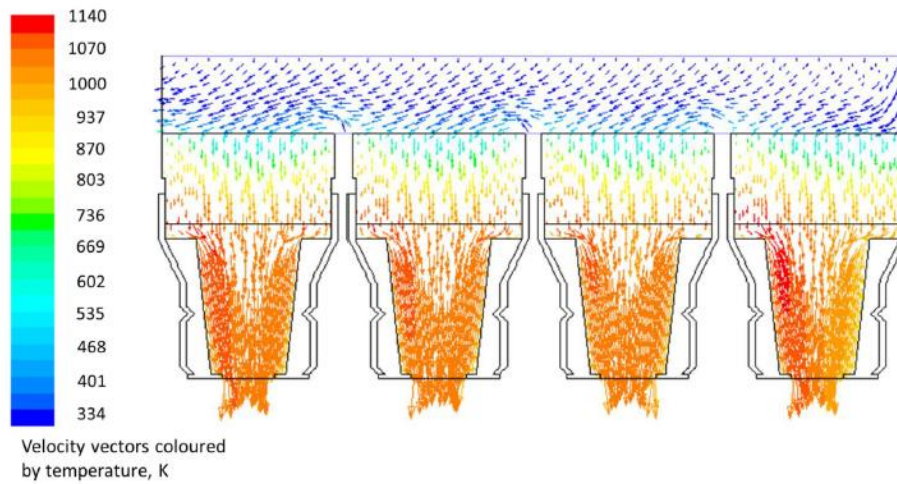


Figure 2-25: The velocity distribution in the absorber modules (Roldán et al., 2016)

Wu et al. (2011) proposed an LTNE-based numerical porous absorber model to study the sensitivity of absorber performance to absorber porosity, pore size and thermal conductivity. The radiative heat transfer was modelled using the P1 method and the steady-state temperature results obtained from the simulations were validated against experimental data obtained at quasi-steady state conditions. Fluid and solid phase temperature profiles were generated for a wide range of porosities, mean velocities and pore sizes. Since the model simulated LTNE conditions, useful information concerning the distinct temperature distribution within the fluid and solid phases could be derived. An example of such distributions is provided in Fig. 2-26 (Wu et al., 2011a).

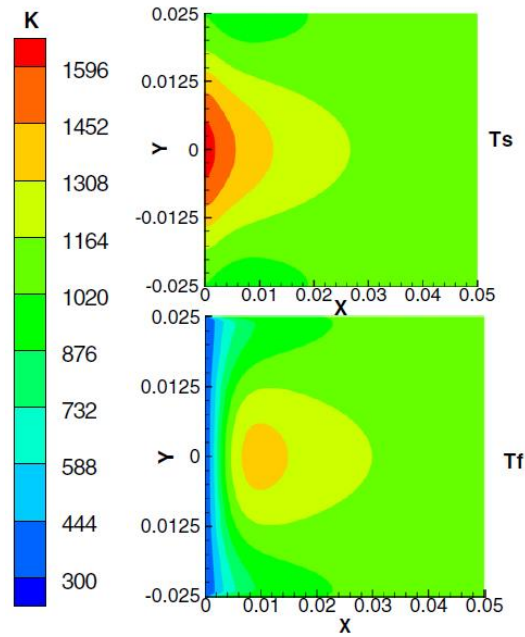


Figure 2-26: Predicted temperature distribution for the solid and fluid phase (Wu et al., 2011a)

A very similar study was conducted by Wang et al. (2013) who developed a volumetric absorber model in Ansys Fluent, with the MCRT method being applied to calculate the solar heat flux and Rosseland approximation model being used to model radiation propagation. A common trend was observed concerning the effect of pore size, mean inlet velocity and incident solar radiation on absorber and the air temperature profiles. A lower porosity, lower mean air velocity and higher incident solar flux were found to be favourable for generation of high outlet air temperatures.

Wang et al. (2013) carried out another LTNE study on a solar thermochemical reactor (featuring a porous absorber) in Ansys Fluent, in which the main focus was to compare the air and absorber temperature profiles generated using the Rosseland conductivity model and the P1 approximation radiation models. Although changes in the absorber temperature profile were found to occur with variations in operating conditions such as solar irradiance, pore cell size and the fluid inlet velocity, the relative difference between the temperature profiles was fairly small, with a maximum difference of 4.97 %.

An LTNE model was proposed by Fend et al. (2013) to investigate potential improvements in receiver thermal efficiency with slight geometric changes to the constituent absorber module. Two models, one of an individual absorber channel and the other of the whole porous continuum of an absorber module, were developed and validated against experimental data. The single-channel model was used to study the effect of wall thickness and channel width on the outlet air temperature. The geometry of the porous continuum was modified to account for a frustum shape in the geometry of the porous medium. The

frustum shaped absorber exhibited a homogenous temperature distribution (Fig. 2-27) and attained a higher thermal efficiency than the absorber without the frustum.

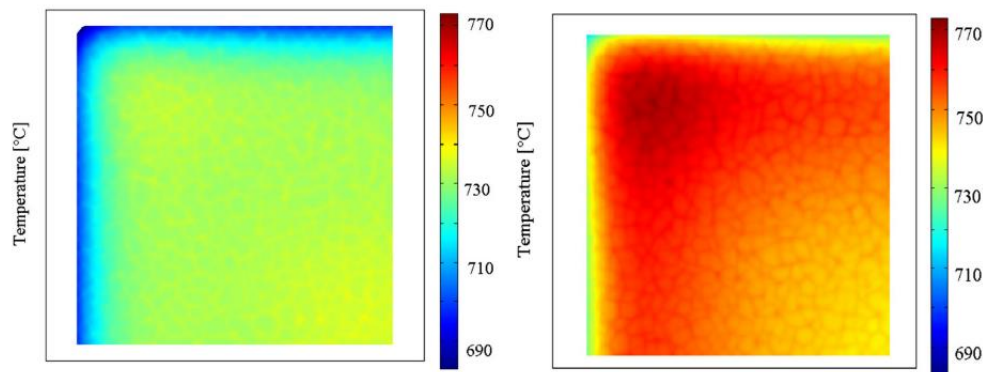


Figure 2-27: Absorber temperatures at the inlet surface (with frustum left, without frustum right) (Fend et al., 2013)

The studies mentioned above have dealt with 1-D analytical modelling for parametric studies and 2-D CFD modelling of individual HiTRec modules and volumetric absorbers. Stadler et al. (2019) proposed a new method of modelling that accounts for an interaction of a whole cluster of absorber modules constituting an OVR, capturing the flow of air around it as well as the effect that the heat and mass transfer within the modules has on the ARR of the receiver.

The CFD model used for the study, shown in Fig. 2-28 (Stadler et al., 2017a), represents the cluster of receivers placed on top of the Solar Tower in Jülich, but with additional external air return ducts on either side of and beneath the receiver. This unique approach does not model the geometric details of the absorber modules themselves, as in Roldán et al. (2016). Instead, the absorbers were represented by a cluster of numerical cells with a few cells in the middle of the cluster acting as outflow domain of the warm air returning from the HTF circuit and the remaining cells providing for an inflow of the air drawn from the atmosphere into the modules, i.e. the individual absorbers were represented by clustered inflow/outflow boundary conditions. The area fraction of the cells that represent the inlet section matches that of the original receiver. The input parameters of the model include the solar flux distribution, the mass flow rate of air drawn into the modules, the mass flow rate of warm return air, ambient air temperatures and pressure loss coefficients for the absorber. The velocity and the temperature field of the whole receiver were then calculated as a function of the mentioned inputs.

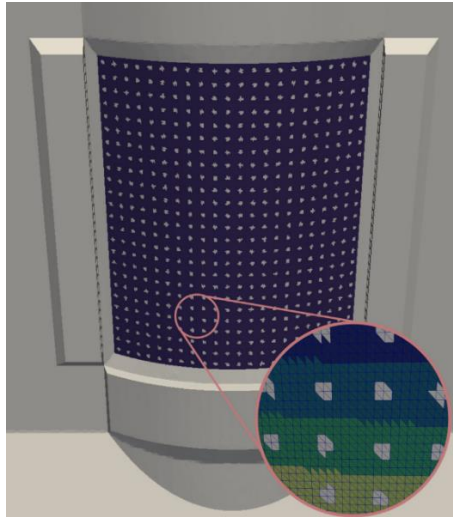


Figure 2-28: CFD model of OVR solar tower in Jülich, with external air return ducts (Stadler et al., 2019)

In the validation study of the model, the ARR obtained from the simulation for different mass flow rates of the warm air showed reasonable agreement with the regression curve obtained from experimentally measured data from the Solar Tower Jülich, with an average deviation of 0.6 % and a maximum deviation of 0.5 %. Figure 2-29 (Stadler et al., 2017a) shows the temperature contour plot of the warm return air from the HTF circuit and the return air concentration of the receiver CFD model.

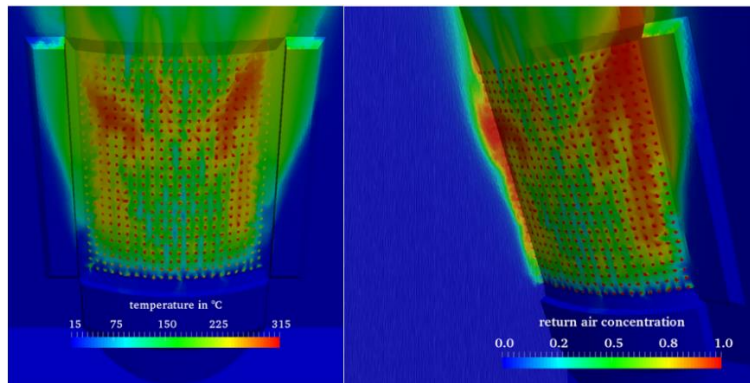


Figure 2-29: Warm air temperature plot (LHS) and return air concentration (RHS) (Stadler et al., 2019)

2.3.3. Alternative OVR designs

A dual receiver concept consisting of a tubular evaporator section and an open volumetric receiver for pre-heating and superheating of steam was proposed by Buck et al. (2006). The schematic diagram of the dual receiver unit is illustrated in Fig. 2-30. The absorber tubes (a.k.a. tubular evaporators) are evenly spaced out in front of the receiver and the volumetric receiver is situated behind the tubes. The

radiative heat emitted by the volumetric absorber to the surrounding atmosphere is partly absorbed by the tube evaporators, thereby reducing the radiative losses. The solar radiation incident on the receiver tube evaporates the saturated water flowing through it into steam. The pre-heating of the feed water and superheating of the steam is carried out in the generator/heat exchanger that is fed with hot air coming from the open volumetric receiver.

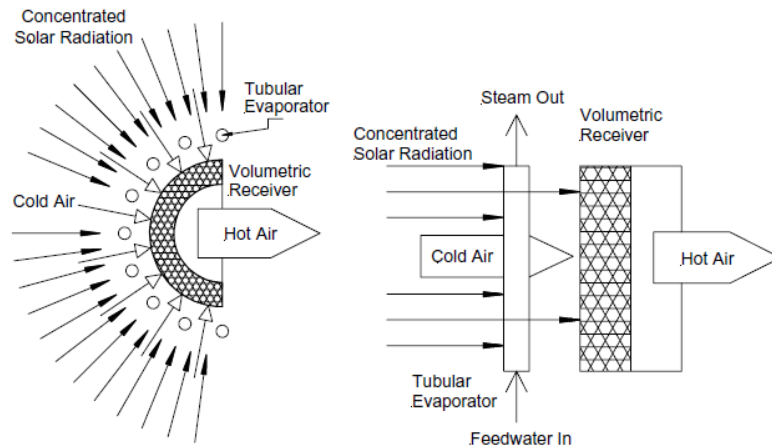


Figure 2-30: Dual receiver concept – top view (LHS), front view (RHS) (Buck et al., 2006a)

The annual performance data of the dual receiver concept was evaluated using the IPSE Pro software and compared to the performance data of a reference plant similar to the original design of the PS10 OVR CSP. The dual receiver concept yielded a 27 % higher annual power output than the reference plant despite having a smaller heliostat field and lower outlet air temperature from the volumetric receiver. However, the complexity of the system brought about by two subsystems of the new receiver concept calls for the implementation of more sophisticated control of the system during start-up and operation (Buck et al., 2006b).

Marcos et al. (2004) investigated the possibility of improving the ARR of an OVR by proposing a multitude of modifications on three main receivers, viz. a conceptual absorber module design, depicted in Fig. 2-31 (Á. Marcos *et al.*, 2004) on which two geometrical additions (secondary concentrator and cavity) were made, a HiTRec-II absorber module and a SIREC (metal wire mesh) absorber module. The simulation data obtained from Ansys Fluent for the conceptual design revealed that the direct contact of the warm return air with the ambient air reduces the ARR significantly, and the cavity and the secondary concentrator additions achieved the highest ARR.

For the HiTRec receiver, an air return mechanism that injects warm air (a) perpendicular to the receiver, (b) parallel to the receiver using an outer injection ring (c) parallel and normal to the absorber as well as (d) the usage of an absorber shield to prevent direct contact of the warm air with the incoming wind,

were tested using Ansys Fluent. Details about the geometry of the absorber shield, or the way in which it was assembled on the HiTRec-II absorber modules were not clearly stated. The ARR for option (c) was the highest followed by options (b) and (d). It was also discovered that chamfering the outer edges of the SolAir-3000 absorber modules increased the ARR by 40 %. Lastly, the SIREC receiver consisting of a circular wire mesh absorber was tested with two different ARR mechanisms which injected warm air using (a) six individual injectors and (b) through a continuous injection ring. The receiver achieved higher outlet temperature values and ARR using the continuous injection ring mechanism.

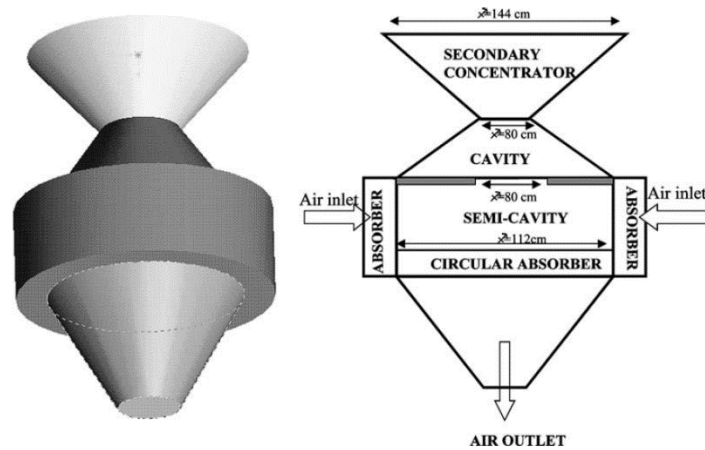


Figure 2-31: Multi-component geometric model (Buck et al., 2006a)

A new type of absorber design was conceived by Capuano et al. (2017) which was shown to exhibit ideal volumetric heating i.e. the air outlet temperature is higher than the absorber inlet temperature. A comparison of the HiTRec absorber channel to the new channel is shown in Fig. 2-32.

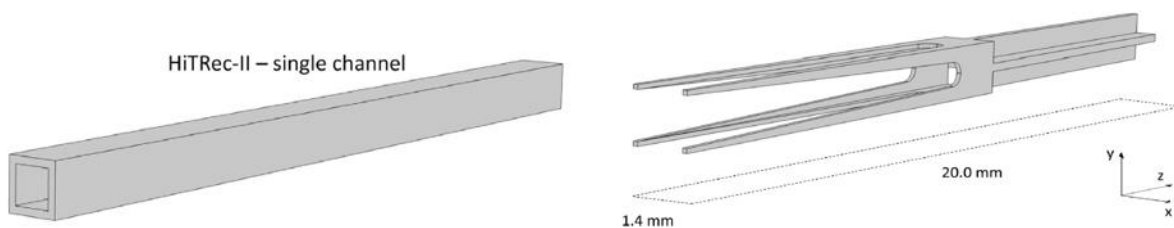


Figure 2-32: HiTRec-II single channel (LHS) and new channel geometry (RHS) (Capuano et al., 2017)

Since a volumetric effect was reported in the simulation results, attempts were made to manufacture the absorber with the new channel geometry. The technique chosen for the fabrication procedure could not manufacture the fine details of the geometry. Therefore, a 3:1 scaled-up version of the new geometry

made out of titanium-aluminium alloy (Ti6Al4V) was manufactured, as shown in Fig. 2-33 (Capuano et al., 2017).

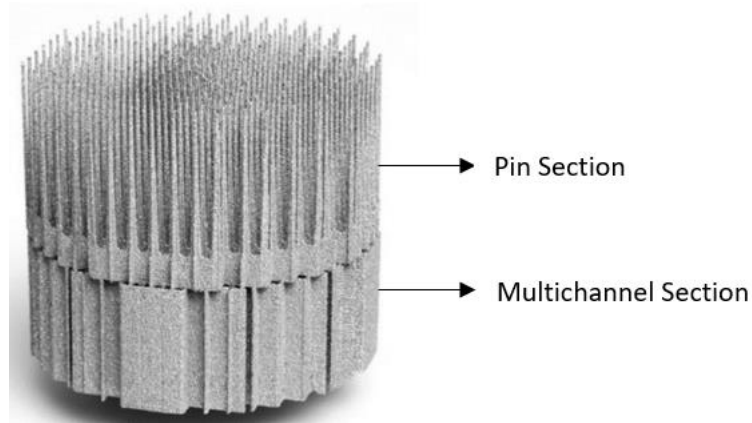


Figure 2-33: New absorber design (Capuano et al., 2017)

The pin section of the absorber allows deeper penetration of the solar radiation and also reduces radiative and optical losses due to the small specific surface area of the pins. A large proportion of the thermal energy transferred in the pin section is through the process of conduction and radiation due to the low specific surface area (which inhibits convection). During the experimental tests, the mass flow rate of the air was varied at constant incident power and high outlet temperatures were achieved at low mass flow rates, but at the expense of the thermal efficiency since the radiative losses increase (by four orders of magnitude) with temperature.

Numerically predicted outlet air temperature, thermal efficiency and pressure drop across the absorber were compared to numerical predictions for the HiTRec receiver as well as the experimental data of the scaled-up version of it. The new absorber design clearly exhibited higher thermal efficiency as well as higher outlet air temperatures than the HiTRec-II absorber modules as shown in Fig. 2-34 (Capuano et al., 2017).

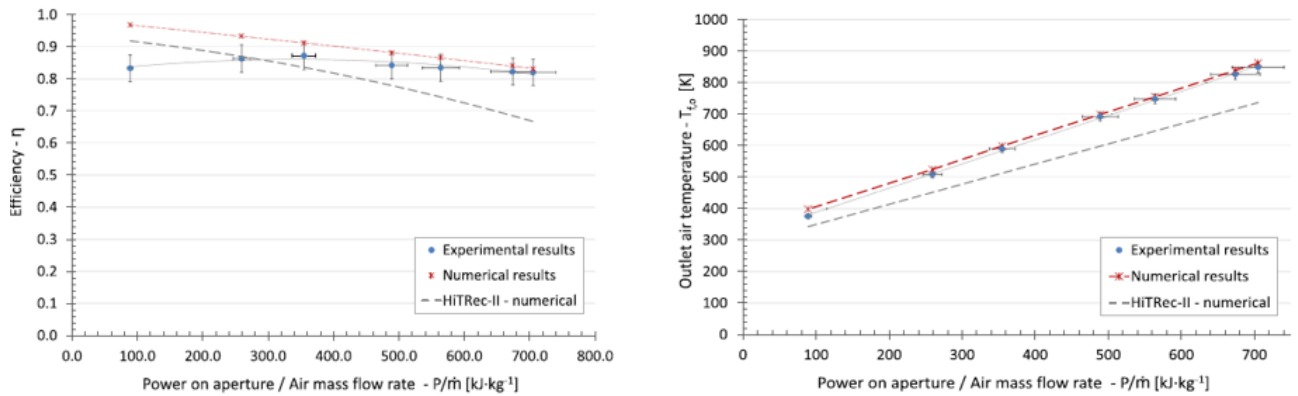


Figure 2-34: Graphs comparing the HiTRec absorber thermal efficiency (LHS) and outlet air temperature (RHS) to those of the new geometry (original numerical and scaled up model) (Capuano et al., 2017)

2.4. Conclusion

The present chapter provides an overview of Open Volumetric Receiver (OVR) technology, categorizing the technology according to the operating mode and further sub-categorizing it based on the type of material used for the absorber. The low thermal efficiency of the current state-of-the-art HiTRec OVR technology can be attributed to the low Air Return Ratio (ARR), estimated to be 45 %, along with a failure in achieving the volumetric effect.

The majority of the research carried out on OVR technology has aimed at either improving the thermal efficiency directly by altering the absorber geometry (the complete absorber or the individual channels of an extruded absorber) or by modifying the geometry of the absorber modules themselves. The methodology of the research carried out can be broadly categorized into analytical modelling and CFD modelling. A plethora of research was concerned with the analytical modelling of volumetric absorbers under LTNE conditions, aimed at studying the effects of changes in thermophysical and geometric properties on the thermal efficiency of the receiver. On the other hand, CFD modelling has dealt with investigating the convective and radiative heat transfer associated with volumetric absorber structures as well as with individual receivers and the receiver system as a whole.

Direct impact of wind on the ARR of the volumetric absorber modules have not been extensively researched in literature. However, certain side-effects of direct wind impingement on these modules, such as reduced mean air outlet temperatures (Roldán et al., 2016) as well as possibility of steep temperature gradients on the absorber surface (Palero et al., 2008) highlight the significance of preventing wind from striking the absorbers directly, reducing its performance. Therefore, the main focus of the Master's work will be on researching ways and means of reducing the impact of wind on the ARR of open volumetric absorber modules.

3. THEORY

One of the main goals of designing an OVR is to heat up the air flowing through it to the highest possible temperatures. The efficiency of the an OVR module can be considered as the ratio of the heat energy gained by the air flowing through it to the total solar energy incident on the porous absorber. The presence of a large temperature difference between the porous absorber and the air flowing through it results in higher convective heat transfer to the air, and therefore higher efficiency of the receiver. The rate of heat transfer to the air is a function of various factors such as the geometric characteristics of the absorber (extruded or OCF), its thermal and optical properties (like absorptivity, thermal conductivity, reflectance). The solar radiation profile incident on the absorber modules, and the nature of pressure drop (linear or quadratic) across the absorber also affect the heat transfer rate. Therefore, knowledge of the various heat transfer mechanisms will lead to a better understanding of the underlying physics of the OVR design that could potentially open up new avenues for improvements in its design.

This chapter aims to provide an insight into the measurement of the ARR, and describes the nature of pressure drop and the heat transfer processes such as conduction, convection and radiation in OVRs. The fundamental concepts of CFD modelling will be described in the context of OVRs, as a vital pre-requisite to the modelling of OVRs in the Chapter 4, 5 and 6.

3.1. Air Return Ratio

As stated in section 2.2.5, the ARR of an OVR can be defined as the proportion of the warm return airflow emitted into the open atmosphere (through the gaps between the modules) that is re-entrained back into the absorber modules. It can be calculated by taking the ratio of the specific enthalpy of the air drawn in at the entrance of the porous absorber to that of the warm air in the return ducting (Stadler et al., 2017b). The ratio of the specific enthalpies is approximately equivalent to the ratio of the temperatures, given by equations (3.1) and an alternative way of defining the ARR is the ratio of the mass flow rate of warm air drawn back in the absorber to the total mass flow rate of air drawn through the absorber, as in equation (3.2).

$$ARR_e = \frac{h_{rec,in} - h_\infty}{h_r - h_\infty} \approx \frac{T_{Rec,in} - T_\infty}{T_r - T_\infty} \quad (3.1)$$

$$ARR_m = \frac{\dot{m}_{r,i}}{\dot{m}_t} \quad (3.2)$$

where $T_{Rec.in}$ is the temperature of the air that is drawn into the porous absorber, T_r is the temperature of the warm air that is recirculated back from the warm return air ducting, T_∞ is the ambient temperature, $\dot{m}_{r,i}$ is the mass flow rate of warm air drawn back into the absorber and \dot{m}_t is the total mass flow rate of the air drawn in through the absorber. The warm air coming from the HRSG will mix with the ambient air before being drawn back into the modules. A high degree of mixing will cool the recirculated air which will in-turn reduce the enthalpy of the air entering the receiver. Therefore, the least amount of mixing with the ambient air is favoured for a higher ARR. The air mixing efficiency of an Open Volumetric Receiver (OVR) can be calculated by equation (3.3) (Á. Marcos *et al.*, 2004).

$$\eta_{mix} = \frac{H_{Rec.out} - H_{Rec.in}}{H_{Rec.out} - H_{mix}} \quad (3.3)$$

Here $H_{Rec.out}$ is the enthalpy of the air leaving the OVR module, H_{mix} is the receiver air mixing enthalpy and $H_{Rec.in}$ is the enthalpy of the air at the absorber inlet. Referring to Fig. 2-17 from Chapter 2, a high air mixing efficiency would imply a high ARR. For the ideal case of no mixing of the return air with the ambient air, the ARR is one.

Since the ARR performance directly impacts the overall thermal efficiency of an OVR, poor ARR performance will compromise the solar-electric efficiency of the associated CSP plant. Unfortunately, measured ARR performance in state-of-the-art OVRs is relatively poor; significantly below one. For example, the measured ARR for the HiTRec-II OVR was 44.6% (maximum) at an air mass flow of 0.09 kg/s and return air at 160 °C (Hoffschmidt *et al.*, 2003), with the SolAir-200 set-up achieving similar results with an ARR ranging from 0.35 – 0.45 (Téllez, 2003).

3.2. Heat conduction

The process of heat transfer between the absorber and the air in OVRs is predominantly convective and radiative in nature, with the process of conduction contributing the least to the heat transfer. The steady-state heat flux equation for conduction in one-dimension (1-D) is described by Fourier's Law given by equation (3.4).

$$q_x'' = -k \frac{dT}{dx} \left[\frac{W}{m^2} \right] \quad (3.4)$$

The heat flux equation can be adapted to account for the dependence of conduction on the porosity of the absorber, as in equation (3.5).

$$q_x'' = -k(1 - \phi) \frac{dT}{dx} \quad (3.5)$$

A way to predict the temperature gradient of a medium is by applying the heat diffusion equation (equation (3.6)),

$$\frac{\partial}{\partial x} \left(k \frac{\partial T}{\partial x} \right) + \dot{q} = \rho c \frac{\partial T}{\partial t} \quad (3.6)$$

where $\frac{\partial}{\partial x} \left(k \frac{\partial T}{\partial x} \right)$ is the rate of change of heat flux in the medium in the direction of transfer, \dot{q} is the rate at which heat is generated per unit volume within the medium and $\rho c \frac{\partial T}{\partial t}$ is the time rate of change of thermal energy of the medium, per unit volume. When assuming that the movement of heat through a medium is steady-state, $\rho c \frac{\partial T}{\partial t}$ becomes zero. In OVRs, the incident solar radiation heats the absorber volumetrically. So it can be assumed that \dot{q} can be a representation of the volumetric energy generation due to solar irradiation in equation (3.6) (Tiwari and Suneja, 1997). Therefore, the heat diffusion equation for a 1-D, transient heat conduction within an OVR can be described by equation (3.7).

$$k(1 - \phi) \frac{\partial^2 T}{\partial x^2} + \frac{\partial I(x)}{\partial x} = \rho c \frac{\partial T}{\partial t} \quad (3.7)$$

3.3. Convection

The heat transfer rate between the air and the absorber mainly relies on the process of convection, when compared to conduction and radiation. Using Newton's Law of Cooling, given by equation (3.8), the local heat flux between the absorber and the surrounding environment can be calculated,

$$q_x'' = h(T_s - T_\infty) \quad (3.8)$$

where, h is the heat transfer coefficient, T_s is the surface temperature and T_∞ is the bulk temperature away from the surface. By integrating the local heat flux over the area of a hypothetical flat surface, the total heat transfer rate due to convection between the absorber surface and the surrounding air can be derived and is given by equation (3.9),

$$\dot{q} = \bar{h} A_s (T_s - T_\infty) \quad (3.9)$$

where \bar{h} is the average convective heat transfer coefficient of the surface under consideration, A_s is the area of a flat surface under consideration. Convection occurs through the volume of the porous absorber, and therefore, equation (3.10) can be adapted to suit the requirements of the OVR as,

$$\dot{q} = h_v(T_s - T_\infty) \quad (3.10)$$

The measure of the convective heat transfer within the volume of a porous absorber is given by a dimensionless parameter, known as volumetric Nusselt number, and it is related to the volumetric convective heat transfer coefficient, as shown in equation (3.11).

$$h_v = Nu_v \frac{k_f}{d^2} \quad (3.11)$$

For fluid flow through the porous material, the dimensionless Nusselt number is a function of the Reynolds number and has a general form shown in equation (3.12) according to Wu et al. (2011),

$$Nu_v = C \phi^{m_1} Re^{m_2} \quad (3.12)$$

where ϕ represents the porosity, m_1 , m_2 and C are constants and Re represents the Reynolds number of the flow. The volumetric Nusselt number is determined using correlations, which are usually formulated from experiments conducted on ceramic and metal mesh absorbers. Various correlations for the Nusselt number have been derived in literature for open cell foam depending on the Reynolds number of the flow, shown below in equations (3.13), (3.14) and (3.15) (Li et al., 2016).

$$Nu_v = \left(0.0426 + 1.236 \frac{d}{L}\right) Re, (2 < Re < 836) \quad (3.13)$$

$$Nu_v = 2.0696 \cdot \phi^{0.38} \cdot a_{vs} \cdot Re^{0.438}, (70 < Re < 800) \quad (3.14)$$

$$Nu_v = 0.456 \cdot a_{vs} \cdot Re^{0.70}, (50 < Re < 266) \quad (3.15)$$

Here, a_{vs} represents the specific surface area of the porous absorber, d represents the diameter of the pore of the absorber and L represents the length of the absorber. The Nusselt number for extruded absorbers has been derived by Jung et al. (2013) and is given by the following equation (3.16).

$$Nu_v = \frac{2.30 \left[\frac{z}{D_h * Re * Pr} \right]}{0.0666 - 0.0071 Pr^{-0.75} + \left[\frac{z}{D_h * Re * Pr} \right]} + (0.799 Pr^{-0.0279} - 0.201) \left[\frac{z}{D_h * Re * Pr} \right]^\alpha \quad (3.16)$$

With

$$\alpha = 0.0479 \log_{10} Pr - 0.439$$

and

$$D_h = \frac{A_{ch}}{P}$$

with D_h being the hydraulic diameter of a pore, A_{ch} being the area of the channel of an extruded absorber and P being the channel perimeter and z being the distance into the channel. The rate of convective heat transfer is also reliant on the nature of the pressure drop in the porous structure, which is discussed further in section 3.6. The nature of the flow through the porous medium, be it laminar or turbulent flow, is determined by the Reynolds number given by equation (3.17),

$$Re = \frac{u_f \cdot \rho_f \cdot d}{\mu_f} \quad (3.17)$$

where, u_f is the superficial velocity of the flow through the porous structure (Wu et al., 2011b), d , represents the characteristic length of the porous structure (mean pore diameter for the open ceramic foams or hydraulic diameter of the flow channel for extruded structures (Gomez-Garcia et al., 2016), and ρ_f and μ_f , are the temperature dependent density and dynamic viscosity of the air.

3.4. Radiation

The rate at which the thermal energy radiated from a surface per unit area is known as the surface emissive power, given by equation (3.18).

$$E(T) = \sigma \epsilon T_s^4 \quad (3.18)$$

Here σ represents the Stefan-Boltzmann's constant of $5.670 \times 10^{-8} \text{ W m}^{-2} \text{ K}^{-4}$, ϵ represents the emissivity of the surface and T_s is the absolute surface temperature. Typically, heat exchange through radiation involves two surfaces, an emitting surface A_e and an absorbing surface A_a . In such cases, the rate of heat transfer from the emitting surface per unit area can be calculated by equation (3.19).

$$\dot{q} = \sigma \epsilon A_e (T_e^4 - T_a^4) \quad (3.19)$$

For the current work, the process of radiation occurring between the frontal surface of the absorber and the surrounding air is taken into consideration. The absorber surface emits thermal energy, which is then absorbed by the surrounding ambient air. Therefore, adapting the above equation for OVRs will give equation (3.20),

$$q_{loss} = \sigma \epsilon A_s ((T_s)^4 - (T_{amb})^4) \quad (3.20)$$

where T_s is the front surface temperature, T_{amb} is the temperature of the surrounding air and A_s is the frontal surface area of the absorber (Incropera and DeWitt, 1995).

3.4.1. Radiation attenuation

The solar radiation, I_λ , incident on the porous absorber travels a certain length during which its intensity is reduced by either absorption or scattering. By assuming that the porous absorber medium within the receiver has homogenous properties, the Beer-Lambert law can be used to describe the transmission of radiation through cellular ceramic material (Fabrisio et al., 2014).

$$I(x) = I(0) * e^{-\beta x} \quad (3.21)$$

The extinction coefficient, β , is dependent on the properties such as temperature, material properties of the porous medium and wavelength of the radiation. It can be expressed as the summation of the absorption coefficient and the scattering coefficient, as in equation (3.22) (Incropera and DeWitt, 1995).

$$\beta = \kappa + \sigma_s \quad (3.22)$$

Here, the absorption coefficient, κ , quantifies the radiation energy that is converted into thermal energy within the absorber, and the scattering coefficient, σ_s , quantifies the change in the direction of the radiation that is not converted to thermal energy within the absorber. The behaviour of the incident radiation in an extruded structure such as that used in HiTRec OVR absorber modules, is such that the radiation that is not absorbed upon first contact with the channel surface undergo subsequent absorption and reflection processes within the channel, with a portion of the incident radiation consequently leaving the front surface of the absorber as lost energy, as shown in Fig. 3-1 (Elnoumeir et al., 2017).

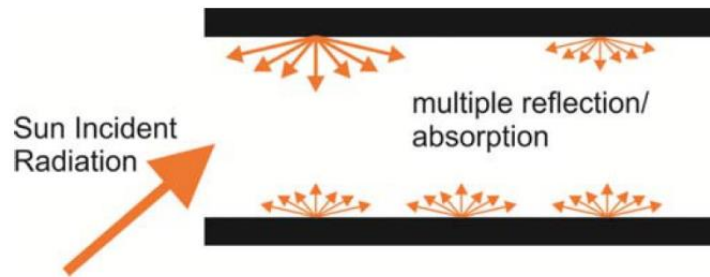


Figure 3-1: Multiple reflections inside the channel of the absorber (Elnoumeir et al., 2017)

Elnoumeir et al. (2017) developed a numerical tool for determining effective radiative parameters, such as the extinction coefficient, for absorbers with extruded structure. This tool accounted for the various possible angles of incidence at which the solar radiation can be reflected off a field of heliostats that usually surrounds a solar tower and strike the OVR system placed on top of the tower. It was concluded that an accurate representation of the extinction coefficient was polynomial in nature, and assuming a

constant value can lead to significant errors from a numerical modelling perspective. Nonetheless, an approximately constant value of the extinction coefficient for the HiTRec absorbers was stated to be 234.7 m^{-1} . It was also discovered that the normal radiative flux leaving the front surface of the honeycomb absorbers after multiple reflection/scattering only accounted for less than 1 % of the total incident thermal power, concluding that the radiation losses emitted from the front of the absorber surface are negligible.

A similar approach was utilized in Roldán et al. (2016) to determine an effective volumetric heat source expression that would account for the re-radiation effects at the entrance region of the channels of the honeycomb absorber of the HiTRec receiver, as well as for the angle of incidence of the incoming solar radiation. The expression took the form of the Beer-Lambert equation with an extinction coefficient of 295.4 m^{-1} .

3.4.2. Optical thickness

The optical thickness, τ_{opt} , is the propensity for a medium to attenuate radiation of a given wavelength. For a medium with homogeneous properties, such as a gas, the optical thickness is directly related to the extinction coefficient and the thickness of the medium and can be defined by equation (3.23).

$$\tau_{opt} = \beta L \quad (3.23)$$

The mean penetration length of the radiation, l_m , is the mean distance travelled by the radiation before being absorbed and scattered. Conventional absorbers are assumed to be opaque and emits energy uniformly in all direction (i.e. diffuse bodies), and the absorption (κ) and scattering (σ_s) coefficients are calculated using equation (3.24) and (3.25),

$$\kappa = \alpha\beta \quad (3.24)$$

$$\sigma_s = (1 - \alpha)\beta \quad (3.25)$$

where α represents for the absorptance of the porous medium. The extinction coefficient for a porous absorber with an OCF structure can be mathematically calculated using equation (3.26) (Gomez-Garcia et al., 2016).

$$\beta = \frac{\Psi}{d_p} (1 - \phi) \quad (3.26)$$

where Ψ is the empirical coefficient that is related to the geometry and the material of the absorber, d_p is the pore diameter and ϕ is the porosity of the absorber.

3.4.3. Radiation modelling: extruded absorber structures versus open ceramic foam

The propagation of solar radiation within the absorber medium of an OVR depends on a multitude of factors, including incidence direction of the solar rays, the incident radiation intensity distribution, the optical properties and the geometry of the absorber. The two commonly used techniques to study the radiation propagation are the Monte-Carlo ray tracing technique, and the use of radiative models that calculate the radiative flux in the absorber energy equation.

The Monte-Carlo (MC) ray tracing method is typically used to study the radiation propagation through the channels of the extruded absorber structures. The simplicity of the internal structure of the absorber makes it convenient to run the simulations on either the complete absorber or just one channel within the absorber. OCF media, due to their complex internal structure, pose an inconvenience for utilizing the MC method. Therefore, OCF absorbers are assumed to be a media comprising of just the solid (absorber) and fluid (air) phases, with the radiation propagation through the media being described by radiative models.

The solar radiation that propagates through the porous absorbers can be split into collimated radiation, represented by the Beer-Lambert equation, and diffuse radiation. The radiation model described in this section mainly account for modelling of diffuse radiation within the absorber. The three commonly used radiative models for OCFs are the Rosseland conductivity model, the P-1 model and the Two-Flux Approximation model.

The Rosseland conductivity model is used for media with A large optical thickness ($\tau > 3$) and assumes the radiation inside the medium to behave as thermal diffusion. The radiative flux is described by equation (3.27) for the Rosseland conductivity model (Mey et al., 2013).

$$q_r = \frac{-16\sigma}{3\beta} (T_s)^3 d_x T_s \quad (3.27)$$

Here q_r is the radiative flux, T_s is the surface temperature, β is the extinction coefficient and σ is the Stefan-Boltzmann's constant.

The Two-Flux Approximation model, a special case of the Discrete Ordinate Method, assumes isotropic scattering in the absorber and accounts for the propagation of the diffuse radiation in two directions, forward (entering the absorber) and backward direction (leaving the absorber i.e. losses). This approach is computationally less expensive but does not accurately represent the directional distribution of radiation inside the porous medium. The mathematical basis of the model is represented by equations (3.28) and

(3.29),

$$\frac{di^+}{dx} = -2\beta i^+(x) + \beta\Omega(i^+(x) + i^-(x)) + \frac{2\beta(1-\Omega)\phi e_b(x)}{\pi} \quad (3.28)$$

$$\frac{-di^-}{dx} = -2\beta i^-(x) + \beta\Omega(i^+(x) + i^-(x)) + \frac{2\beta(1-\Omega)\phi e_b(x)}{\pi} \quad (3.29)$$

where i^+ and i^- represent the forward and backward radiation propagation respectively, $e_b(x)$ is the black body emission flux at the local solid temperature $T_s(x)$, β is the extinction coefficient of the porous absorber and the Ω is the scattering albedo, which is a function of its emissivity, porosity and pore size. Using the two flux model, the net radiative flux is obtained by equation (3.30).

$$q_r = \pi[i^+(x) + i^-(x)] \quad (3.30)$$

The divergence of the radiative flux is represented by equation (3.31).

$$\frac{-dq_r}{dx} = 2\pi\alpha_v(i^+(x) + i^-(x)) - 4\alpha_v\phi e_b(x) \quad (3.31)$$

Here α_v , the volumetric absorption coefficient, is the product of α and β , and e_b is the black body emissive power. The collimated component of the solar radiation can be accounted for in this model by simply adding the Beer-Lambert equation to equation (3.31) (Kribus et al., 2014).

The P1 radiation model is effective for a medium with high scattering but performs poorly close to the boundaries of the medium, which is completely opposite to the optical requirements of the volumetric absorbers where theoretically, the ‘volumetric effect’ occurs close to the front surface of the absorber, according to Kribus et al. (2014). By assuming isotropic scattering within the porous medium, the diffuse radiation propagation is represented by the P1 model as per equations (3.32) and (3.33) (Kribus et al., 2014).

$$\frac{dq_r}{dx} = \alpha_v(4\sigma(T_s(x))^4 - G) \quad (3.32)$$

$$\frac{1}{3\beta} \frac{dG}{dx} = -q_r \quad (3.33)$$

Alternatively, these equations can be combined to form one diffusion equation (equation (3.34)),

$$\frac{d}{dx} \left(\frac{1}{3\beta} \frac{dG}{dx} \right) = \alpha_v (4\sigma(T_s(x))^4 - G) \quad (3.34)$$

where, G is the diffuse irradiation and α_v is the volumetric absorption coefficient. As in the case of the two-flux approximation, the collimated component of the radiation can be accounted for in the model by adding it to equation (3.34).

3.5. Conservation equations of the porous medium

A mathematical model for the flow of the air through the porous media was derived by using the following set of assumptions:

- i. The air flow is steady and in 1-D.
- ii. The air is incompressible in nature.
- iii. The solid phase (absorber) and the fluid phase (air) properties are homogenous i.e. the thermos-physical properties are constant throughout the phase.

The conservation of mass in the porous medium is given by equation (3.35),

$$u \frac{\partial \rho}{\partial x} = 0 \quad (3.35)$$

where, u is the velocity of air and ρ is the density of the air. The conservation of momentum in 1-D in the porous region is represented by the Brinkman-Forchheimer Extended Darcy's equation, which can then be simplified to equation (3.36) to evaluate the pressure drop in the porous region (Xu et al., 2011).

$$\frac{\rho}{\phi} \left(u \frac{\partial u}{\partial x} \right) = \frac{-\partial P}{\partial x} + \mu_{eff} \left(\frac{\partial^2 u}{\partial x^2} \right) - \left(\frac{\mu_f}{k_1} + \frac{\rho_f}{k_2} u \right) u \quad (3.36)$$

Here, u is the superficial velocity of air, $\frac{\partial P}{\partial x}$ is the pressure drop across the porous region, μ_f and ρ_f are the viscosity and the density of the air, k_1 and k_2 are the viscosity and the inertial coefficients respectively and μ_{eff} is the effective viscosity of the porous region, defined by equation (3.37).

$$\mu_{eff} = \frac{\mu_f}{\phi} \quad (3.37)$$

Assuming that the superficial velocity, u , is constant, the equation can be simplified to the Darcy-Forchheimer equation that can be used to calculate the pressure drop across the porous absorber, as given by equation (3.38).

$$\frac{\partial P}{\partial x} = \frac{\mu_f}{k_1} u + \frac{\rho_f}{k_2} u^2 \quad (3.38)$$

The overall energy balance for the porous medium can be represented by separate energy balance equation for the solid and fluid phase coupled by the volumetric convective heat transfer coefficient. This method is known as the Local Thermal Non-Equilibrium (LTNE) method and is represented by the two coupled equations (3.39) and (3.40) (Pitot de la Beaujardiere, 2019).

$$\frac{\partial E_{solid}}{\partial x} = k_{solid}(1 - \phi) \frac{d^2 T_{solid}}{dx^2} - h_v(T_{solid} - T_{air}) - \frac{dq_r}{dx} \quad (3.39)$$

$$\frac{\partial E_{air}}{\partial x} = k_{air}\phi \frac{d^2 T_{air}}{dx^2} + h_v(T_{solid} - T_{air}) - \dot{m}c_p \frac{dT_{air}}{dx} \quad (3.40)$$

Here k_{solid} and k_{air} are the thermal conductivity of the porous absorber and the air flowing through it, respectively, q_r is the radiative flux, \dot{m} and c_p are the mass flow rate and the specific heat of the air, respectively, T_{solid} and T_{air} are the absorber and the air temperature, respectively, and E_{solid} and E_{air} are the total energy in the absorber and the air, respectively. The heat transfer mechanism within the porous absorber is illustrated in Fig. 3-2.

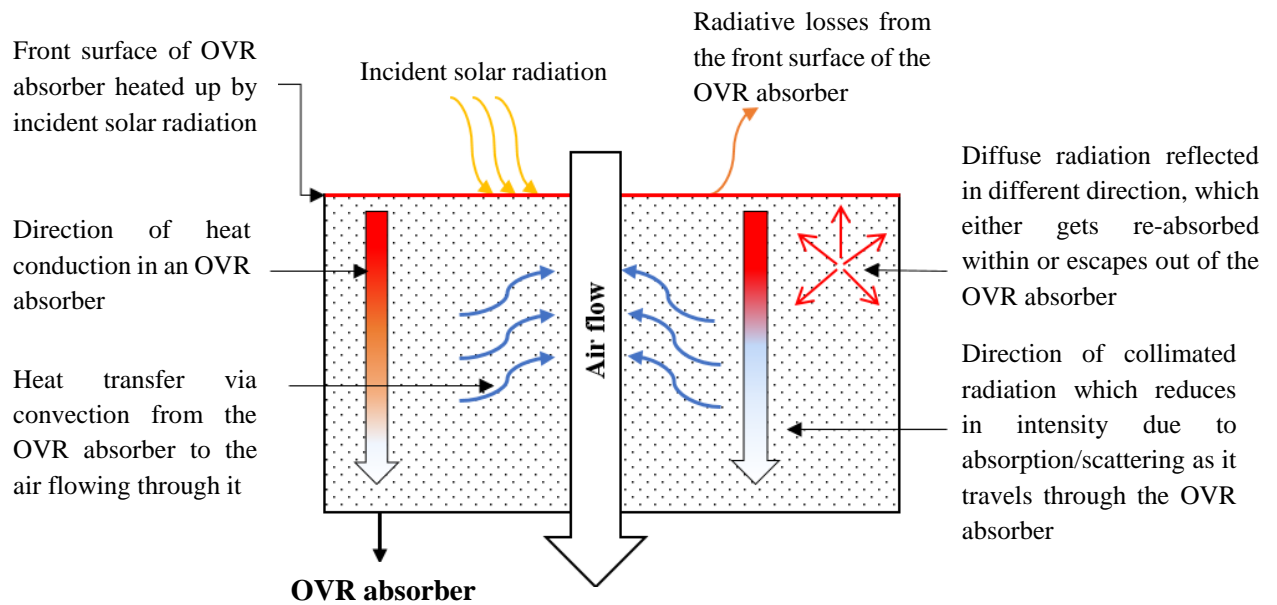


Figure 3-2: Heat transfer mechanism in an OVR

The alternative method of modelling the energy balance, the Local Thermal Equilibrium (LTE) method, is based on the assumption that the volumetric heat transfer coefficient between the solid and the fluid phase can be regarded as infinitely high i.e. there is no temperature difference between the solid and the

fluid phase and the two energy equation coalesce into one, as given in equation (3.41) (Pitot de la Beaujardiere, 2019).

$$\frac{\partial E}{\partial x} = (k_{eff})\varepsilon \frac{d^2 T_{medium}}{dx^2} - \dot{m}c_p \frac{dT_{medium}}{dx} - \frac{dq_r}{dx} \quad (3.41)$$

Here the subscript ‘medium’ represents the homogenous phase representing solid and fluid phase, and k_{eff} denotes its effective thermal conductivity.

3.6. Pressure drop in the porous absorber

Depending on the physical structure of the porous absorber (open cell foam / extruded absorber), the airflow is impeded by varying degrees of viscous and inertial forces, which in turn affects the overall pressure drop experienced across the absorber. The frictional losses that occur in a porous structure due to air viscosity is represented by the viscous losses, while the loss in the mechanical energy of the flow due to the expansions and constriction of the pores within the absorber is represented by the inertial losses. In the case of OCFs, there is an effective mixing of the air molecules due to the tortuous structure (inertial effect) of the porous absorber, which enhances the convective heat transfer between the absorber and the air, at the cost of a relatively high pressure-drop. The flow through the extruded absorbers is dominated by viscous effects, so there is limited heat transfer between the absorber and the air, but the associated pressure drop is relatively lower as compared to that which occurs in an OCF.

In the extruded absorbers, Darcy’s Law defines the pressure drop across the absorber (Fend et al., 2004) as in equation (3.42).

$$\frac{\Delta p}{l} = \frac{\mu}{k_1}(u) \quad (3.42)$$

However, when the inertial effects become significant, as in the case of OCFs, the Darcy-Forchheimer equation defines the pressure drop across the absorber (Wu et al., 2010), as in equation (3.43).

$$\frac{\Delta p}{l} = \frac{\mu}{k_1}(u) + \frac{\rho}{k_2}(u^2) \quad (3.43)$$

Here k_1 is the viscous coefficient and k_2 is the inertial coefficient. The pressure drop characteristics of an extruded medium (800 cells per square inch (cps)) and an OCF (80/20 pores per inch (PPI)) were measured by Fend et al. (2004) and are shown in Fig. 3-3. It is clear that the extruded (parallel channel) absorber has a linear pressure drop and the OCF has a quadratic pressure drop.

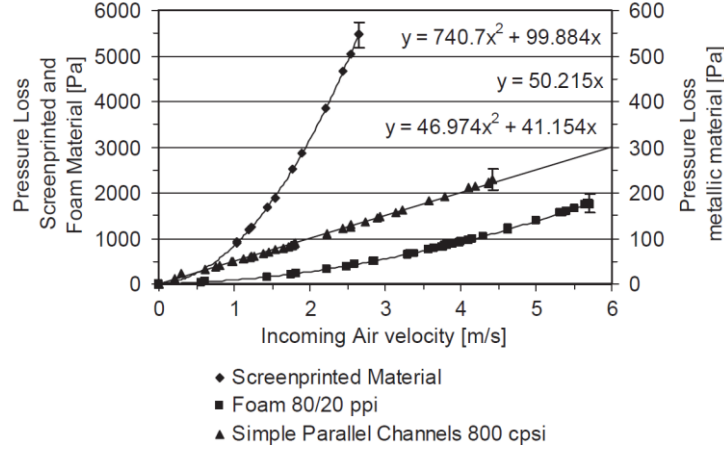


Figure 3-3: Pressure drop in OCF and extruded absorbers (Fend et al., 2004)

3.7. Computational Fluid Dynamics modelling

The fundamental basis of all CFD problems are the time dependent equation for the conservation of mass, three time dependent equations for the conservation of momentum (these are referred to as the Navier-Stokes equation) and a time dependent equation for the conservation of energy. Depending on the system being modelled in CFD, suitable assumptions ought to be made to simplify the problem as it ensures that the computational power available is used as efficiently as possible. In the case of OVRs, the velocity with which the air is drawn through the modules is lower than Mach 0.3, so the flow is assumed to be incompressible in nature. The air is expected to rise from a temperature of 300 K to 1024 K, and mixing of ambient air with warm air from the air return duct over the absorber modules must be modelled effectively, for the purpose of calculating the air return ratio. Furthermore, the effects of buoyancy and gravity can be assumed to be negligible for the sake of simplifying the CFD model.

The generic 3-D equation for a flow variables ϕ of an incompressible unsteady fluid flow is given by equation (3.44), where u_x , u_y , u_z represent the magnitude of velocity in the x, y and z direction, Γ represents the diffusion coefficient and S_ϕ is the source term.

$$\frac{\partial \phi}{\partial t} + \frac{\partial(u_x \phi)}{\partial x} + \frac{\partial(u_y \phi)}{\partial y} + \frac{\partial(u_z \phi)}{\partial z} = \frac{\partial}{\partial x} \left(\Gamma \frac{\partial \phi}{\partial x} \right) + \frac{\partial}{\partial y} \left(\Gamma \frac{\partial \phi}{\partial y} \right) + \frac{\partial}{\partial z} \left(\Gamma \frac{\partial \phi}{\partial z} \right) + S_\phi \quad (3.44)$$

The momentum, continuity and energy equations for a 3-D incompressible, unsteady fluid flow in the Cartesian coordinate system are given by equations (3.45), (3.46), (3.47), (3.48) and (3.49).

x-momentum equation

$$\begin{aligned} \frac{\partial u_x}{\partial t} + \frac{\partial(u_x u_x)}{\partial x} + \frac{\partial(u_y u_x)}{\partial y} + \frac{\partial(u_z u_x)}{\partial z} & \quad (3.45) \\ & = -\frac{\partial P}{\partial x} + \frac{\partial}{\partial x} \left(\mu \frac{\partial u_x}{\partial x} \right) + \frac{\partial}{\partial y} \left(\mu \frac{\partial u_x}{\partial y} \right) + \frac{\partial}{\partial z} \left(\mu \frac{\partial u_x}{\partial z} \right) + S_{u_x} \end{aligned}$$

y-momentum equation

$$\begin{aligned} \frac{\partial u_y}{\partial t} + \frac{\partial(u_x u_y)}{\partial x} + \frac{\partial(u_y u_y)}{\partial y} + \frac{\partial(u_z u_y)}{\partial z} & \quad (3.46) \\ & = -\frac{\partial P}{\partial y} + \frac{\partial}{\partial x} \left(\mu \frac{\partial u_y}{\partial x} \right) + \frac{\partial}{\partial y} \left(\mu \frac{\partial u_y}{\partial y} \right) + \frac{\partial}{\partial z} \left(\mu \frac{\partial u_y}{\partial z} \right) + S_{u_y} \end{aligned}$$

z-momentum equation

$$\begin{aligned} \frac{\partial u_z}{\partial t} + \frac{\partial(u_x u_z)}{\partial x} + \frac{\partial(u_y u_z)}{\partial y} + \frac{\partial(u_z u_z)}{\partial z} & \quad (3.47) \\ & = -\frac{\partial P}{\partial z} + \frac{\partial}{\partial x} \left(\mu \frac{\partial u_z}{\partial x} \right) + \frac{\partial}{\partial y} \left(\mu \frac{\partial u_z}{\partial y} \right) + \frac{\partial}{\partial z} \left(\mu \frac{\partial u_z}{\partial z} \right) + S_{u_z} \end{aligned}$$

Continuity equation

$$\frac{\partial}{\partial x}(u_x) + \frac{\partial}{\partial y}(u_y) + \frac{\partial}{\partial z}(u_z) = 0 \quad (3.48)$$

Energy equation

$$\frac{\partial T}{\partial t} + \frac{\partial(u_x T)}{\partial x} + \frac{\partial(u_y T)}{\partial y} + \frac{\partial(u_z T)}{\partial z} = \frac{\partial}{\partial x} \left(\Gamma \frac{\partial T}{\partial x} \right) + \frac{\partial}{\partial y} \left(\Gamma \frac{\partial T}{\partial y} \right) + \frac{\partial}{\partial z} \left(\Gamma \frac{\partial T}{\partial z} \right) + S_T \quad (3.49)$$

Here μ is the dynamic viscosity of the fluid, p is the pressure drop, S_{u_x} , S_{u_y} and S_{u_z} are the momentum source terms, S_T is the energy source term and T is the temperature of the fluid. The terms on the left hand side of the momentum equations are known as the convection terms, and those on the right hand side are the diffusion terms of the equation.

The equations are discretized using a finite volume method (FVM) by the CFD software.

3.7.1. Grid generation

A meshed domain is essentially a discrete representation of the geometry of the problem, i.e. the CFD domain is divided into control volumes (also known as cells) with the variables of interest such as temperature and pressure located at the centre of the control volumes. The differential form of the conservation equations for that variable are discretized using the Finite Volume Method (FVM) over each of the control volumes. The choice of the cell type for the mesh generation in the domain depends on various factors such as the set-up time, computational time, numerical diffusion, flow domain geometry and the flow behaviour at the various regions within the domain. Another factor to be considered during mesh generation is the quality of the mesh (usually indicated by parameters such as cell skewness, aspect ratio and smoothness) that is essential for stable convergence of a simulation.

3.7.2. Pressure-Velocity coupling scheme

Accurate prediction of parameters such as the outlet air temperatures and mass-flow rates, the absorber temperatures and air pressure at the entrance and exit of the OVR modules are of vital importance to gain an understanding of its fluid dynamic behaviour. Hence, the correct pressure-velocity coupling and convection-diffusion schemes must be applied to the simulation to ensure that all the parameters are accurately calculated.

Calculating an accurate velocity field is a requirement for modelling the effects of processes such as convection and diffusion on the flow variables such as temperature, turbulent kinetic energy, pressure, and mass flow rate, as they are calculated based on the velocity field. Fundamentally, the pressure-velocity (p-v) coupling schemes work by simultaneously solving the momentum and the continuity equations. Initially, the CFD solver predicts a pressure field for the flow domain, and a velocity field is solved using the momentum equation which is then followed by solving for a corrected pressure field. The cycle of predicting and correcting the pressure and velocity field continues until the velocity field satisfies the continuity equation. Another method of solving the correct pressure and velocity field is by solving the momentum and continuity equations simultaneously in a coupled manner, which is more stable, robust and reduces the overall computational time, at the cost of higher computational memory.

3.7.3. Convection –Diffusion modelling

The convection-diffusion modelling describes the movement of a flow property ϕ into and out of a cell in a discretized CFD domain due to processes of convection and diffusion. The solution to the convective-diffusive problem can be found only when the velocity field of the computational domain is accurately predicted (using the pressure-velocity coupling method).

The steady convection-diffusion process of a property ϕ in a one-dimensional flow field u is given by equation (3.50).

$$\frac{d}{dx}(\rho u \phi) = \frac{d}{dx} \left(\Gamma \frac{d\phi}{dx} \right) \quad (3.50)$$

Here ρ is the density, u is the velocity and Γ is the diffusion coefficient. The LHS of the equation represents the net convective flux and the RHS represents the net diffusive flux. And the mass conservation of the convection-diffusion equation is satisfied by the continuity equation given by equation (3.51).

$$\frac{d(\rho u)}{dx} = 0 \quad (3.51)$$

The transport property ϕ is calculated at the centre of the control volumes using the Finite Volume Method and the value at the faces of the control volume is calculated by interpolation schemes such as the Central Differencing Scheme, Upwind Differencing Scheme, Power-Law Scheme and QUICK Scheme.

3.7.4. Turbulence modelling and solution controls

A turbulent flow is characterized by the highly unsteady and random motion of fluid particles and requires a significant amount of computational resources for modelling in comparison to laminar flows. Due to the chaotic nature of the flow, flow properties such as velocity and pressure fluctuate randomly with time, as shown in Fig. 3-4 (Malalasekera and Versteeg, 1995). The flow properties in the turbulent flows can be decomposed into the mean component and the fluctuating component. For example, the velocity u , in the turbulent flow can be written as equation (3.52),

$$u(t) = U + u'(t) \quad (3.52)$$

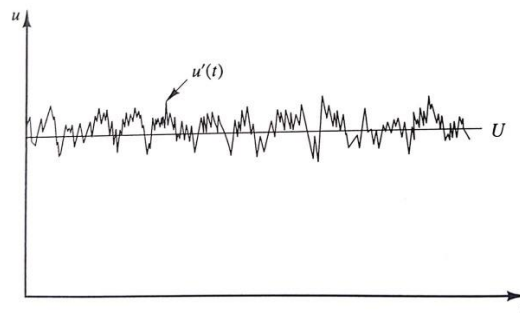


Figure 3-4: Typical point velocity measurement in turbulent flows (Malalasekera and Versteeg, 1995)

Another characteristic phenomenon in turbulent flow is the formation of rotational flow structures known as eddies which aid in the effective mixing of heat, mass and momentum in the flow regime. A wide range of length and time scale can be observed in the eddies, with the large eddies drawing energy from the mean flow component through vortex stretching and the large eddies in-turn transferring their kinetic energy to the smaller eddies, in a process known as energy cascade (Versteeg and Malalasekera, 1995).

The behaviour of the turbulent flow can be described by the Navier-Stokes equations. The three main frameworks for solving these equations are Direct Numerical Simulation (DNS), Large Eddy Simulation (LES) and the Reynolds Average Navier-Stokes (RANS) equation. The most widely used method of turbulence modelling is the Reynolds Average Navier-Stokes (RANS) method. In RANS turbulence models, the flow properties such as velocity, pressure and stresses are time-averaged and the time-averaged Navier-Stokes and continuity equations are presented in equation (3.53) and (3.54).

$$\frac{\partial(\rho u_i)}{\partial t} + \frac{\partial(\rho u_i u_j)}{\partial x_j} = -\frac{\partial P}{\partial x_i} + \frac{\partial}{\partial x_j} \left[\mu \left(\frac{\partial u_i}{\partial x_j} + \frac{\partial u_j}{\partial x_i} \right) - \frac{2}{3} \delta_{ij} \frac{\partial u_l}{\partial x_l} \right] + \frac{\partial}{\partial x_j} (-\overline{\rho u'_i u'_j}) \quad (3.53)$$

$$\frac{\partial \rho}{\partial t} + \frac{\partial(\rho u_i)}{\partial x_i} = 0 \quad (3.54)$$

A consequence of the time-averaging of the governing equation is the generation of an additional term, known as the Reynolds Stress term $(-\overline{\rho u'_i u'_j})$ in equation (3.55), which has to be solved to close the system of equations. The most widely used method for calculating Reynolds Stress is using the Eddy Viscosity Model which implies that the Reynolds stress is aligned to the velocity gradient of the flow and using the Boussinesq hypothesis, the two terms can be related with the aid of the turbulent viscosity, μ_t , as shown in equation (3.55).

$$(-\overline{\rho u'_i u'_j}) = \mu_t \left(\frac{\partial U_i}{\partial x_j} + \frac{\partial U_j}{\partial x_i} \right) - \frac{2}{3} \rho k \delta_{ij} \quad (3.55)$$

Here the turbulence viscosity, μ_t , can be expressed in terms of the local turbulence kinetic energy (TKE), k and the dissipation rate of the TKE, ε given by equation (3.56) (Versteeg and Malalasekera, 1995).

$$\mu_t = \rho C_\mu f_\mu \frac{k^2}{\varepsilon} \quad (3.56)$$

The turbulence models, that are described in the following sections are used to calculate the turbulent viscosity term, by solving for the values of k and ε . The values for k and ε can be solved in three different ways, a zero equation model where it is assumed that k and ε are in equilibrium, a one equation model

where a transport equation for k is solved and ε is calculated using an algebraic expression and finally, the two-equation models that solve a transport equation for k and ε .

The flow pattern of the air over the OVR is characterized by swirling motion and mixing occurs between the warm air from the air return ducting and the ambient air surrounding the OVR. Therefore, the swirling motion of air that can occur during the recirculation and the process of mixing of the warm air and the ambient air must be modelled accurately, using the correct turbulence model. The key to choosing the right turbulence model is to understand the strengths and weaknesses of each one.

i. $k - \varepsilon$ Turbulence Models

The $k - \varepsilon$ turbulence model, proposed by B. Launder in 1972, is the two-equation linear eddy viscosity model, that was used as the industrial standard for turbulence modelling, mainly because the models limitations are well-known in areas such as rotating flows, separation and reattachment of flows. The governing equation of the standard $k - \varepsilon$ model are presented in equation (3.57) and

(3.58).

$$\frac{\partial(\rho k)}{\partial t} + \frac{\partial(\rho k u_i)}{\partial x_i} = \frac{\partial}{\partial x_i} \left[\left(\mu + \frac{\mu_t}{\sigma_k} \right) \frac{\partial k}{\partial x_i} \right] + P_k + P_B - \rho \varepsilon + S_k \quad (3.57)$$

$$\frac{\partial(\rho \varepsilon)}{\partial t} + \frac{\partial(\rho \varepsilon u_i)}{\partial x_i} = \frac{\partial}{\partial x_i} \left[\left(\mu + \frac{\mu_t}{\sigma_\varepsilon} \right) \frac{\partial \varepsilon}{\partial x_i} \right] + C_{\varepsilon 1} f_1 \frac{\varepsilon}{k} (P_k + C_{\varepsilon 3} P_B) - C_{\varepsilon 2} f_2 \frac{\rho \varepsilon^2}{k} + S_\varepsilon \quad (3.58)$$

The versatility of the $k - \varepsilon$ turbulence model can be improved by calibrating the coefficients for σ_ε , σ_k , $C_{1\varepsilon}$, $C_{2\varepsilon}$ and C_μ , to improve upon areas where the standard $k - \varepsilon$ model poorly predicts the flow (Tu et al., 2008). Other variations of the $k - \varepsilon$ turbulence model include the RNG and Realizable $k - \varepsilon$ models.

The RNG $k - \varepsilon$ turbulence models are derived from a statistical method known as Renormalization Group theory, leading to transport equations of ε with an extra term R_ε that improves the numerical prediction of the flow behaviour in highly strained/highly deformed flows, as compared to the Standard $k - \varepsilon$ model. It also accounts for the influence of swirls on the turbulent flow. Hence, the model performs better in flows that include swirls, separation and high strain rates (Ansys Inc, 2006). A common problem in the Standard and the RNG models is the possibility of predicting unrealistic k and ε values.

This is because the normal Reynolds stress ($\overline{u'_i u'_j}$), obtained from the Boussinesq hypothesis is a positive value by definition, but when the rate of deformation of the flow is very large, the normal Reynolds stress (a squared term) becomes negative, making the turbulence model ‘non-realizable’.

Thus, a realizable turbulence model was proposed by T.H. Shih in 1991. The realizable model was compared to the standard model for flows over backward-facing step separated flows, channel flow, and flat plate boundary layers with and without pressure gradient, boundary-free shear flows including a mixing layer, planar and round jets and rotating homogenous shear flows. It was noted by Shih et al. (1994) that the realizable model consistently outperformed the standard model when compared to the data obtained from Large Eddy Simulations (LES) of the mentioned types of flows (Shih et al., 1994).

The modelling of the behaviour of the turbulent viscosity near the wall is a common challenge within the $k - \varepsilon$ class of model. However, the implementation of wall functions and enhanced wall treatment in the standard $k - \varepsilon$ model can improve turbulent viscosity modelling. The realizable and the RNG $k - \varepsilon$ model have also shown improvements in the accuracy of near-wall flow behaviour.

A new set of turbulence models known as the $k - \omega$ turbulence models that were derived to accurately predict the wall-bounded flows are described below.

ii. $k - \omega$ Turbulence Model

The $k - \omega$ model proposed by D. Wilcox excels in predicting the behaviour of the flow in low Reynolds number regions, compressibility and shear layer spreading (Ansys Inc, 2009b). The main difference between the $k - \varepsilon$ models and the $k - \omega$ models is the inclusion of the specific dissipation rate term ω , which is approximately the ratio of k to ε . The transport equations for $k - \omega$ turbulence model is given in equations (3.59) and

(3.60) (Wilcox, 1992a).

$$\frac{\partial(\rho k)}{\partial t} + \frac{\partial(\rho k u_i)}{\partial x_i} = \frac{\partial}{\partial x_i} \left[\left(\mu + \frac{\mu_t}{\sigma_k} \right) \frac{\partial k}{\partial x_i} \right] + \tau_{ij} \frac{\partial u_i}{\partial x_j} - \beta^* \rho \omega k + S_k \quad (3.59)$$

$$\frac{\partial(\rho \omega)}{\partial t} + \frac{\partial(\rho \omega u_i)}{\partial x_i} = \frac{\partial}{\partial x_i} \left[\left(\mu + \frac{\mu_t}{\sigma_\omega} \right) \frac{\partial \omega}{\partial x_i} \right] + \left(\alpha \frac{\omega}{k} \right) \tau_{ij} \frac{\partial u_i}{\partial x_j} - \beta_2 \rho \omega^2 + S_\omega \quad (3.60)$$

Here, $\tau_{ij} \frac{\partial u_i}{\partial x_j}$ represents the generation of the k and ω . The first three terms of both equations represent the rate of change, transport by convection and diffusion of k and ω respectively. The turbulent viscosity calculated for the k - ω class of turbulence models is given by equation (3.61).

$$\mu_t = n^* \frac{\rho k}{\omega} \quad (3.61)$$

Further details about coefficients β^* , β_2 and n can be obtained from (Ansys Inc, 2009b). The correction coefficient α^* is used to dampen the turbulent viscosity to account for the effect of viscous stresses that reduces the effective size of the eddies near the wall. Therefore, the model is capable of integrating the equations right down to the wall without the need for wall functions, an area that the standard $k - \varepsilon$ handles differently, resulting in inaccurate predictions. A drawback of this turbulence model is its sensitivity to the freestream boundary conditions specified for ω . It poorly predicted the flow behaviour in the freestream region as well as the pressure-induced separation of flow (Menter, 1994a).

An attempt at rectifying the freestream sensitivity of the standard k - ω models led to the development of the Baseline Stress Transport (BST) $k - \omega$ model which is a blend of using k - ω functions in the boundary layer of the flow and k - ε functions in the freestream region (Yang et al., 2009). A drawback observed in the BST model is that the formulation of the turbulent viscosity for the $k - \omega$ model leads to an over prediction of the turbulent shear stress close to the wall. Therefore, the BST model was modified by using a viscosity limiter to prevent the over-prediction of the turbulent shear stress. This model is known as the Shear Stress Transport (SST) $k - \omega$ model (Menter, 1994b).

Since recirculation and swirls in the air flow is expected over the OVR modules, the RNG and the realizable $k - \varepsilon$ turbulence might effectively capture such complex flow behaviour. In order to ensure that the flow behaviour adjacent to the walls are effectively captured, the SST $k - \omega$ turbulence model could be the best choice, since it is effectively a blend of the $k - \varepsilon$ model in the freestream region and the standard $k - \omega$ model close to the wall.

4. CFD MODELLING OF AN OVR POROUS ABSORBER

The following sub-sections will elaborate on the various factors affecting the pressure drop across a porous structure as well as establish a suitable methodology to effectively capture the fluid dynamic behaviour of air flow through an open volumetric receiver in the commercial CFD package, Ansys Fluent 19.2. The suitability of the methodology is then evaluated by means of a validation study.

4.1. Introduction

The tortuous internal structure of a porous medium inherently resists flow due to viscous and inertial effects, leading to a pressure drop across the medium. The pressure drop is itself dependent on the superficial velocity of air flowing through the porous medium, and follows a modified Darcy relationship as shown in Fig. 4-1. Other factors such as the porosity, cell size, pores per inch (PPI) and the absorber density affect the pressure-velocity relationship (Wu et al., 2010).

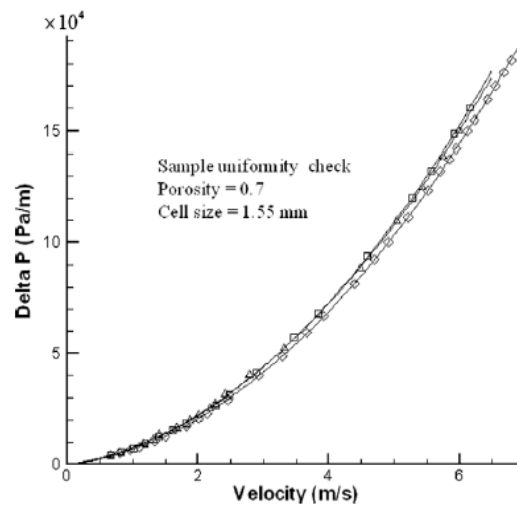


Figure 4-1: Pressure drop in an OCF (Wu et al., 2010)

The pressure-velocity relationship of a porous medium is mathematically represented by a generic equation (4.1).

$$\frac{dp}{dx} = \frac{\mu}{k_1}(u) + \frac{\rho}{k_2}(u^2) \quad (4.1)$$

Knowing the values of the coefficient k_1 and k_2 which are specific to an individual porous structure is vital for numerically modelling the effect of the porous mediums on the air flowing through it.

4.2. Numerical modelling of porous media

The numerical modelling of the OVR was carried out in Ansys Fluent 19.2. The continuity and momentum for a porous medium are provided by equations (4.2) and (4.3) (Ansys Inc, 2015).

$$\frac{\partial(\varepsilon\rho_f)}{\partial t} + \nabla \cdot (\rho_f u) = 0 \quad (4.2)$$

$$\frac{\partial}{\partial t}(\rho_f \phi u) + \nabla \cdot (\rho_f u u) = -\nabla P_{stat} + \nabla \cdot \bar{\tau} + \rho g + F \quad (4.3)$$

Where ρg represents the gravitational body force.

The complex structure of porous absorber media used in OVRs makes it computationally expensive to explicitly account for their detailed internal geometry. The permeability and the viscous resistance coefficient is specific to each porous structure whether it be OCFs or extruded absorbers, and these parameters are used to numerically model the effect that a type of porous structure has on the behaviour of the air flowing through it. An open cell foam structure would have the same value of inertial and viscous coefficients in all directions (i.e. isotropic tensor) whereas for an extruded porous structure such as that used in the HiTRec receivers, the resistance perpendicular to the direction of flow will be set at least three orders of magnitude higher than the one parallel to the flow (Roldán et al., 2014; Roldán et al., 2016). Ansys Fluent 19.2, offers two models for predicting the flow and heat transfer through a porous medium, namely,

1. Local Thermal Equilibrium model (LTE) - One-equation model
2. Local Thermal Non-Equilibrium model (LTNE) - Two-equation model

4.3. Cold flow validation

The purpose of the validation study is to ensure that the CFD model of a porous medium is set up in a way that numerically models the actual fluid dynamic behaviour of air flowing through a real porous structure. The monitored parameter for the current validation study is the pressure drop across the porous medium. An experimental study of a Silicon Carbide (SiC) ceramic foam (OCF) with a porosity of 0.7 and a cell size of 1.55 mm carried out by Wu et al. (2010) was chosen for the study. The air

flowing through the ceramic foam was measured to be at ambient conditions, and therefore, the air temperature was assumed to be 300 K. The experimental pressure-velocity characteristic curve of the ceramic foam is represented in Fig. 4-2 (Wu et al., 2010) and a pressure-velocity curve is defined by equation (4.4).

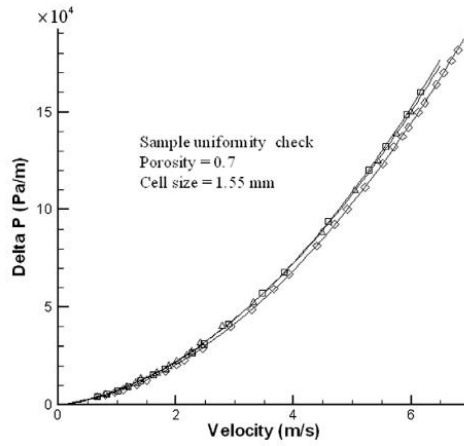


Figure 4-2: Experimental Pressure-Velocity characteristic curve (Wu et al., 2010)

$$\frac{dP}{\Delta L} = 33.158v^2 + 38.463v \quad (4.4)$$

The pressure drop across the porous media is calculated by equation (4.5) in Fluent.

$$\frac{dP}{\Delta L} = \left(\frac{1}{2} C_2 \rho\right) v^2 + \left(\frac{\mu}{\alpha}\right) v \quad (4.5)$$

Here dP [Pa] represents pressure loss. The values of C_2 and $\frac{1}{\alpha}$ can be calculated from the equations (4.4) and (4.5). The solution domain chosen for the validation study was a simple 2-D CFD model to minimize the computational requirements.

Three different continuum zones were defined in the solution domain, namely, an inlet region, the porous absorber region and an outlet region. The flow of air through the porous medium is assumed to be under steady-state conditions. A velocity inlet boundary condition with a uniformly distributed velocity value was set at the entrance to the inlet domain to model the air drawn in from the surrounding atmosphere by the pressure drop across the porous absorber. A pressure outlet boundary condition was specified at the exit of the outlet domain and set to 0 Pa (reference pressure is set to 101325 Pa or 1 atm by default).

The mass, momentum and energy equations were solved using the SIMPLE pressure-velocity coupling scheme and the turbulence model used was the standard $k - \epsilon$ turbulence model. Since the experimental

results were obtained from a reticulated porous ceramic foam, it was assumed that the porous inertial and porous viscous resistance coefficients could be specified as an isotropic tensor (i.e. the resistance is the same in all directions). Figure 4-3 illustrates the cell zones and boundary conditions of the domain used for the cold flow validation study, and Fig. 4-4 illustrates the static pressure contour plot of the domain when the inlet air velocity is set at 2 m/s,

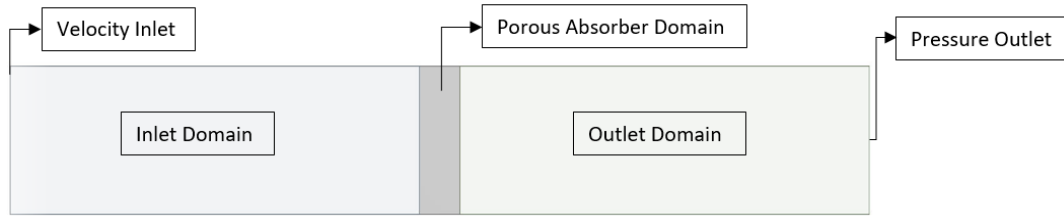


Figure 4-3: Cell zones for cold flow validation

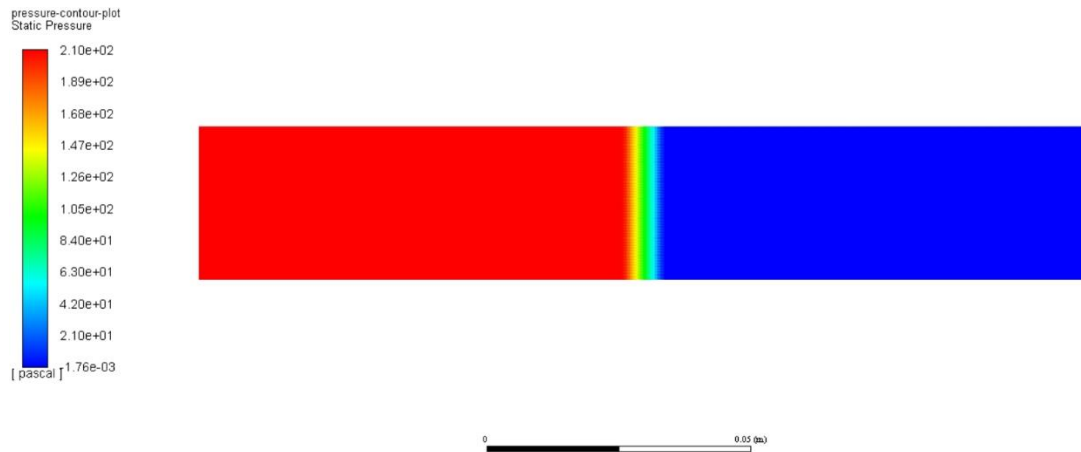


Figure 4-4: Static pressure contour plot at an inlet velocity of 2 m/s

Table 4-1 represents the percentage deviation between the experimental and numerical pressure drop at different values of the superficial velocity of air through the porous medium.

Table 4-1: Percentage deviation between experimental and numerical pressure drop

Velocity (m/s)	Pressure Drop – Experimental (Pa)	Pressure Drop – Numerical (Pa)	Deviation (%)
2	212.50	209.6	1.36%
3	412.50	414.82	-0.56%

4	681.30	685.57	-0.63%
5	1025	1023.24	0.17%
5.5	1212.50	1216.95	-0.37%
6	1425	1427.27	-0.16%

The pressure drop values obtained from the simulations lie within a 2 % deviation of the experimental data for the pressure drop. Hence, the methodology used to set up the porous medium in Fluent for the cold flow study can be relied upon to generate realistic results.

4.4. Hot flow validation

The experimental data from the study carried out on the 200 kW HiTRec-II receiver consisting of 32 HiTRec-II modules (Roldán et al., 2016) were used as the reference for the hot flow validation work. The boundary conditions of the CFD model that will be developed for the hot flow validation will rely on the operating conditions under which the experiment was carried out.

4.4.1. Experimental set-up

The experimental study of the HiTRec-II receiver test rig was carried out at the Plataforma Solar de Almeria (PSA) tower on the Sulzer test bed. The test bed had the provision to measure the rate at which heat is added to the air by the receiver and was equipped with a cooling circuit incorporating an air cooled heat exchanger.

The air was drawn from the atmosphere through the absorber modules (in which it was heated to a temperature of approximately 840 °C) and the heat exchanger (in which it was cooled to approximately 225 °C) by a blower. In order to prevent any damage to the supporting structure due to the possibility of uncontrolled mass flow rate that could lead to local hotspots (and in turn leading to deformation), an auxiliary blower was used to inject ambient air to cool the structure. The outer cups, insulation and the porous absorbers of the modules were made out of infiltrated siliconized silicon carbide, lightweight concrete and recrystallized silicon carbide respectively. Lastly, during the test, the air that was recirculated through the circuit back into the atmosphere near the absorber modules was at ambient temperature (Hoffschmidt et al., 2003). Figure 4-5 depicts the schematic diagram of the test rig.

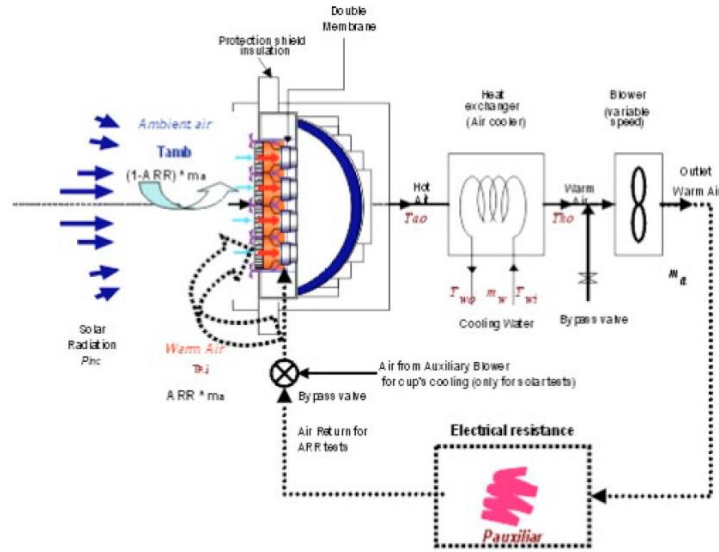


Figure 4-5: Schematic diagram of the test rig (Hoffschmidt et al., 2003)

Five separate tests on the HiTRec-II modules were carried out at quasi-steady state conditions and the operating parameters of the five tests are provided in Table 4-2.

Table 4-2: Experimental data from SolAir 200 Receiver

Test	Air Flow (kg/s)	Wind Velocity (m/s)	Wind Direction	Total Incident Power (kW)
1	0.264	4.20	25.06	263.4 ± 14.2
2	0.246	1.50	22.73	233.3 ± 12.6
3	0.231	2.55	21.28	247.9 ± 13.4
4	0.198	3.70	22.71	253.1 ± 13.7
5	0.310	5.15	23.86	233.2 ± 12.6

Roldán et al. (2016) published the experimentally measured air outlet temperature values of four of the HiTRec-II absorber modules. Since it was uncertain as to which four of the 32 absorber modules were evaluated, it was assumed that the measurements were taken at the four absorber modules in the centre of the test rig (illustrated in Fig. 4-24).

The measured air temperatures, obtained from Roldán et al. (2016) are provided in Table 4-3. The outlet air temperature values obtained from the CFD simulation of the HiTRec-II absorber modules will be individually compared to these experimental measurements for each of the five tests.

Table 4-3: Experimental measurement of outlet air temperatures

Test	T _{module 1} [K]	T _{module 2} [K]	T _{module 3} [K]	T _{module 4} [K]
1	1000.83	1000.83	1025.83	1023.33
2	1048.33	812.5	994.17	1015
3	1060.83	780.33	1047.50	1020.83
4	1167.50	890.83	1106.67	1118.33
5	917.92	693.75	896.25	909.17

4.4.2. Generation of a baseline model for hot flow validation

In literature, the HiTRec-II modules have been modelled in 2-D in Roldán et al. (2016) under LTE conditions using Ansys Fluent 12.0. The dimensions, mesh design and the main boundary conditions associated with the modelling of the modules are shown in Fig. 4-6 and Fig. 4-7 respectively.

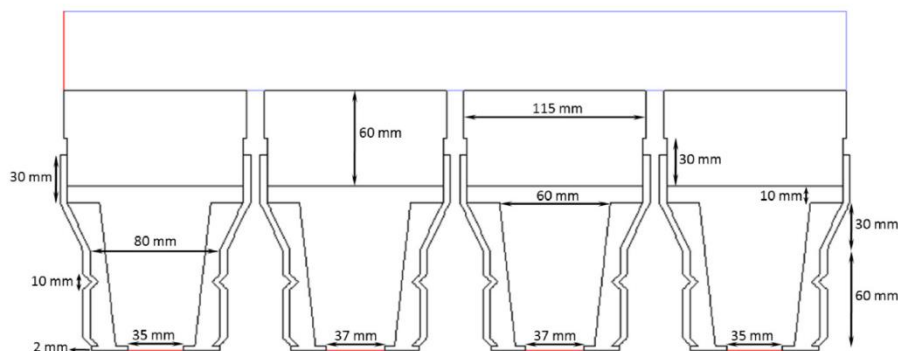


Figure 4-6: Dimensions of the CFD model of the HiTRec-II modules (Roldán et al., 2016)

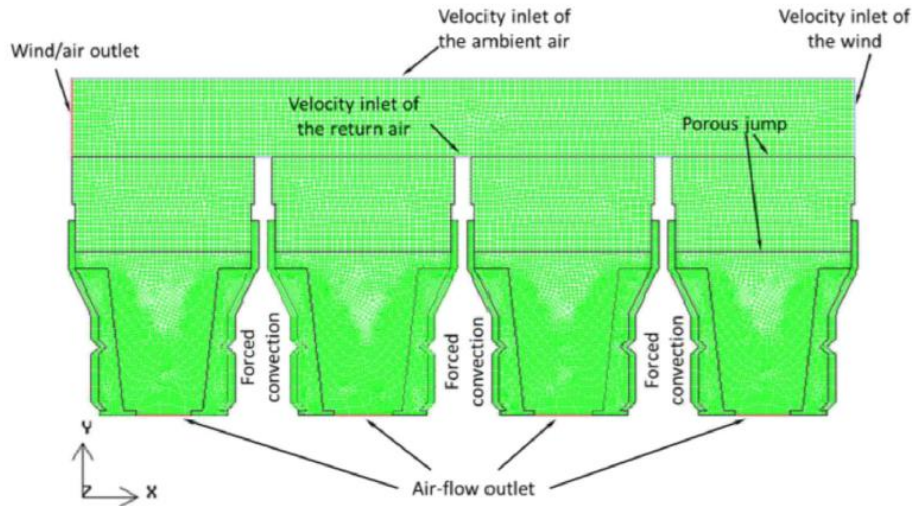


Figure 4-7: Mesh design and boundary conditions of CFD model (Roldán et al., 2016)

The parameter evaluated to confirm the validity of the CFD model and its set-up against experimental data was the outlet air temperature of the absorber modules. Roldán et al. (2016) proposed a CFD model that was validated against the experimental data from PSA presented in Table 4-3. However, a closer look at the actual geometry of the CFD model, simulation set-up and a verification study carried out on the model revealed some limitations of the CFD model in modelling the actual flow through an OVR module. These were identified as follows,

- i. Firstly, carrying out a CFD study in 2-D for an object that is neither planar nor axisymmetric in its geometry limits the physical fidelity of the model since a 2-D simulation does not resolve fluid flow in the third direction which is critical for predicting the aerodynamics of the flow through the module, especially when its cross-section transitions from a hexagon cross-section at the top to circular cross-section at the bottom, as shown in Fig. 4-9 (Hoffschmidt, 2001).
- ii. Although no rule of thumb exists which specifies the size of the atmospheric domain that surrounds an object on which wind analysis is being carried out, Patel et al. (2015) suggested that for a 2-D domain, the atmospheric domain around an object with height H , should at least have a height of $Y = 12H$, windward side length of $L_1 = 5H$ and leeward side length of $L_2 = 12H$ in Ansys CFX, as shown in Fig. 4-8. The atmospheric domain used for the 2-D model of the absorber modules is relatively small with respect to the size of the absorber module domain, which could, in turn, lead to inaccuracies in the calculation of the pressure field.

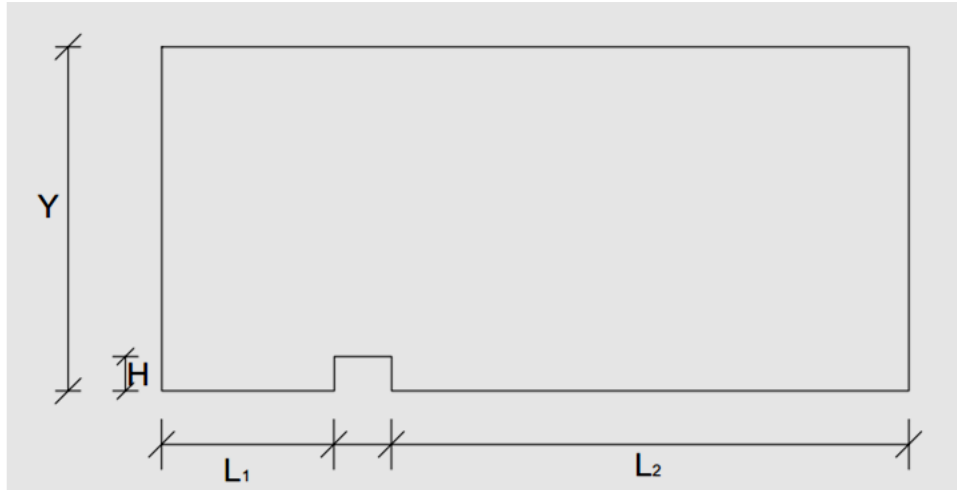


Figure 4-8: Dimensioning notation for 2D atmospheric domain (Patel et al., 2015)

- iii. It is common practice in the setting up the CFD model to place the outlet boundary conditions far away from the region of interest, in this case, the absorber modules. Placing the outlet boundary next to the left-most absorber module as shown in Table 4-7 could potentially affect the solution in the interior region of the computational domain (Tu et al., 2008). Hence, it is vital to show that the position of the outlet boundary does not affect the interior solution by varying its position beforehand. The outlet boundary conditions should be placed at the region where the flow attains a fully-developed state i.e. all the gradients normal to the outlet boundary conditions are equal to zero (Versteeg and Malalasekera, 1995).
- iv. Lastly, an error in the specification of the heat source within the porous absorbers of the HiTRec-II 2-D model was suspected, which is detailed below.



Figure 4-9: Shape of a HiTRec-II module

Volumetric Heat Source

As per the experimental data, the total incident solar radiation measured on the HiTRec-II test rig ranged from 233.2 kW to 263.4 kW over the five tests conducted on it, which means, an average solar radiation of 7287.50 W to 8231.25 W was incident on each of the absorber modules. The energy losses from the absorber usually occur through reflection from the front and the internal surfaces as well as radiation of heat energy from the absorber due to its high temperature leading to a thermal efficiency of around 76 % (Hoffschmidt et al., 2003).

The volumetric heat source equation proposed for the 2-D HiTRec-II CFD model given in Roldán et al. (2016) is in the form of the Beer-Lambert law and it accounts for the re-radiation effects in the first part of the channels, the angle at which the solar beam strikes the absorber after being reflected by the heliostat as well as the extinction coefficient of the absorbers. It is also assumed that all the solar radiation incident is fully absorbed and the energy lost due to reflection/scattering is negligible.

The published validation study carried out on the 2-D HiTRec-II CFD model under the operating conditions provided in Table 4-2, used volumetric heat source equations to model the heat energy in the absorbers for the CFD model for all the five tests. The volumetric heat source equations used by Roldán et al. (2016) are provided in Table 4-4.

Table 4-4: Heat source equations for the tests

Test	Beer-Lambert Equation $[kW/m^3]$
1	$I_v = 1304e^{-295.4y}$
2	$I_v = 1155e^{-295.4y}$
3	$I_v = 1227e^{-295.4y}$
4	$I_v = 1253e^{-295.4y}$
5	$I_v = 1154e^{-295.4y}$

The published CFD results obtained from the 2-D model that was validated against experimental data in Roldán et al. (2016) are given in Table 4-5.

Table 4-5: Results from Roldán et al. (2016) used to validate against the experimental data

	$T_{cup,1}$ [K]	$T_{cup,2}$ [K]	$T_{cup,3}$ [K]	$T_{cup,4}$ [K]	T_{av} [K]
Test 1	995.08	994.26	994.26	990.16	993.44
Test 2	1062.3	1054.91	1045.08	1044.26	1051.64
Test 3	1068.85	1063.11	1057.38	1058.2	1061.89
Test 4	1109.84	1104.92	1104.92	1102.46	1105.54
Test 5	850	848.36	851.64	846.72	849.18

The magnitude of the total power (P) of the volumetric heat source equation can be calculated by integrating the heat source equation along the depth (L) of the absorber and multiplying it by the frontal area of the absorber (A). The coordinate system used is illustrated in Fig. 4-7 and the magnitude of the heat source for test 3 was calculated to be 28.66 W as follows,

$$P = A * \int_0^L (1227 * 10^3) * e^{-295.4.y} . dy$$

Figure 4-10 graphically represents the heat equation for Test 3.

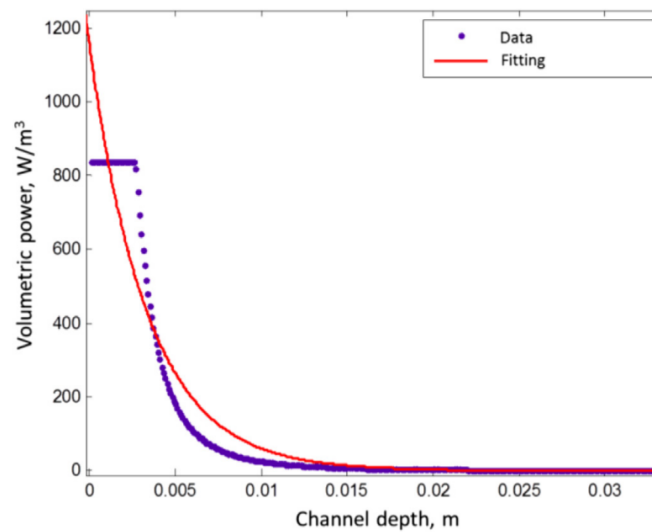


Figure 4-10: 2-D model of the heat source equation for test 3 (Roldán et al., 2016)

The heat source equations used for all the tests, the total power derived from them using the aforementioned method as well as power per module obtained from the experiment for each of the tests is provided in Table 4-6.

Table 4-6: Solar power incident on each module

Test	Heat Source Equation [kW/m ³]	Total Power per Module [W] (CFD)	Total Power per Module (Experimental) [W]
1	$I_v = 1304e^{-295.4y}$	507.64	8231.25
2	$I_v = 1155e^{-295.4y}$	449.64	7290.63
3	$I_v = 1227e^{-295.4y}$	477.67	7746.88
4	$I_v = 1253e^{-295.4y}$	487.80	7909.38
5	$I_v = 1154e^{-295.4y}$	449.26	7287.50

There is a significant discrepancy between the total power derived from the heat source equations and the total power measured from the experimental runs. A rough estimate of the rise in the air temperature as it flows through the absorber can be calculated by equation (4.10),

$$\dot{Q} = \dot{m}c_{p,air}(T_{out} - T_{in}) \quad (4.10)$$

Applying the equation for the experimental operating conditions for Test 3, the approximate temperature rise was estimated to be 1012.13 K, with the $c_{p,air}$ being extrapolated for the average of the inlet (ambient) and the outlet air temperatures, from experimental measurement for Test 3. For the power obtained from the heat source equation derived for the 2-D model under Test 3 operating conditions, the temperature rise is 62.41 K. The discrepancy between the two values of the rise in temperature across the absorber is significant.

A new 2-D model of the HiTRec receivers was designed and set-up in Ansys Workbench 19.2 to verify the published CFD results provided in Roldán et al. (2016). Five separate simulations were conducted, one for each of the test cases, using the volumetric heat source equations specified in Table 4-4. The area-weighted average values of the outlet air temperature of the modules for the five test cases that were conducted for the verification exercise are given in Table 4-7.

Table 4-7: Verification Results

	$T_{cup,1}$ [K]	$T_{cup,2}$ [K]	$T_{cup,3}$ [K]	$T_{cup,4}$ [K]	T_{av} [K]
Test 1	307.67	307.61	305.45	302.91	305.91
Test 2	311.94	312.62	310.47	307.42	310.61
Test 3	311.67	310.89	308.37	305.50	309.12
Test 4	307.95	307.80	305.66	303.17	306.15
Test 5	305.92	305.86	304.08	302.06	304.48

The pressure and temperature contour plots and the velocity vector plot of the computational domain under test 3 as per the published settings are illustrated in Fig. 4-11, Fig. 4-12 and Fig. 4-13 respectively.

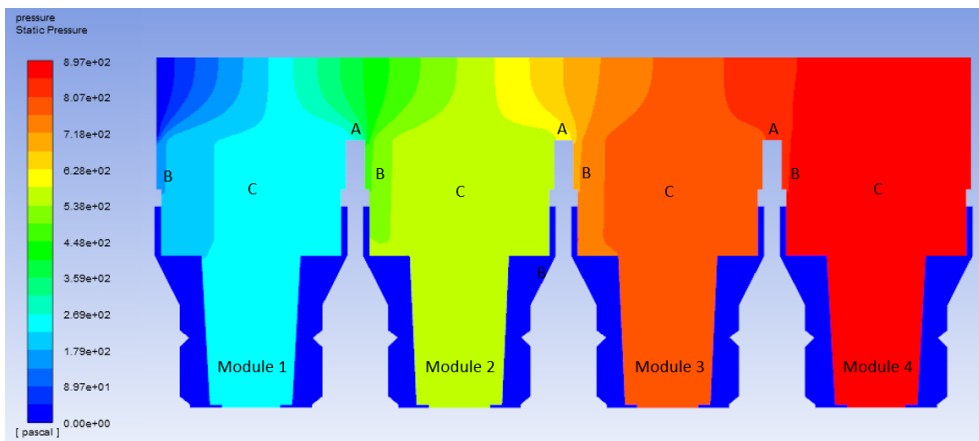


Figure 4-11: Pressure contour plot under test 3 conditions

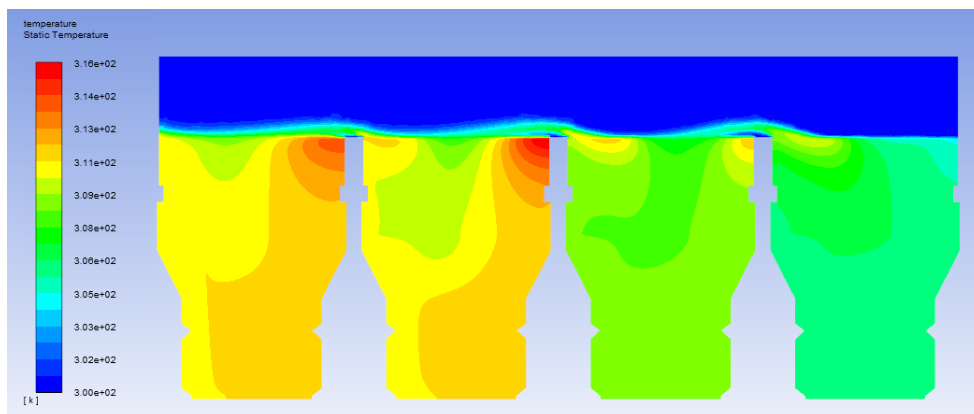


Figure 4-12: Temperature contour plot under test 3 conditions

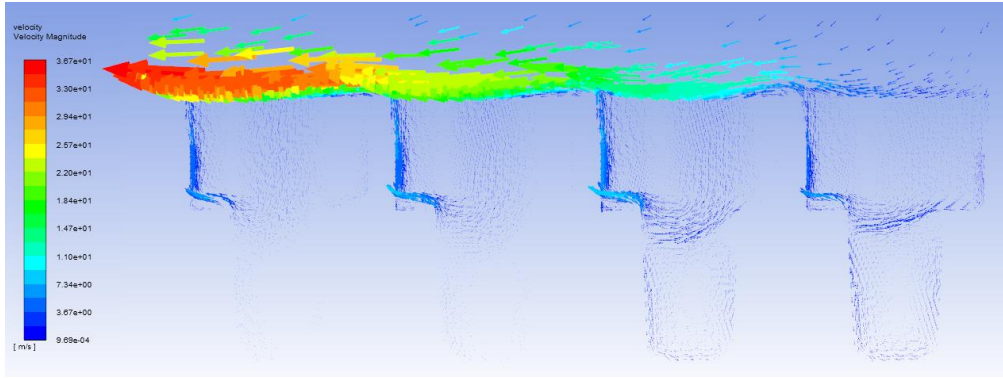


Figure 4-13: Velocity vector plot under test 3 conditions

It is clear, from Table 4-7, that using the volumetric heat source equation proposed for the 2-D model causes a negligible rise in the temperature of the air as it flows through the porous medium. Although the operating conditions prescribed in the simulation were set up as described in the article, the root cause of the discrepancy between the numerical outlet air temperatures presented in Table 4-5 and experimental data in Table 4-7 remains unknown.

In order to model a realistic heat energy in the porous absorber, the solar energy absorbed by the porous medium was simulated with a constant volumetric heat source that was derived by dividing the total power per module obtained from the experimental data (Table 4-5) by the volume of the absorber in 2-D; i.e. the depth of the absorber into the page was taken to be 1 meter. The newly calculated constant volumetric heat source values for the tests and the corresponding outlet air temperatures of the modules obtained from the simulations are detailed in Table 4-8.

Table 4-8: Air outlet temperature for constant volumetric heat source

	Volumetric Heat Source [W/m ³]	T_{mod,1} [K]	T_{mod,2} [K]	T_{mod,3} [K]	T_{mod,4} [K]	T_{av} [K]
Test 1	1224888.39	476.88	458.06	417.01	362.96	429.96
Test 2	1084914.44	654.42	627.22	564.13	526.33	593.10
Test 3	1152808.78	563.78	526.93	471.58	417.16	494.98
Test 4	1176990.33	476.76	455.45	409.70	359.56	425.37
Test 5	1084449.41	430.01	416.18	378.41	336.35	390.24

The pressure and temperature contour plots as well as the velocity vector plot of the modules under test 3 conditions, incorporating the constant volumetric power, are illustrated in Fig. 4-14, Fig. 4-15, Fig. 4-16, and Fig. 4-17 respectively.

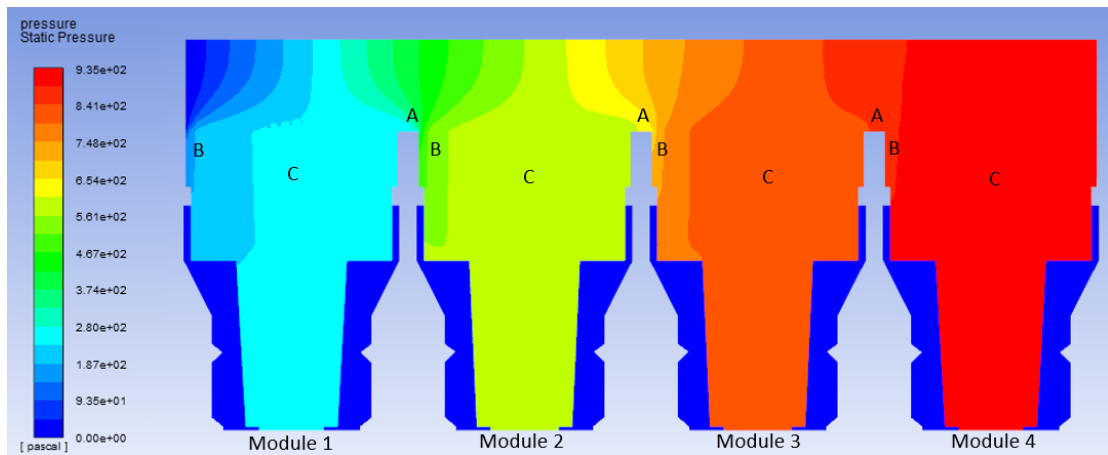


Figure 4-14: Pressure Contour plot under test 3 conditions using constant volumetric heat source

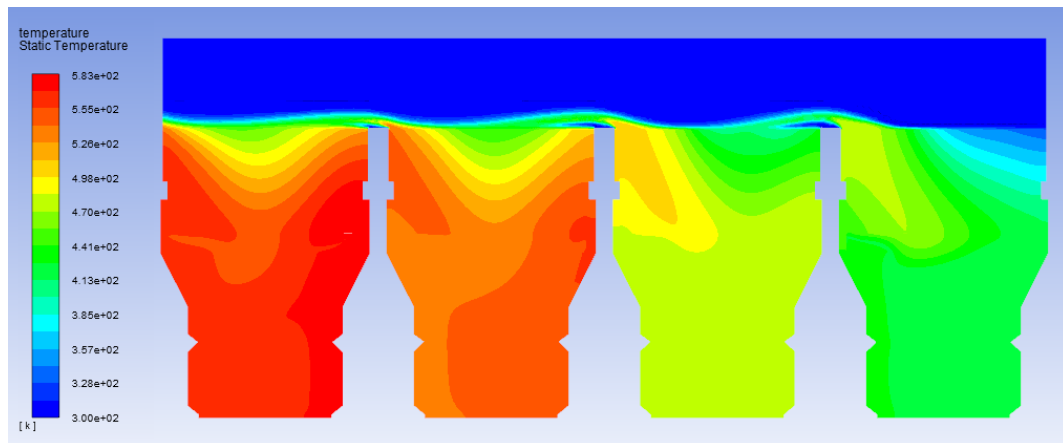


Figure 4-15: Temperature plot under test 3 conditions using constant volumetric heat source

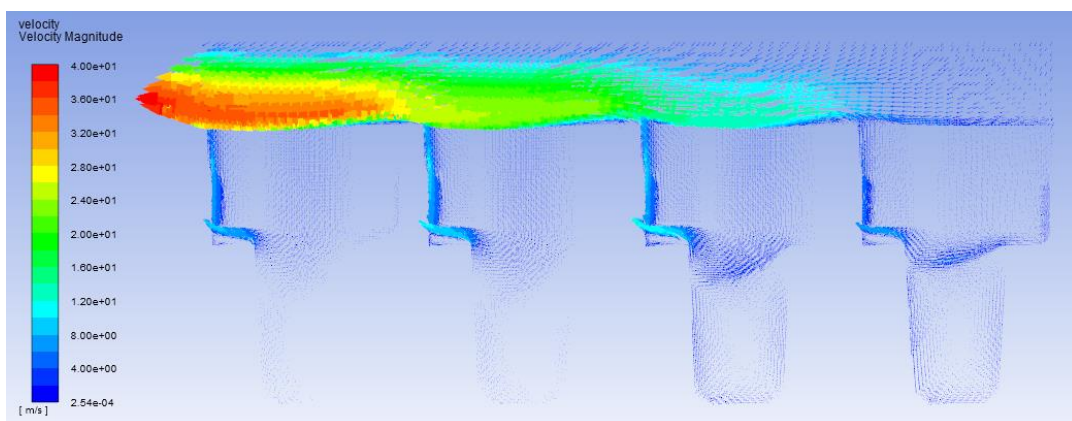


Figure 4-16: Velocity vector plot under test 3 conditions using constant volumetric heat source

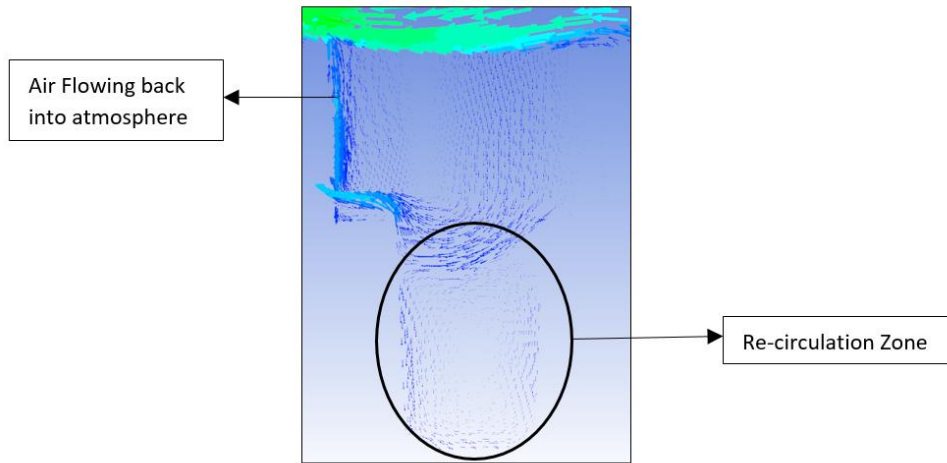


Figure 4-17: Velocity vector in the 3rd module

The air which enters through the porous medium seems to partly recirculate back into the atmosphere, and the portion which enters the tapered region of the module follows a circular path within that region before leaving the module outlet. Such behaviour of the airflow can be attributed to the pressure variations across the module as illustrated in Fig. 4-11 and Fig. 4-14. Regions C within the porous medium are at a higher pressure than regions A and regions B, and the air would naturally move from regions of high pressure to regions of low pressure. It therefore follows a path from regions C to regions B, and then on to regions A.

When the required amount of air is drawn through the modules, the excess air that enters through the atmospheric domain moves in bulk motion towards the adjacent absorber module, cooling the top portion of its porous medium, and in turn reducing the net heat transfer rate to the air flowing through the adjacent module. The speed at which the bulk air moves over the modules increases with distance, as seen in Fig. 4-16. This air movement is shown to cool the top portion of the respective absorber modules, with the rate of cooling decreasing with distance. Therefore, module 1 has the highest outlet temperature and module 4 has the lowest, according to Fig. 4-15. The pattern of the airflow in the absorber modules as shown in Fig. 4-16 resembles the ones previously illustrated in Fig. 4-13, although the air temperature rise in the latter was shown to be negligible.

A larger rise in the air temperature at the outlet of the modules is observed when the constant volumetric power is used in the absorbers (Table 4-8) in comparison to the air temperature values given in Table 4-7. Nonetheless, the simulated air temperature values deviate quite significantly (larger than the allowed tolerance of 10%) from the experimental outlet air measurements shown in Table 4-3, as well as the published CFD data appearing in Table 4-5.

One possible cause for the substantial deviation is that the real volume of the porous absorber is not modelled in the 2-D model, as it works on a per unit length for the depth (into the page) of the model, in addition to the fact that the hexagonal shape of each of the absorber modules is approximated by two rectangles, one stacked on top of the other. Since the true volume of the hexagonal HiTRec-II absorbers was not captured in the 2-D model, the magnitude of the constant volumetric power that was derived (using the two stacked rectangles for calculating the volume) may not be large enough to cause a significant rise in the air temperature at the specified mass flow rate through the module, as in reality (as per experimental data in Table 4-2).

The limitations of the 2-D model of HiTRec-II modules as well as the failure in validating the CFD results obtained from the simulations conducted against experimental data motivated the development of a 3-D model of the HiTRec-II modules in Ansys Fluent 19.2, based on the dimensions of the 2-D model. Figure 4-18 and Fig. 4-19 illustrates the 3-D model of a single HiTRec-II module, while Fig. 4-20, Fig. 4-21, Fig. 4-22 and Fig. 4-23 illustrates the various zones of the 3-D model of the HiTRec absorber module.

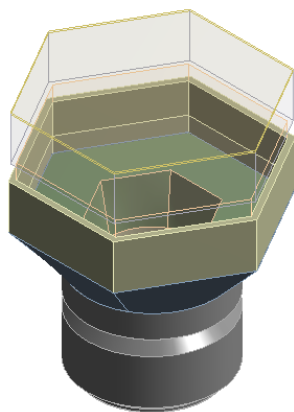


Figure 4-18: HiTRec-II Module (Full assembly) (a)

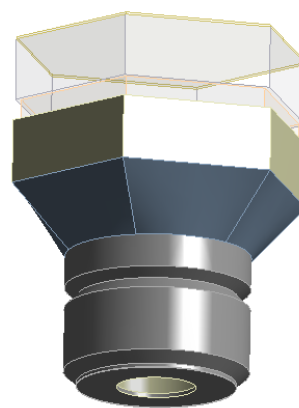


Figure 4-19: HiTRec-II Module (Full assembly) (b)

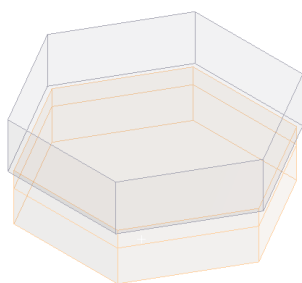


Figure 4-20: Porous Zone

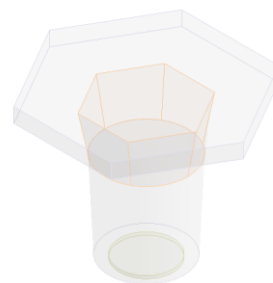


Figure 4-21: Hot Air Zone

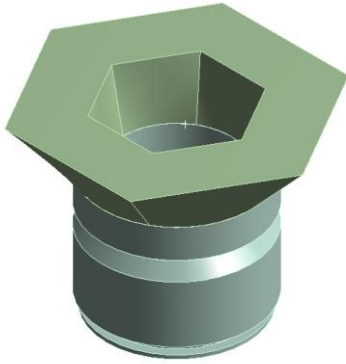


Figure 4-22: Insulation Zone

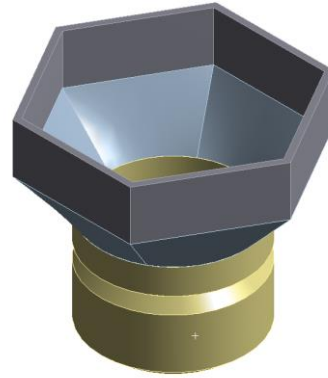


Figure 4-23: Cup Zone

In the HiTRec-II experimental test rig setup as shown in Fig. 4-24, the fourteen modules in the centre highlighted by the yellow box were modelled in Fluent for the validation study in 3-D.

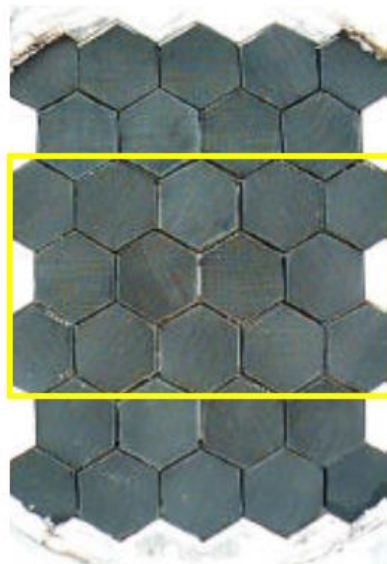


Figure 4-24: HiTRec-II modules that were modelled for CFD simulations (Roldán et al., 2016)

The model also consists of a domain for the returned air coming from the HRSG as well as one for the atmospheric domain upstream of the absorber modules. The CFD model of the HiTRec-II modules represented by the yellow box in Fig. 4-24 is illustrated in Fig. 4-25 and the full CFD model domain that was used for the validation study is shown in Fig. 4-26.



Figure 4-25: 14 HiTRec-II Modules CFD Model



Figure 4-26: Full computational model used for the validation study

4.4.3. Cell zones and boundary conditions

The computational domain was separated into solid and fluid cell zones. Details about the cell zones are given in Table 4-9.

Table 4-9: The various zones of the CFD model

Solid Zone	<ol style="list-style-type: none"> 1. Insulation (Fig. 4-22) 2. Cup (Fig. 4-23)
Fluid Zone	<ol style="list-style-type: none"> 1. Porous Absorber Zone (Fig. 4-20) 2. Hot Air Zone - Region for the airflow inside the module (Fig. 4-21) 3. Air Returned Zone - Region for the air returning from the warm return air ducting (Fig. 4-27) 4. Recirculation Zone - Region for capturing the re-entry path of the warm return air back into the absorbers (Fig. 4-27) 5. Atmospheric Zone - Around of the recirculation zone (Fig. 4-27)

The top and bottom surfaces of the porous domain were specified according to the porous jump condition with material permeability and pressure jump coefficients of $1.1e + 07 \text{ m}^2$ and 139.84 m^{-1} . The porosity was set to 0.495, the inertial resistance coefficients parallel to the flow was set to 34.96 m^{-1} and perpendicular to the flow was set to 1000 m^{-1} . Similarly, the viscous resistance coefficient parallel to the flow was set to 9060000 m^{-2} and perpendicular to the flow was set to $1 * 10^{10} \text{ m}^{-2}$ (Roldán et al., 2016).

The experimental data for the incident solar radiation on the HiTRec-II absorbers was used to derive a constant volumetric heat source [W/m^3] for the 3-D model. The total incident solar power on the HiTRec-II test rig was divided by the number of absorber modules in the rig. The total incident solar power per module was then divided by the volume of the porous absorber to obtain the average volumetric heat source per module.

The choice of the materials of the porous absorbers, outer cups and insulation were recrystallized silicon carbide (SiC), infiltrated siliconized silicon carbide (SiSiC) and lightweight concrete respectively as per Roldán et al. (2016). The material properties of the solid zone such as the density, thermal conductivity and the specific heat value as well as the thermophysical properties of air were obtained from the 2-D model and are provided in Table 4-10. The thermophysical properties of air were calculated using a user-defined function (UDF) in Fluent, and the code used to define these functions in Fluent are provided in Appendix A.

Table 4-10: Material Properties of the Solid Zones

	Density $\left[\frac{kg}{m^3}\right]$	Thermal Conductivity $\left[\frac{W}{m.K}\right]$	Specific Heat $\left[\frac{J}{kg.K}\right]$
Recrystallized Silicon Carbide	2700	26	900
Infiltrated Siliconized Silicon Carbide	3100	32	1270
Lightweight Concrete	990	0.16	1050

The thermophysical properties defined for air is given by equation (4.11) to (4.14) (Roldán et al., 2016).

$$\rho_{air} = 3.656e^{-0.006611(T_f)} + 0.923e^{-0.000966(T_f)} \quad (4.11)$$

$$\mu_{air} = \frac{(1.458 * 10^{-6}) * (T_f)^{\frac{3}{2}}}{(T_f) + 110.4} \quad (4.12)$$

$$c_{p,air} = 1.973 * 10^{-10} (T_f)^4 - 8.349 * 10^{-7} (T_f)^3 + 0.00189 (T_f)^2 - 0.469 (T_f) + 1064 \quad (4.13)$$

$$k_{air} = 7.66 * 10^{-6} (T_f)^3 - 3.159 * 10^{-8} (T_f)^2 + 7.502 * 10^{-5} (T_f) + 0.000647 \quad (4.14)$$

The recirculation zone, atmospheric zone and the air returned zone are illustrated in Fig. 4-27, and the boundary conditions of the computational domain are illustrated with the aid of Fig. 4-28 to Fig. 4-32 and Table 4-11.

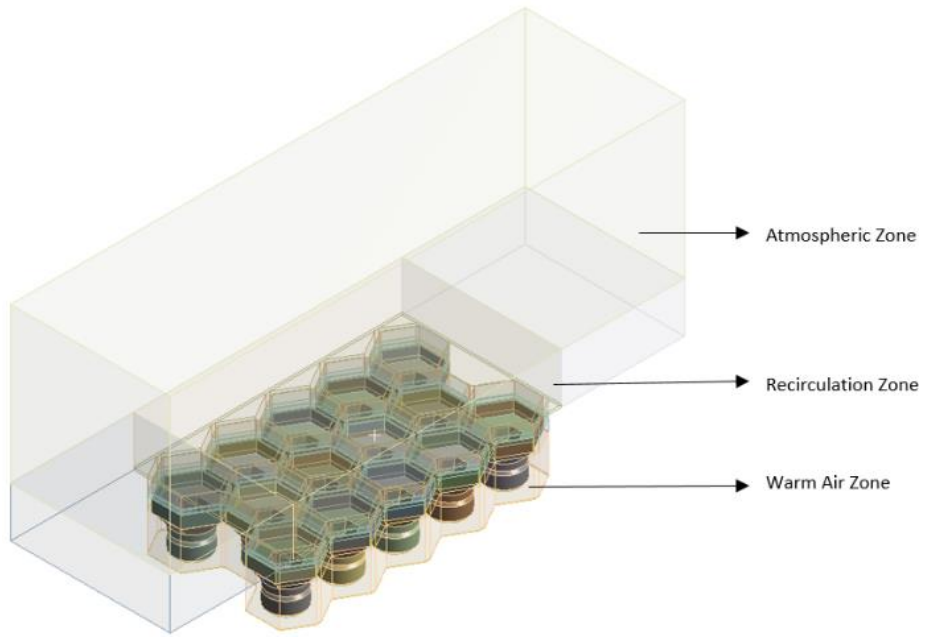


Figure 4-27: Cell zones of the computational model

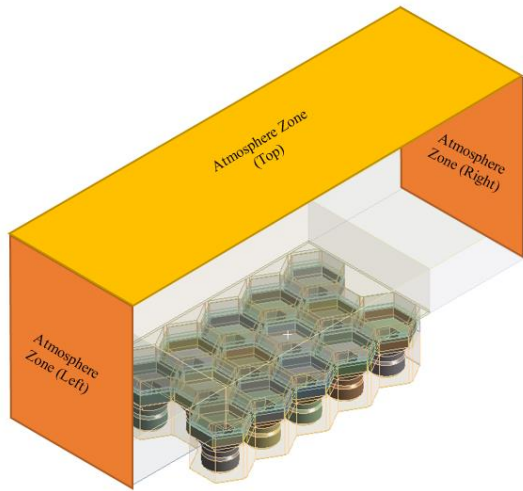


Figure 4-28: Location of boundary condition (a)

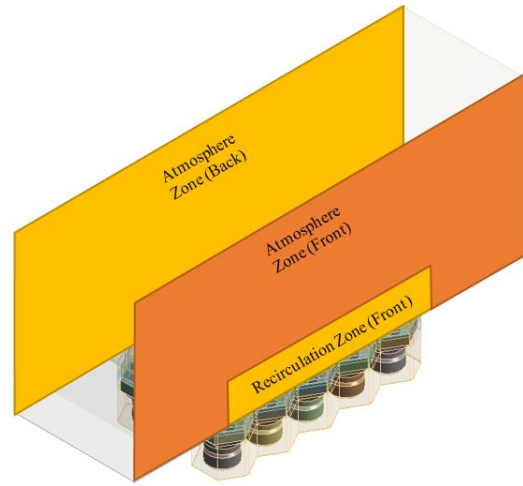


Figure 4-29: Location of boundary condition (b)

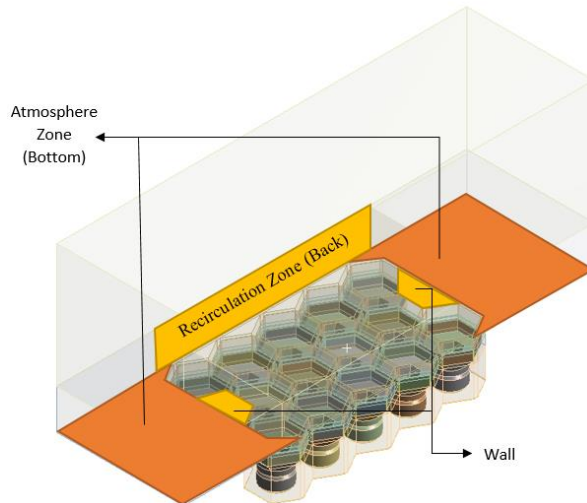


Figure 4-30: Location of boundary condition (c)

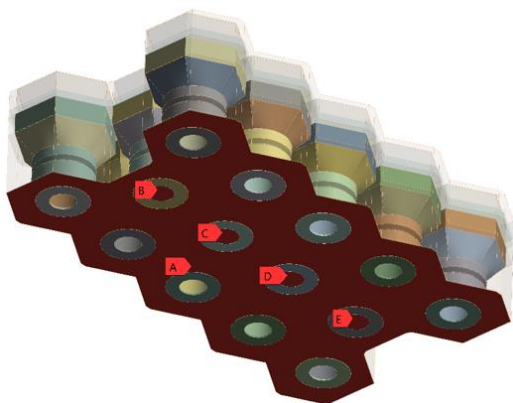


Figure 4-31: Location of boundary condition (d)

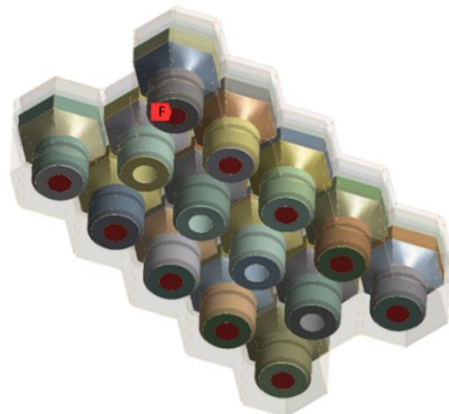


Figure 4-32: Location of boundary condition (e)

The stability of the simulation and the realistic behaviour of the flow of air through the computational domain will depend on the choice of the boundary conditions selected for the model. Boundary conditions can be divided into two types: Dirichlet and Neumann boundary conditions. With Dirichlet boundary conditions, the physical quantity of a transport property, such as pressure, mass flow rate and velocity represented by ϕ is specified as,

$$\phi = \text{constant}$$

Examples of Dirichlet boundary conditions include the velocity inlet, mass flow inlet and mass flow outlet type boundary conditions. In the Neumann-type boundary condition, the gradient of the physical quantity ϕ normal to the boundary is specified at the boundary as,

$$\frac{\partial \phi}{\partial n} = 0$$

with n being the direction normal to the boundary. An example of a Neumann boundary condition is the pressure outlet type boundary condition.

The air enters the computation domain through the Atmospheric zone (as wind) and the Air Returned zone (as the warm air returned from HRSG). The boundary conditions chosen for the atmospheric domain were recommended by two studies independent of each other; the first, where the atmospheric domain over buildings was modelled to study the dispersion of pollutants over a town (Labovský and Jelemenský, 2013), where the CFD approach was validated by experimental data and the second, involving the modelling of atmospheric flow for general-purpose CFD solvers (Balogh, 2014).

Dirichlet boundary conditions were set at the inlets to the atmospheric domain of the 3-D model, which are the top and right face of the atmospheric zone shown in Fig. 4-28, by specifying the velocity magnitude and direction of the air entering the domain. This was done by using a velocity inlet boundary condition. The front and back faces of the atmosphere, shown in Fig. 4-29 were set as symmetry conditions. The outlet boundary conditions used for the atmospheric zones were the atmospheric zone (left) and atmospheric zone (bottom), shown in Fig. 4-28 and Fig. 4-30 respectively. These boundaries were specified as the pressure outlet boundary conditions with a gauge pressure of 0 Pa and at temperatures of 300 K.

For the simulations, it was assumed that the air that flow through the absorber modules is fully recirculated back from the heat recovery steam generator (HRSG) and emitted into the surrounding atmosphere through the gaps between the neighbouring modules. Therefore, the total mass flow rate of air entering the absorber modules is equal to the total mass flow rate of the air that is recirculated back from the HRSG. The bottom face of the Air Returned Zone, labelled A was thus set to a mass-flow inlet

boundary condition with air flowing in at 300 K. The outlet to the absorber modules, with the labels B, C, D, E and F were set to a mass-flow outlet condition.

Table 4-11: Summarized boundary conditions

Domain Face	Boundary Condition
Atmosphere Zone (Front)	Symmetry Plane
Atmosphere Zone (Back)	Symmetry Plane
Atmosphere Zone (Right)	Velocity Inlet
Atmosphere Zone (Left)	Pressure Outlet
Atmosphere Zone (Top)	Velocity Inlet
Atmosphere Zone (Bottom)	Pressure Outlet
A	Mass Flow Inlet
B, C, D, E, F	Mass Flow Outlet
Walls	Slip

The magnitude of the mass flow rate of air through each module was obtained by dividing the total mass flow rate from Table 4-2 by the total number of modules in the test rig. Since the computational domain only accounts for 14 of the 32 modules of the experimental test rig, the mass flow rate of air flowing into the boundary labelled A is equal to the sum total of the mass flow rate of the air flowing through the 14 modules through the boundaries labelled B, C, D, E and F.

4.4.4. Model setup

To adequately capture turbulent flow in the absorber module for the validation study, the two-equation SST $k - \omega$ turbulence model was chosen due to its two-fold ability in predicting the near-wall and the freestream behaviour of the flow better than the other available two-equation turbulence models (Wilcox, 1992b). The pressure-velocity solver used for the simulation is the Pressure Based Coupled Solver (PBCS), simply known as Coupled in Fluent.

The data obtained from the experimental runs (which was inherently transient in nature) were taken at instances when the air outlet temperatures from the absorber modules and power gained by the air were

at steady-state conditions (Hoffschmidt et al., 2003). Lastly, the simulations were carried out under Local Thermal Equilibrium (LTE) conditions, and it was assumed that the radiation losses from the front surface of the absorber were negligible and that all the power incident on the absorber was transferred without losses to the air flowing through it. The effects of buoyancy were assumed to be negligible and were also not accounted for in the model.

4.4.5. Mesh design

The meshing of the computational domain was carried out using the Meshing Module of Ansys Workbench. The meshing module does not have the capability of generating polyhedral cells itself, but the tetrahedral cells of the computational domain can be converted to polyhedral cells within Fluent to improve the mesh quality and to reduce the cell count in the domain. Therefore, the computational domain was first discretized with tetrahedral cells, with prism layer cells being used in regions where capturing the boundary layer flow was deemed necessary. The tetrahedral cells of the discretized domain were then converted to polyhedral cells.

Each zone of the domain was manually selected and meshed in a sequence that would generate good quality cells, and a Worksheet was used to record the sequence of the meshing process. This is known as Selective Meshing and the recorded sequence was later used for generating cells of different sizes for the grid convergence study. The meshing sequencing is presented in the flow chart in Fig. 4-33.

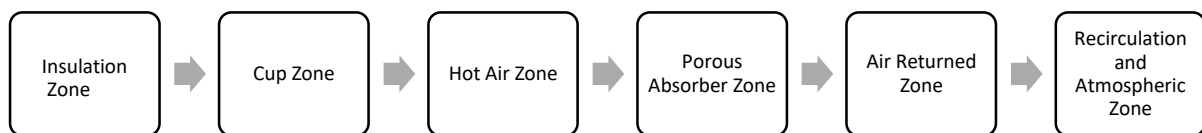


Figure 4-33: Selective Meshing Flowchart

4.4.6. Grid convergence study

The operating conditions and the volumetric power derived for Test 3 of the HiTRec-II experimental run was used for the grid convergence study. The convergence criteria for all the simulation runs were kept at default settings of 10^{-3} for all the residuals except the energy residual which was set to 10^{-6} . The pressure interpolation scheme set for the study was PRESTO! due to the presence of a porous media in the computational domain (Ansys Inc, 2009a). The spatial discretization scheme set for Temperature, Energy, Turbulence Kinetic Energy and Specific Dissipation Rate was the Second Order Upwind Scheme. The physical parameter used to monitor the grid convergence was the mean outlet air temperature associated with each of the four absorber modules in the centre of the computational domain.

The grid convergence study was conducted by progressively refining the cell sizes in the atmosphere zone, recirculation zone, hot air zone and the porous absorber zone while the cell sizes in the air returned zone and the solid zones were kept constant throughout the study. The cells size applied in the hot air zone and the porous absorber zone was used as the reference value, x , with the cell size in the recirculation zone being $2x$ and the cell size in the atmospheric zone being $5x$. A gradual growth rate of 1.05 was set and the domain was meshed completely with tetrahedral cells in Ansys Meshing Module for the sole purpose of converting it to polyhedral cells after importing the meshed model into Fluent 19.2. The study included cell sizes of 6 mm, 3 mm, 2 mm, 1.5 mm and 1 mm. Views of the domains discretized according to the reference cell sizes of 6 mm, 3 mm and 1.5 mm are shown in Fig. 4-34, Fig. 4-35 and Fig. 4-36 respectively.

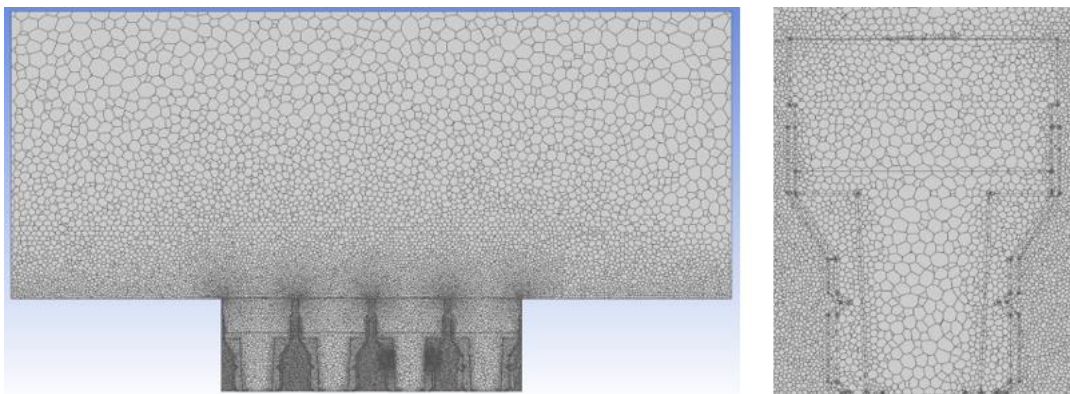


Figure 4-34: Reference cell size of 6 mm

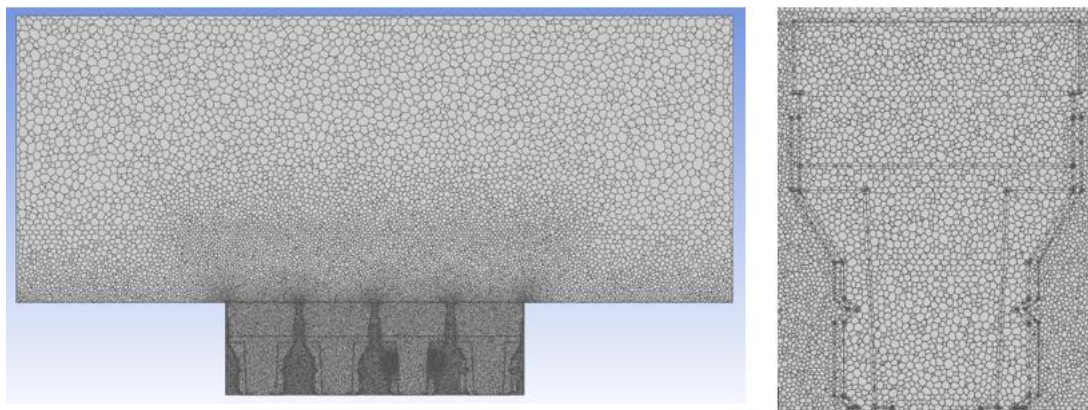


Figure 4-35: Reference cell size of 3 mm

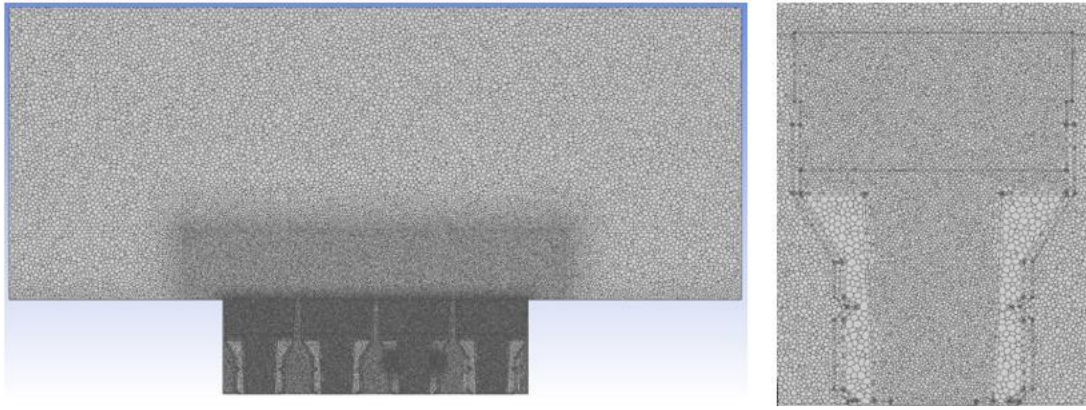


Table 4-36: Reference cell size of 1,5 mm

Due to the sheer size of the computational domain, even for the largest reference cell size, the available desktop computer with 64 GB RAM, Intel ® Core (TM) i7-8700K CPU @ 3.7 GHz (12 CPUs) processor, Windows 10 with SSD proved to be insufficient for the running the required simulations. The computational resources available at the Centre for High Performance Computing (CHPC) were therefore utilized. The facility employs 1368 computing nodes with 24 cores per node, 128 GB of memory per node, 5 large memory ‘fat’ nodes with 1TB per nodes and 9 compute nodes that contain 30 Nvidia V100 GPUs (Crossby, 2019). The results of the grid convergence study are provided in Table 4-12 and graphically illustrated in Fig. 4-37.

Table 4-12: Grid Convergence Study

Element Size	T_{module 1} [K]	T_{module 2} [K]	T_{module 3} [K]	T_{module 4} [K]
6 mm	1171.74	1172.20	1178.55	1177.17
3 mm	1145.94	1168.32	1172.09	1170.97
2 mm	1185.33	1167.71	1156.21	1163.38
1.5 mm	1157.60	1143.60	1150.50	1159.90
1 mm	1155.60	1150.40	1154.30	1150.90

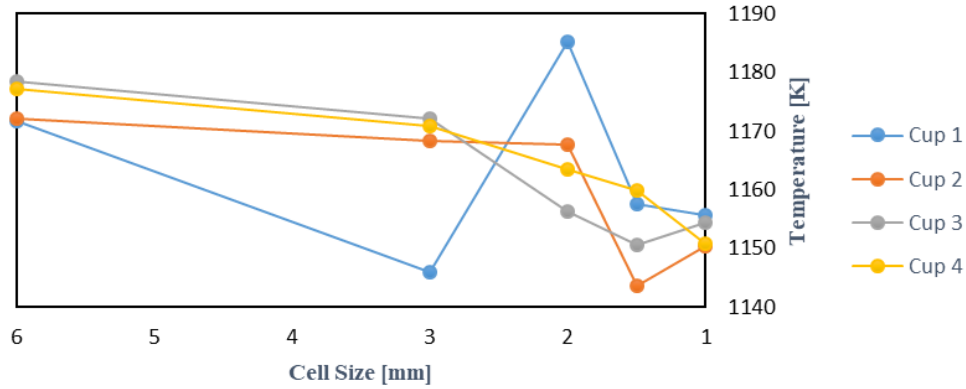


Figure 4-37: Graphical representation of the grid convergence study

As the grid is refined, the measured temperature values at the outlet of the absorber modules should, in theory, tend towards an asymptotic numerical value. That is, the changes in temperature values between successive meshes should approach zero as the grid is refined and the cell size approaches 0 mm. The deviation between the numerical values for consecutive grids is indicated in Table 4-13.

Table 4-13: Percentage deviation of temperatures between consecutive meshes

	$T_{\text{module 1}}$ [K]	$T_{\text{module 2}}$ [K]	$T_{\text{module 3}}$ [K]	$T_{\text{module 4}}$ [K]	Average Deviation
6 mm \rightarrow 3 mm	2.20 %	0.33 %	0.55 %	0.53 %	0.90 %
3 mm \rightarrow 2 mm	3.44 %	0.05 %	1.35 %	0.65 %	1.37 %
2 mm \rightarrow 1,5 mm	2.34 %	2.06 %	0.49 %	0.30 %	1.30 %
1,5 mm \rightarrow 1 mm	0.17 %	0.59 %	0.33 %	0.78 %	0.47 %

It was observed that only the domains discretized with 1.5 mm and 1 mm cells achieved the convergence criteria for all the residuals, unlike the other cases, where the convergence criteria for the energy residual only reduced by just under five orders of magnitude, instead of the set convergence criteria of 10^{-6} . The study also had to be halted at the cell size of 1 mm, because reducing the cell size any further would generate results files that could not be opened on the local PC for post-processing due to the limitations on the available computational resources. The lowest deviations of the temperature values are seen for the two smallest cell sizes i.e. 1.5 mm and 1 mm with an average deviation of 0.47 % which is assumed

to be negligible for the current analysis and therefore, a reasonable level of grid independence was judged to occur at the critical cell size of 1.5 mm.

A sensitivity analysis was carried out to investigate the changes in outlet temperature which occurred when the spatial discretization scheme was switched between the available options in Fluent (under test 3 conditions). The results of this analysis are presented in Table 4-14.

Table 4-14: Sensitivity of the air outlet temperatures to spatial discretization schemes

Spatial-Discretization Scheme	T_{module 1} [K]	T_{module 2} [K]	T_{module 3} [K]	T_{module 4} [K]
First Order Upwind	1136.80	1115.10	1126.10	1129.30
Power Law	1141.50	1125.40	1134	1136.20
Second Order Upwind	1157.60	1143.60	1150.50	1159.90
Third Order MUSCL	1165.20	1146.40	1152.10	1165.40
Experimental Measurements (Test 3 Conditions)	1068.85	1063.11	1057.38	1058.2

All spatial discretization schemes, except the first order upwind scheme met the convergence criteria set for the simulation. Of these, the power law scheme, was found to predict temperatures closest to the experimental data. Hence, another grid convergence study was carried out using the power law, with the results presented in Table 4-15 and graphically illustrated in Fig. 4-38.

Table 4-15: Stage 1 grid convergence study using power law scheme

Cell Size	T_{module 1} [K]	T_{module 2} [K]	T_{module 3} [K]	T_{module 4} [K]
6 mm	1153.10	1159.20	1155.20	1182.90
3 mm	1165.70	1154.70	1129.10	1148.60
2 mm	1147.40	1122	1130	1133.3
1.5 mm	1141.50	1125.40	1134	1136.20
1 mm	1145.20	1126.20	1130.20	1132.70

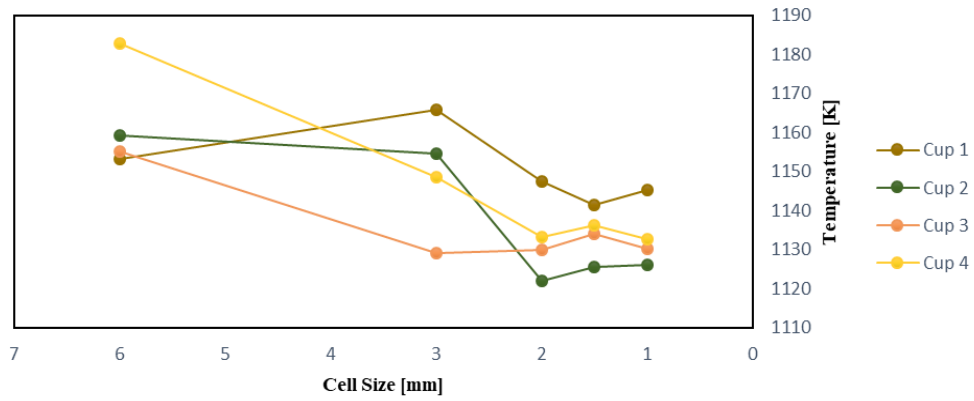


Figure 4-38: Graphical representation of the grid convergence study

The percentage deviation between the temperature values of the various grid sizes were calculated and given in Table 4-16.

Table 4-16: Percentage deviation of temperature between consecutive meshes

	$T_{\text{module 1}}$ [K]	$T_{\text{module 2}}$ [K]	$T_{\text{module 3}}$ [K]	$T_{\text{module 4}}$ [K]	Average Deviation (%)
6 mm – 3 mm	1.09%	0.39%	2.26%	2.90%	1.66%
3 mm – 2 mm	1.57%	2.83%	0.08%	1.33%	1.45%
2 mm – 1.5 mm	0.51%	0.30%	0.35%	0.26%	0.36%
1.5 mm – 1 mm	0.32%	0.07%	0.34%	0.31%	0.26%

Similar to the previous study, the domains with 1 mm and 1.5 mm achieved the convergence criteria set for the residuals whereas the domain with the cells sizes 6 mm, 3 mm and 2 mm achieved the convergence criteria for all the residuals expect the energy residual, which reduced by only five orders of magnitude. Hence, it was concluded that the critical cell size for the validation study would be 1.5 mm.

4.4.7. Validation study

Table 4-17 presents all of the final Fluent settings that were used for the validation study.

Table 4-17: Solution Controls

Viscous Regime	SST k-omega Turbulence Model
Pressure Discretization Scheme	PRESTO!
Gradient Discretization	Least Square Cell Based
Spatial Discretization of Temperature, Energy, Turbulence Kinetic Energy and Specific Dissipation Rate	Power Law Scheme
Pressure-Velocity Coupling	Coupled
Under-Relaxation Factors – Density, Body Forces, Turbulence Kinetic Energy, Specific Dissipation Rate, Turbulent Viscosity, Energy	1, 1, 0.8, 0.8, 1, 0.98

Using the above solution controls, as well as the cell zones and boundary condition settings mentioned beforehand, the operating parameters of the experimental tests mentioned in Table 4-2 were simulated to draw a comparison between the numerically predicted and experimentally measured data given in Table 4-3. The numerical results obtained from the simulations are given in Table 4-18 and the deviation of the numerical temperature values from the experimental data are presented in Table 4-19.

Table 4-18: Numerical results of temperature values obtained from the validation study

	T_{module 1} [K]	T_{module 2} [K]	T_{module 3} [K]	T_{module 4} [K]
Test 1	1071.8	1059.3	1064	1072.9
Test 2	1063.7	1037.7	1044.7	1032.3
Test 3	1141.5	1125.4	1134	1136.2
Test 4	1257.8	1241	1240	1241.6
Test 5	889.83	874.88	876.85	882.38

Table 4-19: Percentage deviation of the numerical results from the experimental measurement of outlet air temperatures

	$T_{\text{module 1}}$ [K]	$T_{\text{module 2}}$ [K]	$T_{\text{module 3}}$ [K]	$T_{\text{module 4}}$ [K]
Test 1	-7.09 %	-6.54 %	-3.72 %	-4.84 %
Test 2	-1.47 %	1.63 %	-5.08 %	-1.70 %
Test 3	-7.60 %	-5.86 %	-8.26 %	-11.30 %
Test 4	-7.73 %	-12.32 %	-12.05 %	-11.02 %
Test 5	3.06 %	-3.13 %	2.16 %	2.95 %

The temperature field of the computational domain under test 3 conditions is illustrated in Fig. 4-39 and a magnified image of the absorber modules is given in Fig. 4-40.

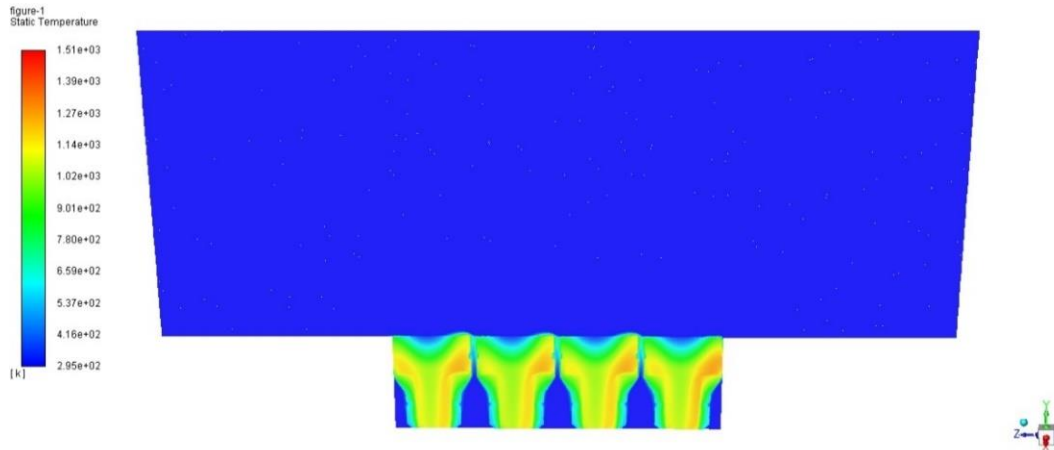


Figure 4-39: Static Temperature Contour Plot (under Test 3 conditions)

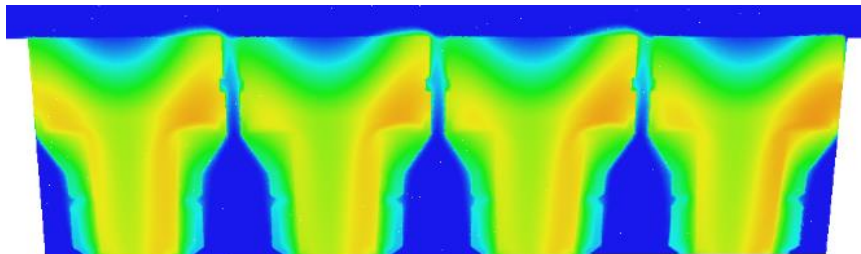


Figure 4-40: Magnified image of the temperature contour plot

The velocity vector plot in the region just above the absorber modules is given in Fig. 4-41 and within the module is illustrated in Fig. 4-42.

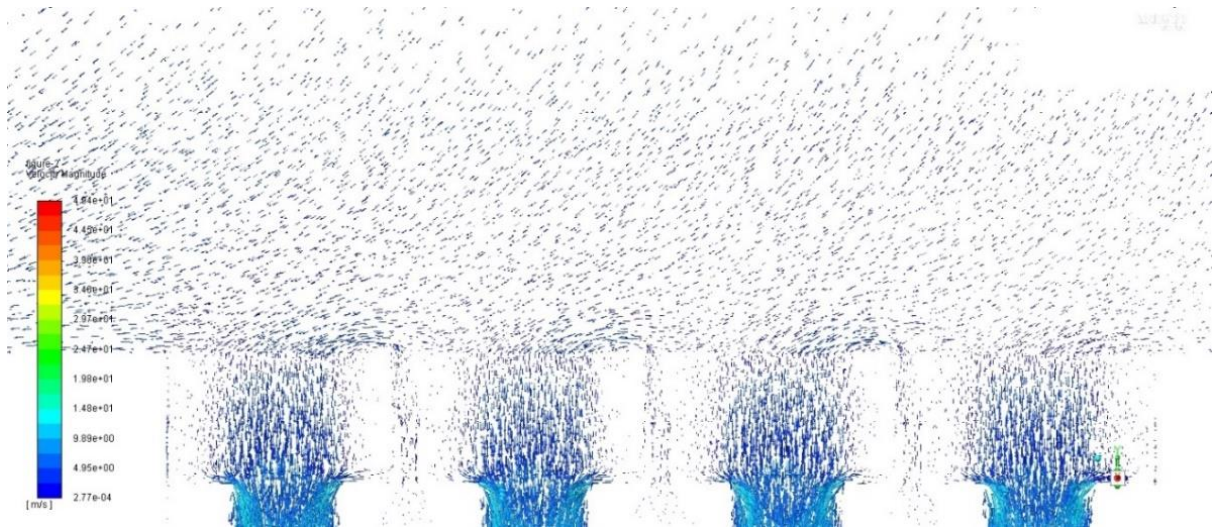


Figure 4-41: Velocity Vector Plot (a) (under Test 3 conditions)

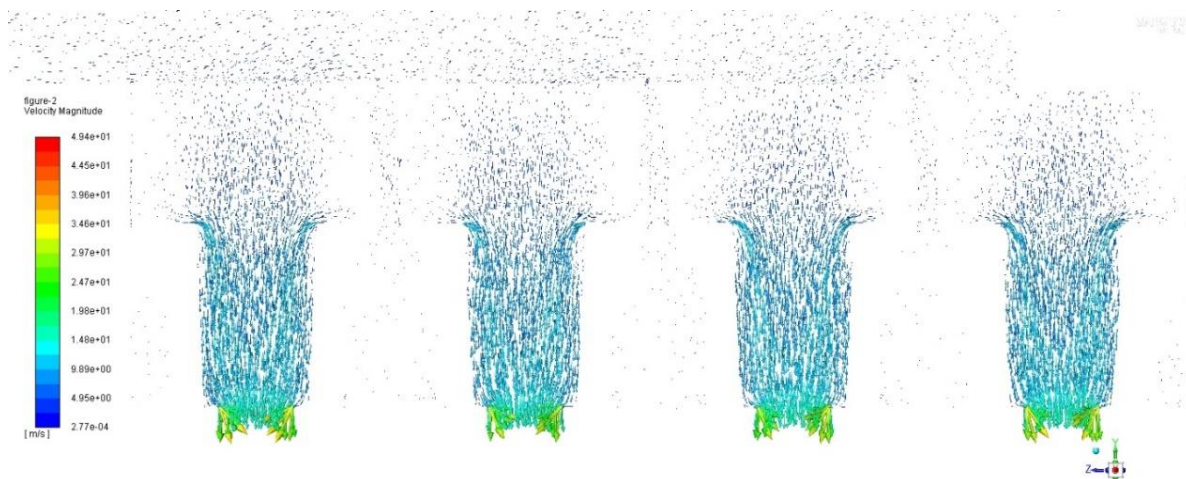


Figure 4-42: Velocity Vector Plot (b) (under Test 3 conditions)

4.5. Discussion

The pressure drop imposed by the porous absorber of an OVR is a function of the air velocity and the internal structure of the absorber module porous medium. It is vital to accurately simulate the flow behaviour of air inside this medium. Therefore, an experimental study involving the flow of air through a porous medium with (hot flow analysis) and without (cold flow analysis) a heat source was chosen to

model in Fluent and attempt to obtain numerical results that are within the 10 % tolerance of the experimental data.

An experimental study that investigated the sensitivity of the pressure drop across a porous absorber to the velocity of air flowing through it was chosen for the cold flow validation. The porous absorber was modelled in Ansys Fluent and the operating conditions in the CFD model were set in an identical manner to the experimental set-up. Table 4-1 compares the experimental and the numerical pressure drop values and it is clear that the largest deviation from the experimental data was 1.36 %, and therefore, the method of setting up the porous medium in Fluent in the cold flow validation study was deemed suitable to model the flow of air through a porous structure.

To capture the behaviour of the air as it flows through a heated porous medium, a 2-D model of the HiTRec-II absorber modules proposed in (Roldán et al., 2016) was initially chosen. Details about the procedure for setting up the model as well as the successful validation of the model against experimental data obtained from the HiTRec-II prototype testing carried out at the Plataforma Solar de Almeria (PSA) motivated its use as a reference case for the hot flow validation study. However, after a closer examination, the proposed computational domain of the CFD model, the 2-D geometry of the absorber modules as well the modelling of the thermal energy in the porous mediums revealed some inconsistencies with respect to good CFD practices and its capability to realistically model the flow behaviour within the absorber modules.

The atmospheric domain was comparatively small with respect to the size of the absorber module and could falsely predict the pressure field in the domain, as the outlet was situated adjacent to the absorber modules. Furthermore, a 2-D model cannot accurately model the behaviour of air flowing through a module where the cross-section transitions from a hexagonal shape at the top to a circular shape at the bottom. Since neither of the length, breadth and height of the module is ten times larger than the other two dimensions, there is no justification to represent the model in a 2-D domain other than to save on computational resources by compromising the accuracy of the numerical result.

The heat energy in the porous medium was simulated using a function representing the Beer-Lambert law which accounts for the rate at which the solar radiation attenuates with the depth of the porous medium. Although the idea behind modelling the heat source was representative of reality, the total magnitude of the thermal power that was simulated in the porous medium in the 2-D domain was not large enough to heat the air from ambient temperatures to over 1000 K as proven through the calculations carried out in section 4.4.2 and the CFD simulations results presented in Table 4-7. The outlet temperature values were significantly different from the published CFD results in the article, drawing suspicion on the validity of the setup of the model and the published results in Fluent.

In an effort to avoid the modelling of the localized heat energy in the porous medium, a constant volumetric power was derived by dividing the experimentally measured solar power per absorber module by the 2-D volume of the porous medium (the depth of the absorber is assumed to be 1 meter in length since 2-D models work on a per unit basis). The resulting outlet air temperatures presented in Table 4-8 imply that the transfer of heat energy to the air flowing through the heated porous medium was enhanced when the constant volumetric heat energy was applied, yielding outlet air temperatures ranging from 336 K to 655 K.

In spite of the improvements in the heat transfer was observed when the volumetric heat source derived directly from experimental measurement was used in the 2-D HiTRec-II model, the predicted temperature fell outside of the 10 % deviation margin of the experimental data. The geometry of the porous absorbers was represented by two rectangular shapes, and the depth of the absorber is assumed to be one-meter-long in the 2-D model. Therefore, the formulation of the volumetric power in the absorbers totally neglects its true shape and depth, inevitably leading to non-physical temperature predictions. Therefore, a 3-D model consisting of 14 HiTRec-II absorber modules was developed and used for the hot flow validation study.

A constant volumetric power was derived once again using the measured solar power incident on the absorbers per module, and the 3-D volume (the true volume) of the absorbers. A grid convergence study was conducted under test 3 operating conditions assuming steady-state conditions for the simulations. The model achieved grid convergence at a cell size of 1.5 mm and the sensitivity of the model to the available spatial discretization schemes (First Order Upwind, Second-Order Upwind, Power Law and Third Order MUSCL) was investigated, again under test 3 operating conditions. All schemes over-predicted the temperature values, with the first order upwind scheme predicting outlet temperatures values closest to the experimental data. Unfortunately, it did not achieve the convergence criteria set for the energy residual, unlike the other schemes. The next best prediction of the absorber module outlet temperature achieved all the convergence criteria. Hence, the next best prediction of temperatures was done using the Power Law scheme, which was then finalized for the validation study.

The simulations were run under the operating conditions for the five tests (detailed in Table 4-2) that were conducted at PSA on the HiTRec-II prototypes. Under test 1, 2 and 5 operating conditions, the outlet air temperatures obtained from the simulations were well within the 10 % margin around the experimental data. The temperature values at the outlet of absorber module 4 under test 3 conditions and absorber modules 2, 3 and 4 under test 4 conditions fell outside the 10% tolerance range. Since the simulated temperature value for three out of the five test cases fell within the acceptable deviation margin of 10 %, the methodology was deemed suitable for the numerical studies presented in the upcoming chapters.

The velocity vector plot that was generated under the test 3 conditions for the 3-D model was strikingly different from that obtained for the 2-D model. Unlike in Fig. 4-17 where there is recirculation of the air within the absorber modules, the pattern of airflow illustrated in Fig. 4-42 represents a more realistic flow path that would be expected in the absorber module, quite similar to that shown in Fig. 2-25. Such a contrast between the velocity vector plots sheds light on the significance of ensuring that the correct domain (2-D/3-D) is chosen for modelling a problem.

4.6. Conclusion

The chapter mainly addressed the development of a suitable modelling methodology to capture the flow behaviour through a porous medium in an OVR via hot and cold flow validation studies, where the acceptable deviation of the simulation results from the experimental data was set to 10 %. The validation studies were conducted in Ansys Fluent 19.2.

An experimental study conducted on porous absorbers of different porosities to determine the change in the pressure drop across the absorber at different values of velocity was used for the cold flow validation study. The main parameters used for replicating a porous medium in Fluent were the porosity, porous inertial and porous viscous resistance coefficients, with the latter two being derived from a pressure velocity curve that was generated from the experimental data. The numerical results from the simulations were well under 2 % deviation from the experimental data

Initially, a 2-D CFD study that successfully validated a CFD model of the HiTRec-II absorber modules against experimental data collected from the HiTRec-II test runs carried out at PSA was chosen for the hot flow validation study. Limitations in the 2-D model were discovered that prevented it from effectively predicting the behaviour of the airflow through the modules. Hence, a 3-D model was designed and used for the validation study. Finer details of the meshing procedure, grid independence study and the settings used in Fluent 19.2 were detailed in the chapter. The outlet air temperatures obtained from the four central absorber modules, for five separate tests carried out on HiTRec-II modules at PSA, were used as the reference data points against which the numerical results were compared to determine the success of the validation study. Out of the 20 data points, only four fell outside the 10 % margin with the largest deviation of 12.32 %. Nonetheless, the procedure used for modelling the HiTRec-II CFD model was deemed suitable to be used for the upcoming simulations of the OVR modules.

5. WIND EFFECTS STUDY ON SOLAIR-200 ABSORBER MODULES

The warm air from the HRSG should ideally be re-entrained through the absorbers of the OVR modules. However, the warm air return loop of OVRs such as HiTRec and SolAir is an open-circuit loop that exhausts the warm air from the HRSG into the open environment, through the gaps present in between the modules, as shown in Fig. 5-1. There is a significant heat loss in the warm air that escapes into the atmosphere due to convective effects, resulting in the proportion of the air that is partly re-entrained into the absorber having lower thermal energy than the warm air in the air return loop. Thus for any OVR, an ARR value of less than unity indicates a loss of thermal energy by this mechanism, which in turn has a detrimental effect on the overall thermal efficiency of the receiver.

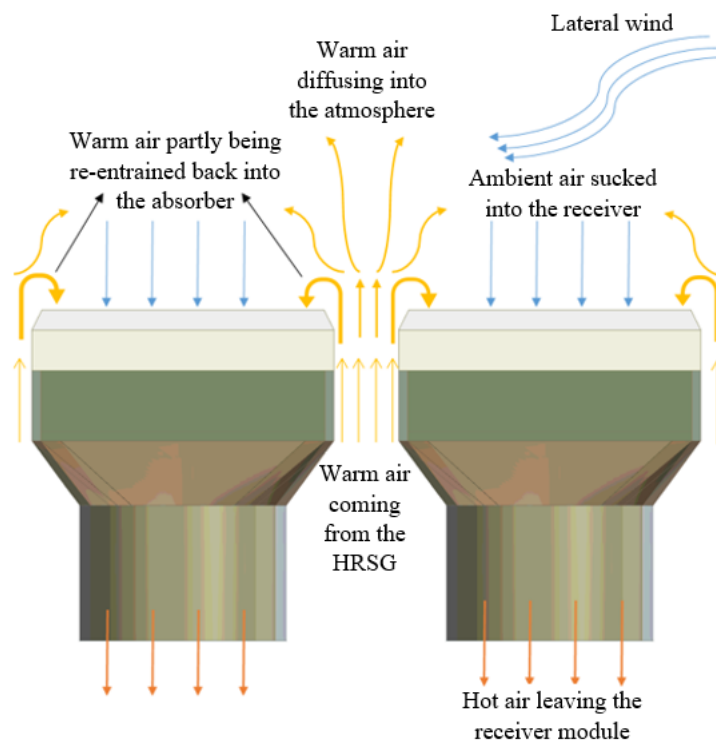


Figure 5-1: Mechanism of ARR in OVRs

Experimentally determined values of the ARR associated with the HiTRec and the SolAir absorbers have been observed to be quite low; in the range of 0.35 – 0.45, with corresponding overall thermal efficiency to be only 75 %. For commercial application of the OVR technology, however, efficiencies above 90 % were targeted (Marcos et al., 2004).

Wind exposure of the OVR can lead to reduced ARR (Á. Marcos *et al.*, 2004) and uneven distribution of the temperature in the absorber medium (Palero *et al.*, 2008), leading to the formation of hotspots. As per a CFD study conducted by Marcos *et al.* (2004), addition of geometrical features such as secondary concentrators and conical structures at the inlet of a module (that also enclose the gaps around the individual modules, through which warm escapes into the atmosphere) can prevent the convective loss of heat due to wind exposure, resulting in an ARR of up to 0.90. Unlike the standard way of emitting the warm air from the air return loop upwards perpendicular to the absorber surface, as illustrated in Fig. 5-1, the study by Marcos *et al.* (2004) also highlighted the significance of the change in the direction at which the warm air is emitted using external air return ducts situated around the perimeter of a group of HiTRec-II absorber modules, where air returned in the direction parallel to the surface of the absorbers resulted in an ARR close to 0.6. Implementing a physical obstruction such as an absorber shield on the modules to prevent direct impingement of wind on the absorbers was also shown to improve the ARR of the HiTRec receivers, which stood at 0.55 as per the same study, although details about the absorber shield configuration were not provided.

The improvement in the ARR of the HiTRec absorber modules with the aid of the wind protection shield as well as parallel air injection angle inspired the idea of implementing air flow baffles in between the SolAir modules to potentially improve its ARR. In order to quantify the improvements in performance brought about by the air flow baffles, a baseline performance of the receiver without the baffles must be established. This chapter details the development of the CFD model of the standard SolAir modules and discuss the effects of the wind at various speeds and direction on its ARR.

A 3-D model of a 3 x 6 configuration of the standard SolAir receiver absorber modules was generated in Ansys Design Modeller to replicate three rows of the SolAir-200 receiver test rig. The formulation of the CFD model was followed by the conduction of a wind effects study, in which the sensitivity of the configuration's performance to wind speed and orientation was investigated.

5.1. SolAir material properties

The physical dimensions of the SolAir absorber as well as the thermophysical properties of the solid materials used in the absorber module were obtained from the German Aerospace Centre (DLR) (Schwarzboezl, 2019b). The absorbers of the SolAir modules were made out of recrystallized silicon carbide (SiC) (140 mm x 140 mm front surface and length of 60 mm), the outer cups were made out of siliconized silicon carbide (SiSiC) and the inner circumferential region of the modules were layered with a 10 mm thick insulation. The basic dimensions of a CFD model of a SolAir module is shown in

Fig. 5-2. The thermophysical properties of the air were adopted from the validation study carried out on the HiTRec-II CFD model in Chapter 4.

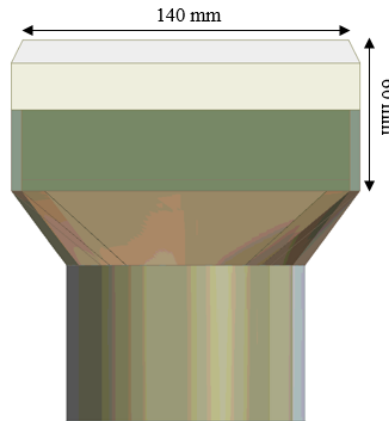


Figure 5-2: Basic dimensions of a SolAir module

The porous absorber made of silicon carbide has a density of 2700 kg/m^3 , a thermal conductivity defined by $40417 * T^{-1.019}$ and a specific heat capacity of 900 J/kg-K . The infiltrated silicon carbide that was used to manufacture the outer cups of the modules has a density of 3051 kg/m^3 , a thermal conductivity of $140042 * T^{-1.142}$ and a specific heat capacity of 1200 J/kg-K . The insulation material lining the inner circumference of the absorber module has a density of 990 kg/m^3 , specific heat capacity of 1050 J/kg-K and thermal conductivity of 0.2 W/m-K .

5.2. Porous medium characteristics of the SolAir module

The pressure characteristic curve, which defines the behavior of air at $25 \text{ }^\circ\text{C}$ through the SolAir absorbers is given by equation (5.3) (Schwarzboezl, 2019a).

$$\frac{\Delta P}{l} = 3.5187 v^2 + 5.9161 v \quad (5.3)$$

The porous inertial [m^{-1}] and viscous resistance [$\frac{1}{m^2}$] coefficient of the SolAir absorber that were specified in Fluent were derived by equating equation (4.5) to equation (5.3), which results in a porous inertial coefficient of 5.92 m^{-1} and a porous viscous coefficient of $2.692 \times 10^{-8} \text{ m}^{-2}$ in the direction of flow. The coefficients in the direction perpendicular to the flow was set three orders of magnitude higher than the ones in the direction of flow, while the porosity of the absorber medium was set to 0.495.

5.3. Limitations of the Local Thermal Equilibrium (LTE) model

The heat transfer modelling in the porous medium was carried out assuming local thermal equilibrium (LTE) conditions; that is, the absorber and the air flowing through it is assumed to be a single medium with an effective thermal conductivity (equation (5.4)) due to the assumption of infinite heat transfer coefficient between the absorber and the air.

$$k_{eff} = \phi k_f + (1 - \phi)k_s \quad (5.4)$$

A drawback of the LTE assumption in porous medium modelling reveals itself when the ARR of an absorber module is calculated. In order to calculate this parameter, the temperature of air at the immediate inlet of the absorber is required. Due to the assumption of a single zone for the solid (absorber) and fluid (air) phases and the consequential utilization of an effective thermal conductivity, the temperature measured of the air at the inlet of porous medium is the effective temperature of the single zone evaluated using the effective thermal conductivity, resulting in a value that is artificially much higher than it would be in reality.

In order to derive an alternative method of measuring the ARR, a control volume enclosing the porous region of an absorber module (which includes the absorber substrate and the air) was modelled, as shown in Fig. 5-3.

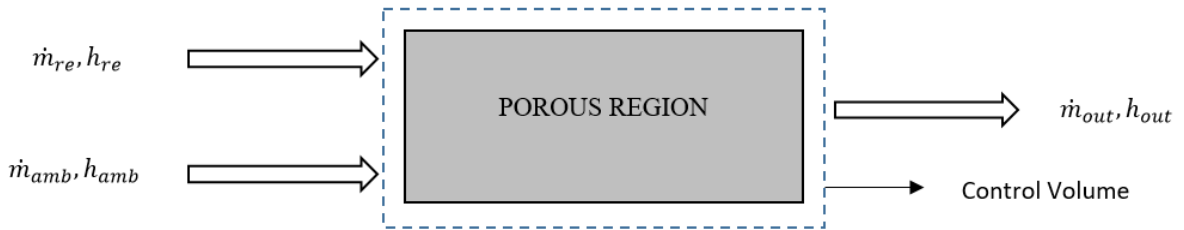


Figure 5-3: Energy balance of porous medium

The energy rate balance equation for the control volume in its most general form can be written as:

$$\frac{dE_{cv}}{dt} = \dot{Q}_{cv} - \dot{W}_{cv} + \sum_i \dot{m}_i \left(h_i + \frac{(V_i)^2}{2} + gz_i \right) - \sum_e \dot{m}_e \left(h_e + \frac{(V_e)^2}{2} + gz_e \right)$$

In the context of the study, the following assumptions were considered to be appropriate:

1. The energy transfer through the control volume is in steady-state, so $\frac{dE_{cv}}{dt} = 0$.

2. The kinetic and potential energies of the flow were assumed to be negligible at the inlets and outlets, so $\frac{(V_i)^2}{2}, gz_i, \frac{(V_e)^2}{2}, gz_e = 0$.
3. The only heat transfer between the porous medium and the surrounding is the solar energy transferred into the system, so $\dot{Q}_{cv} = \dot{Q}_{solar}$ – as such, thermal losses were neglected.
4. There is no work transfer into or out of the system, $\dot{W}_{cv} = 0$.
5. All of the air drawn through the absorber is emitted back into the surrounding environment, through the return air ducts (between adjacent absorber modules), without any leakage losses.

With these assumptions taken into account, the simplified energy rate equation for a porous absorber of an open volumetric receiver absorber modules can be written as:

$$0 = \dot{Q}_{solar} + \sum_i \dot{m}_i(h_i) - \sum_e \dot{m}_e(h_e)$$

Expanding further,

$$0 = \dot{Q}_{solar} + \dot{m}_{re}(h_{re}) + \dot{m}_{amb}(h_{amb}) - \dot{m}_{out}(h_{out})$$

where \dot{Q}_{solar} is the total heat transferred into the absorber through solar radiation, \dot{m}_{re} and h_{re} are the mass flow rate and specific enthalpy of the warm air that is re-entrained back into the absorber, \dot{m}_{amb} and h_{amb} are the mass flow rate and the specific enthalpy of the ambient air drawn through the absorber and finally, \dot{m}_{out} and h_{out} are the mass flow rate and specific enthalpy of the heated air leaving the absorber.

Assuming that all of the air flowing out of the porous absorber is ultimately returned to the receiver through the warm air duct, the mass flow rate of the air that is re-entrained into the absorber, \dot{m}_{re} , can be related to the mass flow rate of air returned to the receiver through the return air duct, which is equivalent to \dot{m}_{out} as per assumption (5) above, by the ARR as follows,

$$ARR = \frac{\dot{m}_{re}}{\dot{m}_{out}}$$

The mass flow rate of the ambient air drawn through the absorber can be represented as follows,

$$(1 - ARR) = \frac{\dot{m}_{amb}}{\dot{m}_{out}}$$

Therefore, the energy balance equation can be reformulated as,

$$0 = \dot{Q}_{solar} + (ARR * \dot{m}_{out})(h_{re}) + (1 - ARR)\dot{m}_{out}(h_{amb}) - \dot{m}_{out}(h_{out})$$

$$ARR = \frac{\dot{m}_{out}(h_{out} - h_{amb}) - \dot{Q}_{solar}}{\dot{m}_{out}(h_{re} - h_{amb})}$$

Any improvement in the air outlet temperature would mean a proportional improvement in the air outlet specific enthalpy, and the ARR. As such, the absorber module outlet air temperature can be used as a proportional but indirect measure of the ARR, and therefore as a measure of the improvement in the performance brought about by geometrical modifications/additions to the SolAir receiver configuration.

5.4. Operating parameters for wind effects study

The following assumptions about the operating conditions of the SolAir absorber modules have been made to ensure that the wind effects study is within the scope of the work:

- i. The variation of the incident solar power on the receiver test rig due to the diurnal variation of radiation intensity, the passing of clouds or errors that can occur in the control system of the heliostat field is not accounted for in the study. Hence the solar power incident is assumed to be constant.
- ii. The gradual decay of the solar energy through the depth of the absorber is not taken into consideration, and it is assumed that there is an even distribution of the solar energy in the porous absorbers and specified as a constant heat source. Such an assumption has a negligible impact on the accuracy of the simulation setup since the total solar energy that is contained in the absorber was captured with the constant heat source assumption.
- iii. The controlled change in the mass flow rate of air through the absorber modules in response to the incident radiation non-homogeneity is not accounted for in the study. It is assumed that a constant mass flow rate is drawn through all the absorber modules by the blower.
- iv. Any leakage loss in the air circuit of the warm air that is returned to the receiver is assumed to be negligible. Therefore, the mass flow rate of air in the air return ducts is equal to the mass flow of the air drawn in through all of the absorber modules.

As per the research carried out by Pitot de la Beaujardiere, (2019), the heliostats used in central receiver systems have been known to be stowed safely at a maximum allowable ground-level, lateral wind speed

of 17 m/s (Grasse and PHOEBUS, 1991). This would translate to almost 25 m/s at a typical solar tower height of 150 m, using the 1/7th Power Law (Wesley et al., 1983) given by equation (5.5).

$$V_{rec} = V_g \left(\frac{h_{tower}}{10} \right)^{\frac{1}{7}} \quad (5.5)$$

Here, V_{rec} is the lateral speed of the wind on the receiver at the top of the tower, V_g is the lateral ground speed of the wind and h_{tower} is the height of the solar tower. The wind speeds of 5 m/s, 10 m/s, 15 m/s, 20 m/s and 25 m/s each at angles of 0°, 30°, 60° and 90° with respect to the vertical axis was finalized for the study.

An experimental study was carried out on a 200 kW_{th} SolAir module test rig to determine the durability, efficiency and modularity of the SolAir design. The test rig was subjected to various magnitudes of incident solar radiation, and the corresponding mass flow rates as well as the mean air outlet temperatures at the exit of the absorber modules were recorded and published in Téllez (2003). An equation relating the air outlet temperature to the total incident solar power and the mass flow rate, was derived from the recorded data as shown in Fig. 5-4. The raw data of the SolAir-200 experimental campaign used to derive the equation are provided in Appendix B.

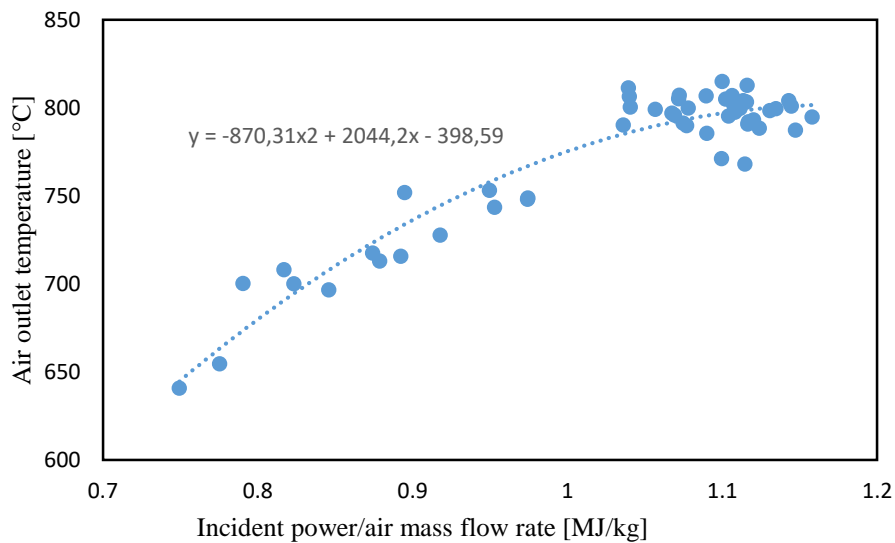


Figure 5-4: Scatter plot of the SolAir-200 experimental campaign data

The equation to the regression curve is represented by equation (5.6),

$$T_{rec,o} = -870.31 \left(\frac{\dot{Q}_{int}}{\dot{m}_r} \right)^2 + 2044.2 \left(\frac{\dot{Q}_{int}}{\dot{m}_r} \right) - 398.59 \quad (5.6)$$

where \dot{Q}_{int} is the magnitude of the solar radiation [MW/m^2] incident on the receiver, \dot{m}_r is the total mass flow rate of air through all the absorber modules and $T_{rec,o}$ is the temperature of the air leaving the modules.

The recorded data for the incident solar radiation, mean air outlet temperature and total mass flow rate of the air through the absorber modules of the test rig, along with equation (5.6), was used to finalize the design parameters for the wind effects study. The average incident solar radiation imposed on the absorber modules was close to 300 kW_{th} which was taken to be the design incident solar radiation along with the design outlet air temperature of 800 °C. Therefore, the nominal mass flow rate at the outlet of the absorber modules worked out to be 0.265 kg/s using equation (5.6). The nominal mass flow rate of air through each of one of the 36 modules in the test rig is 0.00736 kg/s. It was assumed that a constant solar power of 300 kW was incident on the receiver test rig and the solar power was evenly distributed through the depth of the absorbers. Hence, the total power per module was calculated to be 8333.33 W and the volumetric power per absorber was derived as follows,

$$\begin{aligned} \text{Volumetric Power [W/m}^3\text{]} &= \frac{\text{Total power per absorber}}{\text{Absorber Volumetric}} \\ &= 6621899.96 \text{ W/m}^3 \end{aligned}$$

and total mass flow rate of warm air returning from the HRSG was 0.265 kg/s and its temperature was set to 423.15 K.

5.5. Cell zones and boundary conditions

The CFD model of each one of the SolAir modules is sub-divided into multiple zones (to separately define them with their respective material properties), identical to those of the HiTRec modules considered in the previous chapter. These include solid zones such as the absorber cup and insulation, and fluid zones such as the porous absorber zone, hot air zone, a zone for the warm air from the return air circuit, a recirculation zone above the absorber modules and the atmospheric zone. The zones are graphically displayed in Fig. 5-5 to Fig. 5-8.

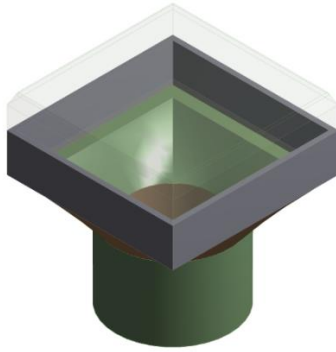


Figure 5-5: SolAir absorber module

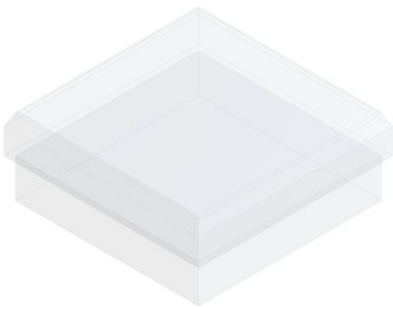


Figure 5-6: Porous absorber

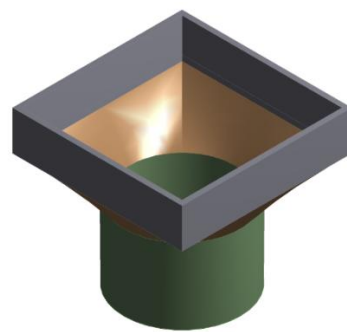


Figure 5-7: Outer Cup

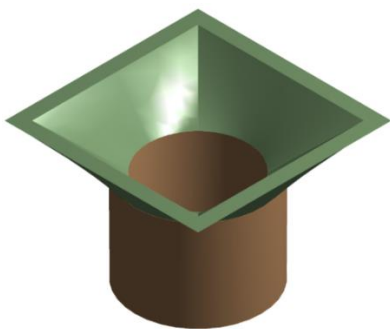


Figure 5-8: Insulation

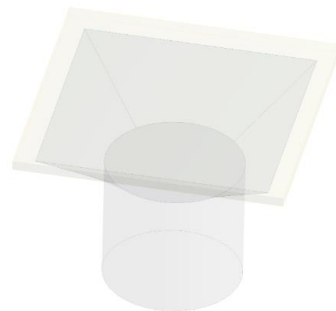


Figure 5-9: Hot Air Zone

The 3 x 6 configuration of the SolAir absorber modules and the full CFD model that was used for the wind effects study are illustrated in Fig. 5-10 and Fig. 5-11.

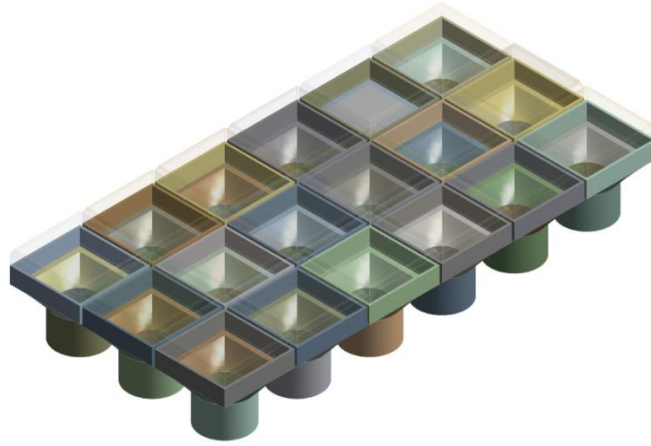


Figure 5-10: 3 x 6 configuration of SolAir modules

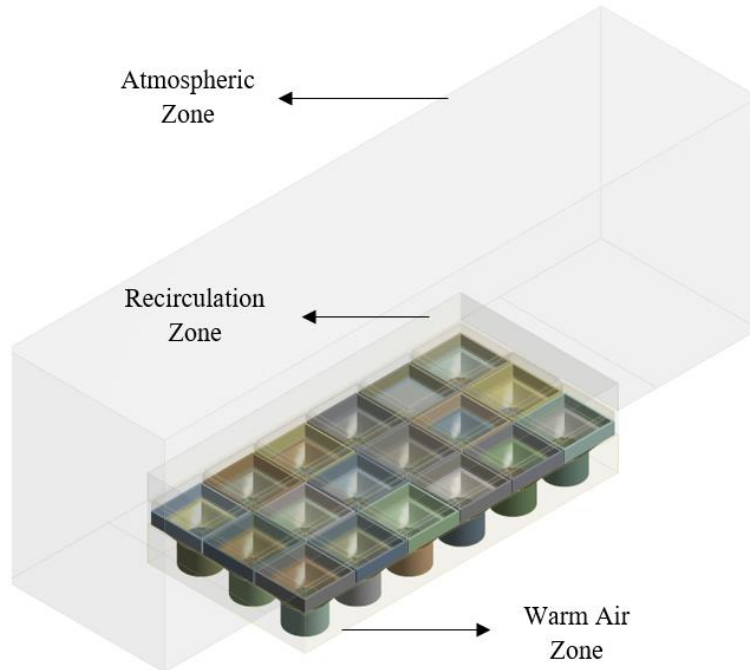


Figure 5-11: CFD model used for the wind analysis

The individual boundary conditions used in the SolAir model are illustrated in Fig. 5-12 and Fig. 5-13.

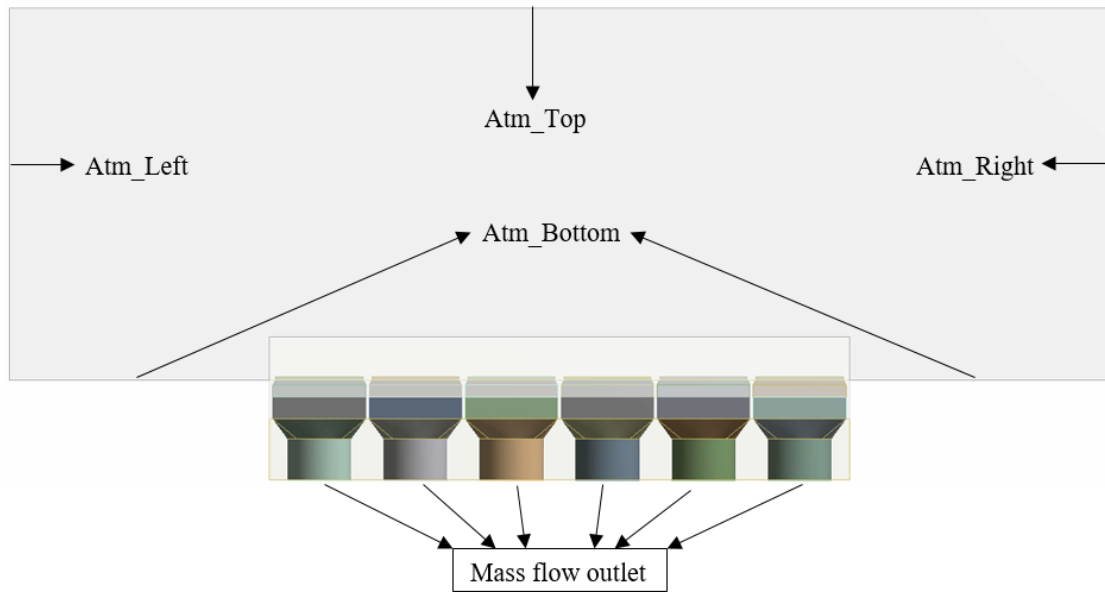


Figure 5-12: Front view of the SolAir model, with boundary conditions



Figure 5-13: Side view of the SolAir model with boundary conditions

Table 5-1 Characterises of the atmospheric boundary conditions used for the wind effects study.

Table 5-1: Atmospheric boundary conditions for the SolAir model

Incidence Angle	Atm_Right	Atm_Top	Atm_Left	Atm_Bottom
0° (parallel) to absorber surface	Velocity Inlet	Outflow	Outflow	Outflow
Between 0° and 90°	Velocity Inlet	Velocity Inlet	Outflow	Outflow
90° (normal) to absorber surface	Outflow	Velocity Inlet	Outflow	Outflow

The wind enters the atmospheric domain, with respect to the vertical axis through the top and right faces of the atmospheric domain. The simulation settings used for running the wind effects study simulations in Fluent are provided in Table 5-2.

Table 5-2: Fluent settings for the wind effects study of standard SolAir receiver

Viscous Regime	SST k-omega Turbulence Model
Pressure Discretization Scheme	PRESTO!
Gradient Discretization	Least Square Cell Based
Spatial Discretization of Temperature, Energy, Turbulence Kinetic Energy and Specific Dissipation Rate	Second Order Upwind Scheme
Pressure-Velocity Coupling	Coupled
Under-Relaxation Factors – Density, Body Forces, Turbulence Kinetic Energy, Specific Dissipation Rate, Turbulent Viscosity, Energy	1, 1, 0.8, 0.8, 1, 0.98

5.6. Grid convergence study

A grid convergence study was carried out for the SolAir model to obtain the most economical cell size for the domain, using the outlet air temperatures of the absorber modules in the centre row of the CFD model (Fig. 5-14) as the monitored variables.

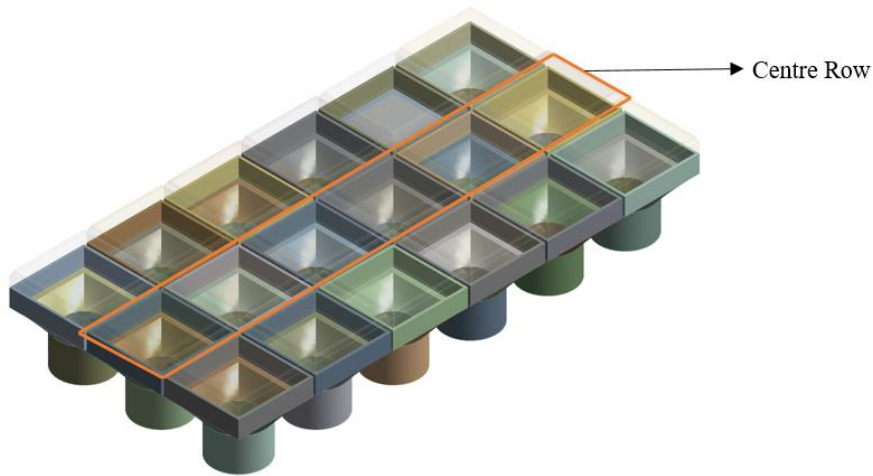


Figure 5-14: Centre row of the SolAir model

The stark difference between the HiTRec validation model and the SolAir model is the geometry of the absorber and the corresponding changes in the geometry of the other cell zones in the model, as shown in the previous section. The methodology of meshing the model i.e. the sequence used for selective meshing, setting of the boundary conditions, turbulence model, discretization schemes and solution controls used for the model are identical to those used for the validation study. A general cross-section view of a an example model mesh and a magnified cross-sectional view of the corresponding absorber module mesh are illustrated in Fig. 5-15 and Fig. 5-16 respectively.

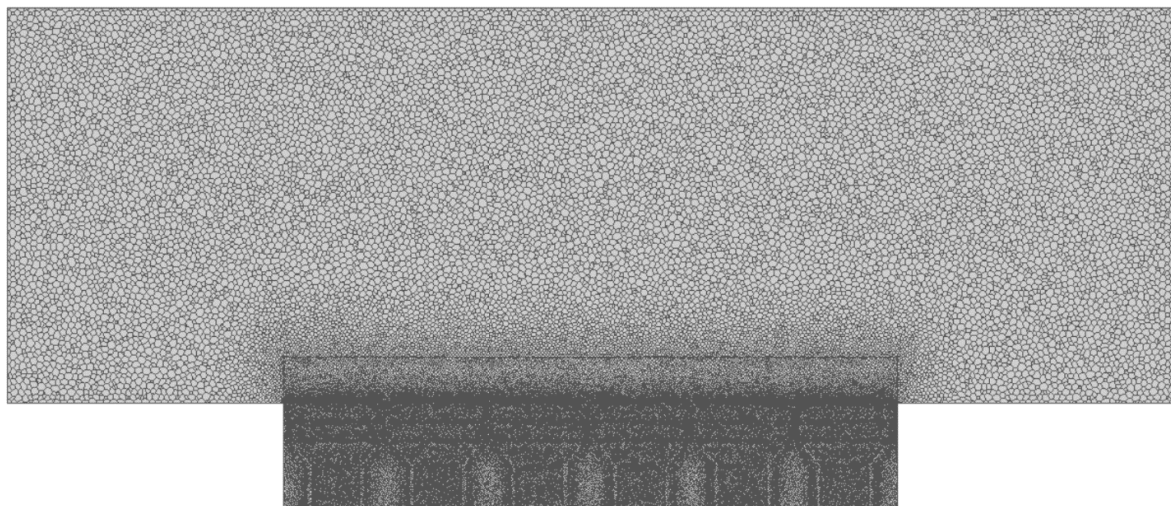


Figure 5-15: General cross-sectional view of an example model mesh

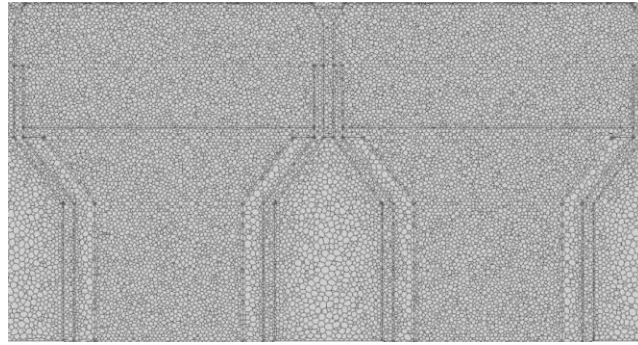


Figure 5-16: Magnified cross-sectional view of an example absorber module mesh

Similar to the sizing criteria used in mesh generation of the HiTRec-II receiver for the hot flow validation study, the cell size of the hot air zone and the porous absorber zone was used as the reference value, x , with the cell size in the recirculation zone being set as $2x$ and the cell size in the atmosphere zone being set as $5x$. A gradual growth rate of 1.05 was set and the domain was meshed completely with tetrahedral cells in the Ansys Meshing Module, which was then converted to polyhedral cells after importing the meshed model into Fluent 19.2.

Wind at 5 m/s that is incident on the absorber modules at an angle of 45° , was chosen as the operating condition for the study. Predicted outlet air temperatures of the six monitored modules with respect to cell size are indicated in Table 5-3.

Table 5-3: Grid convergence study conducted on the SolAir receiver model

Cell Size	Module 1 [K]	Module 2 [K]	Module 3 [K]	Module 4 [K]	Module 5 [K]	Module 6 [K]
6 mm	948.72	1016.2	1058.5	1095.7	1131.1	1114.6
4 mm	952.03	1020.8	1069.4	1112.9	1146.2	1121.3
3 mm	948.67	1019.2	1066.8	1114.5	1153.3	1116
2 mm	944.26	1014.7	1063.1	1111.8	1165.6	1124.3
1.5 mm	942.75	1012.4	1059.8	1107	1165.3	1129.5

The data provided in Table 5-3 is graphically illustrated in Fig. 5-17 and the percentage difference between the temperature values of consecutively finer grids for all cups is given in Table 5-4.

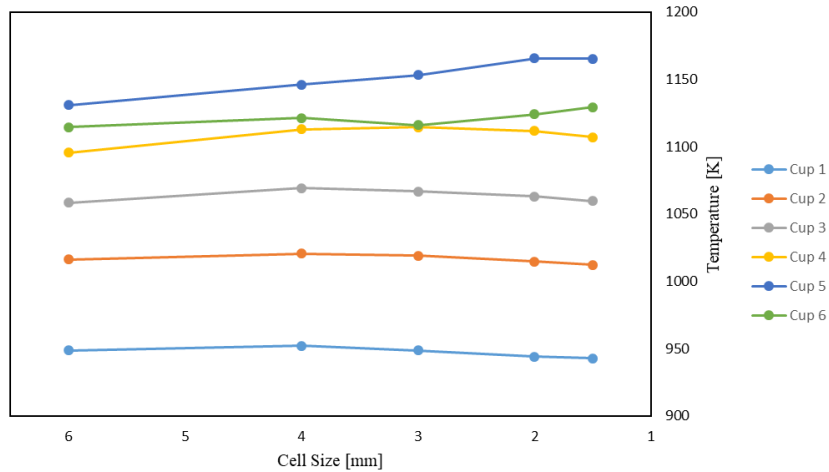


Figure 5-17: Graphical illustration of the grid convergence study of the SolAir receiver model

Table 5-4: Percentage deviation in the module air outlet temperatures between the consecutive cell sizes

Cell Size	Module 1 [K]	Module 2 [K]	Module 3 [K]	Module 4 [K]	Module 5 [K]	Module 6 [K]	Mean Change
6 → 4	0.35 %	0.45 %	1.03 %	1.57 %	1.33 %	0.60 %	0.89 %
4 → 3	0.35 %	0.16 %	0.24 %	0.14 %	0.62 %	0.47 %	0.33 %
3 → 2	0.46 %	0.44 %	0.35 %	0.24 %	1.07 %	0.74 %	0.55 %
2 → 1.5	0.16 %	0.23 %	0.31 %	0.43 %	0.03 %	0.46 %	0.27 %

The change in the air outlet temperatures between the cell sizes analysed for the grid independence study is quite small across the board, as shown in Table 5-4. However, meshing the computational domain with cell sizes smaller than 1.5 mm would result in very high computational cost, and as such, a deviation of 0.27 % was considered negligible and a reasonable grid independence was considered to have been achieved at a cell size of 2 mm.

5.7. Results - Wind effects study on the SolAir receiver

The outlet air temperature of the modules that were predicted as functions of wind speed are graphically represented in Fig. 5-18 to Fig. 5-21, for incidence angles of 90°, 60°, 30° and 0° respectively.

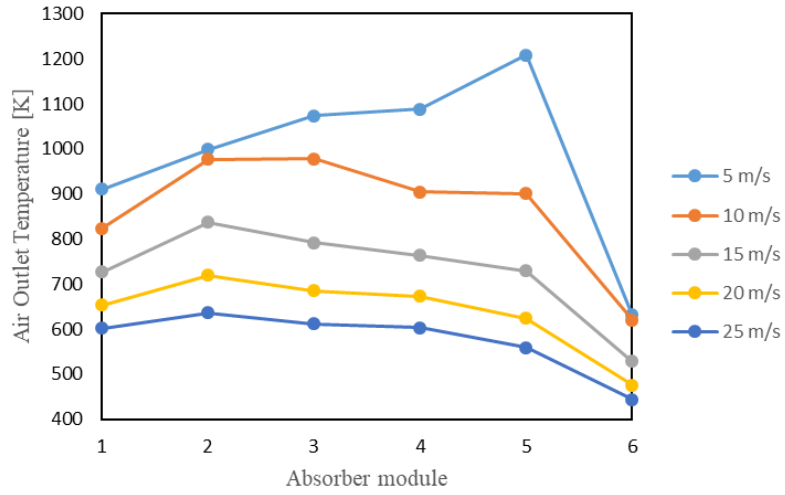


Figure 5-18: Outlet temperature of the absorber modules for various wind speeds at an incidence angle of 90°

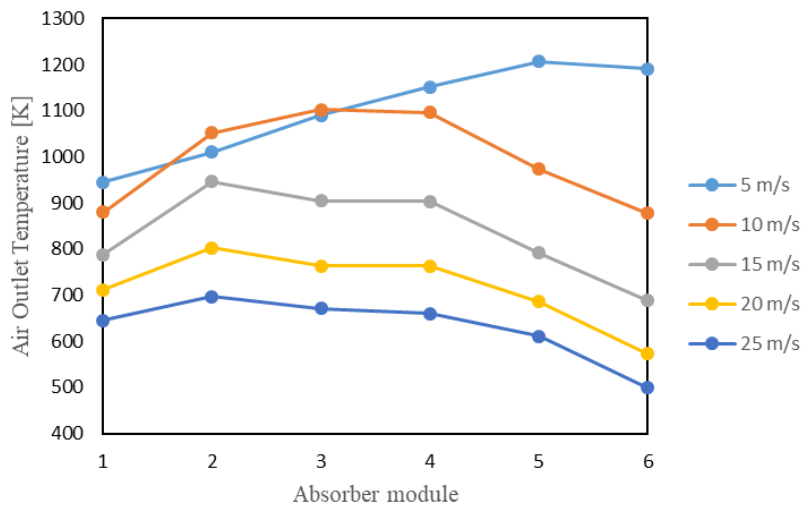


Figure 5-19: Outlet temperature of the absorber modules for various wind speeds at an incidence angle of 60°

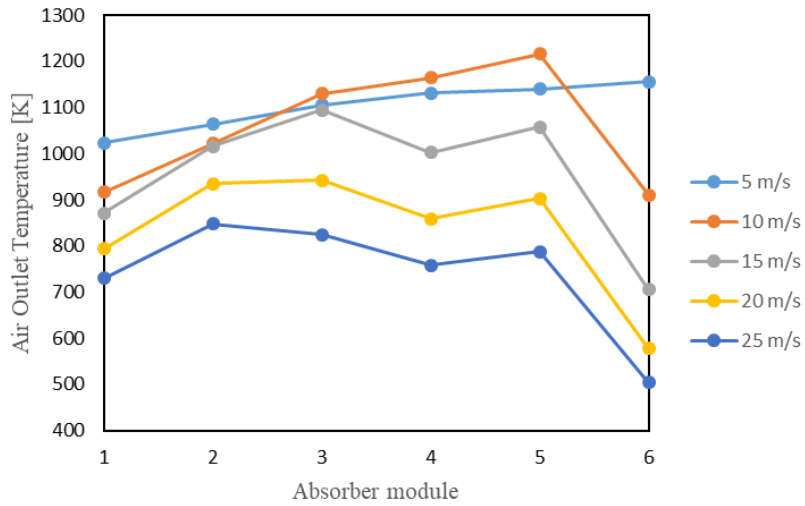


Figure 5-20: Outlet temperature of the absorber modules for various wind speeds at an incidence angle of 30°

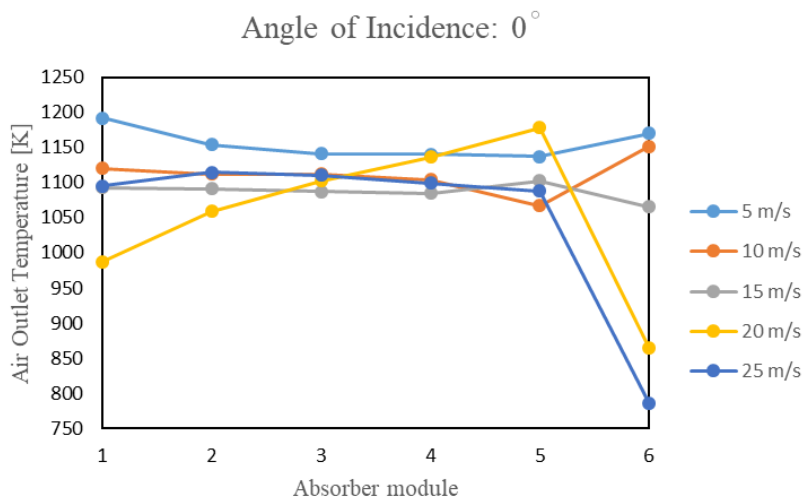


Figure 5-21: Outlet temperature of the absorber modules for various wind speeds at an incidence angle of 0°

In broader terms, the relationship between the average value of outlet air temperatures and angle of incidence, for each of the wind speeds analysed, is graphically illustrated in Fig. 5-22.

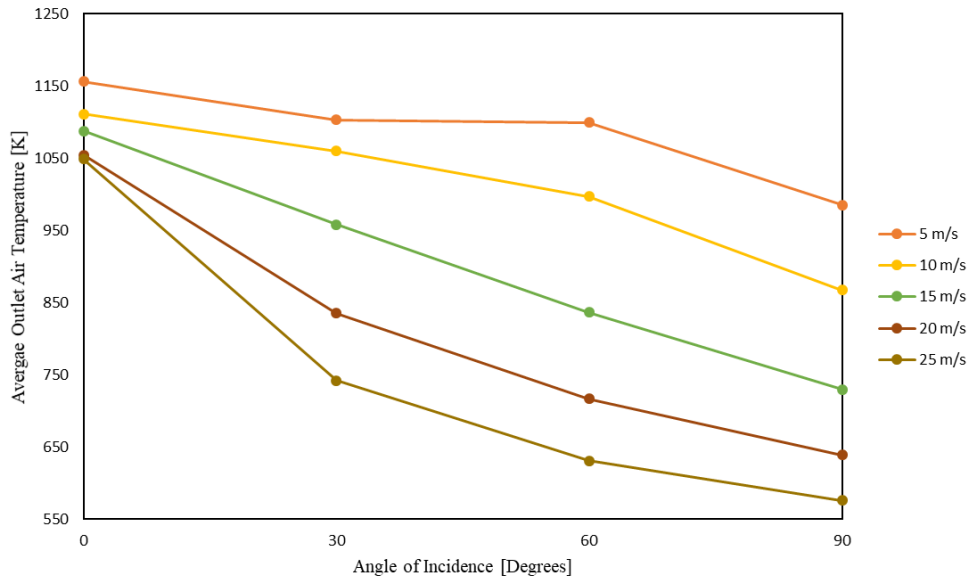


Figure 5-22: Outlet air temperature of the SolAir receiver in the wind analysis

The mean air outlet temperature values of the SolAir-200 absorber modules simulated under all of the wind loading conditions are provided in Appendix C.

In order to obtain insight into the nature of the flow in the CFD domain, especially in and around the absorber modules, the temperature contour plot and the velocity vector plot of the SolAir receivers at the wind speed of 15 m/s has been illustrated in this section. The temperature contour plot of the SolAir absorber modules under the influence of wind at a magnitude of 15 m/s at various angles of incidences are illustrated in Fig. 5-23, Fig. 5-24, Fig. 5-25 and Fig. 5-26.

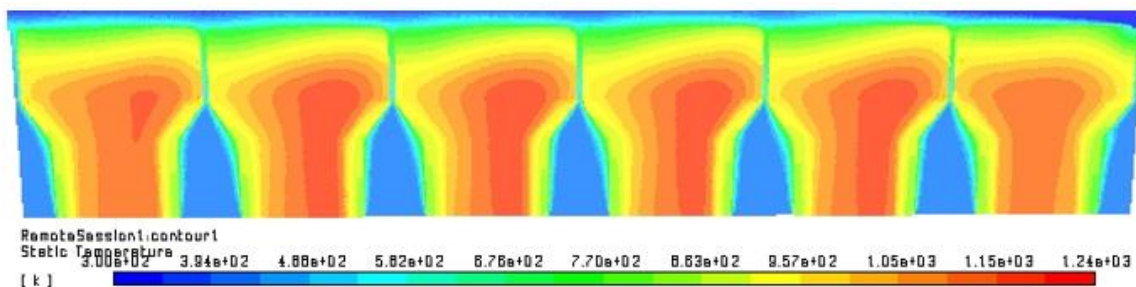


Figure 5-23: Flow domain temperature contour plot for a wind speed of 15 m/s flowing at an incidence angle of 0°

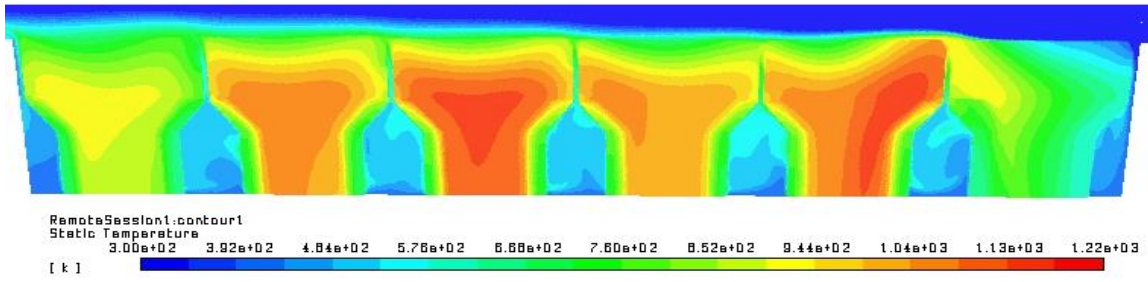


Figure 5-24: Flow domain temperature contour plot for a wind speed of 15 m/s flowing at an incidence angle of 30°

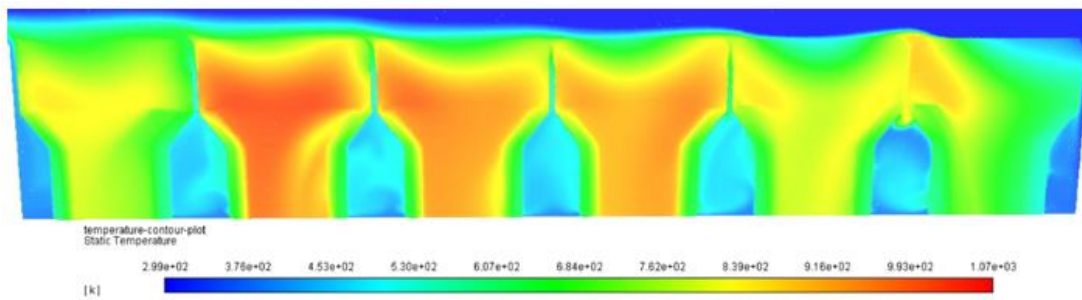


Figure 5-25: Flow domain temperature contour plot for a wind speed of 15 m/s flowing at an incidence angle of 60°

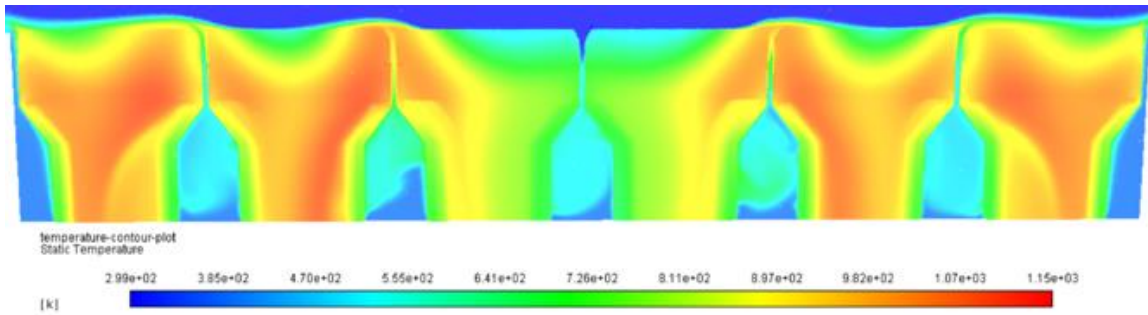


Figure 5-26: Flow domain temperature contour plot for a wind speed of 15 m/s flowing at an incidence angle of 90°

Flow domain velocity vector plots of the solution for a wind speed of 15 m/s are presented in Fig. 5-27, Fig. 5-28, Fig. 5-29 and Fig. 5-30, for incidence angles of 0°, 30°, 60° and 90° respectively.

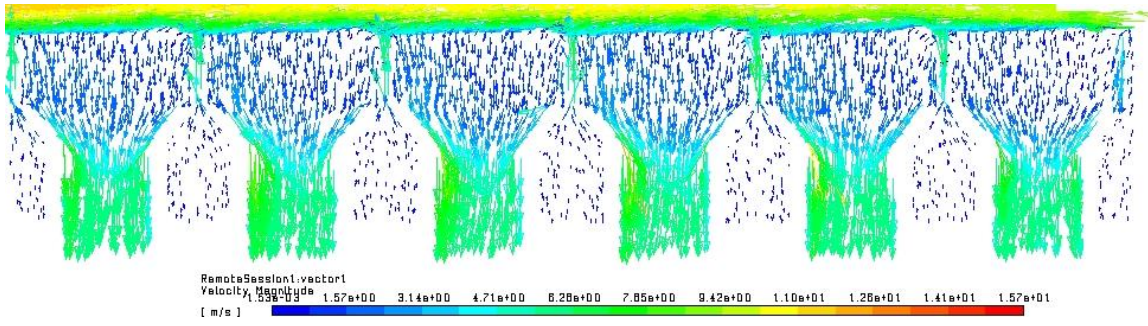


Figure 5-27: Flow domain velocity vector plot for a wind speed of 15 m/s flowing at an angle of 0°

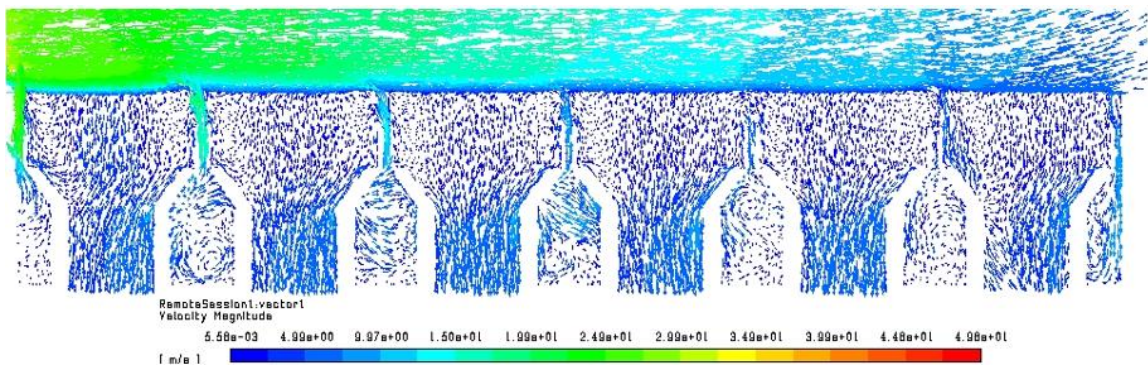


Figure 5-28: Flow domain velocity vector plot for a wind speed of 15 m/s flowing at an angle of 30°

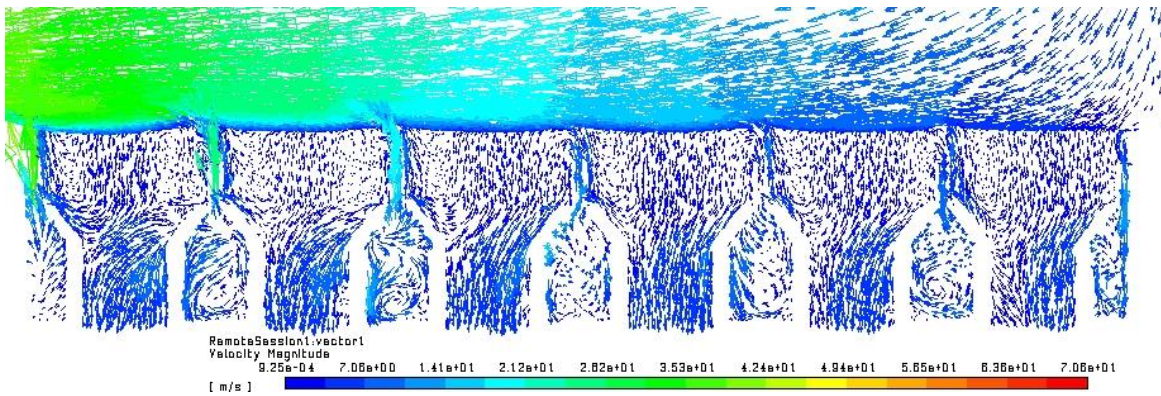


Figure 5-29: Flow domain velocity vector plot for a wind speed of 15 m/s flowing at an angle of 60°

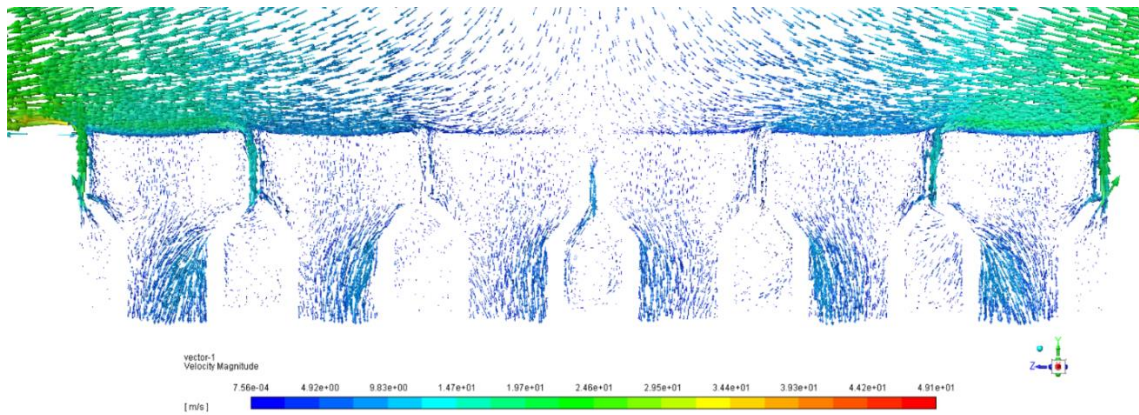


Figure 5-30: Flow domain velocity vector plot for a wind speed of 15 m/s flowing at an angle of 90°

5.8. Discussion

The established modelling methodology used for simulating the flow of air through the HiTRec-II absorber modules in Chapter 4 was used for wind effects study of the standard SolAir modules.

The behaviour of air as it flows through the modules at the wind incidence angle of 0° (Fig. 5-27) is ideally the type of flow that is favoured for OVR applications. A similar flow behaviour is observed for the wind incidence angle of 30°, but reverse flow of air out of some of the absorber modules and recirculation of air in the warm air zone was observed for the wind incidence angle of 60°. The velocity of the air flowing over the absorber surface of all the modules is higher at higher incidence angles. As a consequence, it leads to a higher heat transfer coefficient between the absorbers and the surrounding environment, which in-turn leads to higher heat loss from the absorbers. At higher wind speed, a higher proportion of the warm air returned to the receiver is also blown away before it is re-entrained back into the modules, reducing the ARR of the receiver. When the wind flows parallel to the absorber surface, the difference between the air outlet temperatures of the modules is the least for wind speeds of 5 m/s, 10 m/s and 15 m/s. Figure 5-23 also illustrates an almost identical air temperature distribution in all absorber modules when the wind flow is parallel, which is ideal. At steeper incidence angles of 30° and 60°, a variation in the air temperature distribution across the absorbers occurs, with the centre absorber modules producing higher air outlet temperatures whereas wind incidence angles of 90° resulted in lower air temperatures being generated in the centre as compared to the outer absorber modules.

The results extracted from the simulation was presented in two different forms. The first involved monitoring the individual mean air outlet temperatures values at each of the six absorber modules, for all of the operating conditions (Fig. 5-18 to Fig. 5-21). The second form involved plotting the mean air outlet temperatures of the monitored absorber modules against the wind incidence angles for all the

wind speeds analysed in the study (Fig. 5-22). A careful observation of these results provides the following insights on the optimal operating conditions for the SolAir modules:

1. Figure 5-18, Fig. 5-19 and Fig. 5-20 indicate that when the wind enters the atmospheric zone at angles 90° , 60° , 30° , and the relative air outlet temperature trend across the six monitored absorbers remained the same i.e. the graph has a similar shape (although they differed in magnitude) for the two wind speeds that were monitored in the study.
2. As per Fig. 5-22, the outlet air temperature of the modules is inversely proportional to the magnitude of the wind. This in turn clearly implies that the associated ARR degrades as wind speed increases. Hence, a low wind speed conditions allows for greater levels of warm return air re-entrainment, higher outlet air temperatures, and thus a higher overall receiver efficiency.
3. The air outlet temperature of the modules is inversely proportional to the angle of incidence of the wind at all of the wind magnitudes taken into consideration. Hence, a flow of wind parallel to the surface of the absorber is favourable for higher values of ARR and overall receiver efficiency.

The data extracted from the wind effects study shows the importance of preventing the wind from directly impinging on the absorber module array, and artificially reducing the speed of the air flowing over the absorbers to prevent excess heat loss. These favourable characteristics suggest the importance of using vertical inter-module baffles to help with the improvement of the ARR.

5.9. Conclusion

The chapter described a comprehensive wind effects study on the standard SolAir absorber modules, for different wind speeds and wind directions. The modelling methodology established in Chapter 4 for the HiTRec-II validation study was adopted for the CFD modelling of the SolAir-200 receiver. Certain assumptions including constant volumetric heating and perfect re-entrainment of the warm air returned to the receiver were also made to simplify the CFD model.

Although the main goal of the wind effects study was to gain insight into the changes in the Air Return Ratio (ARR) of the absorber modules with varying wind loads, use of the LTE condition prevented the direct evaluation of ARR. Therefore, an alternative measurement parameter, absorber module outlet air temperature, was used to indirectly evaluate the impact of changing wind conditions on ARR. The air

outlet temperature data was collected for the absorber modules under the various wind conditions and their relationship to wind speed and angle of incidence was established and discussed.

In the next chapter, the data collected from the wind effects study will be used as a baseline to check for any improvement in the ARR with the implementation of the vertical air flow baffles between the adjacent SolAir modules.

6. WIND EFFECTS STUDY ON BAFFLED SOLAIR-200 RECEIVER DESIGN

The importance of preventing the direct impact of lateral wind on OVR modules to improve the ARR (Marcos et al., 2004), obtaining uniform distribution of outlet air temperature, and preventing steep temperature gradients on the absorber (Palero et al., 2008) motivated the current study; to investigate the effect of placing vertical baffles between the SolAir modules on air return ratio. New CFD models of the SolAir receiver were developed with baffles of varying length placed in between the adjacent modules.

Using baffles will inevitably introduce complications to the overall design and working conditions of the receiver. For instance, it is possible that a fair amount of incident solar radiation will be obstructed by the baffles. Depending on the angle of incidence of the solar radiation, a shadow may be cast on part or all of the absorber surface, as shown in Fig. 6-1. In addition, changes to the structural arrangement of the SolAir receiver would also be necessary to assemble the baffles between the absorber modules, and further research into the ideal material for manufacturing the baffles would also have to be conducted.

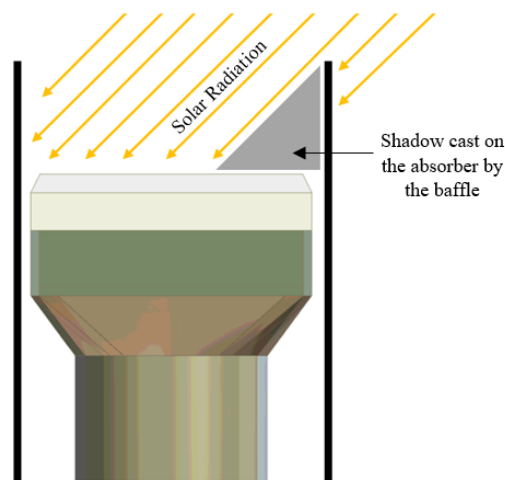


Figure 6-1: Potential obstruction of solar radiation caused by baffle

A wind study on the SolAir model with baffles (of varying lengths) was carried out to gain insight into the behaviour of the air flow in the vicinity of the baffles, and its effect on the mean outlet air temperature, at different wind speeds and incidence angles. The participation of the baffles in the conjugate heat transfer process that occurs to and from surrounding environment is not accounted for in the study i.e. the baffles are assumed to be adiabatic in nature.

Unlike the wind effects study carried out on the standard SolAir model which dealt with four different wind speeds, the study conducted on the baffled SolAir model only considered wind speeds of 15 m/s and 25 m/s at orientations of 0°, 30°, 60° and 90° to the vertical axis, in order to minimize the computational cost of running the simulations at the CHPC. The term ‘baffle length’ which is commonly referred to in the chapter represents the perpendicular distance between the absorber surface and the top end of the baffle. Three baffle lengths were considered in the wind effects study viz. 70 mm, 50 mm and 30 mm, each with a thickness of 2 mm.

6.1. Simulation methodology of the wind effects study

The computational domain of the baffled SolAir model was identical to the SolAir model used in Chapter 5 (referred to as the standard SolAir model) with the additional feature of having vertical baffles placed in between the absorber modules. An example of such a computational domain is shown in Fig. 6-2.

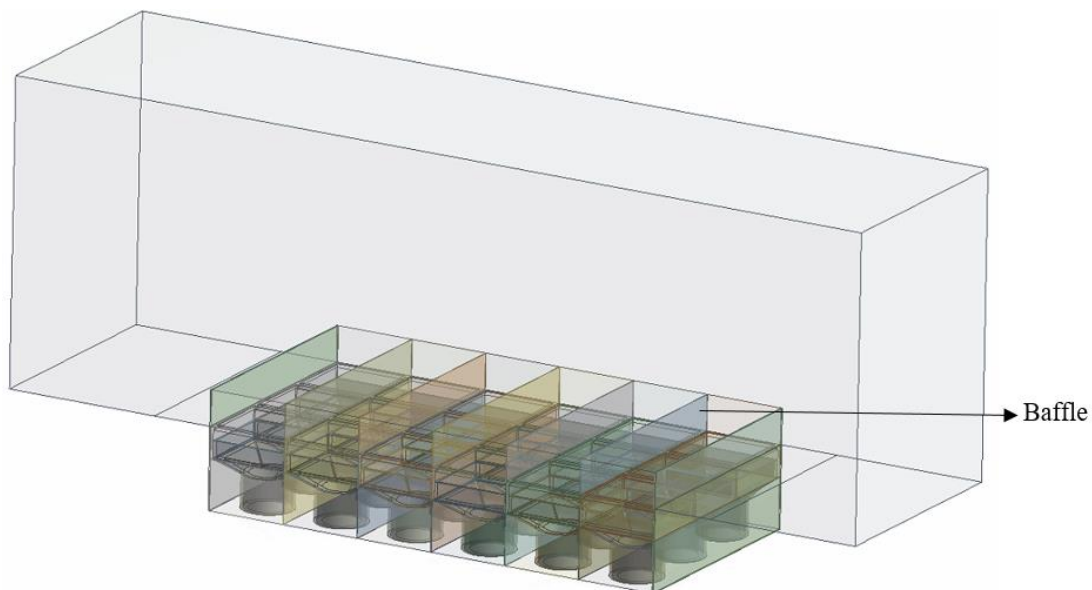


Figure 6-2: Baffled SolAir receiver model computational domain

The meshing methodology, boundary conditions, heat source and other Fluent settings such as convergence criteria and pressure –velocity coupling method that were used for the baffled SolAir model are identical to that of the standard SolAir model, provided in Table 5-2.

Initial simulations on the baffled SolAir model resulted in the divergence of the residuals of turbulent kinetic energy, k , and the rate of turbulence dissipation, ω . One possible reason for the divergence is

the failure in predicting a suitable velocity and pressure field by the solver which would allow for stable convection-diffusion modelling of the k and ω terms, due to the default initial values set for flow variables such as temperature, pressure, velocity, k and ω . In order to simplify the calculation of the initial velocity and pressure field, the turbulence model was specified to be laminar and the thermo-physical properties of the air were specified as constant values at 300 K, instead of using the temperature dependent equations, at the beginning of the simulation.

The simulation was staged over multiple steps, where a necessary physics model, material property, turbulence model was activated at the start of a new step after which the simulation was run for around 200 iterations before initiating the next step. This step-by-step convergence method was used to gradually include the necessary setting (such as turbulence mode, boundary condition, and user-defined function) in the simulation. It also ensured that stable initial values of the various flow variables such as temperature, pressure, velocity, k and ω were obtained before introducing a new simulation setting (such as different solver or a new turbulence model) in the new step. The general simulation workflow used for the wind effects study of the baffled SolAir model is provided in the flow chart in Fig. 6-3.

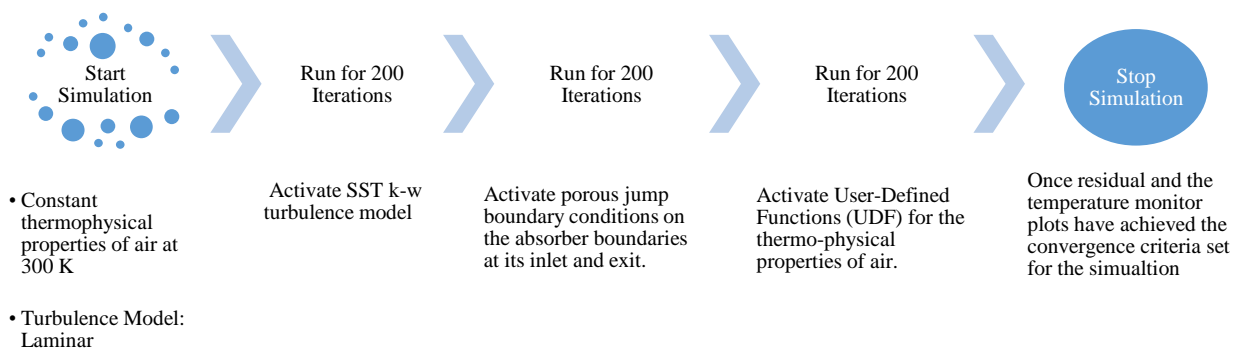


Figure 6-3: Baffled SolAir simulation workflow

6.2. Results - Wind effects study on the baffled SolAir receiver models

This section presents the results obtained from the wind effects study carried out on the baffled SolAir models, where the outlet air temperatures of the centre row of the baffled SolAir model are extracted from the simulation for each case of wind speed and wind incidence angle. For all of the vector plots illustrated in the section, where the direction of the vectors is not perfectly visible, the following labels are used, unless otherwise stated:

- i. Red Circle: Indicates a region where the air flows in a circular motion
- ii. Black Circle: Indicates a region where the air flows out of the absorber module

6.2.1. Baffle length: 70 mm

A 3-D model of the SolAir modules with baffle length of 70 mm is shown in Fig. 6-4. Figure 6-5 illustrates a cross-sectional view of the centre row of the associated meshed model.

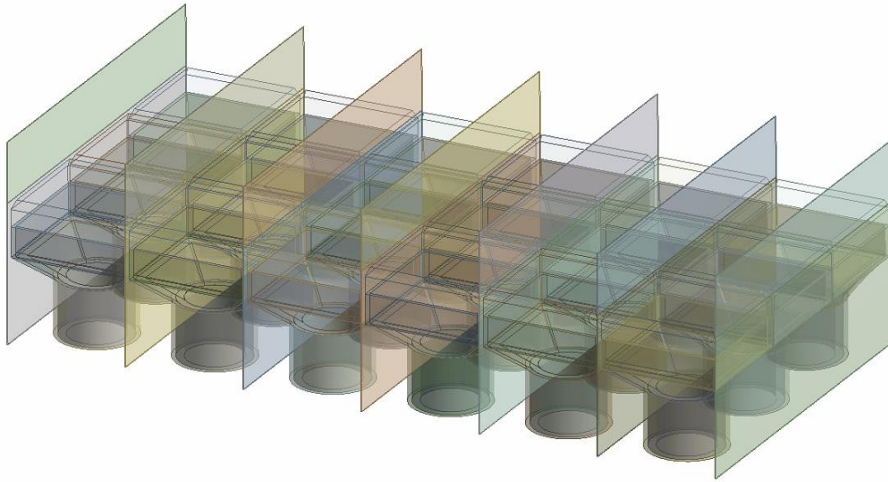


Figure 6-4: 3-D model of the baffled SolAir model with baffle length of 70 mm

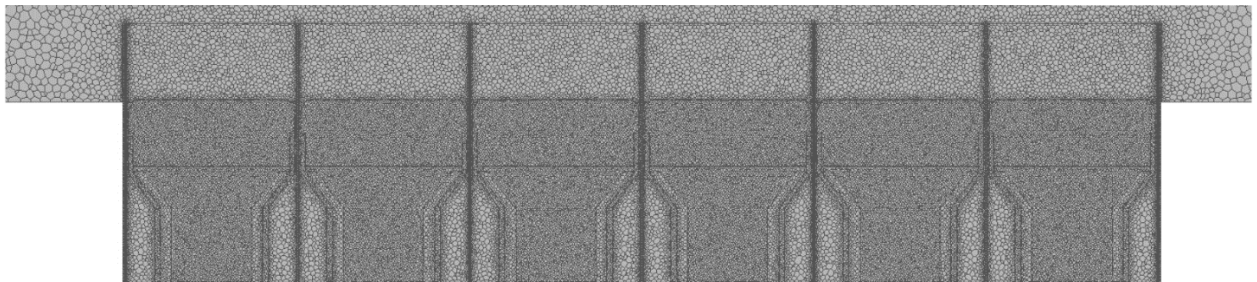


Figure 6-5: Cross-sectional view of the meshed model of the SolAir receiver with 70 mm vertical baffles

The changes in the air outlet temperature of the modules for wind speeds of 15 m/s and 25 m/s at each wind incidence angle are shown in Fig. 6-6, Fig. 6-7, Fig. 6-8 and Fig. 6-9.

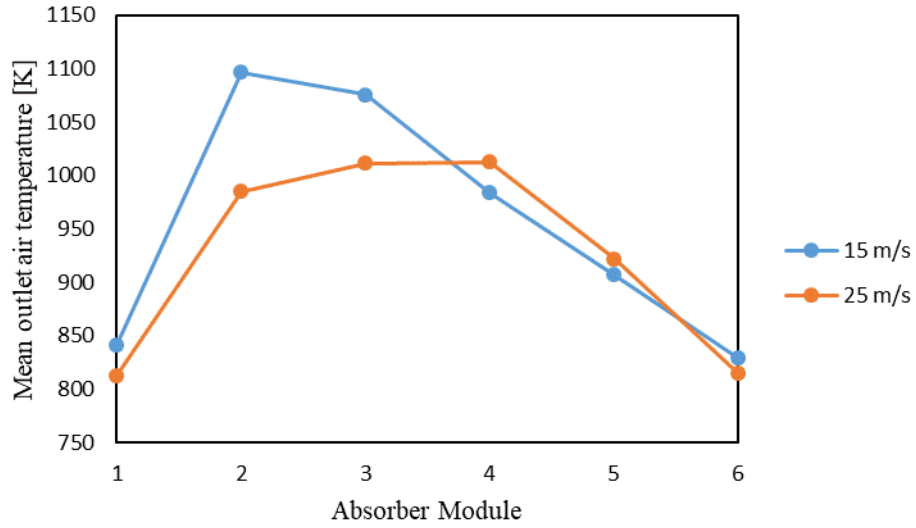


Figure 6-6: Outlet temperature of the absorber modules for wind direction perpendicular to the modules

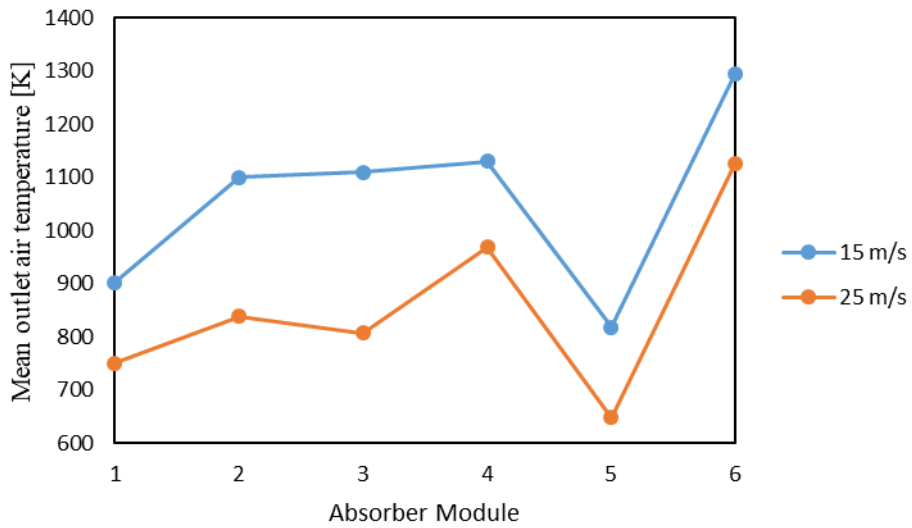


Figure 6-7: Outlet temperature of the absorber modules for wind direction 60° to the modules

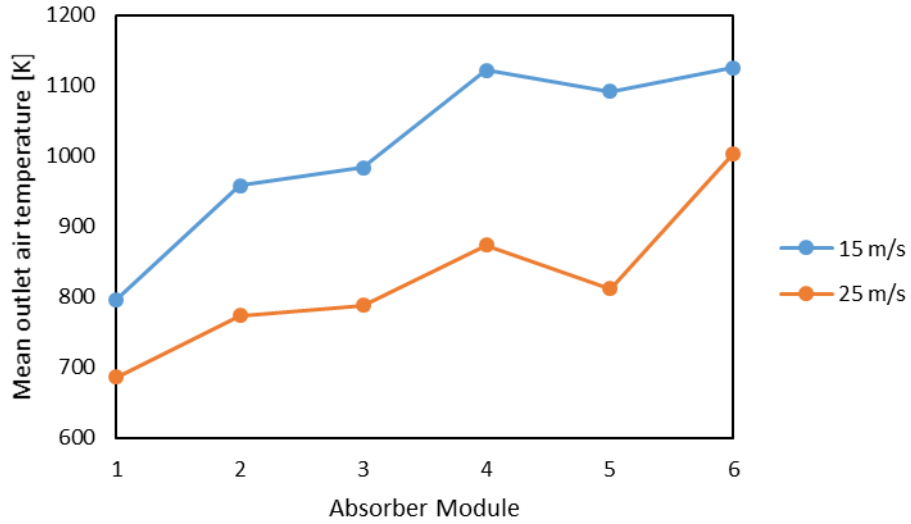


Figure 6-8: Outlet temperature of the absorber modules for wind direction 30° to the modules

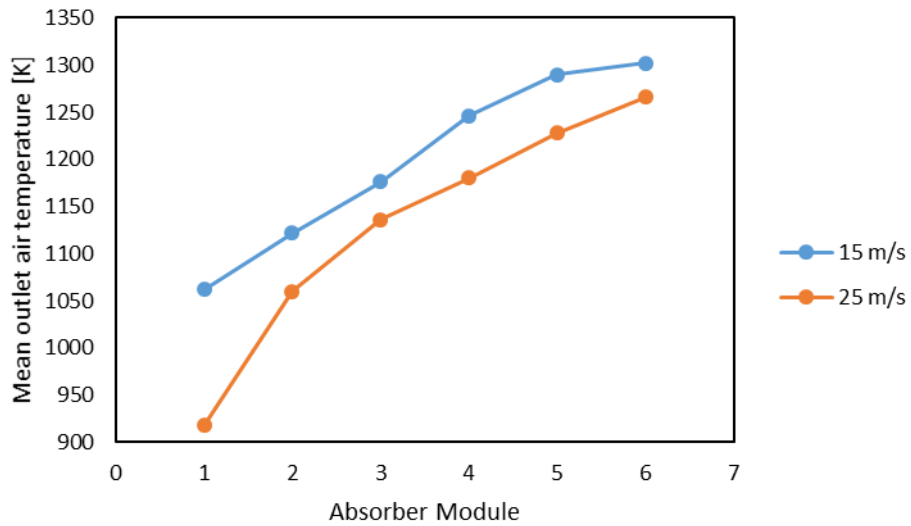


Figure 6-9: Outlet temperature of the absorber modules when wind flows parallel to the absorber surface

The temperature contour and the velocity vector plots of the SolAir receivers with 70 mm baffles, when a wind at 15 m/s flows parallel to the absorber surface are illustrated in Fig. 6-10 and Fig. 6-11.

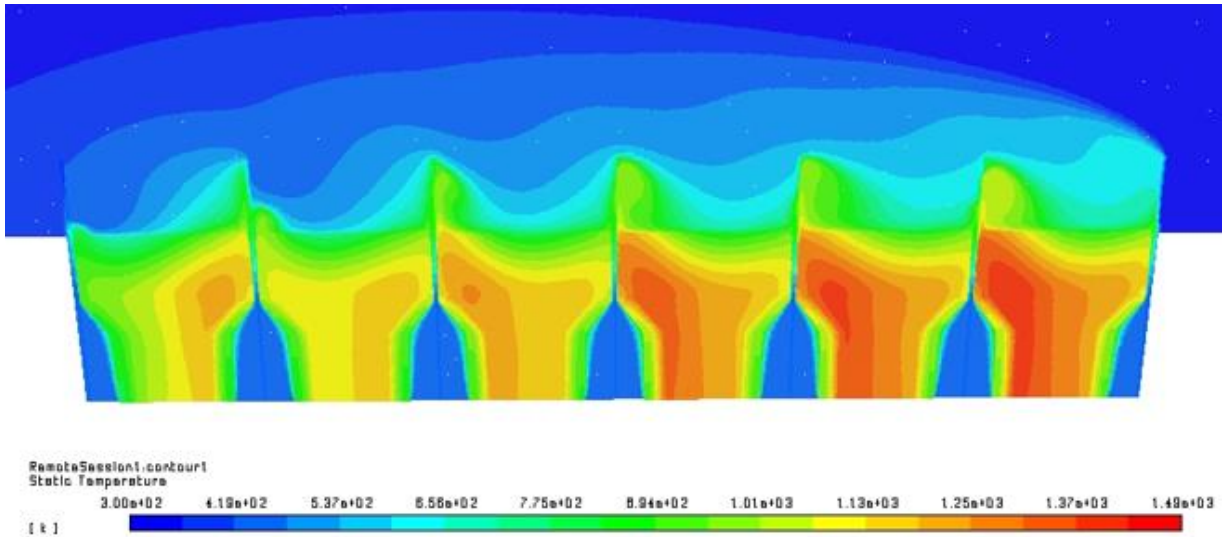


Figure 6-10: Temperature contour plot for wind speed at 15 m/s flowing parallel to the absorber surface, for the 70 mm baffled SolAir model

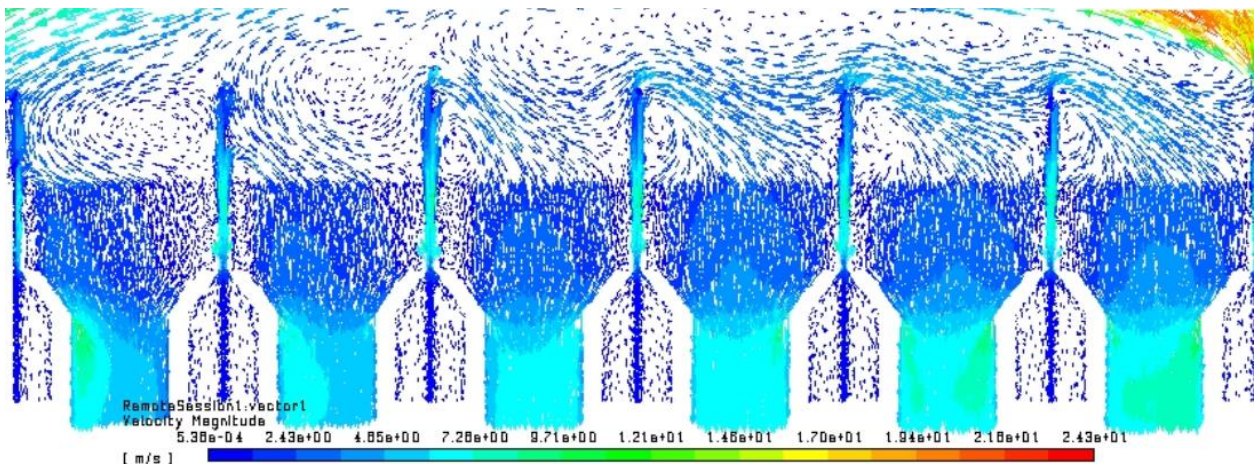


Figure 6-11: Velocity vector plot for wind at 15 m/s flowing parallel to absorber surface, for the 70 mm baffled SolAir model

The temperature contour and the velocity vector plots of the SolAir receivers with 70 mm baffles for a wind speed of 15 m/s incident at an angle of 30° is shown in Fig. 6-12 and Fig. 6-13.

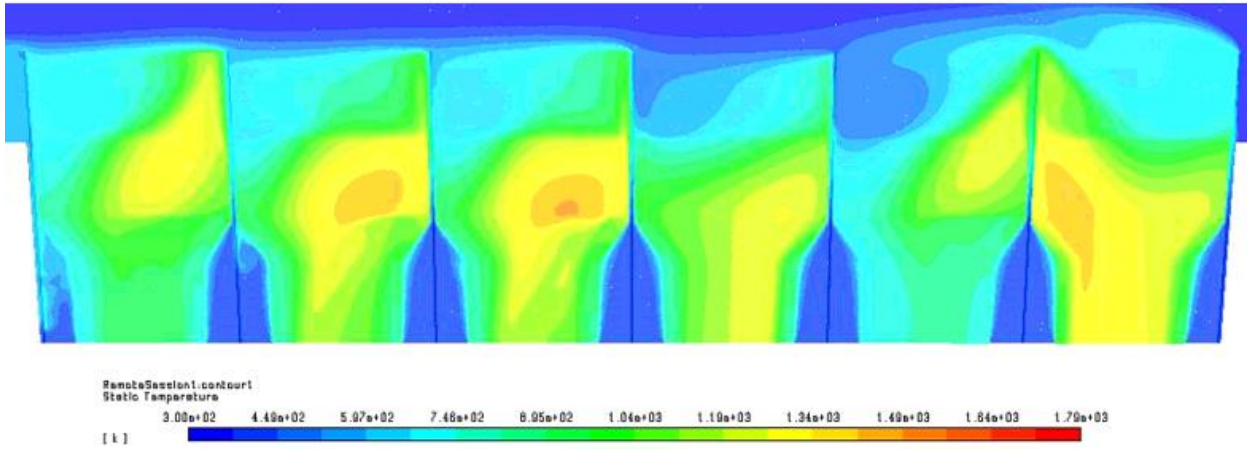


Figure 6-12: Temperature contour plot for wind speed at 15 m/s incident at angle of 30°, for of the 70 mm baffled SolAir model

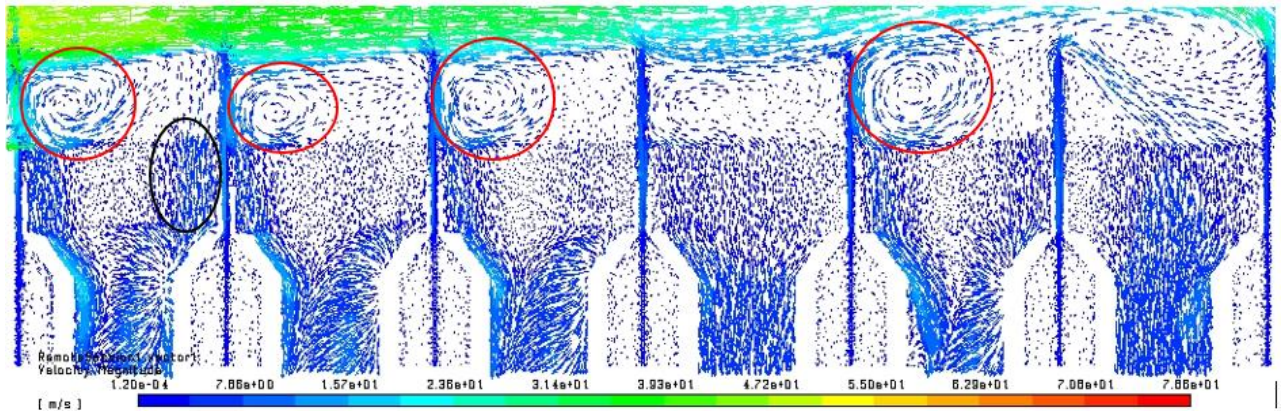


Figure 6-13: Velocity vector plot for 15 m/s incident at an angle of 30°, for the 70 mm baffled SolAir model

The temperature contour and the velocity vector plots of the SolAir receivers with 70 mm baffles for a wind speed of 15 m/s incident at an angle of 60° is shown in Fig. 6-14 and Fig. 6-15.

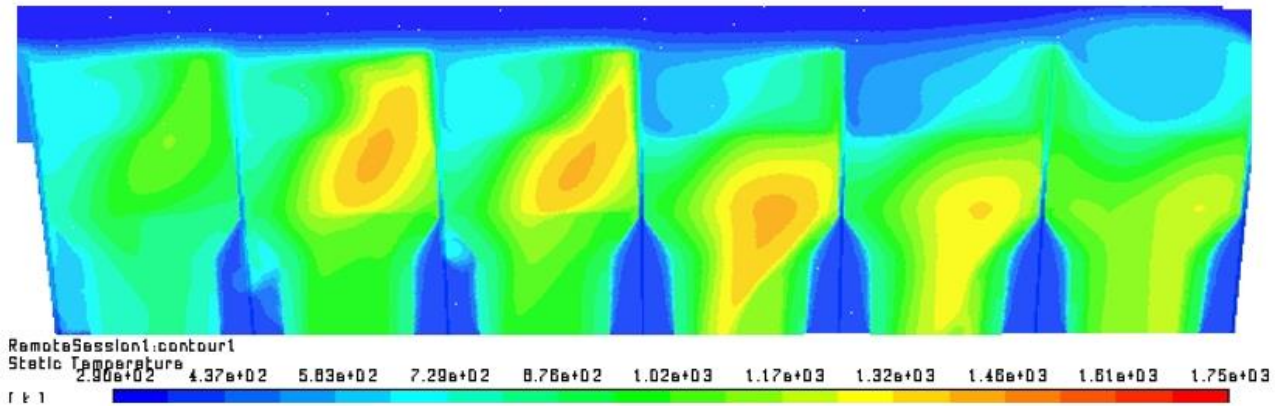


Figure 6-14: Temperature contour plot for wind speed at 15 m/s incident at angle of 60°, for of the 70 mm baffled SolAir model

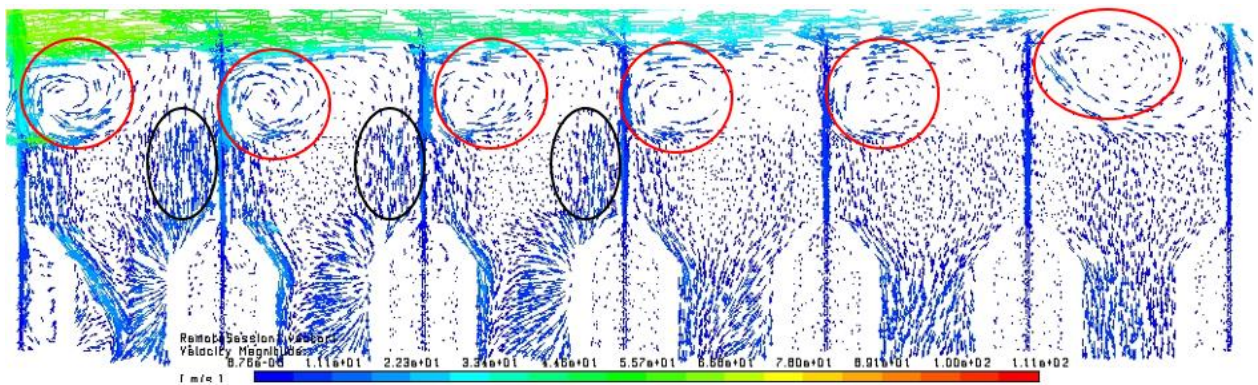


Figure 6-15: Velocity vector plot for 15 m/s incident at an angle of 60°, for the 70 mm baffled SolAir model

The temperature contour and the velocity vector plots of the SolAir receivers with 70 mm baffles for a wind speed of 15 m/s incident at an angle of 60° are shown in Fig. 6-16 and Fig. 6-17 respectively.

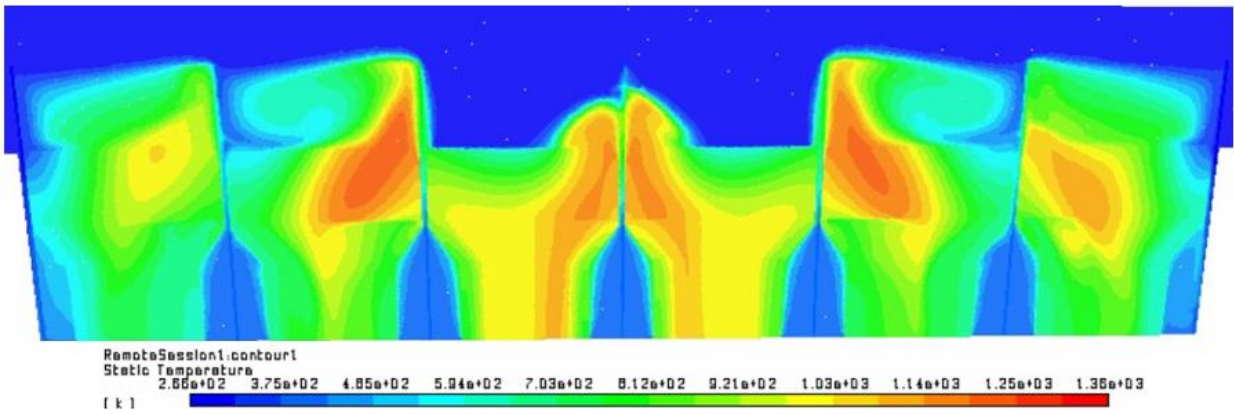


Figure 6-16: Temperature contour plot for wind speed at 15 m/s incident at angle of 90°, for the 70 mm baffled SolAir model

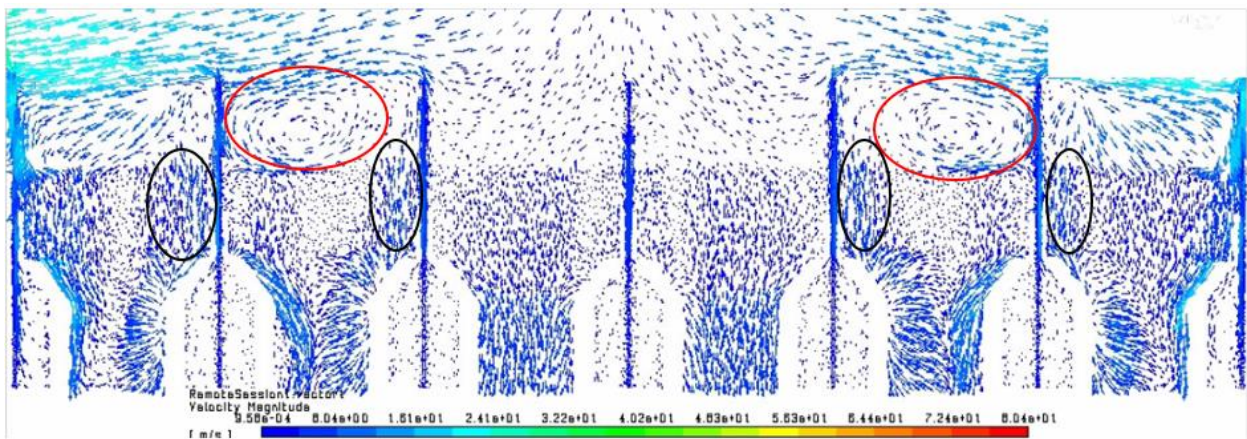


Figure 6-17: Velocity vector plot for 15 m/s incident at an angle of 90°, for the 70 mm baffled SolAir model

The relationship between the average outlet air temperature and wind angle of incidence for the 70 mm baffled SolAir model at wind speeds of 15 m/s and 25 m/s, at wind incidence angles of 0°, 30°, 60° and 90° are graphically illustrated in Fig. 6-18.

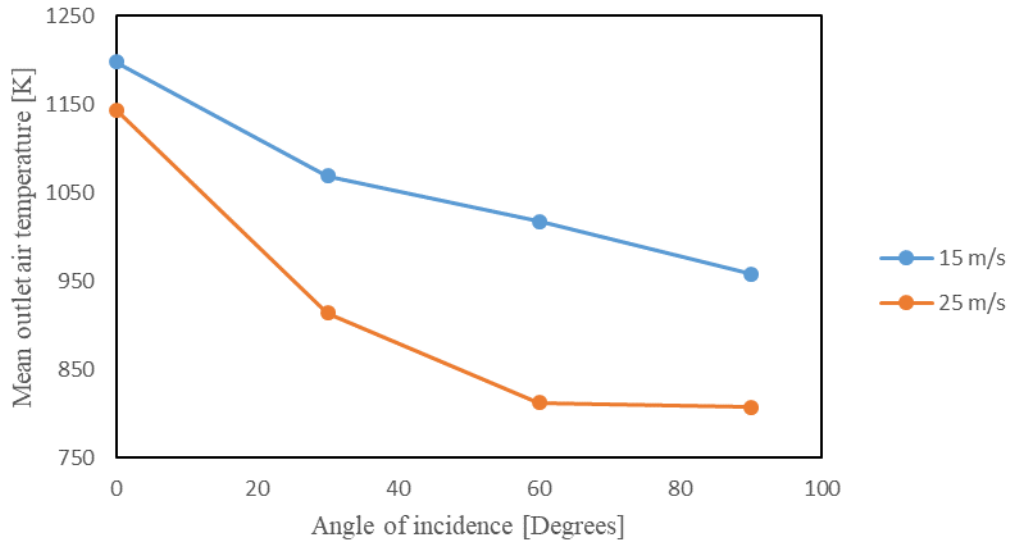


Figure 6-18: Outlet air temperature of the 70 mm Baffled SolAir receiver as a function of the angle of incidence for wind speeds of 15 m/s and 25 m/s

6.2.2. Baffle length: 50 mm

A 3-D model of the SolAir modules with baffles of length 50 mm is shown in Fig. 6-19. Figure 6-20 illustrates the cross-sectional view of the centre row of the associated meshed model.

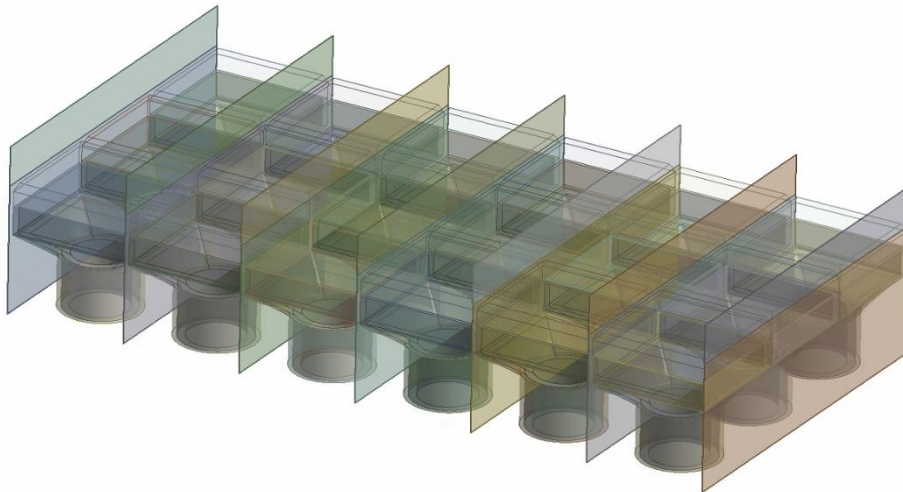


Figure 6-19: 3-D model of the SolAir model with a baffle length of 50 mm

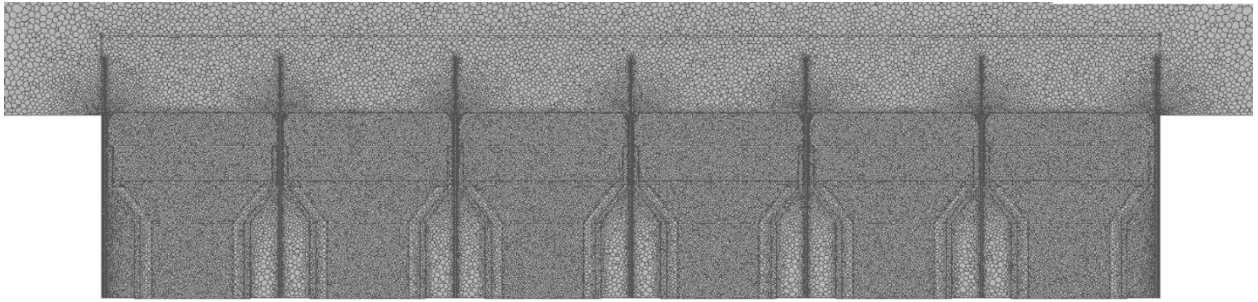


Figure 6-20: Meshed model of the SolAir receiver with 50 mm vertical baffles

The changes in the air outlet temperature of the modules for wind speeds of 15 m/s and 25 m/s at each angle of incidence for the 50 mm baffled SolAir model is shown in Fig. 6-21, Fig. 6-22, Fig. 6-23 and Fig. 6-24.

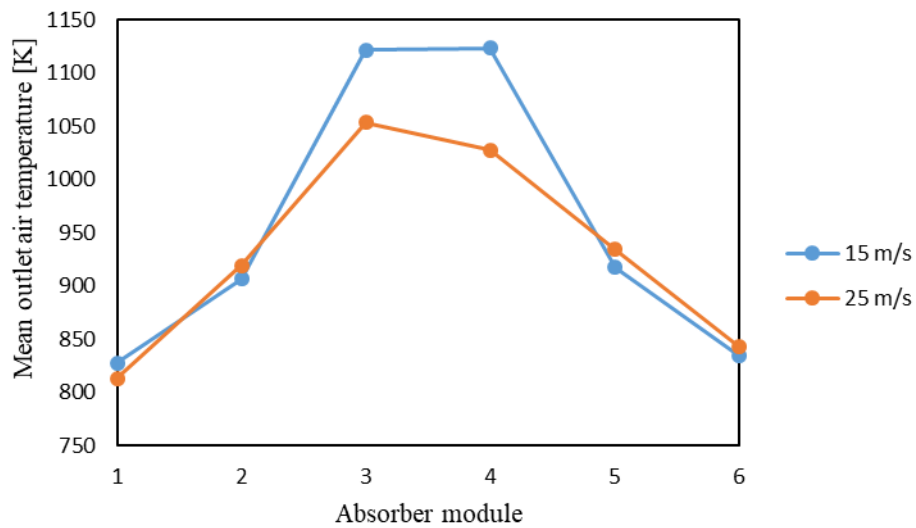


Figure 6-21: Outlet temperature of the absorber modules for wind direction perpendicular to the modules

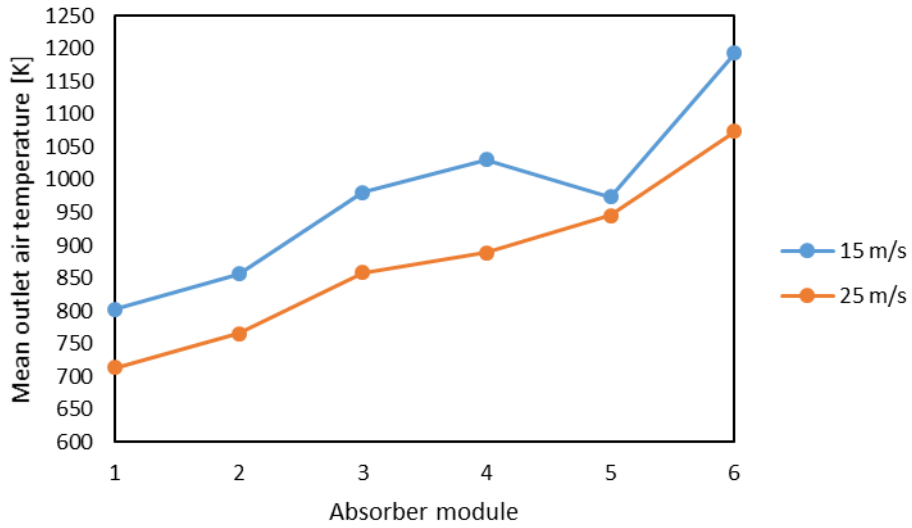


Figure 6-22: Outlet temperature of the absorber modules for wind direction 60° to the modules

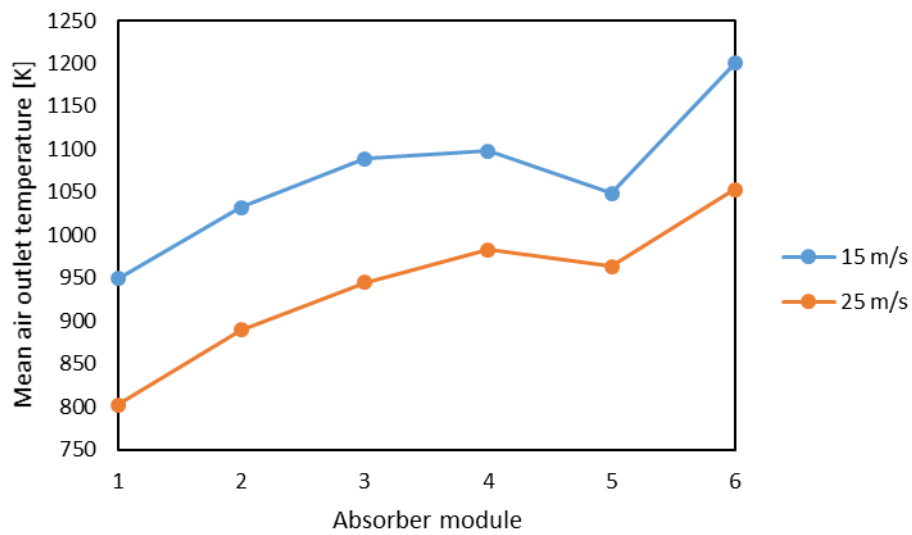


Figure 6-23: Outlet temperature of the absorber modules for wind direction 30° to the modules

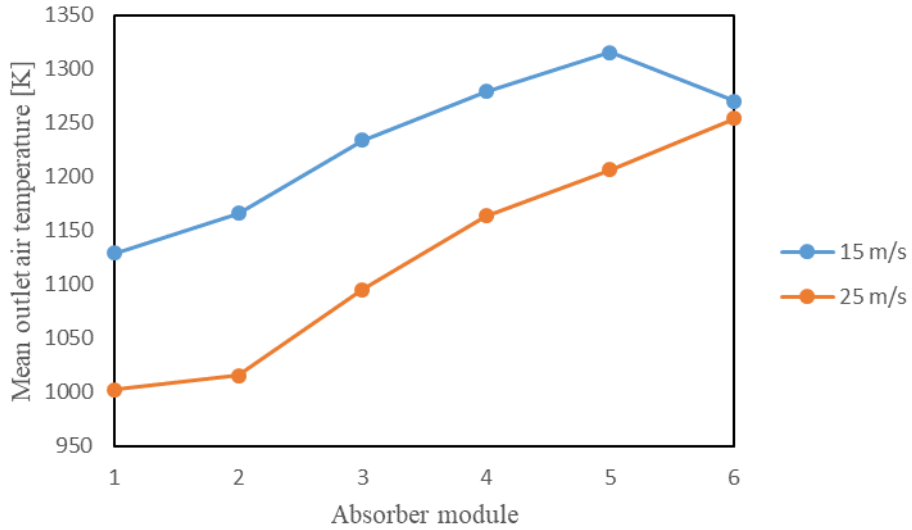


Figure 6-24: Outlet temperature of the absorber modules when wind flows parallel to the absorber surface

The temperature contour and the velocity vector plot of the SolAir module array with 50 mm baffles are shown in Fig. 6-25 and Fig. 6-26.

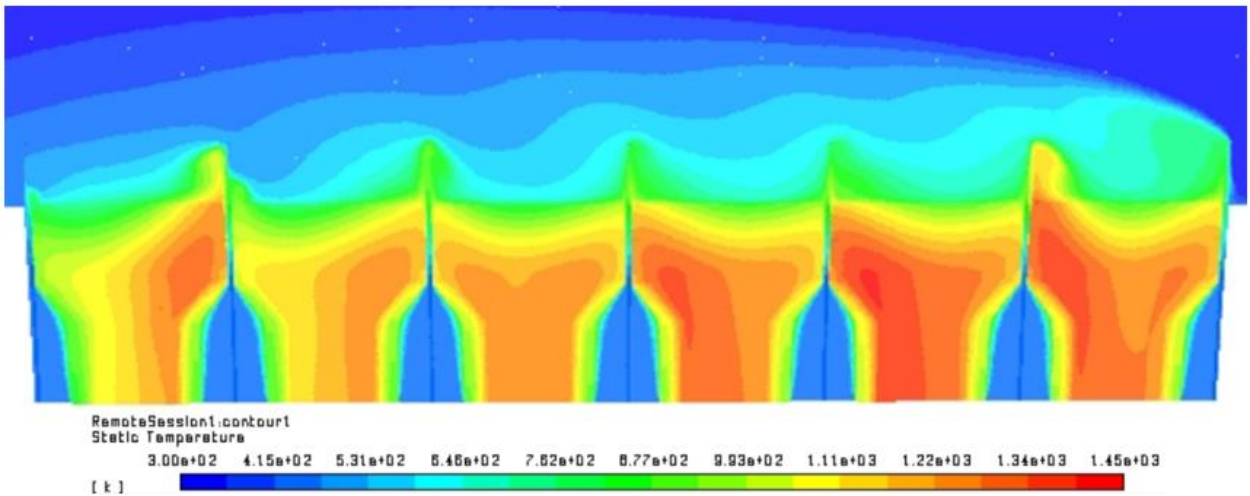


Figure 6-25: Temperature contour plot for wind speed at 15 m/s flowing parallel to the absorber surface, for the 50 mm baffled SolAir model

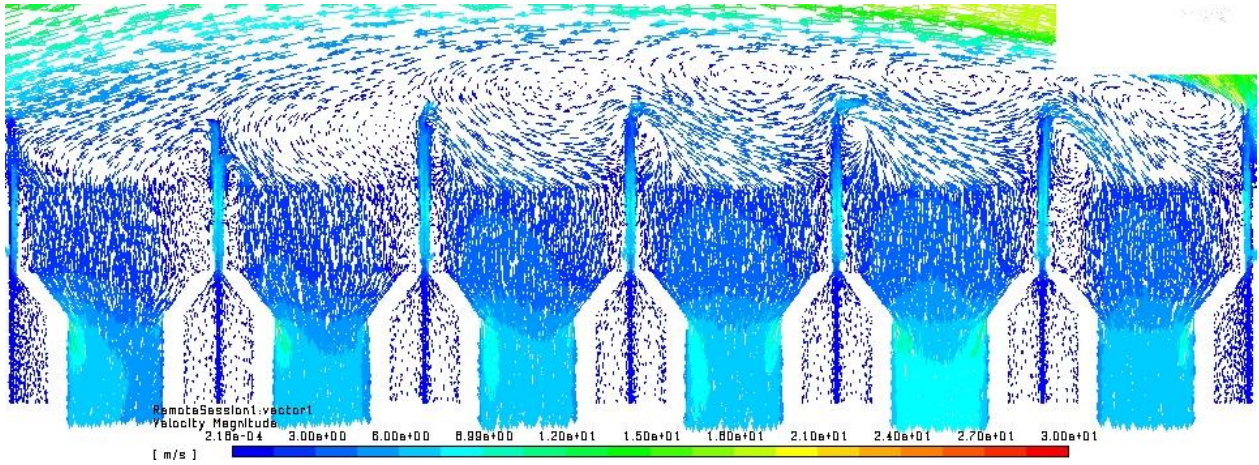


Figure 6-26: Velocity vector plot for a wind speed of 15 m/s for wind flowing parallel to the absorber surface, for the 50 mm baffled SolAir model

The temperature contour and the velocity vector plot of the SolAir module array with 50 mm baffles, for a wind speed of 15 m/s at an angle of 30° is shown in Fig. 6-27, Fig. 6-28 and Fig 6-29.

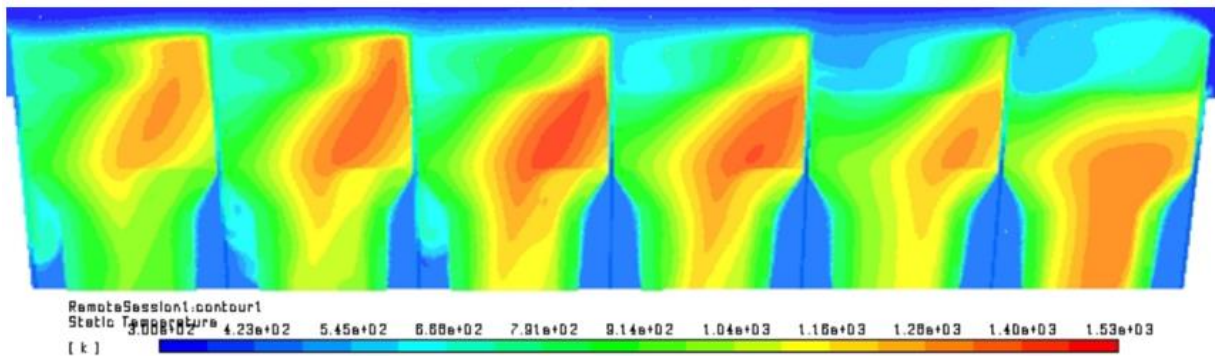


Figure 6-27: Temperature contour plot for wind speed at 15 m/s incident at angle of 30°, for the 50 mm baffled SolAir model

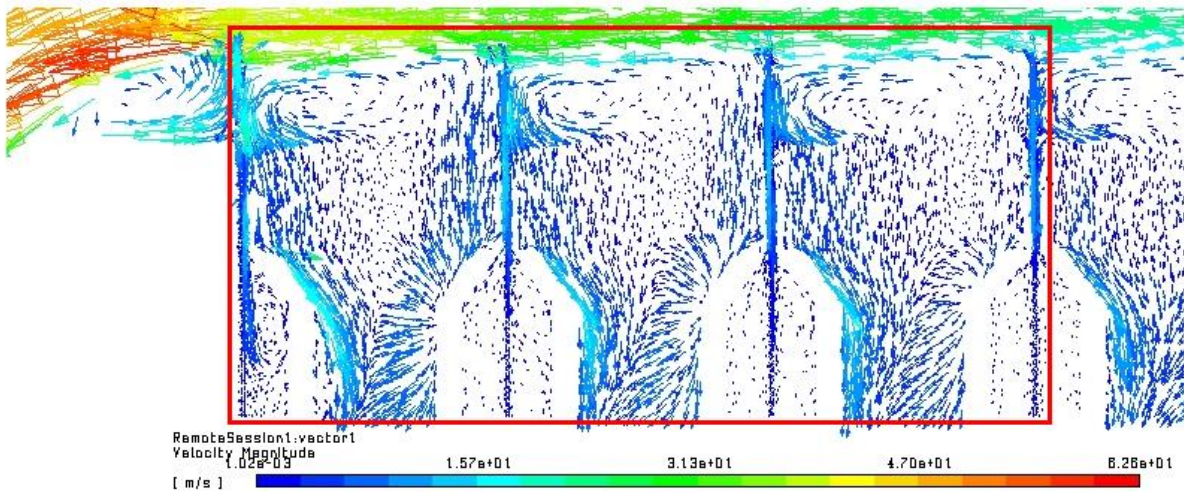


Figure 6-28: Velocity vector plot for a wind speed of 15 m/s at an angle of 30°, for the first three absorber modules from the left of the 50 mm baffled SolAir model

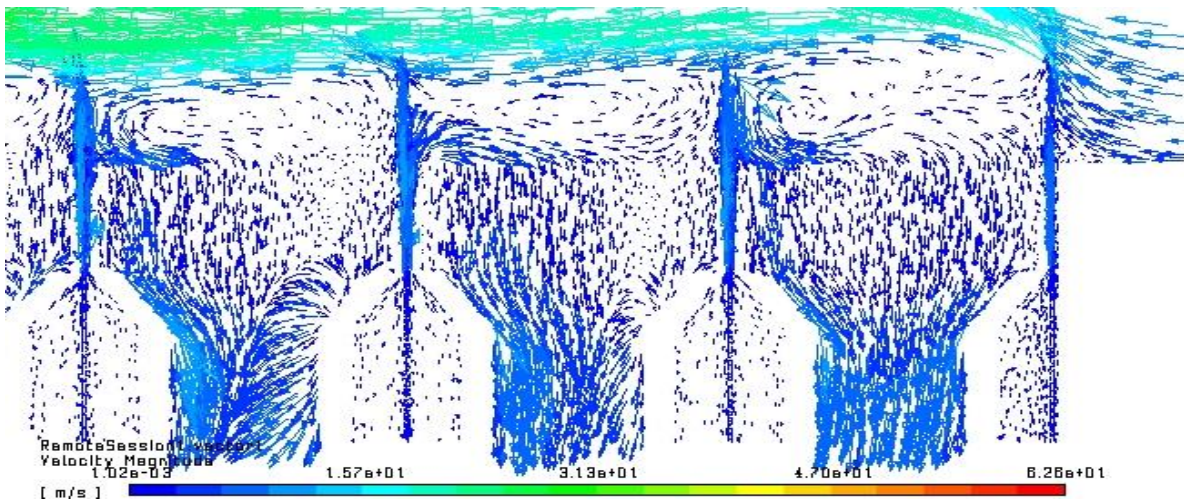


Figure 6-29: Velocity vector plot for a wind speed of 15 m/s at an angle of 30°, for the first three absorber modules from the right of the 50 mm baffled SolAir model

The temperature contour and the velocity vector plot of the SolAir receivers with 50 mm baffles, for a wind speed of 15 m/s at an angle of 60° is shown in Fig. 6-30, Fig. 6-31 and Fig. 6-32 respectively.

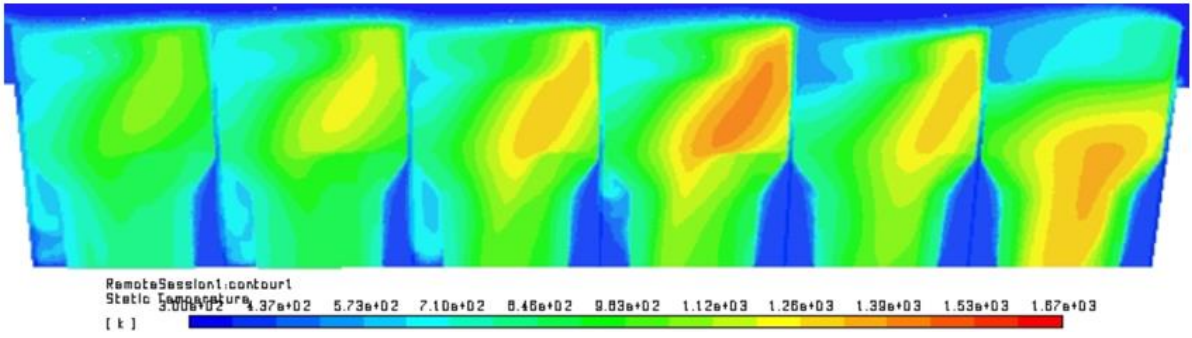


Figure 6-30: Temperature contour plot for wind speed at 15 m/s incident at angle of 60°, of the 50 mm baffled SolAir model

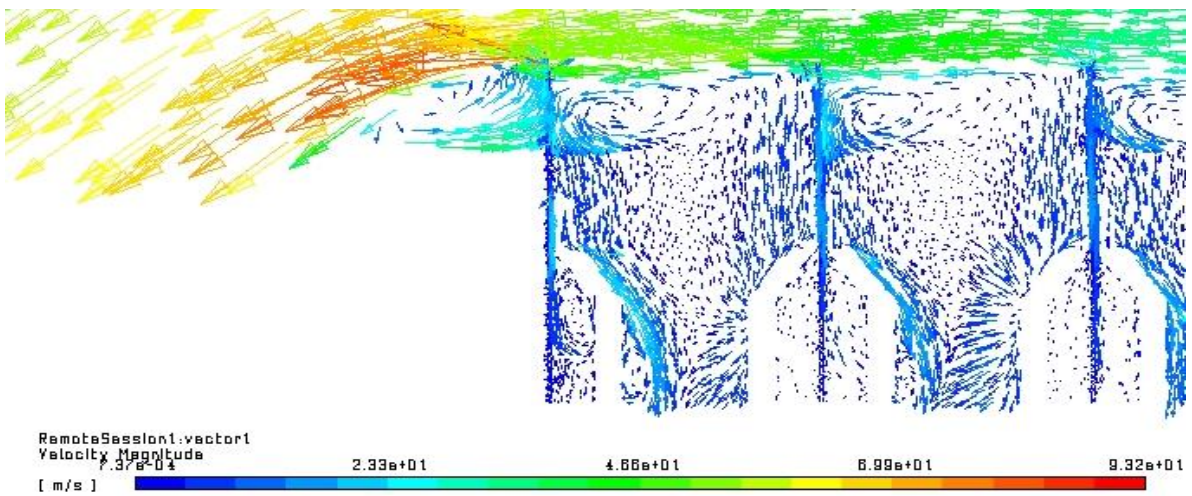


Figure 6-31: Velocity vector plot for a wind speed of 15 m/s at an angle of 60°, for the first two absorber modules from the left of the 50 mm baffled SolAir model

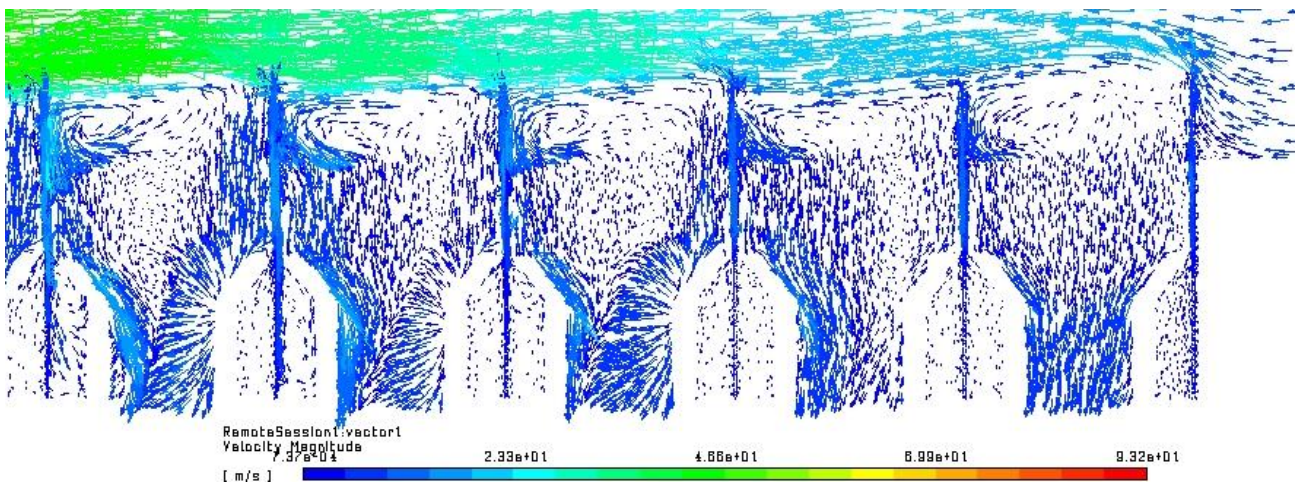


Figure 6-32: Velocity vector plot for a wind speed of 15 m/s at an angle of 60°, for the first four absorber modules from the right of the 50 mm baffled SolAir model

The temperature contour and the velocity vector plot of the SolAir receivers with 50 mm baffles for a wind speed of 15 m/s at an angle of 90° to the absorber surface is shown in Fig. 6-33, Fig. 6-34, Fig. 6-35 and Fig. 6-36.

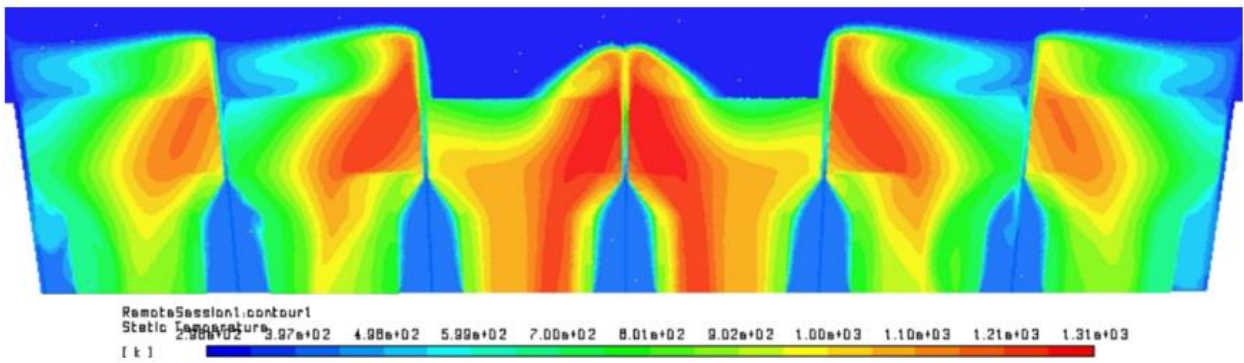


Figure 6-33: Temperature contour plot for wind speed at 15 m/s incident at angle of 90°, for the 50 mm baffled SolAir model

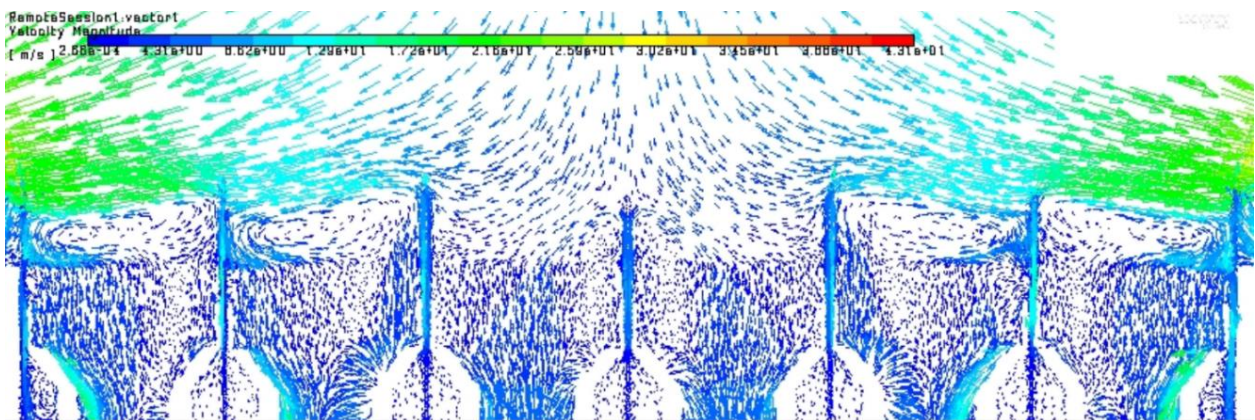


Figure 6-34: Velocity vector plot for a wind speed of 15 m/s at an angle of 90°, for the 50 mm baffled SolAir model

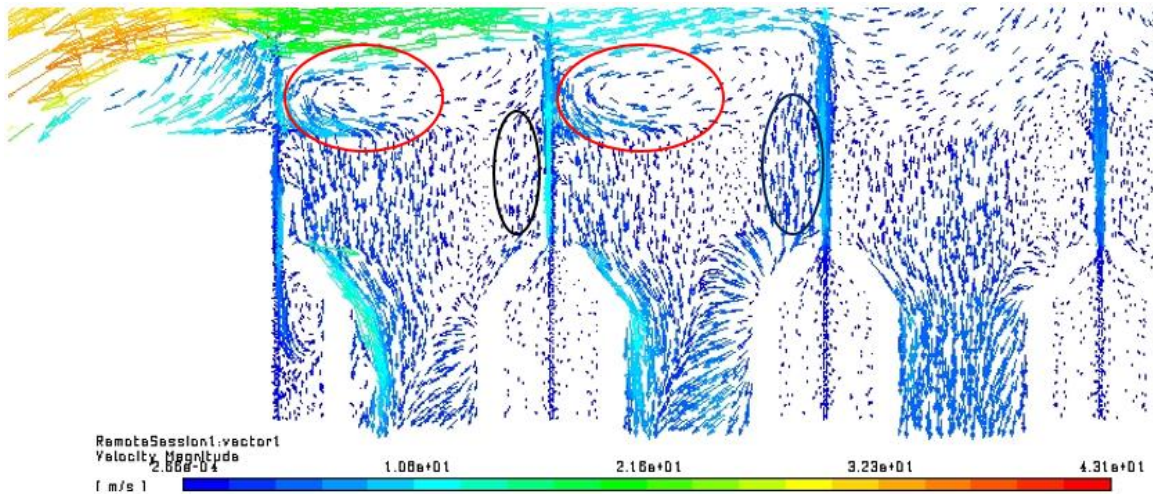


Figure 6-35: Velocity vector plot for a wind speed of 15 m/s at an angle of 90°, for the first three absorber modules from the left of the 50 mm baffled SolAir model

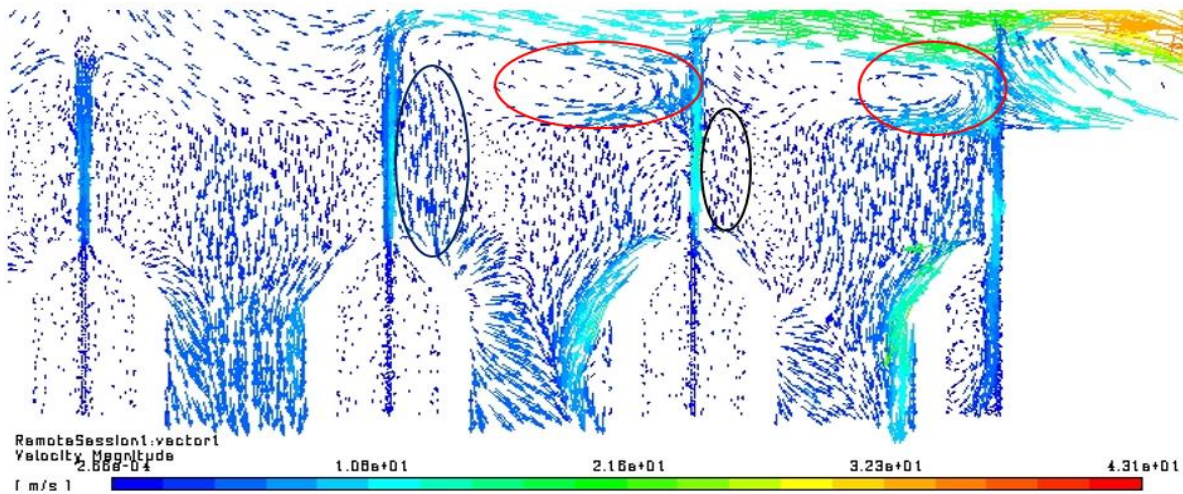


Figure 6-36: Velocity vector plot for a wind speed of 15 m/s at an angle of 90°, for the first three absorber modules from the right of the 50 mm baffled SolAir model

The variation in the mean outlet air temperatures of the 50 mm baffles SolAir receiver model for wind speeds of 15 m/s and 25 m/s at the wind incidence angles of 0°, 30°, 60° and 90° is illustrated in Fig. 6-37.

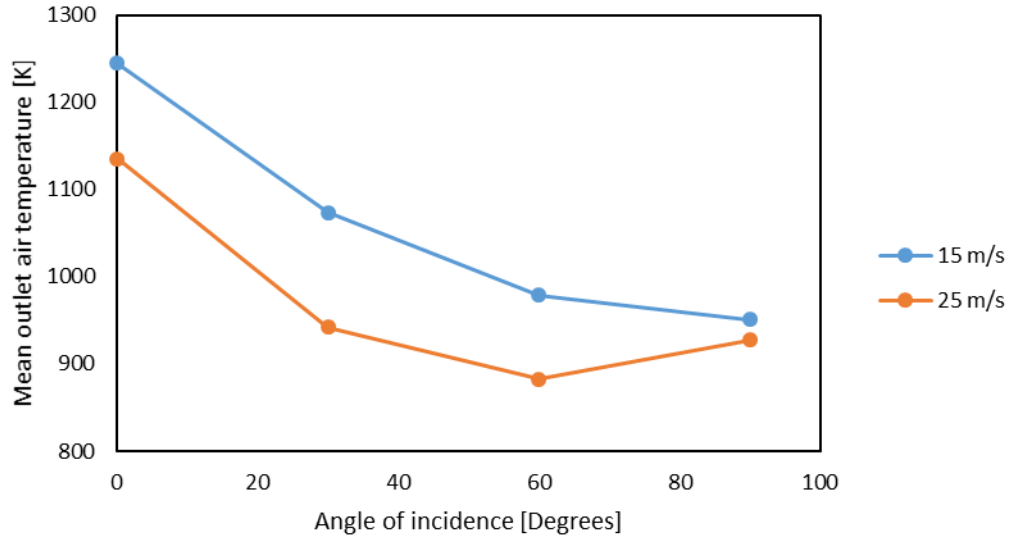


Figure 6-37: Outlet air temperature of the 50 mm baffled SolAir receiver as a function of the incidence angle for wind speeds of 15 m/s and 25 m/s

6.2.3. Baffle length: 30 mm

The 3-D model of the SolAir modules with baffles of length 30 mm used for the wind effects study is shown in Fig. 6-38. Figure 6-39 illustrates a cross-section plane of the meshed model of this baffled SolAir model.

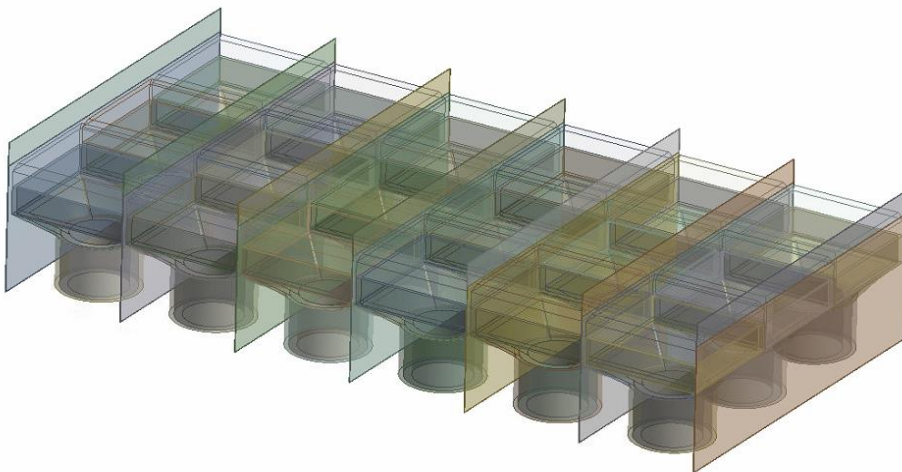


Figure 6-38: 3-D model of the SolAir model with baffle length of 30 mm

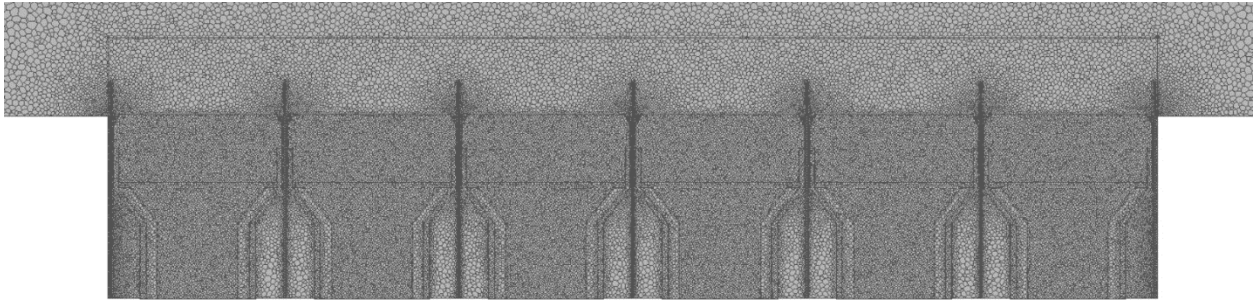


Figure 6-39: Meshed model of the SolAir receiver with 30 mm vertical baffles

The changes in the air outlet temperature of the modules for wind speeds of 15 m/s and 25 m/s for each angle of incidence of the wind on the 30 mm baffled SolAir model is shown in Fig. 6-40, Fig. 6-41, Fig. 6-42 and Fig. 6-43.

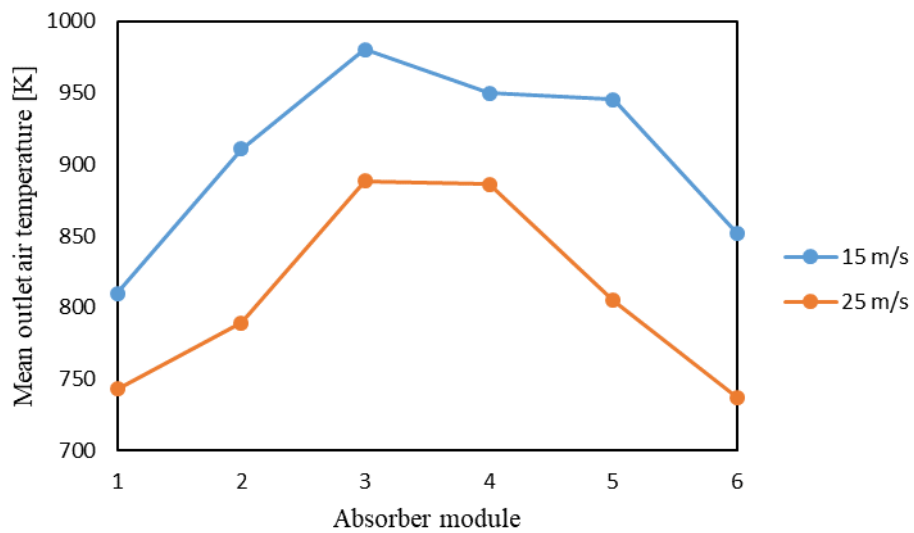


Figure 6-40: Outlet temperature of the absorber modules for wind direction perpendicular to the modules

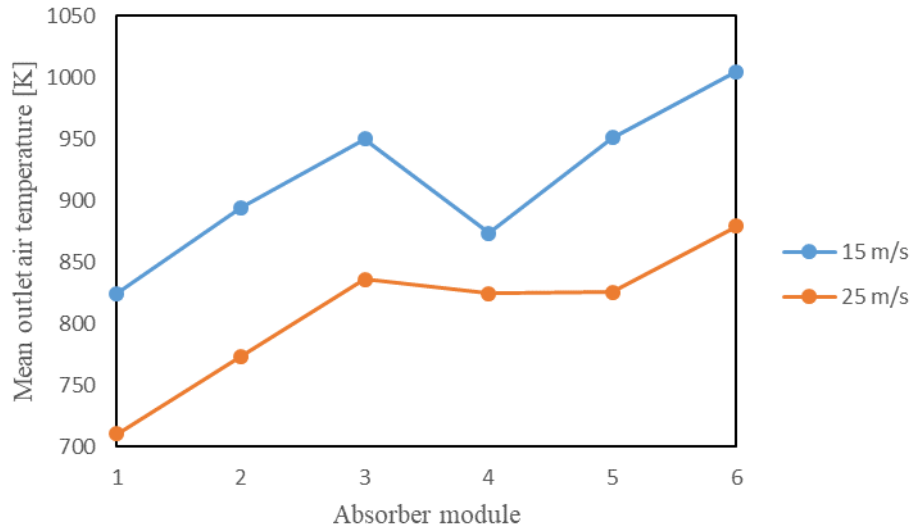


Figure 6-41: Outlet temperature of the absorber modules for wind direction 60° to the modules

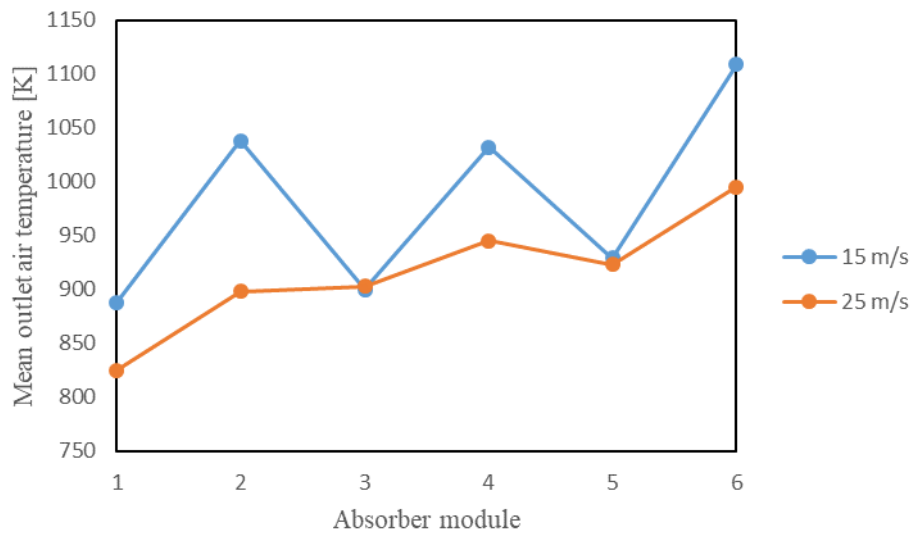


Figure 6-42: Outlet temperature of the absorber modules for wind direction 30° to the modules

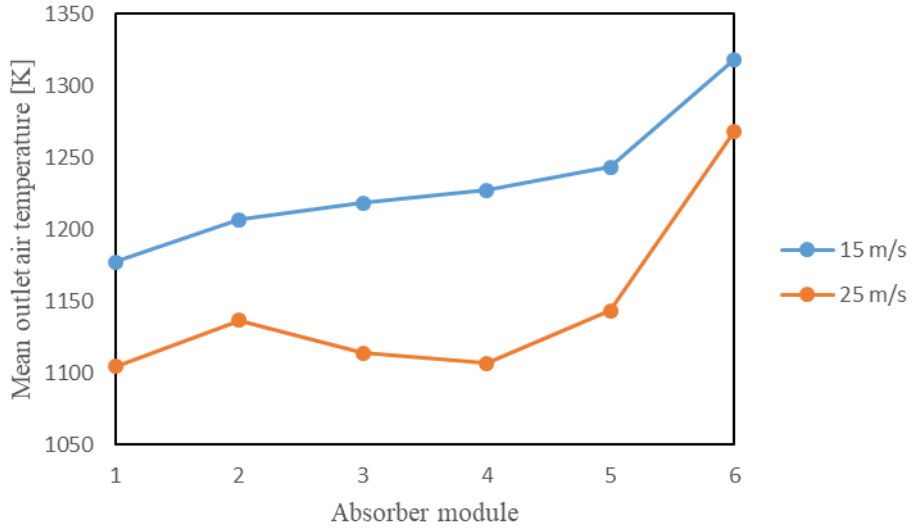


Figure 6-43: Outlet temperature of the absorber modules when wind flows parallel to the absorber surface

The temperature contour and the velocity vector plots of the SolAir receivers with 30 mm baffles are shown in Fig. 6-44 and Fig. 6-45 respectively.

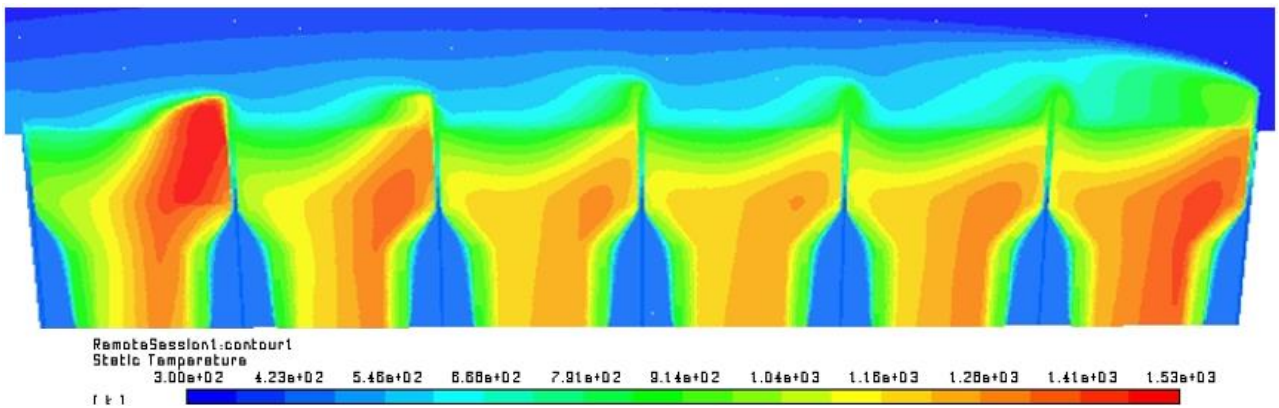


Figure 6-44: Temperature contour plot for wind speed at 15 m/s flowing parallel to the absorber surface, for the 30 mm baffled SolAir model

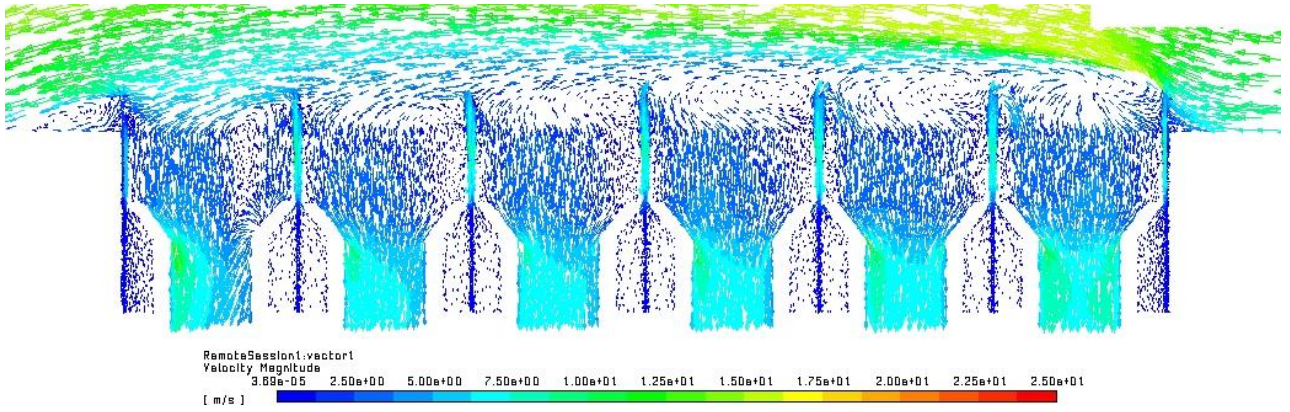


Figure 6-45: Velocity vector plot for a wind speed of 15 m/s for wind flowing parallel to the absorber surface, for the 30 mm baffled SolAir model

The temperature contour of the SolAir receivers with 30 mm baffles, for a wind speed of 15 m/s at an angle of 60° is shown in Fig. 6-46 and the velocity vector plot is shown in Fig. 6-47 and Fig. 6-48.

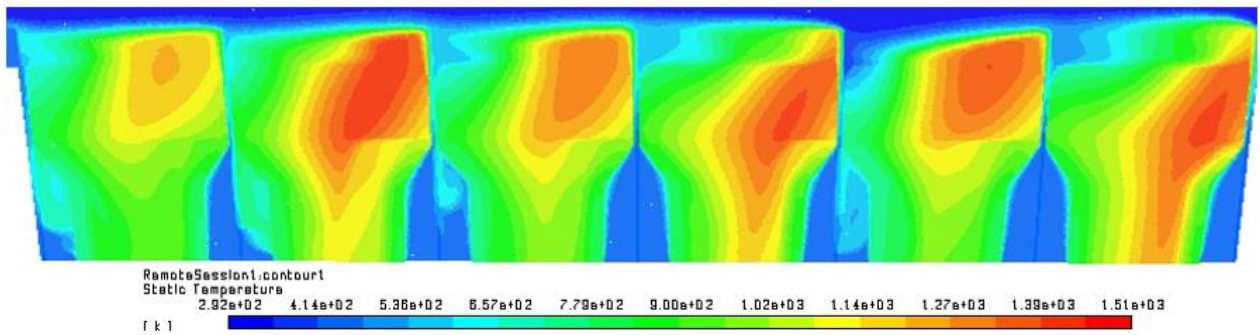


Figure 6-46: Temperature contour plot for wind speed at 15 m/s incident at angle of 30°, for the 30 mm baffled SolAir model

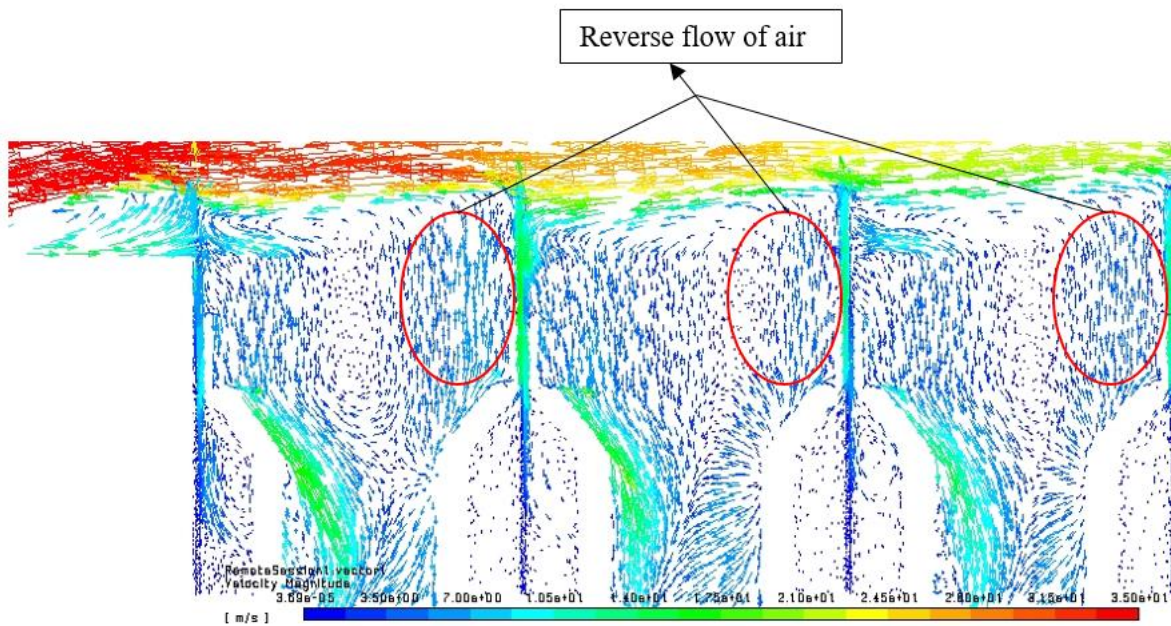


Figure 6-47: Velocity vector plot for a wind speed of 15 m/s at an angle of 30°, for the first three absorber modules from the left of the 30 mm baffled SolAir model

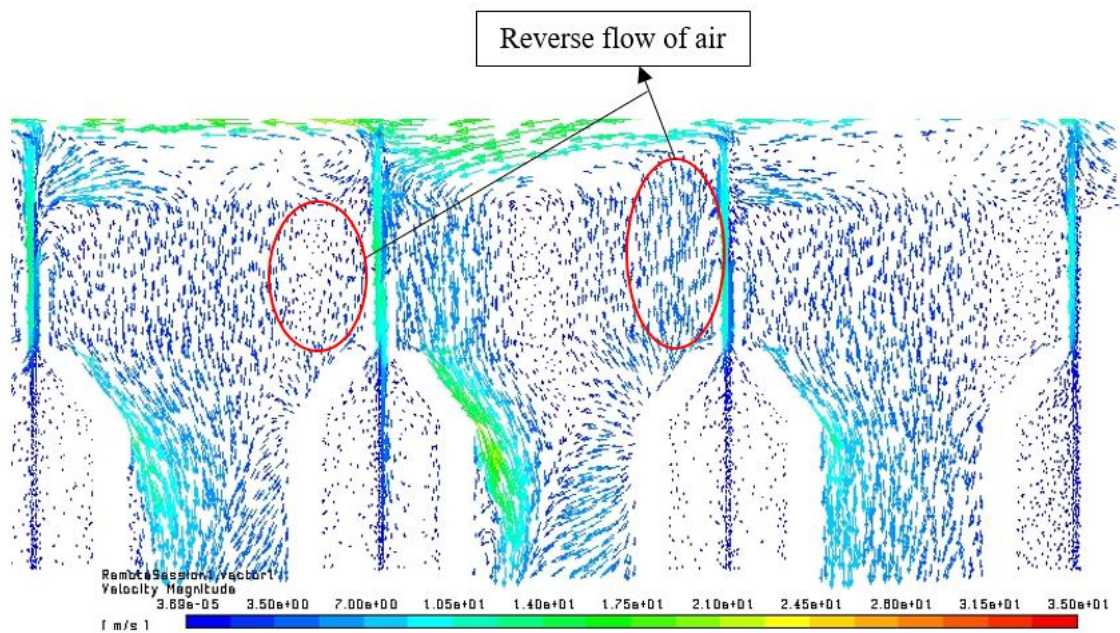


Figure 6-48: Velocity vector plot for a wind speed of 15 m/s at an angle of 30°, for the first three absorber modules from the right of the 30 mm baffled SolAir model

The temperature contour and the velocity vector plots of the SolAir receivers with 50 mm baffles, for a wind speed of 15 m/s and at an angle of 60°, is shown in Fig. 6-49, Fig. 6-50 and Fig. 6-51.

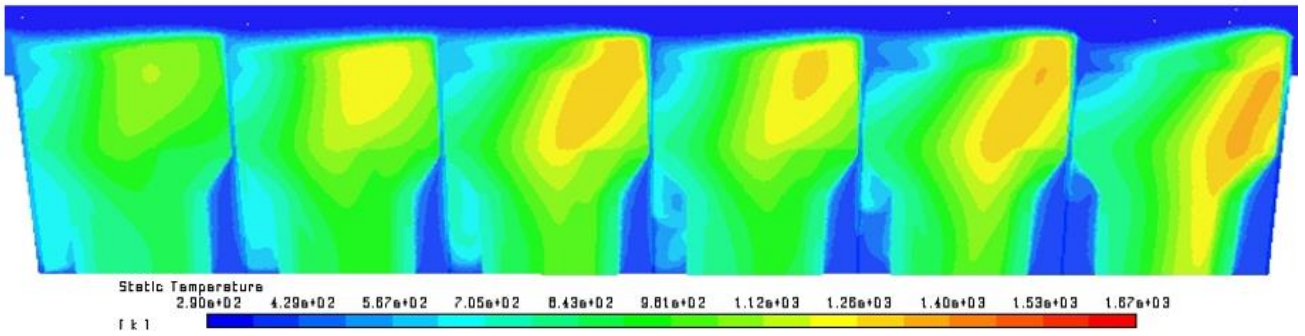


Figure 6-49: Temperature contour plot for wind speed at 15 m/s incident at angle of 60°, of the 30 mm baffled SolAir model

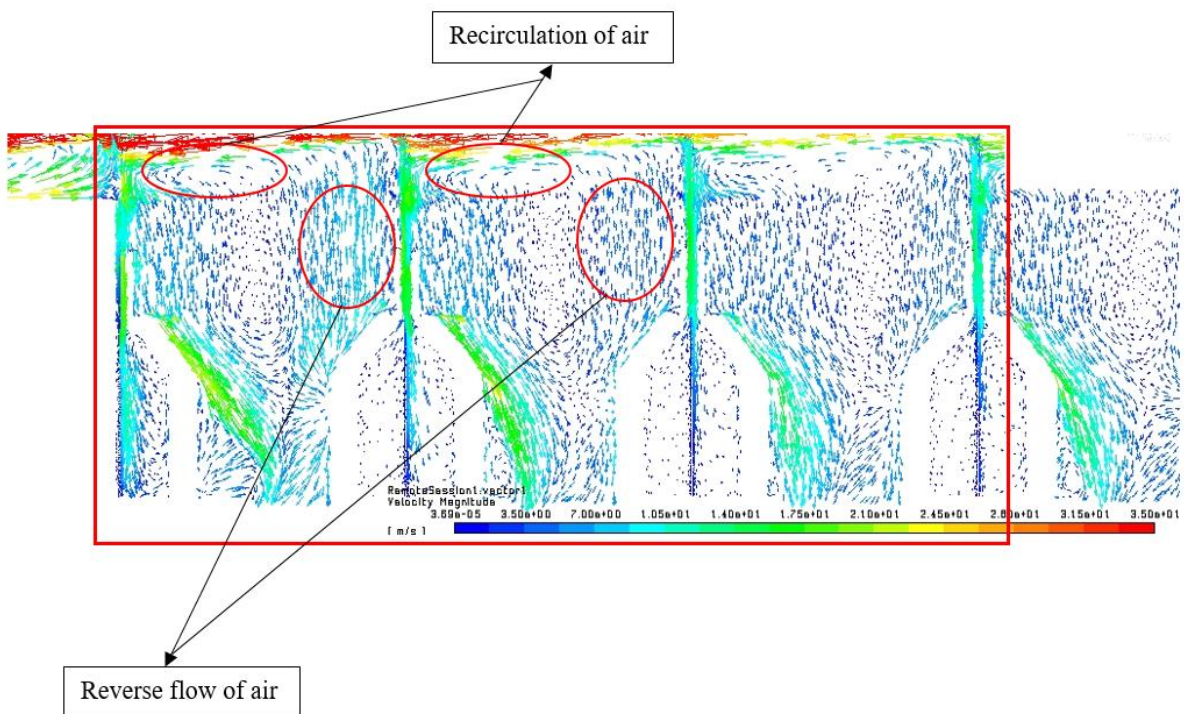


Figure 6-50: Velocity vector plot for a wind speed of 15 m/s at an angle of 60°, for the first three absorber modules from the left of the 30 mm baffled SolAir model

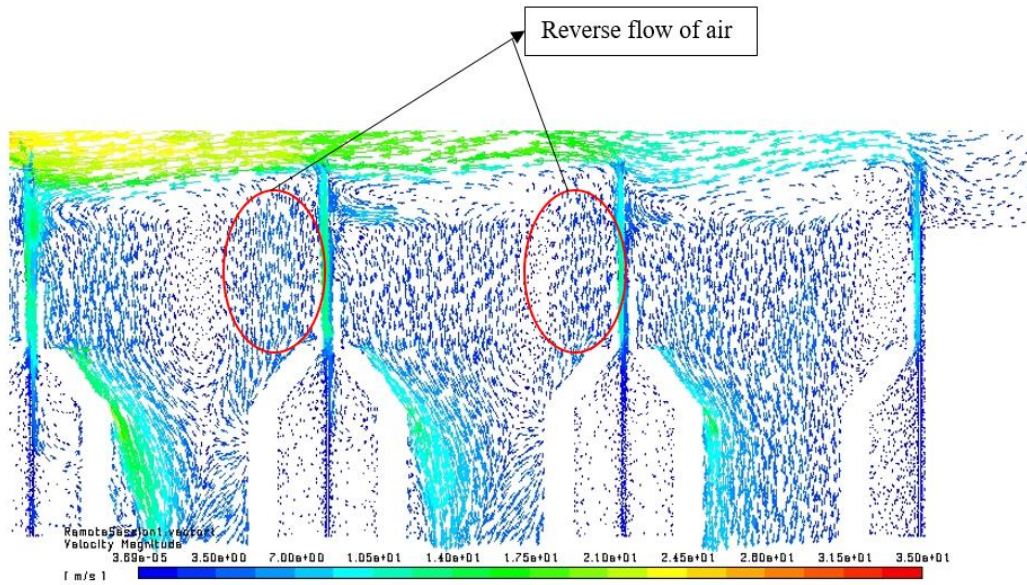


Figure 6-51: Velocity vector plot for a wind speed of 15 m/s at an angle of 60°, for the first three absorber modules from the right of the 30 mm baffled SolAir model

Temperature contour plot for wind speed at 15 m/s incident at angle of 90°, of the 30 mm baffled SolAir model are shown in Fig. 6-52.

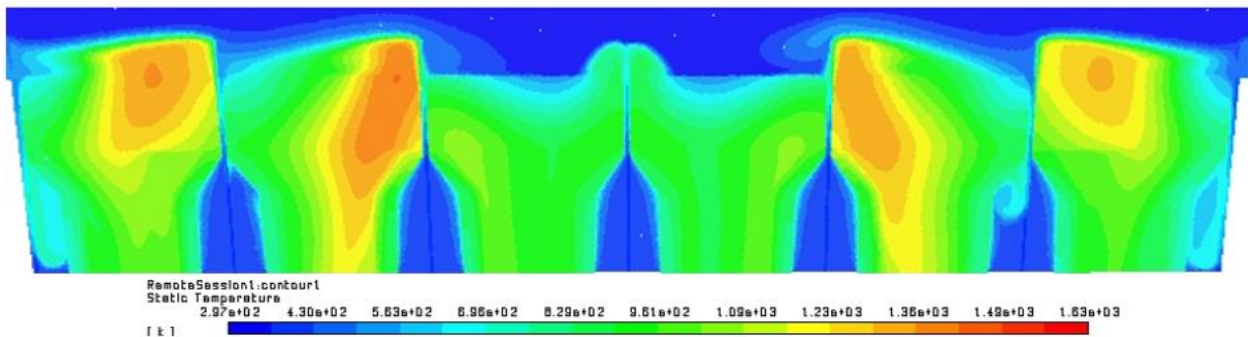


Figure 6-52: Temperature contour plot for wind speed at 15 m/s incident at angle of 90°, for the 30 mm baffled SolAir model

The velocity vector plots for the 30 mm baffled SolAir model are shown in Fig. 6-53, Fig. 6-54 and Fig. 6-55.

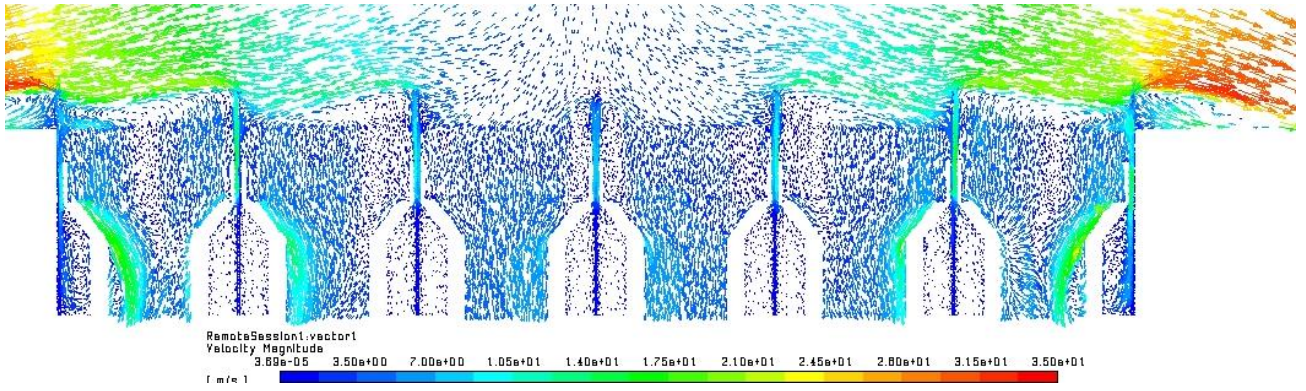


Figure 6-53: Velocity vector plot for a wind speed of 15 m/s at an incident angle of 90°, for the 30 mm baffled SolAir model

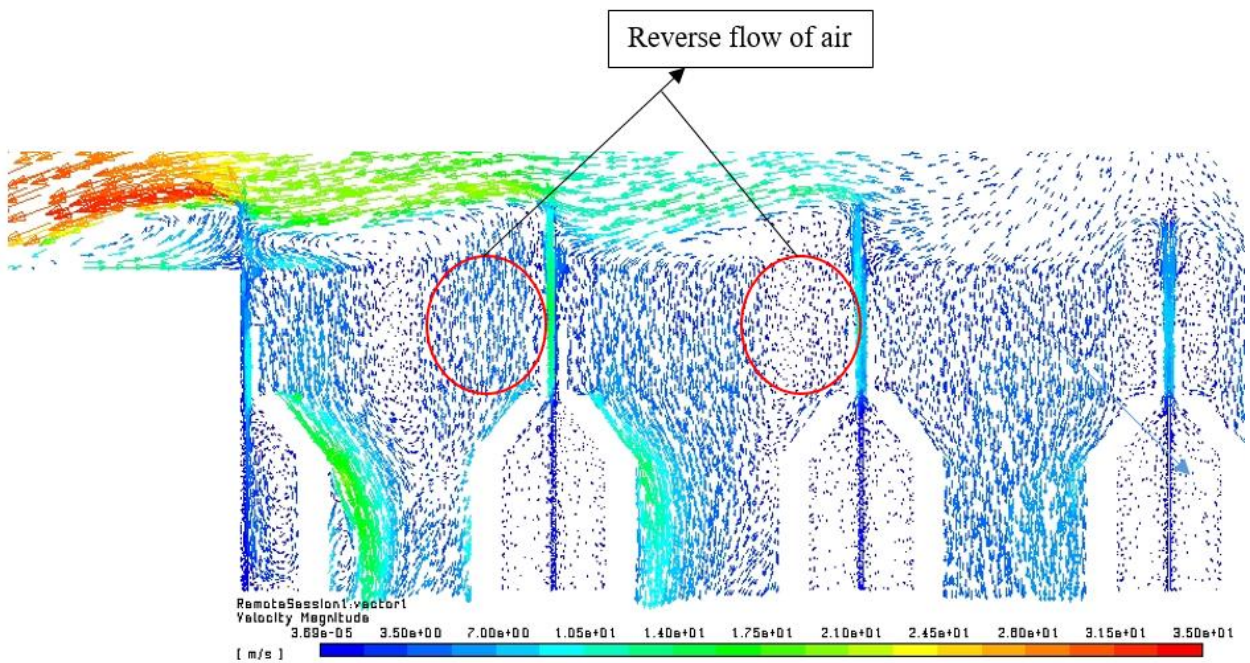


Figure 6-54: Velocity vector plot for a wind speed of 15 m/s at an angle of 90°, for the first two absorber modules from the left of the 30 mm baffled SolAir model

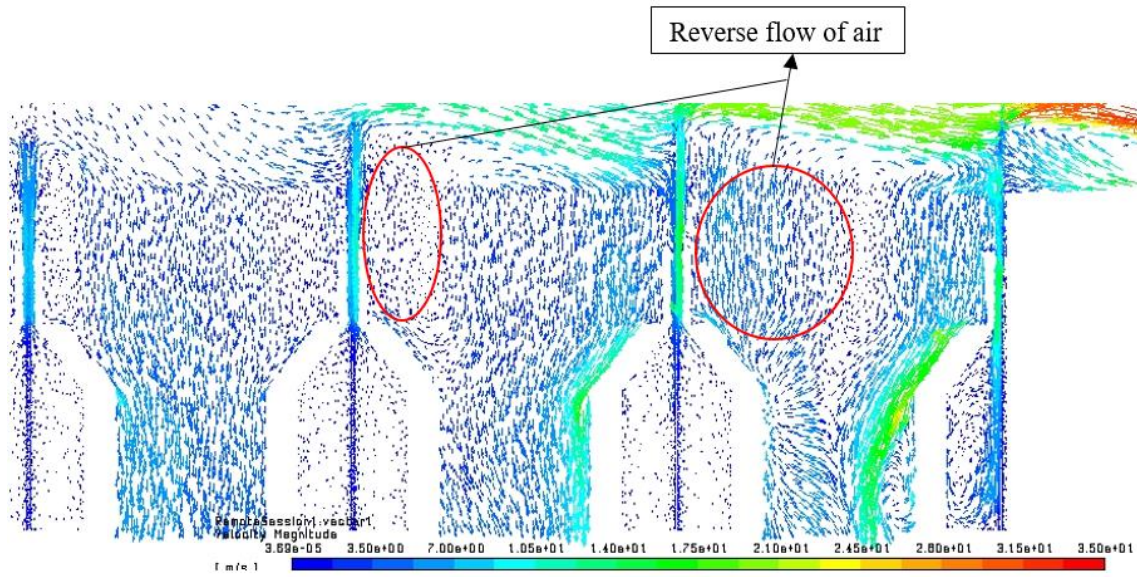


Figure 6-55: Velocity vector plot for a wind speed of 15 m/s at an angle of 90°, for the first two absorber modules from the right of the 30 mm baffled SolAir model

The changes in the outlet air temperatures of the 50 mm baffles SolAir model for wind speeds of 15 m/s and 25 m/s at wind incidence angles of 0°, 30°, 60° and 90° are illustrated in Fig. 6-56.

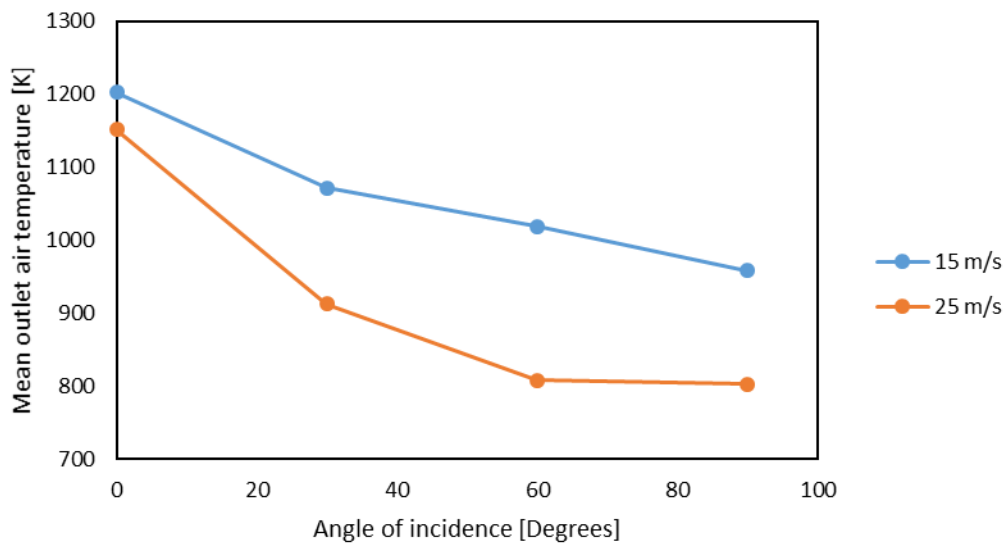


Figure 6-56: Outlet air temperature of the 30 mm Baffled SolAir receiver for wind speeds of 15 m/s and 25 m/s

6.2.4. Performance comparison of the baffled SolAir models

Figure 6-57 and Fig. 6-58 graphically compares the outlet air temperatures predicted for the baffled models and the standard SolAir model at a wind speed of 15 m/s and 25 m/s respectively, for all the angles of incidence considered.

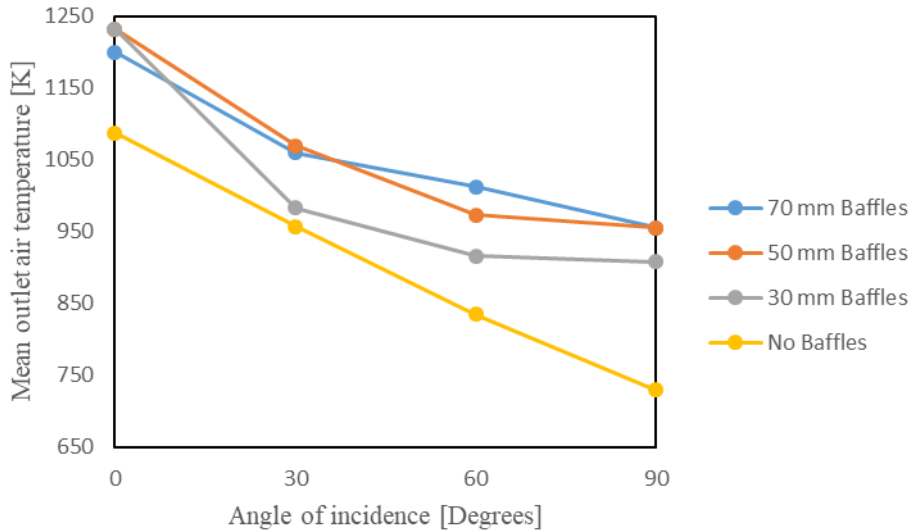


Figure 6-57: Comparative illustration of the outlet air temperatures for the baffled model at wind speed of 15 m/s

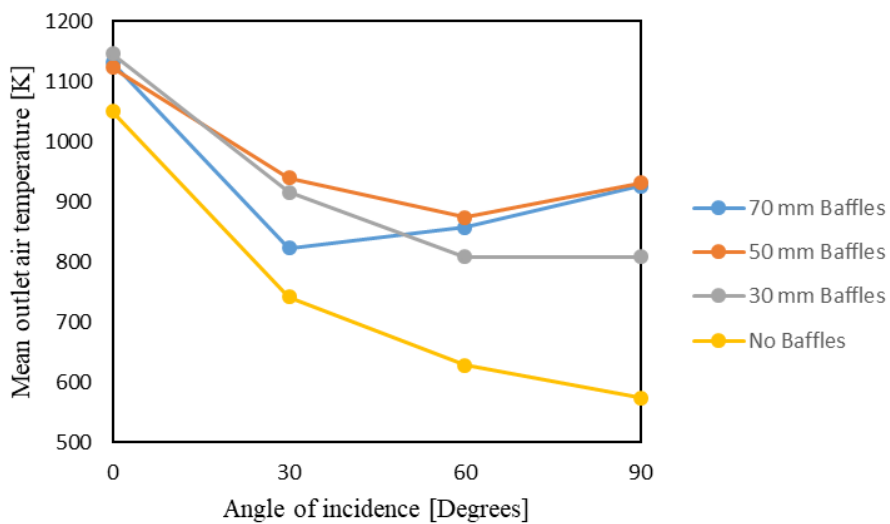


Figure 6-58: Comparative illustration of the outlet air temperatures for the baffled model at wind speed of 25 m/s

Figure 6-59 and Fig. 6-60 graphically illustrates the percentage increase in the outlet air temperatures for each of the baffled models by using the standard SolAir model as the reference, at wind speeds of 15 m/s and 25 m/s respectively.

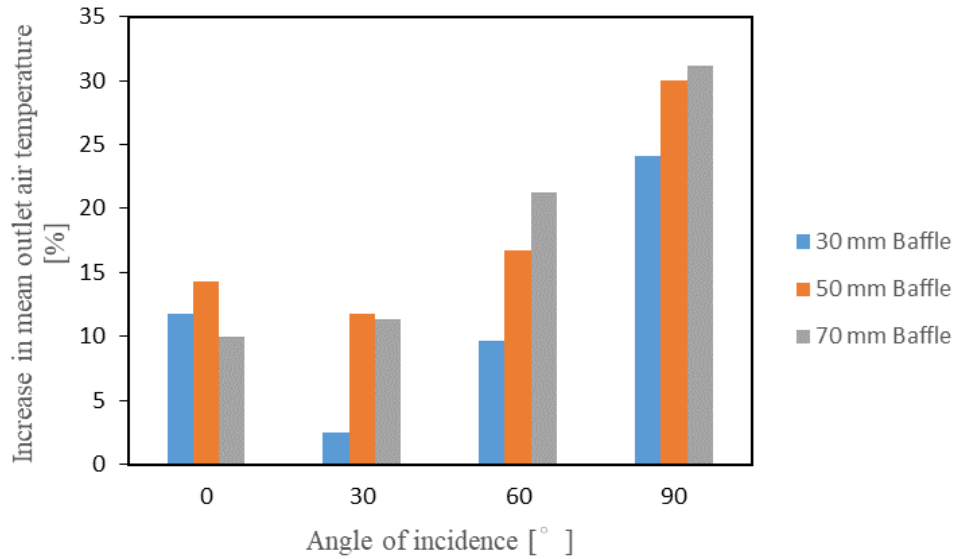


Figure 6-59: Increase in the outlet air temperature of the baffled SolAir models at wind speed of 15 m/s

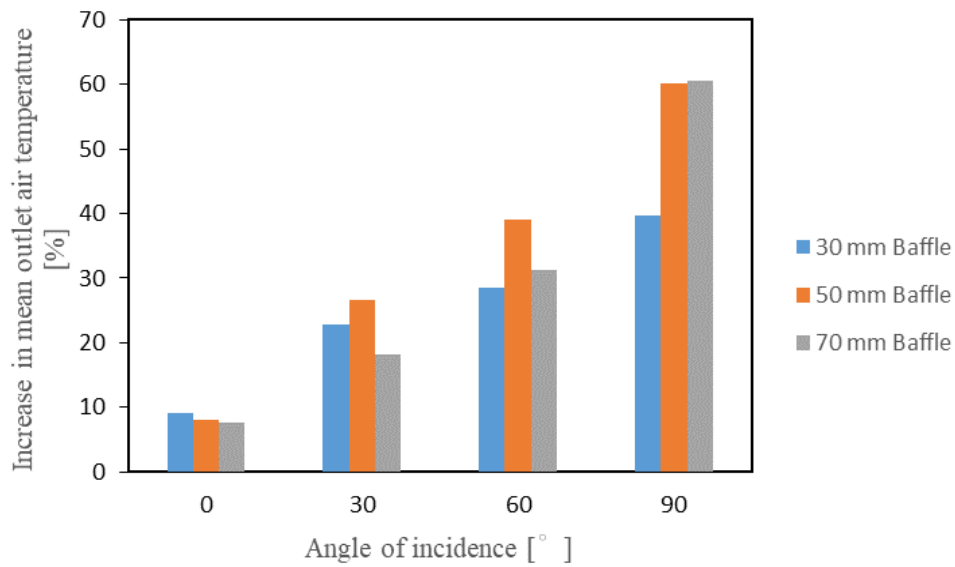


Figure 6-60: Increase in the outlet air temperature of the baffled SolAir models at wind speed of 25 m/s

6.3. Discussion

Three baffled SolAir models were developed to research possible improvement in the ARR of the receivers. The wind study was carried out on SolAir models with vertical baffles with lengths of 70 mm, 50 mm and 30 mm placed vertically between adjacent absorber modules as shown in Fig. 6-4, Fig. 6-19 and Fig. 6-38. The study accounted for wind speeds of 15 m/s and 25 m/s at angles of incidence of 0°, 30°, 60° and 90°.

Certain air flow behaviour seemed common for all baffled models, such as in the case of the wind oriented parallel to the surface of the absorber, where the presence of baffles prevents the air brought in by the wind from directly striking the absorbers at high velocity. The air flowing parallel to the absorber surfaces are tipped towards them, preventing a certain degree of heat from being taken away by the wind otherwise. This can be seen very clearly in Fig. 6-11 and Fig. 6-26. The baffles also prevent a higher proportion of the warm return air from being blown away by the wind, and improves the chances of it being re-directed back into the absorber. This would increase the thermal energy of the air that is being drawn through the absorbers when compared to the other angles of incidences.

At incident angles of 30° and 60°, the baffles appear to cause a circular motion of air just above some of the absorber module, and also causes air to flow out of some of the modules through the absorbers. The air that flows out is then recirculated back into the module as seen in Fig. 6-50, for example. When wind is perpendicular to the absorber modules, the air flow pattern and the temperature distribution in the first four absorber modules from the left appears to almost be a mirror image of the air flow pattern and temperature distribution in the last four modules from left, as in Fig. 6-52, Fig. 6-53, Fig. 6-54, and Fig. 6-55 with the line of symmetry being the baffle between the centre two absorber modules. There is a higher chance for the formation of the circular motion of the air in the vicinity of the baffles when they are longer. This flow behaviour plays a role in promoting the warm return air from being re-entrained back into the absorber instead of diffusing into the surrounding atmosphere, or being blown away by the lateral wind.

Three main sets of data were formulated to better understand the effect of wind as well as the baffle length on the mean air outlet temperature of the absorber modules, which in-turn was an indicator of the ARR as proven in Chapter 5. The first set of data involved the monitoring of the air temperature at the outlet of the individual absorber modules at each wind speed, for all the wind incidence angles. In general, higher air temperatures are achieved at lower wind speeds, quite similar to the case with the standard SolAir receiver CFD model. For each angle of incidence, the relative air outlet temperature trend across the six monitored absorbers remained the same i.e. the graph has a similar shape, for the two wind speeds that were monitored in the study. The vector plot for the perpendicular wind direction

depicts a symmetrical air flow pattern as detailed above, but the mean air outlet temperature from the absorber modules for that wind orientation did not exhibit a perfectly symmetrical result. One possible explanation for this phenomenon is that the air flow in and around the absorber modules is inherently unsteady, and could not accurately be captured due to the steady state assumption of the simulation.

The second set of data provides a comparative assessment of the standard and baffled SolAir model performance, as illustrated in Fig. 6-18, Fig. 6-37 and Fig. 6-56. In general, it shows that the mean air outlet temperature, and therefore the ARR, decreases with higher wind incidence angles. Some exceptions to this rule exists, as illustrated in Fig. 6-58, for the 70 mm and 50 mm baffle length at the wind speed of 25 m/s.

Another peculiar observation is that the mean air temperature for the baffled models seems to come closer to each other as the wind speed was ramped from 15 m/s to 25 m/s. The 50 mm baffled model performed comparatively as good as the 70 mm baffled model at 15 m/s but performed the best at wind speed of 25 m/s. Such a behaviour prompts the possibility of a critical baffle length beyond which the receiver performance deteriorates with increasing wind speed and wind incidence angles.

Lastly, the third set of data (Fig. 6-59 and Fig. 6-60) compared the performance improvement brought about by the baffled models against each other with reference to the standard SolAir model. Quite similar to the conclusions drawn from Fig. 6-57 and Fig. 6-58, a clear optimum among the baffled models did not emerge, although the 50 mm baffled model seemed to have either outperformed and was performing almost as good as the 70 mm baffled model, in almost all of the wind incidence angles and wind speeds that were accounted for in the study.

In a cumulative sense, the computational predictions described above appear to indicate clearly that the inclusion of vertically-oriented baffles in between SolAir absorber modules results in the attainment of higher mean air outlet temperatures (within the limits imposed by the assumptions made for the simulations), which, in turn, implies the attainment of a higher ARR index. This is a significant and novel finding.

6.4. Conclusion

Inspired by the improvements in the ARR brought about by the usage of absorber shields in the HiTRec-II receiver design, as researched by Marcos et al. (2004), vertical air flow baffles were added to the standard SolAir design to investigate the potential for improving the ARR of OVRs. The air outlet temperature was used as an indicator of the improvement in the ARR, since the two parameters have a proportional relationship, as demonstrated in Chapter 5.

The wind effects study revealed that higher mean air outlet temperatures were achieved at lower wind speeds. In general, an inverse relationship was found to be present between the air temperature and wind incidence angle, although there were exceptions to this rule, especially at a higher wind speed of 25 m/s. A strict relationship between the baffle length and air outlet temperatures could not be established, and results also indicated the existence of a critical baffle length, beyond which the receiver performance might deteriorate at higher wind speeds. All in all, the presence of baffles was shown to improve the ARR, with clear indications of higher mean air outlet temperatures at all of the operating parameters considered. Such a performance improvement can be attributed to certain flow behaviour induced by the presence of the baffles, such as circular motion of air in the vicinity of the baffles, preventing the warm air in the return air circuit from dissipating into the surrounding atmosphere.

7. CONCLUSION

The thesis was aimed at addressing the common problem of low Air Return Ratio (ARR) in a new type of solar receivers, called the Open Volumetric Receiver (OVR) that are used in Central Receiver System (CRS). A main cause for the low air return ratio is the open loop air circuit that is used to dispose the warm air from the HRSG or the TES into the open atmosphere through the gaps present in between OVR modules. The lateral wind that flows over the OVR modules tend to blow away a significant portion of the warm air while the rest is drawn back in through the modules.

A modular design of the OVR technology was tested in two iconic experimental campaigns that were conducted to study the scalability of the OVR, called the HiTRec-II and the SolAir test campaigns. In both of the campaigns, tests were carried out to measure the ARR, which resulted in a low value of 35 % to 45 %. The most vital component of an OVR is the porous absorber that acts as a heat exchanger imparting thermal energy received from solar radiation to the air flowing through it. Hence, modelling the absorber accurately to predict the behaviour of the flow in a conjugate heat transfer process occurring within the absorber module will be necessary.

An experimental setup that was used to collect the pressure drop data across a porous absorber for varying velocities was replicated in 2-D in Ansys Fluent, a computational fluid dynamic (CFD) modelling software. The simulation results were within 10 % deviation margin of the experimental ones, and the method of modelling the porous absorber used for the cold flow validation study was deemed accurate enough to predict a realistic flow behaviour of air through an absorber.

A 2-D model of the HiTRec-II absorber modules on which a successful hot flow validation study was previously conducted was adopted and replicated for the research work. A few errors in modelling HiTRec-II modules in 2-D and effectively representing the heat energy in the porous medium of the model was discovered and a 3-D model of the centre three rows of the HiTRec-II receiver test rig was developed in Ansys. The operating conditions for the validation study such as wind speed, wind direction, total mass flow rate of air, total incident power on the absorbers as well as the air outlet temperatures of the modules under these conditions were obtained from the experimental data of the HiTRec-II experimental campaign. The simulations of the hot flow validation study were run using the resources at the Centre for High Performance Computing (CHPC) in Cape Town. The maximum deviation of the outlet air temperatures obtained from the simulation and the experimental ones was 12.32 %, and the hot flow validation study was deemed a success.

The latest iteration of the OVR technology, known as the SolAir receiver, were developed in Ansys for a wind effects study. Although the initial goal was to calculate its ARR under various wind loading conditions, the limitations of the LTE conditions for porous media modelling prevented the accurate

modelling of the air temperature at the inlet of the absorber modules. In order to formulate an alternative method of measuring the ARR without compromising on the accuracy of the result, the porous absorber was isolated and an equation defining the ARR as a function of the air outlet temperature was derived successfully. Therefore, the outlet air temperature of the modules was used as the comparison parameter of the OVR performance at different operating conditions. The data collected from a wind effects study on the SolAir receiver model was then be used as a baseline to check for improvement in the receiver performance with the implementation of baffles in the design.

Three SolAir models with vertical baffles placed longitudinally between the absorber modules were developed and a wind effects study was conducted to investigate improvements in the ARR of the receiver design. Baffle lengths of 70 mm, 50 mm and 30 mm were analysed and the data collected from the wind study suggested a clear improvement in the performance of the baffled SolAir model when compared to the standard model. Therefore, the usage of baffles seems to be a promising option for improving the ARR of the OVRs.

The research work can be further improved by modelling the porous medium of the OVR using the Local Thermal Non-Equilibrium (LTNE) conditions. The LTNE condition accommodates for the calculation of the temperature profile of the solid absorber and the air flowing through it separately, which would in-turn allow an accurate measurement of the air inlet temperature for calculating the Air Return Ratio (ARR). Secondly, a ray-trace analysis of the SolAir model with the baffles should be carried out to understand the amount of solar power that is obstructed by the baffles. Modelling all of the energetics of the system would also allow the calculation of the thermal efficiency of the receiver. Investigating a wide variety of shapes of the baffles as well as its participation in the conjugate heat transfer process would give an insight into its true effectiveness in improving the ARR of the OVR sub-system.

REFERENCES

- Agrafiotis, C. C., Mavroidis, I., Konstandopoulos, A. G., Hoffschmidt, B., Stobbe, P., Romero, M. and Fernandez-Quero, V. (2007) 'Evaluation of porous silicon carbide monolithic honeycombs as volumetric receivers/collectors of concentrated solar radiation', *Solar Energy Materials and Solar Cells*, 91(6), pp. 474–488. doi: 10.1016/j.solmat.2006.10.021.
- Al-juboori, S. (2018) 'Solar Energy Assessment of Molten Salts as Thermal Storage Mediums', in X (ed.) *13th International Scientific Forum*. x, pp. 4–5.
- Anderson, R., Bates, L., Johnson, E. and Morris, J. F. (2015) 'Packed bed thermal energy storage: A simplified experimentally validated model', *Journal of Energy Storage*, 4, pp. 14–23. doi: 10.1016/j.est.2015.08.007.
- Ansys Inc (2006) 'Modeling Turbulent Flows What is Turbulence?' Available at: http://www.southampton.ac.uk/~nwb/lectures/GoodPracticeCFD/Articles/Turbulence_Notes_Fluent-v6.3.06.pdf.
- Ansys Inc (2009a) *Choosing the Pressure Interpolation Scheme*. Available at: <https://www.afs.enea.it/project/neptunius/docs/fluent/html/ug/node781.htm> (Accessed: 22 January 2020).
- Ansys Inc (2009b) *Standard k-omega Model*. Available at: <https://www.afs.enea.it/project/neptunius/docs/fluent/html/th/node66.htm> (Accessed: 18 January 2020).
- Ansys Inc (2015) *Lecture 8 - Heat Transfer in Porous Media*.
- Ávila-Marín, A. L. (2011) 'Volumetric receivers in Solar Thermal Power Plants with Central Receiver System technology: A review', *Solar Energy*, 85(5), pp. 891–910. doi: 10.1016/j.solener.2011.02.002.
- Bai, F. (2010) 'One dimensional thermal analysis of silicon carbide ceramic foam used for solar air receiver', *International Journal of Thermal Sciences*, 49(12), pp. 2400–2404. doi: 10.1016/j.ijthermalsci.2010.08.010.
- Balogh, M. (2014) *Numerical simulation of atmospheric flows using general purpose CFD solvers Declaration of Authorship*. Budapest University of Technology and Economics.
- Becker, M., Fend, T., Hoffschmidt, B., Pitz-Paal, R., Reutter, O., Stamatov, V., Steven, M. and Trimis, D. (2006) 'Theoretical and numerical investigation of flow stability in porous materials applied as volumetric solar receivers', *Solar Energy*, 80(10), pp. 1241–1248. doi: 10.1016/j.solener.2005.11.006.
- Buck, R., Bräuning, T., Denk, T., Pfaender, M., Schwarzbözl, P. and Tellez, F. (2001) 'Solar-Hybrid Gas Turbine-based Power Tower Systems (REFOS)', in *ASME 2001 Solar Engineering: International Solar Energy Conference (FORUM 2001: Solar Energy — The Power to Choose)*, pp. 2–9. doi: 10.1115/SED2001-144.
- Buck, R., Barth, C., Eck, M. and Steinmann, W. D. (2006a) 'Dual-receiver concept for solar towers', *Solar Energy*, 80(10), pp. 1249–1254. doi: 10.1016/j.solener.2005.03.014.
- Buck, R., Barth, C., Eck, M. and Steinmann, W. D. (2006b) 'Dual-receiver concept for solar towers', *Solar Energy*, 80(10), pp. 1249–1254. doi: 10.1016/j.solener.2005.03.014.
- Capuano, R., Fend, T., Stadler, H., Hoffschmidt, B. and Pitz-paal, R. (2017) 'Optimized volumetric

solar receiver : Thermal performance prediction and experimental validation’, *Renewable Energy*, 114, pp. 556–566. doi: 10.1016/j.renene.2017.07.071.

Crossby (2019) *CHPC Quick Start Guide*. Available at: <http://wiki.chpc.ac.za/quick:start> (Accessed: 22 January 2020).

Dieterich, R. (2018) *24-Hour Solar Energy: Molten Salt Makes It Possible, and Prices Are Falling Fast, Inside Climate News*. Available at: <https://insideclimatenews.org/news/16012018/csp-concentrated-solar-molten-salt-storage-24-hour-renewable-energy-crescent-dunes-nevada> (Accessed: 30 December 2019).

Elnoumeir, R., Capuano, R. and Fend, T. (2017) ‘Numerical Evaluation of the Extinction Coefficient of Honeycomb Solar Receivers’, 7(1).

Fabrisio, G. G., Jose, G. A., Sergio, T. P., Gabriel, O. and Manuel, R. (2014) ‘Numerical analysis of radiation attenuation in volumetric solar receivers composed of a stack of thin monolith layers’, *Energy Procedia*, 57, pp. 457–466. doi: 10.1016/j.egypro.2014.10.199.

Fend, T., Pitz-Paal, R., Reutter, O., Bauer, J. örg and Hoffschmidt, B. (2004) ‘Two novel high-porosity materials as volumetric receivers for concentrated solar radiation’, *Solar Energy Materials and Solar Cells*, 84(1–4), pp. 291–304. doi: 10.1016/j.solmat.2004.01.039.

Fend, T. (2010) ‘High porosity materials as volumetric receivers for solar energetics’, *Optica Applicata*, 40(2), pp. 271–284.

Fend, T., Schwarzbözl, P., Smirnova, O., Schöllgen, D. and Jakob, C. (2013) ‘Numerical investigation of flow and heat transfer in a volumetric solar receiver’, *Renewable Energy*, 60, pp. 655–661. doi: 10.1016/j.renene.2013.06.001.

Gomez-Garcia, F., González-Aguilar, J., Olalde, G. and Romero, M. (2016) ‘Thermal and hydrodynamic behavior of ceramic volumetric absorbers for central receiver solar power plants: A review’, *Renewable and Sustainable Energy Reviews*, 57, pp. 648–658. doi: 10.1016/j.rser.2015.12.106.

Goswami, Y. and Kreith, F. (2008) *Energy Conversions*, CRC Press. Boca Raton: CRC Press.

Grasse, W. and PHOEBUS (1991) ‘international 30 MWe solar tower plant.’, *Solar Energy Materials*, 24(1–4), pp. 82–94. doi: 10.1016/0165-1633(91)90050-U.

Hennecke, K., Schwarzbozl, P., Beuter, M., Hoffschmidt, B., Gottsche, J. and Hartz, T. (2009) ‘The Solar Power Tower Jülich — A Solar Thermal Power Plant for Test and Demonstration of Air Receiver Technology’, in Goswami, Y. D. and Zhao, Y. (eds) *Proceedings of ISES World Congress 2007 (Vol. I – Vol. V)*. Springer Berlin Heidelberg, pp. 1749–1753. doi: 10.1007/978-3-540-75997-3_358.

Hoffschmidt, B. (2001) ‘Development of ceramic volumetric receiver technology’, *Mitteilung - Deutsche Forschungsanstalt fuer Luft- und Raumfahrt*, (10), pp. 51–61.

Hoffschmidt, B., Téllez, F. M., Valverde, A., Fernández, J. and Fernández, V. (2003) ‘Performance Evaluation of the 200-kWth HiTRec-II Open Volumetric Air Receiver’, *Journal of Solar Energy Engineering*, 125(1), p. 87. doi: 10.1115/1.1530627.

Hoffschmidt, P. B. (2014) *Receivers for Solar Tower Systems*, DLR. Available at: https://elib.dlr.de/94540/1/SFERA2014_SolarTowerReceivers_final.pdf (Accessed: 28 November 2020).

Incropera, F. P. and DeWitt, D. P. (1995) ‘Radiation Exchange Between Surface’, in *Fundamentals of Heat and Mass Transfer*. Fourth. John Wiley & Sons, Inc, pp. 749–754.

IRENA (2018) *Renewable Power Generation Costs in 2018*.

IRENA (2019) *Global Energy Transformation: A Roadmap to 2050 (2019 Edition)*.

Jung, E. G., Boo, J. H., Kang, Y. H. and Kim, N. H. (2013) 'Effectiveness of a multi-channel volumetric air receiver for a solar power tower', *Heat and Mass Transfer/Waerme- und Stoffuebertragung*, 49(8), pp. 1181–1190. doi: 10.1007/s00231-013-1164-5.

Kribus, A., Doron, P., Rubin, R., Reuven, R., Taragan, E., Duchan, S. and Karni, J. (2001) 'Performance of the Directly-Irradiated Annular Pressurized Receiver (DIAPR) Operating at 20 bar and 1200 degree Celsius', *Journal of Solar Energy Engineering*, 123, pp. 10–17. doi: 10.1115/1.1345844.

Kribus, A., Grijnevich, M., Gray, Y. and Caliot, C. (2013) 'Parametric study of volumetric absorber performance', *Energy Procedia*, 49, pp. 408–417. doi: 10.1016/j.egypro.2014.03.044.

Kribus, A., Gray, Y., Grijnevich, M., Mittelman, G., Mey-Cloutier, S. and Caliot, C. (2014) 'The promise and challenge of solar volumetric absorbers', *Solar Energy*, 110, pp. 463–481. doi: 10.1016/j.solener.2014.09.035.

Labovský, J. and Jelemenský, E. (2013) 'CFD-based atmospheric dispersion modeling in real urban environments', 67(12), pp. 1495–1503. doi: 10.2478/s11696-013-0388-7.

Lee, H., Kim, J., Lee, S., Yoon, H., Kang, Y. and Park, M. (2015) 'Calculation of optical efficiency for the first central-receiver solar concentrator system in Korea', *Energy Procedia*, 69, pp. 126–131. doi: 10.1016/j.egypro.2015.03.015.

Li, Q., Bai, F., Yang, B., Wang, Z., El Hefni, B., Liu, S., Kubo, S., Kiriki, H. and Han, M. (2016) 'Dynamic simulation and experimental validation of an open air receiver and a thermal energy storage system for solar thermal power plant', *Applied Energy*, 178, pp. 281–293. doi: 10.1016/j.apenergy.2016.06.056.

Lubkoll, M., Von Backström, T. W. and Kröger, D. G. (2014) 'SURVEY ON PRESSURIZED AIR RECEIVER DEVELOPMENT', in *Southern African Solar Energy Conference*.

Malalasekera, W. and Versteeg, H. K. (1995) 'Turbulence and its modelling', in *An Introduction to Computational Fluid Dynamics*. London: Longman Scientific & Technical, p. 42.

Marcos, Ñ., Romero, M., Palero, S. and Jesu, M. (2004) 'Analysis of air return alternatives for CRS-type open volumetric receiver', 29, pp. 677–686. doi: 10.1016/S0360-5442(03)00176-2.

Marcos, M. J., Romero, M. and Palero, S. (2004) 'Analysis of air return alternatives for CRS-type open volumetric receiver', *Energy*, 29(5–6), pp. 677–686. doi: 10.1016/S0360-5442(03)00176-2.

Menter, F. R. (1994a) 'Two-Equation Eddy-Viscosity Turbulence Models for Engineering Applications', 32(8). doi: 10.2514/3.12149.

Menter, F. R. (1994b) 'Two-Equation Eddy-Viscosity Turbulence Models for Engineering Applications', 32(8). doi: 10.2514/3.12149.

Mey, S., Caliot, C., Flamant, G., Kribus, A. and Gray, Y. (2013) 'Optimization of high temperature SiC volumetric solar absorber', *Energy Procedia*, 49(0), pp. 478–487. doi: 10.1016/j.egypro.2014.03.051.

Moses, M. (2017) *Ocean acidification is global warming's forgotten crisis*, *Climate Home News*. Available at: <https://www.climatechangenews.com/2017/05/15/ocean-acidification-global-warmings-forgotten-crisis/> (Accessed: 10 January 2020).

- Palero, S., Romero, M. and Castillo, J. L. (2008) ‘Comparison of Experimental and Numerical Air Temperature Distributions Behind a Cylindrical Volumetric Solar Absorber Module’, *Journal of Solar Energy Engineering*, 130(1), p. 011011. doi: 10.1115/1.2807046.
- Patel, R. and Ramani, S. (2015) ‘Determination of Optimum Domain Size for 3D Numerical Simulation in ANSYS CFX’, pp. 4671–4679. doi: 10.15680/IJRSET.2015.0406126.
- Pitot de la Beaujardiere, J.-F., Reuter, H. C. R., Klein, S. A. and Reindl, D. T. (2016) ‘Impact of HRSG characteristics on open volumetric receiver CSP plant performance’, *Solar Energy*, 127, pp. 159–174. doi: 10.1016/j.solener.2016.01.030.
- Pitot de la Beaujardiere, J.-F. P. (2019) *Performance Modelling of an Open Volumetric Receiver CSP Plant Incorporating Rock Bed Thermal Storage*.
- Poživil, P., Aga, V., Zagorskiy, A. and Steinfeld, A. (2014) ‘A pressurized air receiver for solar-driven gas turbines’, *Energy Procedia*, 49, pp. 498–503. doi: 10.1016/j.egypro.2014.03.053.
- Price, T. (2010) *Integrated solar combined cycle plants: Right place, right time, New Energy Update*. Available at: <https://analysis.newenergyupdate.com/csp-today/technology/integrated-solar-combined-cycle-plants-right-place-right-time> (Accessed: 24 February 2020).
- Relancio, J., Cuellar, A., Walker, G. and Ettmayr, C. (2017) ‘South African CSP projects under the REIPPP programme – Requirements, challenges and opportunities South African CSP Projects Under the REIPPP Programme – Requirements, Challenges and Opportunities’, in *AIP Conference Proceedings*. doi: 10.1063/1.4949199.
- Río, A., Korzynietz, R., Brioso, J. A., Gallas, M., Ordóñez, I. and Quero, M. (2015) ‘Soltrec - Pressurized volumetric solar air receiver technology’, *Energy Procedia*, 69, pp. 360–368. doi: 10.1016/j.egypro.2015.03.042.
- Roldán, M. I., Smirnova, O., Fend, T., Casas, J. L. and Zarza, E. (2014) ‘Thermal analysis and design of a volumetric solar absorber depending on the porosity’, *Renewable Energy*, 62, pp. 116–128. doi: 10.1016/j.renene.2013.06.043.
- Roldán, M. I., Fernández-Reche, J. and Ballestrín, J. (2016) ‘Computational fluid dynamics evaluation of the operating conditions for a volumetric receiver installed in a solar tower’, *Energy*, 94, pp. 844–856. doi: 10.1016/j.energy.2015.11.035.
- Samanes, J., García-barberena, J. and Zaversky, F. (2015) ‘Modeling solar cavity receivers: a review and comparison of natural convection heat loss correlations’, *Energy Procedia*, 69, pp. 543–552. doi: 10.1016/j.egypro.2015.03.063.
- Schwarzboezl, P. (2019a) *Pressure-Velocity Characteristic Curve*. Cologne.
- Schwarzboezl, P. (2019b) *Thermophysical properties of SolAir module material*. Cologne.
- Shih, T.-H., Liou, W. W., Shabbir, A., Yang, Z. and Zhu, J. (1994) ‘A New k-epsilon Eddy Viscosity Model for High Reynolds Number Turbulent Flows-Model Development and Validation’, (September 2014).
- Stadler, H., Tiddens, A., Schwarzbözl, P., Göhring, F., Baumann, T. and Trautner, J. (2017a) ‘Improved performance of open volumetric receivers by employing an external air return system’, *Solar Energy*, 155, pp. 1157–1164. doi: 10.1016/j.solener.2017.07.050.
- Stadler, H., Tiddens, A., Schwarzbözl, P., Göhring, F., Baumann, T. and Trautner, J. (2017b) ‘Improved performance of open volumetric receivers by employing an external air return system’, *Solar Energy*, 155, pp. 1157–1164. doi: 10.1016/j.solener.2017.07.050.

- Stadler, H., Maldonado, D., Matthias, O., Schwarzbözl, P. and Trautner, J. (2019) ‘CFD model for the performance estimation of open volumetric receivers and comparison with experimental data’, 177(November 2018), pp. 634–641. doi: 10.1016/j.solener.2018.11.068.
- Téllez, F. M. (2003) ‘Thermal Performance Evaluation of the 200 kWh SolAir Volumetric Receiver’, *Performance Evaluation*.
- Tiwari, G. N. and Suneja, S. (1997) *Solar Thermal Engineering Systems*. Narosa Publishing House.
- Tu, J., Yeoh, G. H. and Liu, C. (2008) ‘Guidelines on Grid Generation’, in *Computational Fluid Dynamics A Practical Approach*. First. Oxford: Elsevier, pp. 224–244.
- Uhlig, R., Flesch, R., Gobereit, B., Giuliano, S. and Liedke, P. (2014) ‘Strategies enhancing efficiency of cavity receivers’, *Energy Procedia*, 49, pp. 538–550. doi: 10.1016/j.egypro.2014.03.058.
- Versteeg, H. . and Malalasekera, W. (1995) ‘Implementation of boundary conditions’, in *An Introduction to Computational Fluid Dynamics The Finite Volume Method*. London: Longman Scientific & Technical, pp. 196–197.
- Versteeg, H. K. and Malalasekera, W. (1995) ‘Solution Algorithms for Pressure-Velocity Coupling in Steady Flows: A Finite Volume Method’, in *An Introduction to Computational Fluid Dynamics*. London: Longman Scientific & Technical, pp. 135–140.
- Wang, F., Shuai, Y., Tan, H., Zhang, X. and Mao, Q. (2013) ‘Heat transfer analyses of porous media receiver with multi-dish collector by coupling MCRT and FVM method’, *Solar Energy*, 93, pp. 158–168. doi: 10.1016/j.solener.2013.04.004.
- Wang, F., Shuai, Y., Tan, H. and Yu, C. (2013) ‘Thermal performance analysis of porous media receiver with concentrated solar irradiation’, *International Journal of Heat and Mass Transfer*, 62(1), pp. 247–254. doi: 10.1016/j.ijheatmasstransfer.2013.03.003.
- Wang, P., Vafai, K. and Liu, D. Y. (2014) ‘Analysis of radiative effect under local thermal non-equilibrium conditions in porous media-application to a solar air receiver’, *Numerical Heat Transfer; Part A: Applications*, 65(10), pp. 931–948. doi: 10.1080/10407782.2013.850917.
- Wesley, M. L., Coulter, R. L., Hicks, B. B. and Sisteron, D. L. (1983) ‘Difficulties in Using Power Laws for Wind Energy Assessment’, *Solar Energy*, 31(2), pp. 201–204. doi: 10.1016/0038-092X(83)90082-8.
- Wilcox, D. C. (1992a) ‘The Remarkable Ability of Turbulence Model Equation To Describe Transition’, 1(9).
- Wilcox, D. C. (1992b) ‘The Remarkable Ability of Turbulence Model Equation To Describe Transition’, in *The Fifth Symposium on Numerical and Physical Aspects of Aerodynamic Flows*. Available at: <https://strives-uploads-prod.s3.us-gov-west-1.amazonaws.com/19930018243/19930018243.pdf?AWSAccessKeyId=AKIASEVSKC45ZTTM42XZ&Expires=1602850813&Signature=yzw%2BtrmarOYAMUv%2F1%2BRbmX11axA%3D>.
- WMO (2019) *WMO confirms past 4 years were warmest on record*, *World Meteorological Organization*. Available at: <https://public.wmo.int/en/media/press-release/wmo-confirms-past-4-years-were-warmest-record>.
- Wu, Z., Caliot, C., Bai, F., Flamant, G., Wang, Z., Zhang, J. and Tian, C. (2010) ‘Experimental and numerical studies of the pressure drop in ceramic foams for volumetric solar receiver applications’, *Applied Energy*, 87(2), pp. 504–513. doi: 10.1016/j.apenergy.2009.08.009.
- Wu, Z., Caliot, C., Flamant, G. and Wang, Z. (2011a) ‘Coupled radiation and flow modeling in ceramic foam volumetric solar air receivers’, *Solar Energy*, 85(9), pp. 2374–2385. doi:

10.1016/j.solener.2011.06.030.

Wu, Z., Caliot, C., Flamant, G. and Wang, Z. (2011b) 'Numerical simulation of convective heat transfer between air flow and ceramic foams to optimise volumetric solar air receiver performances', *International Journal of Heat and Mass Transfer*, 54(7–8), pp. 1527–1537. doi: 10.1016/j.ijheatmasstransfer.2010.11.037.

Xu, C., Song, Z., Chen, L. der and Zhen, Y. (2011) 'Numerical investigation on porous media heat transfer in a solar tower receiver', *Renewable Energy*, 36(3), pp. 1138–1144. doi: 10.1016/j.renene.2010.09.017.

Yang, Y., Gu, M. and Jin, X. (2009) 'NEW INFLOW BOUNDARY CONDITIONS FOR MODELING THE NEUTRAL EQUILIBRIUM ATMOSPHERIC BOUNDARY LAYER IN SST k- ω M ODEL', in *Asia-Pacific Conference on Wind Engineering*. Taipei, pp. 1–8.

APPENDIX

a. Appendix A

The C codes that were used to define the temperature dependent thermophysical properties of air as user-defined functions in Fluent for the HiTRec-II model as well as the standard and baffled SolAir models are as follows,

```
#include "udf.h"

DEFINE_PROPERTY(cell_density, cell, thread)
{
    real rho_f;
    real temp = C_T(cell, thread);
    rho_f = 3.565*exp(-0.006611*temp) + 0.923*exp(-0.000966*temp);
    return rho_f;
}

DEFINE_PROPERTY(cell_viscosity, cell, thread)
{
    real mu_f;
    real temp = C_T(cell, thread);
    mu_f = (((1.458e-06)*pow(temp,3/2))/(temp + 110.4));
    return mu_f;
}
```

The C codes that were used to define the temperature dependent thermal conductivity of recrystallized silicon carbide and siliconized silicon carbide for the standard and baffled SolAir model are as follows,

```
#include "udf.h"

DEFINE_PROPERTY(thermal_conductivity_resic, cell, thread)
{
    real ktc;
    real temp = C_T(cell, thread);
```

```
    ktc = 40417*pow(temp, -1.019);  
    return ktc;  
}  
DEFINE_PROPERTY(thermal_conductivity_sisic, cell, thread)  
{  
    real ktc, I;  
    real temp = C_T(cell, thread);  
    ktc = 140042*pow(temp, -1.142);  
    return ktc;  
}
```

b. Appendix B

The regression curve, which established the relationship between outlet air temperature, mass flow rate and the incident solar irradiation of the SolAir-200 test rig, was derived from the experimental data provided in Table A-1 (Télez, 2003).

Table A-1: SolAir-200 receiver test rig experimental data

Air Mass Flow [kg/s]	Power Incident/Airflow [kJ/kg]	Outlet Temperature [K]
0.378	672.051	600.521
0.387	669.279	600.863
0.364	689.821	599.815
0.356	724.163	602.775
0.38	779.32	646.204
0.383	818.133	651.671
0.381	829.737	647.335
0.373	808.746	642.64
0.368	791.642	644.173
0.377	771.227	647.623
0.382	750.824	656.981
0.372	831.695	697.576
0.374	826.961	698.121
0.373	822.141	699.677
0.355	818	687.781
0.377	885.509	720.486
0.355	971.011	750.55
0.361	963.32	746.574
0.367	931.972	754.466
0.354	954.022	748.867
0.364	948.571	757.397
0.36	971.257	753.499
0.359	988.974	756.345
0.355	980.481	747.564
0.345	1127.922	801.601
0.345	1069.867	770.666
0.347	1100.727	803.402
0.349	1057.077	799.35
0.297	704.642	597.299
0.298	763.006	629.164
0.296	691.426	641.821
0.3	791.116	653.682

0.301	759.867	649.294
0.3	764.263	653.757
0.298	764.281	625.218
0.32	880.926	704.899
0.32	862.722	701.866
0.317	878.183	705.359
0.309	896.71	704.033
0.286	860.271	685.571

c. Appendix C

The outlet air temperatures of the six absorber modules in the centre row of the SolAir-200 CFD model obtained from the wind loading simulations are recorded in Table A-2.

Table A-2: Outlet air temperatures obtained from wind study of standard SolAir model

		$T_{\text{module 1}}$ [K]	$T_{\text{module 2}}$ [K]	$T_{\text{module 3}}$ [K]	$T_{\text{module 4}}$ [K]	$T_{\text{module 5}}$ [K]	$T_{\text{module 6}}$ [K]	T_{av} [K]
5 m/s	0°	1192	1153.90	1141.70	1140.80	1137.30	1170.10	1155.97
	30°	1023.50	1063.90	1106.30	1131.40	1139.70	1155.80	1103.43
	60°	945.79	1009.80	1089.70	1151.90	1207.30	1190.60	1099.18
	90°	910.34	999.35	1073.60	1088.10	1208.10	631.72	985.20
10 m/s	0°	1120.20	1112.40	1112.70	1104.30	1067	1152.20	1111.47
	30°	916.28	1022.70	1130.30	1164.60	1216.60	910.49	1060.16
	60°	879.61	1051.70	1101.90	1096.40	973.74	878.23	996.93
	90°	824.32	977.26	977.73	904.43	901.49	620.02	867.54
15 m/s	0°	1093.20	1091.70	1087.50	1084.80	1102.40	1065.40	1087.53
	30°	870.76	1015.70	1095.10	1003.10	1058.10	704.76	957.92
	60°	787.75	945.85	904.36	903.03	791.15	688.57	836.79
	90°	726.81	836.91	791.78	763.37	729.26	528.78	729.485
20 m/s	0°	987.68	1059.30	1102.30	1136.80	1178.30	863.84	1054.7
	30°	793.22	935.65	943.03	858.45	903.42	578.04	835.3
	60°	711.87	802.30	763.81	763.55	686.27	572.87	716.78
	90°	653.21	719.69	685.32	673.62	623.91	476.39	638.69
25 m/s	0°	1095.71	1115.10	1110.80	1099.7	1087.8	785.80	1049.1
	30°	730.32	848.16	825	757.93	787.82	503.94	742.2
	60°	645.44	697.37	671.28	660.50	611.43	498.66	630.78
	90°	601.68	635.98	612.03	603.49	559.7	444.02	576.15

The values of the outlet air temperatures measured for the baffled SolAir model for the wind analysis are given in Table A-3.

Table A-3: Wind study carried out on SolAir model with 70 mm vertical baffle

		$T_{\text{module 1}}$ [K]	$T_{\text{module 2}}$ [K]	$T_{\text{module 3}}$ [K]	$T_{\text{module 4}}$ [K]	$T_{\text{module 5}}$ [K]	$T_{\text{module 6}}$ [K]	T_{av} [K]
15 m/s	0°	1063.1	1120.4	1171.1	1243.1	1286.2	1297.8	1197.5
	30°	908.56	1111.9	1121.7	1141.9	818.89	1307.4	1068.4
	60°	799.05	960.71	986.29	1124.3	1097.5	1133	1016.8
	90°	843.58	1097.10	1076.70	987.47	912.86	835.38	958.85
25 m/s	0°	920.56	1058.8	1133.4	1179.4	1225	1262.3	1129.91
	30°	751.30	844.39	813.31	976.52	645.67	1242.8	879
	60°	690.97	778.96	793.26	878.85	823.67	1014.9	830.1
	90°	814.73	985.34	1013.7	1015.8	926.2	822.67	929.74

The values of the outlet air temperatures measured for the SolAir receivers with 50 mm baffles for the wind analysis are given in Table A-4.

Table A-4: Wind study carried out on SolAir model with 50 mm vertical baffle

		$T_{\text{module 1}}$ [K]	$T_{\text{module 2}}$ [K]	$T_{\text{module 3}}$ [K]	$T_{\text{module 4}}$ [K]	$T_{\text{module 5}}$ [K]	$T_{\text{module 6}}$ [K]	T_{av}
15 m/s	0°	1133	1173.20	1244.40	1292.20	1332	1288.30	1243.85
	30°	952.31	1032.50	1091.80	1099.10	1052.60	1202.20	1071.75
	60°	805.48	862	981.97	1033.40	986.21	1200.80	978.31
	90°	826.21	908.59	1115.70	1116.80	908.27	826.53	950.35
25 m/s	0°	1006	1023.1	1105.6	1174.5	1221.6	1273.8	1134.10
	30°	803.04	890.65	946.24	984.24	966.01	1054	940.69
	60°	715.12	769.05	866.12	896.36	954.84	1081.40	880.48
	90°	815.01	915.4	1049.3	1021.9	926.36	832.78	926.79

The values of the outlet air temperatures measured for the SolAir receivers with 30 mm baffles for the wind analysis are given in Table A-5.

Table A-5: Wind study carried out on SolAir model with 30 mm vertical baffle

		T_{module 1} [K]	T_{module 2} [K]	T_{module 3} [K]	T_{module 4} [K]	T_{module 5} [K]	T_{module 6} [K]	T_{av}
15 m/s	0°	1182.1	1207.4	1222.2	1227.1	1243.9	1326.4	1234.85
	30°	887.75	1035.3	897.93	1032.8	926.66	1107.5	981.32
	60°	825.87	894.57	951.12	876.63	953.83	1009.7	918.62
	90°	807.99	910.33	979.97	949.55	943.94	851.13	907.15
25 m/s	0°	1105	1132.80	1110.9	1103.9	1143.1	1274.5	1145.03
	30°	823.03	896.85	899.30	944.90	922.43	994.73	913.54
	60°	713.34	776.53	839.63	828.91	831.62	884.87	812.48
	90°	742.62	787.81	887.26	886.02	804.53	737	807.54